Model development for efficient simulation of CO2 storage

Tore Ingvald Bjørnarå

Avhandling for graden philosophiae doctor (ph.d.)
Universitetet i Bergen
2018

UNIVERSITETET I BERGEN

Model development for efficient simulation of CO2 storage

Tore Ingvald Bjørnarå

Avhandling for graden philosophiae doctor (ph.d.)
ved Universitetet i Bergen

2018

Dato for disputas: 16.02.2018

År: 2018

Tittel: Model development for efficient simulation of CO2 storage

Navn: Tore Ingvald Bjørnarå

Trykk: Skipnes Kommunikasjon / Universitetet i Bergen

Preface

A thesis is submitted as a partial fulfillment of the requirements for the degree of Doctor of Philosophy at the University of Bergen.

The advisory committee has consisted of Prof. Jan M. Nordbotten (University of Bergen) and Dr. Joonsang Park (Norwegian Geotechnical Institute, Oslo, Norway).

Acknowledgements

It has truly been an interesting journey and period of my life from the initial spark of an idea of doing a PhD, to formulating the application and description of my topic, writing papers and presentations, and finally completing this thesis. I consider myself lucky for getting this opportunity to stimulate my general curiosity and there are several people I would like to acknowledge and thank for their contributions to this PhD-event in various ways. First, I want to express my gratitude to my two supervisors, Prof. Jan M. Nordbotten and Dr. Joonsang Park. I highly appreciate our discussions which have always been fruitful and insightful. It is comforting to know you have someone to ask that will push you in the right direction.

Going back a few years, to my pre-PhD time, I was employed by NGI (Oslo, NO) that encourages and supports their employees to continuously develop, both personally and professionally, to acquire new knowledge, including studying for a PhD while still being employed. I had recently started looking into CO_2 storage (there is something oddly satisfying about watching a numerical solution of CO_2 migrate through a porous medium) but there were many things related to the physical processes and the equations behind them that I did not understand, yet. I knew that a PhD-study would give me the opportunity to really delve into and explore this interesting topic, and it was Simon A. Mathias at Durham University (UK) that kick-started the process by asking if I ever considered doing a PhD. Together we formulated the initial description of my PhD-plan and I eventually spent about 18 months between 2012 and 2014 in Durham, working alongside Simon and enjoying and benefitting from every moment of it. I want to thank him for the good time in Durham.

Also, I want to express my gratitude to NGI, and Knut H. Andersen and Suzanne Lacasse in particular, for giving me this opportunity by granting my application in 2011 to partially sponsor my PhD-plan. This PhD was also sponsored by the research project MatMoRA-II (Geological Storage of CO_2: Mathematical Modelling and Risk Assessment, 2012-2015), which was in part funded by the CLIMIT-programme at the Research Council of Norway (project number 215641) and in part by the industry. I gratefully acknowledge this support.

As a PhD-student I was affiliated to the University in Bergen, the Department of Mathematics, and I spent a lot of time in Bergen, about four months every year between 2012 and 2014. In addition, through the Porous Media Group at the Department of Mathematics in Bergen, I was also affiliated to NUPUS, an international and interdisciplinary cooperation of Universities and Scientists, and I have many fond memories from the workshops I attended in Freudenstadt (DE), getting to know the other great students and members of NUPUS. All this time in both Durham and Bergen has given me the opportunity to meet and get to know a lot of nice and interesting people. I want to thank them all for both work-related and non-work related conversations and good

times in general, both inside and outside the universities. And last, but definitely not least, I would like to thank my family, friends at home and colleagues at NGI, demonstrating very well that life goes on in parallel with doing a PhD... and "Yes, I finally submitted!"

Thank you (also for asking)!

Abstract

Carbon capture and storage (CCS) is an important component of several initiatives to reduce global greenhouse gas emissions by injecting and storing CO_2 in underground reservoirs. Simulation technology plays an important role in providing storage capacity estimates and analyzing long-term safety and risk factors of leakage to the surface. Two of several important questions that need to be answered before a storage project may be approved is how fast and how much CO_2 can be injected without compromising the integrity of the sealing caprock, which stops it from migrating to the surface.

To evaluate the integrity we rely on mathematical models, but due to the large extent of the area that needs to be considered and the many processes that are involved the calculations can quickly become large and complicated and very time consuming to solve. For screening purposes of potential storage sites, or investigation of potential storage sites when little data is available, many model realizations are needed, thus fast and robust yet accurate numerical techniques are not only tractable but also essential.

To understand what happens to the CO_2, formation water and rock during injection and storage, we have thoroughly reviewed the main processes that are relevant to the integrity of the reservoir and sealing formations. These main processes are fluid flow, stress change and temperature change and they are all coupled where for instance a change in pore pressure and temperature due to CO_2 injection causes deformations and stress alterations that can affect the integrity of the injection reservoir and caprock.

Considering the low solubility of CO_2 in formation water under typical storage conditions (depth, temperature, pressure and salinity) we have illustrated that it is a good approximation to treat the injected CO_2 and formation water as two separate fluids. Miscibility is therefore not an important process to consider in relation to long-term mechanical integrity and this simplifies the mathematical description of fluid flow.

Whether the thermo-hydro-mechanical coupling, where the temperature change is also considered, is important to evaluate is less obvious. Through examples we show that the in situ temperature is important to consider when estimating material properties, but the effect of the cold (CO_2) injection, relative to the storage formation, is very local and mainly affects the near-field of the injector. The cooling effect reduces the spreading of the CO_2, but has little effect on the pore pressure. In general, cold injection (relative to formation temperature) lowers the fracture pressure of the rock and the limit for maximum sustainable injection rate, and therefore, ignoring non-isothermal effects can underestimate the risk of failure, and vice versa for hot injection. A risk analysis of reactivation of faults in the sealing formation in the CO_2 storage project at In Salah, Algeria, revealed that the thermal effect can make the difference between safe and risky storage.

To achieve a procedure for faster numerical evaluation, the layering structure and high aspect ratio of typical storage reservoirs can be used to simplify the mathematical

description of the internal physical processes using a method of dimensional reduction. This has previously been found particularly attractive in simulating the migration of CO_2 in the context of CCS. Since hydro-mechanical coupling is particularly essential to consider when evaluating the integrity of the caprock, we have extended this concept to also include the geomechanical processes. The underlying assumptions of negligible vertical flow compared to horizontal flow (Vertical Equilibrium, VE, assumption) and linearly varying displacement across the thickness of the reservoir (Linear Vertical Deflection, LVD, assumption) has proved promising in providing significant savings in computational time and effort with up to more than ten times faster calculations compared to a full-dimensional model. It has also been demonstrated that such models can retain a high accuracy when applied to realistic field data, such as the conditions at the CO_2 storage plant at In Salah, Algeria. Also, the range of applicability of the dimensionally reduced model is to a leading order the thickness of the reduced domain and accurate solutions in the order of 0.1 % and less difference in solution compared to a full-dimensional formulation for aquifers up to 100 meters thick has been achieved.

List of papers

The following publications were written during and within the scope of the PhD project.

Title: ***A Pseudospectral Approach to the McWhorter and Sunada Equation for Two-Phase Flow in Porous Media with Capillary Pressure*.**
Authors: **Tore I. Bjørnarå**[1,3] and Simon A. Mathias[2].
Journal: Computational Geosciences.

Division of work between the authors: This paper was the result of a joint effort. Simon A. Mathias (SAM) proposed the topic, Tore I. Bjørnarå (TIB) did a literature review, coded the equations and wrote an initial draft. The final version was co-written by SAM and TIB.

Title: ***Fast Evaluation of Fluid-rock Coupling in CO_2 Storage*.**
Authors: **Tore I. Bjørnarå**[1,3], Simon A. Mathias[2], Jan M. Nordbotten[3] and Joonsang Park[1].
Conference paper: Fourth EAGE CO_2 Geological Storage Workshop 22-24. April 2014, Stavanger, Norway.

Division of work between the authors: The topic was raised by Tore I. Bjørnarå and Joonsang Park, Simon A. Mathias helped formulating the outline of the scope of studies and all authors help in proof-reading the final version.

Title: ***Capturing the Coupled Hydro-Mechanical Processes Occurring During CO_2 Injection - Example from In Salah*.**
Authors: **Tore I. Bjørnarå**[1,3], Simon A. Mathias[2], Jan M. Nordbotten[3], Joonsang Park[1] and Bahman Bohloli[1].

[1]NGI
[2]Durham University
[3]University of Bergen

Conference/journal paper: GHGT-12 conference/Energy Procedia.

Division of work between the authors: The scope and outlines of the studies was formulated by Tore I. Bjørnarå (TIB). TIB derived the formulations with valuable help from Jan M. Nordbotten (JMN) and Joonsang Park (JP). TIB implemented the code and did the numerical calculations and wrote the draft of the paper. The co-authors supported and contributed at various capacity: Simon A. Mathias, JP and JMN contributed with valuable discussion during the development of the mathematical formulation and the underlying mathematics and Bahman Bohloli (BB) helped define the geological model. JP, JMN and BB also helped in proof-reading the final paper version.

Title: ***Vertically Integrated Models for Coupled Two-Phase Flow and Geomechanics in Porous Media*.**
Authors: **Tore I. Bjørnarå**[1,3], Jan M. Nordbotten[3] and Joonsang Park[1].
Journal: Water Resources Research.

Division of work between the authors: The scope and outlines of the studies was formulated by Tore I. Bjørnarå (TIB). TIB derived the formulations with valuable help from Jan M. Nordbotten (JMN) and Joonsang Park (JP). TIB implemented the code, did the numerical calculations and wrote most of the initial paper-draft. JMN contributed significantly in the writing of the final paper, e.g. the abstract and introduction, parts of the governing equations and results and discussion, JP proof-read several versions of the paper.

Title: ***Field-data analysis and hydromechanical modeling of CO_2 storage at In Salah, Algeria*.**
Authors: **Tore Ingvald Bjørnarå**[1,3], Bahman Bohloli[1] and Joonsang Park[1].
Journal: Submitted (International Journal of Greenhouse Gas Control).

Division of work between the authors: Bahman Bohloli (BB) started writing a paper on surface uplift and hydromechanical modeling of CO_2 storage at In Salah, but with emphasis on and analysis of unpublished surface uplift data. The paper was split into a paper focusing on the material related to surface uplift [26] and this paper, which was largely re-written to the current version by Tore Ingvald Bjørnarå (TIB), but without the surface uplift data, and numerical modeling was given more emphasis. Joonsang Park did some of the early numerical simulations, has been proof-read the drafts and contributed in writing parts of the conclusion.

Contents

Chapter 1

Introduction

1.1 Background

The first main conclusion from the fifth, and latest, report by the Intergovernmental Panel on Climate Change (IPCC) reads: *"Warming of the climate system is unequivocal, and since the 1950s, many of the observed changes are unprecedented over decades to millennia. The atmosphere and ocean have warmed, the amounts of snow and ice have diminished, sea level has risen, and the concentrations of greenhouse gases have increased."* [107]. The effect is more extreme weather at increasingly higher material and human cost and the rapidly rising levels of carbon in the atmosphere, which is currently at its highest in the last 800,000 years, is believed, beyond reasonable doubt, to be the the main cause.

Carbon dioxide is a by-product of fossil fuels combustion, and because 80% of the worlds energy supply comes from fossil fuels [e.g. Fig. 2.13 56], it will continue to be an important and valuable source for decades to come. The only viable solution to achieve mitigation goals of carbon neutrality is through Carbon Capture and Storage (CCS) [43]. CCS is a process that captures carbon dioxide emissions from point sources, e.g. coal-fired power plants, and either reuses it, for instance for the purpose of enhanced oil and gas recovery (EOR and EGR, respectively), or stores it safely underground. Geologic formations suitable for carbon dioxide storage typically include oil and gas reservoirs, unmineable coal seams and deep saline reservoirs - structures that have stored crude oil, natural gas, brine and carbon dioxide over millions of years. In fact, CO_2 have been used for EOR for decades already, since the 1970s, and later in several sequestration projects, hence the technology is proven, at least on small to moderate scale of up to 1 megatons CO_2 injected per year. When it comes to site selection, it is argued, that storage in abandoned and under-pressurized oil and gas reservoirs is the preferred choice. This is mainly due to the amount of data and knowledge available of the sites, its proven ability to store oil and gas for millions of years and that the infrastructure for CO_2 transport is already partly in place. However, there are doubts about the capacity and integrity and there are also concerns whether there are considerable oil and gas resources left yet to be recovered with improved technology and techniques. The contribution to indefinite storage is presumably low [57, p. 12].

In order to be part of the solution to reduce the anthropogenic emissions, the deployment of CCS needs to be on the scale of hundreds of gigatons of CO_2 over the course of the 21'st century, according to the stabilization scenarios described by IPCC [ch. 6 and

7.11 in 43]. Unfortunately, pressure build-up from the injection of CO_2 causes stress alterations in the formation that can affect the integrity of not only the reservoir and caprock, but also the surrounding formations. Thus, higher injection rates and injection volumes increases the stress and exposes a larger area to potential leakage. In addition, far-field pressure effects can interfere with hydrocarbon production, geothermal reservoirs and underground water reservoirs and there are concerns about significant induced seismic events due to large-scale CCS. Assuming that the earths crust is close to being critically stressed, a lot of potential stored strain energy can be released when the stress field is disturbed by changing the pressure, and in the worst case lead to large earthquakes [127]. On the other hand, there is also doubt about whether this concern is justified for typical CCS projects, considering the rather shallow depths (1-3 km) compared to typical earthquake hypocenters (typicaly 8-16 km) [59]. And according to Davies et al. [37], from a compilation of hundreds of fracturing operations only three examples of induced seismicity high enough to be felt, by people, had been documented. Thus, although large faults and fractures can often be identified and avoided, it cannot be ruled out that reactivation of existing faults can induce felt seismicity. This emphasizes the need for improved understanding of the connection between induced seismicity and fault activation and geological characterization in the context of CCS, relating to the stress alterations due to injection. These are some of the challenges faced by successful CCS.

The CCS Directive[1] provides a legal framework for safe geological storage of carbon dioxide in the EU. It applies to storage projects larger than 100 kilotons of carbon dioxide and contains an extensive list of criteria for "*characterisation and assessment of the potential storage complex and surrounding area*", highlighting the need for assessing the many uncertainties by considering a range of scenarios. These uncertainties can for instance be related to parameters in the geological description and material properties. Teletzke and Lu [108] highlight key topics in modeling of the different stages of a CO_2 storage project; from initial screening and selection of potential sites through to development planning, implementation and operation and finally to site closure and post-injection monitoring. The level of required details in the models will change as the project moves through the various phases, expressing the need for different fit-for-purpose models. When evaluating different scenarios, well configurations, injection strategies and the many uncertainties in geology and material properties, many model realizations will be required. Therefore, particularly in the initial stages of CCS planning, fast and accurate numerical techniques are essential.

There are several mechanisms that contribute to trap the injected carbon dioxide. In the long-term perspective of several hundreds to thousands of years, injected CO_2 will be trapped and stabilized due to capillary forces in small pores, dissolution in brine and mineralization with the host rock. However, in shorter terms, safe storage is relying on structural and stratigraphic trapping as the main trapping mechanism. Thus, one of the major aspects of safe CO_2 storage is therefore the integrity of the confining rock; the caprock. It is necessary to avoid exceeding the fracture pressure of the caprock during injection and the amount that can be stored is therefore pressure limited and one critical parameter is the maximum sustainable injection rate.

[1] EU Directive 2009/31/EC on the geological storage of carbon dioxide.

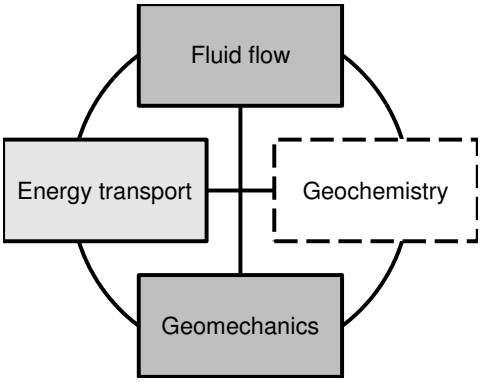

Figure 1.1: A schematic description of the various main processes in a reservoir model during production or injection.

CO_2 storage involves considering many physical processes, as indicated in Fig. 1.1. The various processes are affecting each other, indicated by the connections, but how strongly they are coupled varies with the particular condition. Considering non-isothermal conditions, temperature has an affect on fluid properties such as density and viscosity, affecting the fluid flow; temperature changes in a reservoir can induce thermal stresses, affecting the stress distribution and deformation; the fluid can react with the host rock by dissolution or precipitation, affecting the hydraulic properties and the fluid flow, and these reaction rates are often highly temperature dependent. Thus, there are many ways the various processes in Fig. 1.1 are affecting and interacting with each other. It can become complex and difficult to describe, but often times assumptions can be made that greatly simplifies the mathematical description of a particular problem. For instance, the density of brine depends on the fluid pressure, temperature and salinity. By increasing the pressure the density will increase as well. However, if the pressure change is small and temperature is almost constant, salinity will not change and a good approximation can be to consider the density as constant. This kind of reasoning and assumptions can greatly simplify the complexity of a system and represents one of the main challenges in numerical modeling; how to make good assumptions that gives good approximations.

The overall objective of this project is to *"derive the mathematical description of the main relevant processes involved in CO_2 injection and storage to assess the geomechanical integrity of the storage reservoir and the surrounding formations and analyze how these can be simplified for a faster numerical evaluation while keeping an acceptable level of accuracy"*. To achieve this, the focus in this project is the thermo-hydro-mechanical coupling; the interaction of fluid flow, energy transport and geomechanics, the grey shaded boxes in Fig. 1.1. Regarding the geochemistry branch, in the short term (decades) it is generally assumed that mineral reactions are of less importance compared to dissolution of CO_2 in the formation water and structural and stratigraphic trapping. However, on longer time scales, the mineral reactions can be significant [50]. Rocks contain different kinds of minerals where some dissolve in contact with carbonic acid (from CO_2 dissolving in water) and some precipitate and these reactions can be beneficial and/or detrimental for trapping CO_2. For instance, by allowing CO_2 to

form carbonates will promote permanent storage. Dissolving minerals can change the permeability [61] that in turn affect the flow regime in the reservoir and sealing formations and this can have both positive and negative effects on storage. Hellevang [50] showed that reactivity varies greatly between the reservoir minerals and understanding of geochemical processes are therefore important when selecting long-term storage sites. Hence, the geochemistry branch in Fig. 1.1 are considered as site specific compared to the thermo-hydro-mechanical processes and therefore will not be covered in this project.

From the above discussion, it is apparent that the models can quickly become complex and thereby difficult and time consuming to solve numerically. Geometrical simplifications, reducing the problem to a two-dimensional, axially symmetric or even one-dimensional problem, can greatly reduce the computational size and the calculation time, but such simplifications are not always possible and in this project an alternative type of simplification is exploited. By making assumptions on the variability of the solution in some direction, e.g. the vertical direction in a reservoir model, the balance equations can be integrated to obtain a dimensionally reduced form. This means that a three dimensional problem can be reduced to a two-dimensional problem while still retaining the full dimensional solution. The computational benefits of the dimensionally reduced models for two-phase flow in porous media is tremendous. Exploiting this benefit by coupling it with a complementary formulation for poroelasticity is therefore natural when also considering geomechanical effects. It greatly reduces the calculation time, the drawback is the added complexity to the mathematical description, but that is addressed in this project and honors the main objective of this project.

Dimensionally reduced models for fluid flow, single- and two-phase flow, in thin reservoirs are well established. Reduced models for single-phase flow coupled with geomechanics is well documented in early works by Bear and Corapcioglu [10, 11, 34], but little has appeared later, see for instance [105], and the analysis is limited to the aquifer, and not considering the surrounding formations. On the other hand, dimensionally reduced models for two-phase flow has received more recent attention, from simple immiscible two-phase flow models without capillary pressure [53, 82] to models including capillary pressure and hysteresis [84], partially miscible phases with convective mixing [47] and variable thermodynamic properties of the phases [5]. However, no work has shown how to couple the dimensionally reduced equations for two-phase flow, including capillary pressure, with geomechanical deformation. In addition, pore pressure and stress communication with the surrounding formations is considered.

1.2 Thesis outline

This thesis contains two parts. The first part introduces the mathematical background of the relevant processes for CO_2 injection and storage; geomechanics, single- and two-phase fluid flow and energy transport. The emphasis is on evaluation of various simplifying assumptions that can reduce the mathematical model while retaining an acceptable accuracy for evaluating the integrity of the storage reservoir and the surrounding formations. Some topics that are not covered in my papers, e.g. miscible two-phase flow and non-isothermal effects related to cold/hot injection are described in more detail.

The second part contains the journal and conference papers published during the course of the project followed by the appendices.

Chapter 2 introduces the concept of stress in a geological setting; the various stress regimes, possible stress states and how the stress-field is affected by change in pore pressure; fluid pressure in the pore space of rocks. The pore pressure and the stress-field are directly coupled to each other and a review on how this affects the stability and integrity of rocks and faults/fractures are given. Various mechanisms for failure, when and how they occur, are also reviewed, together with ways it can be illustrated, e.g. Mohr diagrams and allowable stress diagrams.

Chapter 3 introduces the theory of poromechanics which is the study of the mechanical deformation of a fluid saturated porous media. This is an extension to chapter 2, by also considering spatial and temporal changes in stress due to pore pressure and temperature changes. Here the momentum balance equation together with the constitutive relations for stress and strains for linear elasticity, poroelasticity and thermoporoelasticity is defined. The two stress conventions that are frequently encountered in the literature, compressive and extensional, are explained and some typical simplifications of the governing equation for solving linear elastic deformation are derived.

Chapter 4 introduces the governing equations for single- and multi-phase flow in porous media with detailed derivations. Although seemingly trivial, single-phase flow is reviewed in detail because of its importance in reservoir models. Multi-phase flow is important inside a reservoir, but outside the reservoir, in the surrounding formations, the flow is usually approximated as a single-phase flow problem. Typically used simplifications are derived and compared to illustrate the impact of the resulting storage coefficient. Then the equations for immiscible two-phase flow are derived and it is shown how the mass conservation equations and auxiliary equations can be manipulated to arrive at various formulations of different dependent variables. These formulations are benchmarked against a new, semi-analytic solution, using pseudospectral methods and Chebychev polynomials, of the McWhorter-Sunada equations [72] for one dimensional two-phase flow with capillary pressure [22]. A formulation for partially miscible, two-phase flow is also derived and compared to a two-component, two-phase flow extension of the Buckley-Leverett equation.

In chapter 5 the governing equation for energy transport is reviewed. A typical CO_2 storage model is defined and two models; a THM- (Thermo-Hydro-Mechanical, model considering temperature, fluid flow and geomechanics) and an HM-model (Hydro-Mechanical) is compared to analyze non-isothermal effects on phase saturation and pore pressure. The thermal effect on stresses and strains in relation to integrity and risk failure is discussed in chapter 7.

Chapter 6 introduces dimensionally reduced models. The theory from Chapters 3 and 4; linear proelasticity, single-phase flow and immiscible two-phase flow in particular (phase miscibility and non-isothermal effects are not evaluated) is used to derive the dimensionally reduced formulations of the governing equations. For single- and two-phase flow the assumption of vertical equilibrium (VE); vertical phase pressure gradients are assumed constant, is reviewed. The momentum balance equation with linear elastic and linear poroelastic constitutive relations are integrated to give the corresponding dimensionally reduced forms; Linear Vertical Deflection (LVD) equation and the Poroelastic Linear Vertical Deflection (PLVD) equation where the name reflects the assumed structure of the displacement within the dimensionally reduced domain.

Solutions and the performance of the LVD and PLVD equations are compared with the full-dimensional solution.

In Chapter 7 some findings from the previous chapters are discussed. The difference in performance for the various formulations for immiscible two-phase flow is further discussed and compared to partially miscible two-phase flow. Due to the direct coupling between the pore pressure and stresses, the effect of diffusion/dispersion and miscibility on pore pressure is evaluated. The non-isothermal effect that was reviewed in chapter 5 is discussed further in relation to stresses and strains, integrity and risk of failure. And finally, the performance of the dimensionally reduced models are discussed.

Finally, in chapter 8 Conclusion, some concluding remarks are made on the obtained results.

1.3 Thesis preface

It should be noted that in this project the focus is on the mathematical model; the description of the various physical processes related to CO_2 storage modeling, and not the choice of numerical method, solvers and mesh generators or mathematical analysis of uniqueness and existence of solution. The aim is to describe the mathematical model in a rigorous manner, highlight the various simplifying assumptions and their justifications, and present it on a form that can be implemented in a numerical framework of choice. Here, the finite element method has been chosen for the discrete approximated solution of the resulting partial differential equations. The finite element method is globally mass conservative (as opposed to, for instance, the finite volume method which is locally mass conservative) and may suffer from weaknesses such as stability for discontinuous processes, e.g. sharp saturation fronts in multi-phase flow problems, and may therefore not be the most suitable method. However, the finite element method is the standard method of choice for mechanical problems. Thus, when solving a problem that considers several physical processes, the choice of numerical tool will be a compromise of not only accuracy and stability, but also usability and ease of implementation. The particular tool of choice in this project is COMSOL Multiphysics®. It is a general purpose mathematical modeling tool designed for solving an arbitrary number of partial differential equations in arbitrary dimensions. A real strength of the chosen software is its usability and ease at which multiple physical processes can be coupled together in a model that can become progressively more complex as new data comes to light and it is easy to switch on and off different effects and adjust parameters for sensitivity studies.

1.4 Main findings

- The first complete model including a consistent, vertically integrated approach for fully coupled multi-phase flow and mechanical deformation.
  - General and dimensionally reduced equations for immiscible two-phase, with capillary pressure, and Biot's theory for linear poroelasticity are derived by integration of the governing equations across the thickness of the dimensionally reduced domain, here the vertical direction. This results in a

set of equations that can be solved very efficiently compared to solving the full-dimensional formulation.

  - The coupled model retains all the simplicities of previously developed reduced-dimensional models for flow, including less stiff nonlinear systems of equations (allowing longer time steps by the numerical solver) and less degrees of freedom (since the computational space has been reduced), making it much faster at lower computational cost.
  - Such dimensionally reduced models can retain reasonable accuracy when applied to realistic field data and the range of applicability is to a leading order the thickness of the reduced domain, e.g. the injection reservoir. When applied to a realistic CO_2 storage scenario (In Salah, Algeria) the accuracy of the solution was found to be in the order of less than 0.1% different compared to a full-dimensional formulation for up to 100 m thick reservoirs.

- A fast and robust solution procedure for one-dimensional, immiscible, two-phase flow in porous media with capillary pressure using Chebyshev spectral collocation (pseudospectral) method.

  - As a general solution to two-phase flow, and an analogue to the Buckley-Leverett equation, the equations, which were originally proposed by McWhorter and Sunada [73], has many applications that go beyond the verification of numerical codes. However, the original, iterative solution procedure by McWhorter and Sunada [73] is highly sensitive to the input parameters (particularly viscosity, relative permeability and for high saturations at the inlet), and the use of a pseudospectral method proved to be robust and converge fast.

- Analysis of non-isothermal effects related to CO_2 storage (injection of cold CO_2 relative to the warmer storage formation) has led to the following general observations:

  - Temperature is very important when evaluating the material properties of the fluid, thus temperature should not be assumed constant in space (it increases with depth). However, the thermal effect of cold injection is very local, the main transport mechanism is heat convection, but typical thermal properties results in a temperature footprint much smaller than the migration of the injected CO_2 (less than 1:10), compared to the pressure footprint. This leads to another important finding:
  - If fluid migration is the main concern then temperature can be considered constant in time (although not necessary in space). However, for the stress field it is different:
  - For cold injection, ignoring non-isothermal effects can underestimate the risk of failure (and vice versa for warm injection) around the injection well (due to the local effect). Reducing temperature induces thermal stress similar to reducing pressure.

Chapter 2

Pore pressure-stress coupling

2.1 Introduction

When considering CO_2 storage, one of the concerns is the integrity of the storage reservoir and surrounding formations. In response to injection, the fluid pressure in the pores change with a concomitant change in the mechanical stresses within the reservoir. When a rock is stressed it deforms and the stress is transferred far beyond the injected fluid and the injection reservoir to the surrounding formations. How much and how it deforms depends on the mechanical properties. If, for instance, the stress is high enough it can also fail, and weaknesses such as fractures and faults can slide, creating new leakage pathways for CO_2, and it is therefore necessary to avoid that the stress increases above the fracture pressure limit, or rock strength, or friction of fault-/fracture planes. When the stress state of a rock is altered, its physical properties can also change. However, throughout this study mechanical properties will be assumed constant.

In this chapter various typical failure mechanisms of rocks will be reviewed. Which of the mechanisms is most likely to occur is determined by the stress field. The tensor character of the coupling between pore pressure and stress leads to changes in the differential stress (difference between the maximum and minimum principal stresses) of the system, how this relates to possible failure of the rock depends on the stress regime. Stress distribution/orientation and principal stress components are critical parameters when evaluating the impact of CO_2 injection and this will also be reviewed.

2.2 Failure mechanisms

When concerned with the integrity of the aquifer and caprock, comparing the stress field to failure criteria is essential. In this section some commonly used failure criteria and failure mechanisms is reviewed, some of these will be used in later chapters when solving illustrative examples of injection processes. Three modes of failure are generally considered, see Fig. 2.1:

1. Shear failure of intact rock (red dash-dotted line)
2. Tensile failure of intact rock (red dashed line, $\sigma_n^{'} < 0$)

3. Reactivation of existing weaknesses, e.g. (cohesionless) faults and fractures (blue solid line)

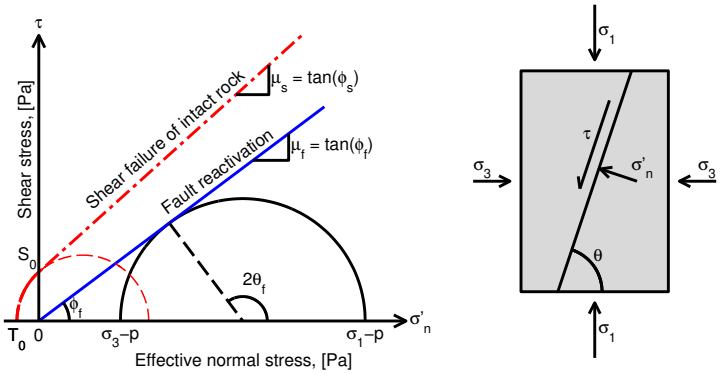

Figure 2.1: Left: Mohr diagram showing various failure modes (modified from Mathias et al. [70]). The shear failure envelope and fault reactivation are here shown as Coulomb failure envelopes. The slope of the Coulomb failure envelope, μ_s [-], is also termed the coefficient of internal friction, μ_f [-] and ϕ_f [rad] are the sliding friction coefficient and the friction angle of a fault/fracture. S_0 [Pa] is the cohesion (cohesive strength) and T_0 [Pa] is the tensile strength (at $\tau = 0$). The extensional failure envelope (red dashed line, $\sigma_n' < 0$) is described by the Griffith criterion, Eq. (2.5), which gives $S_0 = 2T_0$. Right: Sketch of a triaxial test, a laboratory test to measure the mechanical properties of rocks. θ [rad] is the angle between the normal effective stress σ_n' and the maximum principal stress σ_1.

Fig. 2.1 shows a Mohr diagram of a rock sample. The Mohr circle (black half-circle in Fig. 2.1) describes the possible states of effective normal stress[1], σ_n' [Pa], and shear stress, τ [Pa], in a fluid saturated porous sample with pore pressure p [Pa] as it is subjected to the loads σ_1 [Pa] and σ_3 [Pa], where $\sigma_1 > \sigma_3$. Note that there are an infinite number of possible stress states within a rock, but failure occurs when the Mohr circle intersects with either the shear failure envelope (red dashed-dotted line), the fault reactivation envelope (blue solid line) or tensile failure envelope (red dashed line). Coulomb failure envelopes, or compressive failure envelopes, are defined as straight lines in a shear-/normal-stress diagram where the slope of the line is the coefficient of internal friction, μ_s [-] and μ_f [-] for shear failure and fault reactivation, respectively. Typical values for the friction coefficients are $0.5 < \mu_s < 1$ and $0.6 < \mu_f < 0.85$ [104]. The Coulomb failure envelopes can be obtained from a series of triaxial tests (Fig. 2.1, right) by varying the confining stresses σ_1 and σ_3 (and pressure p). The tensile failure envelope is here exemplified by the Griffith extensional failure envelope [e.g. 104]. When positive stress is compressive the effective stress is expressed as the difference between the applied stress and the pore pressure inside the sample:

$$\sigma_n' = \sigma_n - p \tag{2.1}$$

[1]Effective stress is the part of the total stress which is carried by the solid/grains in a porous media and will be reviewed in detail in section 3.3.

Expressions for shear stress τ and normal stress σ_n acting on a plane with angle θ in terms of principal stress magnitudes can be found in [92]. In 2D they are expressed as [e.g. 118, 126]:

$$\tau = \frac{\sigma_1 - \sigma_3}{2} \sin 2\theta, \quad \sigma_n = \frac{\sigma_1 + \sigma_3}{2} + \frac{\sigma_1 - \sigma_3}{2} \cos 2\theta \tag{2.2}$$

Expressions for the principal stresses in terms of the spatial stresses are given in App. F and the stress tensor (of spatial stresses) will be reviewed in chapter 3. The angles in Fig. 2.1 are related according to:

$$2\theta_f = \pi/2 + \phi_f, \quad 2\theta_s = \pi/2 + \phi_s \tag{2.3}$$

As can be seen from Fig. 2.1, reactivation of an existing fault or fracture is normally more likely to occur before shear failure of intact rock, assuming there are faults and they are favorably oriented. However, the values of μ_s and μ_f differs between materials/rocks and they can intersect such that the likely failure mechanism may also depend on the magnitude of the normal and shear stress.

Failure criteria

It should be noted that there are many different failure criteria that are described in the literature, e.g. Griffith, Hoek-Brown, Lade, Drucker-Prager, Tresca, Von Mises and Barton-Bandis to name a few. Depending on the material, some failure criteria are preferred to others. The various criteria have different fitting parameters and as more experimental data become available they can be refined to better describe a particular rock. However, it is common to present experimental results using Mohr diagrams and Coulomb failure envelopes [126], as in Fig. 2.1 (left).

The uniaxial/unconfined compression strength (UCS, often denoted with C_0) [Pa] is a commonly used rock property. It can be determined by uniaxial stressing of a sample (no confining stress: $\sigma_2 = \sigma_3 = 0$) and the rock strength is defined as the applied load at failure: $C_0 = \sigma_1$.

The cohesive strength (cohesion), S_0 [Pa], is defined as the internal strength of the sample and can be obtained by the following relation [126]:

$$\text{UCS} = 2S_0 \left[\left(\mu_s^2 + 1 \right)^{1/2} + \mu_s \right] \tag{2.4}$$

The different failure modes in Fig. 2.1 are illustrated in Fig. 2.2. Which mode that can occur depends on the stress-state.

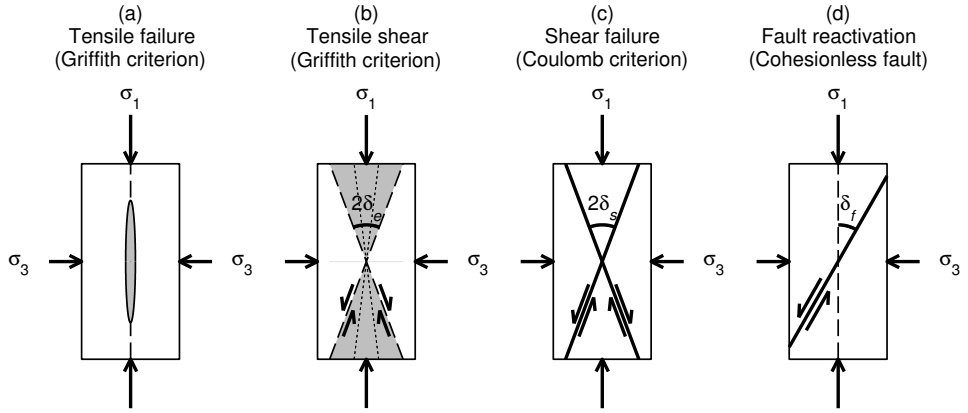

Figure 2.2: Sketch of the various failure modes in Fig. 2.1 (modified from Sibson [104]). The angles δ_i are related to the angles θ_i in Fig. 2.1 according to $\delta_i = \pi/2 - \theta_i$ (note that $0 < \delta_e < \delta_s$). With reference to Fig. 2.1 (left) the failure mechanisms are: (a) Tensile failure at $\tau = 0$, (b) Tensile shear (red dashed line), (c) Shear failure (red dashed-dotted line) and (d) fault reactivation (blue line).

Griffith criterion for tensile failure can be expressed as [e.g. 104]:

$$\tau^2 = 4T_0\sigma_n' + 4T_0^2, \quad p = \sigma_n + \frac{4T_0^2 - \tau^2}{4T_0} \tag{2.5}$$

In order for tensile failure and fractures to develop, the Mohr circle must touch the failure envelope where the shear stress is zero and the differential stress is less than $4T_0$ (see Fig. 2.2 (a)):

$$(\sigma_1 - \sigma_3) < 4T_0 \tag{2.6}$$

A conservative assumption is that a tensile fracture could develop as soon as the fluid pressure exceeds the least compressive principal stress and tensile strength T_0, leading to a critical fluid pressure for fracturing according to:

$$\boxed{p = \sigma_3 + T_0} \tag{2.7}$$

For $4T_0 < (\sigma_1 - \sigma_3) < 6T_0$ the rock can fail in a mixed mode of shear and tensile failure. The angle of the failure band is typically between tensile failure plane (pependicular to σ_3) and shear failure plane: $0 < \delta_e < \delta_s$, indicated by the shaded area in Fig. 2.2 (b).

The onset of shear failure, according to Coulomb failure criteria, occurs when $(\sigma_1 - \sigma_3) > 6T_0$, see Fig. 2.2 (c):

$$\boxed{\tau_s \geq S_0 + \sigma_n'\mu_s, \quad p = \sigma_n + \frac{S_0 - \tau_s}{\mu_s}} \tag{2.8}$$

and similarly for faults, reactivation (of cohesionless faults; $S_0 = 0$), Fig. 2.2 (d), occurs when

$$\boxed{\tau_f \geq \sigma_n'\mu_f, \quad p = \sigma_n - \frac{\tau_f}{\mu_f}} \tag{2.9}$$

In general, a failure of a favorably oriented fault or fracture can occur when (see e.g. Jaeger et al. [58], Vidal-Gilbert et al. [118], Zoback [126]):

$$\frac{\sigma_1'}{\sigma_3'} = \frac{\sigma_1 - p}{\sigma_3 - p} \geq \left[\sqrt{\left(\mu_f^2 + 1\right)} + \mu_f\right]^2 \tag{2.10}$$

where positive stress is defined compressive. Thus, by calculating the changes in the effective stress field as a result of for instance injection-induced changes in fluid pressure, the Coulomb failure criterion can be used to evaluate the likelihood of shear slip reactivation and associated induced (micro-) seismicity as slip will first occur in optimally oriented fractures or faults. If one assume randomly oriented cohesionless fractures of $\phi_f = 30°$ (a typical and conservative value for failure [95]), the onset of slip can be expressed by Eq. (2.10):

$$\sigma_1' \geq 3\sigma_3' \tag{2.11}$$

This implies that shear slip, and therefore induced seismicity, can occur whenever the maximum principal effective stress is 3 times higher than the minimum principal effective stress.

Slip-tendency T_s [-] analysis can also provide a means for assessing relative risk of earthquakes and fault slip:

$$T_s = \frac{\tau}{\sigma_n'} \tag{2.12}$$

Compared to Eq. (2.9), it can be seen that the sliding friction coefficient μ_f is the value of T_s when a cohesionless fault starts to slip [75].

When a material approaches tensile failure, when the Mohr circle in Fig. 2.1 is shifted to the left due to increasing pore pressure, there is a transition between tensile failure and shear failure (tensile shear, Fig. 2.2 (b)), depending on where the Mohr circle intersects the failure envelope. This can also be described by the dilation tendency T_d [-] which is the ability of a fracture to dilate and thus to serve as a potential path for fluid flow. The ability to transmit fluid is directly related to the aperture, which is in turn related to the effective normal stress acting on the fracture. The effective normal stress imposed on a fracture depends on the magnitude and direction of the principal stress relative to the fracture plane and the dilation tendency T_d [-] for a surface is defined as [45]:

$$T_d = \frac{\sigma_1 - \sigma_n}{\sigma_1 - \sigma_3} \tag{2.13}$$

Faults oriented perpendicular to the minimum principal stress are therefore most likely to dilate and behave in a transmissive manner.

Both slip and dilation tendency analysis (Eqs. (2.12) and (2.13)) are techniques to visually assess the stress states and potential fault activity. However, the distinction is that the dilation tendency T_d expresses the potential for dilation of fractures and thereby increase in permeability, whereas slip-tendency T_s expresses the potential for failure through fracture slip.

A few ways to determine failure or risk of events that can be crucial to successful CO_2 storage has been given above. These criteria define the upper bound to maximum injection rate and storage capacity and are therefore key considerations when designing a CO_2 storage project. As shown, this relate very much to the stress regime and stress state through the principal stresses σ_1, σ_2 and σ_3, which will be reviewed next.

2.3 Stress regimes

The surface of the earth is normally considered a principal stress plane. Since principal stresses are always perpendicular to each other, the surface of the earth, and by assumption to some shallow depth below the surface, has two horizontal principal stresses, often termed σ_H and σ_h [Pa]. The capital H indicates that the magnitude of $\sigma_H > \sigma_h$. The third principal stress is normally considered to be the vertical stress; σ_v [Pa] and is approximately the weight of the rock. The magnitude and order of these principal stresses must be measured and can vary between locations.

Faults are geological fractures in a rock where the two blocks are displaced relative to each other and a principle in structural geology is that the type of faulting is related to the stress field which has three principle stress components; $\sigma_1 > \sigma_2 > \sigma_3$. The Andersonian classification [6] defines three types of faults and associated stress regimes. Depending on which of the principal stresses is in the vertical direction, the following main faults/stress regimes can be defined:

- Normal faulting/extensional stress regime:
  - $\sigma_v > \sigma_H > \sigma_h$, see Fig. 2.3, (a).
  - failure on steeply dipping planes at $< 45°$ to σ_1 (the vertical stress)
- Reverse (thrust) faulting/compressional stress regime:
  - $\sigma_H > \sigma_h > \sigma_v$, see Fig. 2.3, (b).
  - failure on shallowly dipping planes at $< 45°$ to σ_1 (the maximum horizontal stress)
- Strike-slip or wrench faulting/strike-slip stress regime:
  - $\sigma_H > \sigma_v > \sigma_h$, see Fig. 2.3, (c).
  - failure is horizontal on near-vertical planes striking/trending $< 45°$ to σ_1 (the maximum horizontal stress)

Note that the angle of failure, 45°, is the theoretical value, typically failure occurs at angles of 30°. Note also that intermediate stress regimes can occur between (1) extensional and strike-slip stress regimes, resulting in a combination of normal and strike-slip faulting, and (2) between compressional and strike-slip stress regimes, resulting in a combination of reverse and strike-slip faulting.

Knowledge of the stress state allows the identification of fault orientations that has the greatest potential for reactivation. Note that the stress-regime can change during production/injection, especially when the stress state is close to the limit between the various regimes.

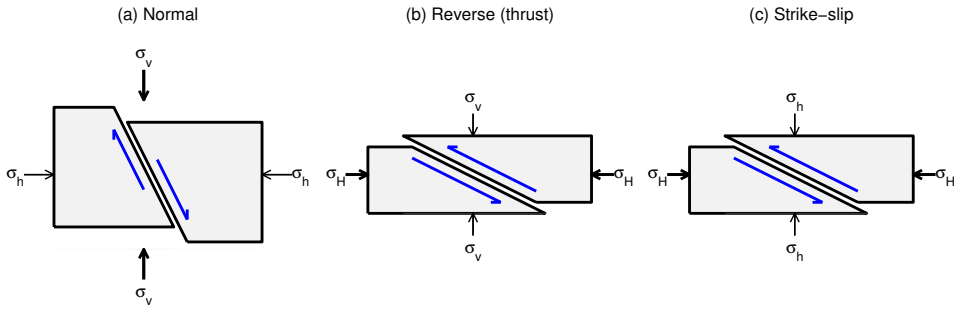

Figure 2.3: Andersonian fault classification (figure is modified from [58]). (a) Normal, (b) reverse (thrust) and (c) strike-slip stress regimes. The intermediate principal stress is perpendicular to the plane shown in the figure.

The effect of stress arching; the transfer of stress, is an important aspect of stress analysis. When stress is induced in the reservoir, e.g. by injection or production, some of the stress will also be transferred to the overburden and underburden, even if the pore pressure does not change outside the reservoir. Due to the tensor character of stress, changes in pore pressure and deformation leads to changes in the differential stress (difference between the minimum and maximum principal stresses) of the system which can be essential for fault reactivation. Imagine the depletion of an oil-field, as illustrated in Fig. 2.4, and assume further that the permeability inside the reservoir is high compared to the outside of the reservoir such that the pressure drop is mainly inside the reservoir. This is essentially the consolidation model by Geertsma [48], noting that the Geertsma model is assuming constant mechanical properties everywhere (see App. C.1 for details and examples). The depletion causes the reservoir to contract and consequently the surface subsides. The open arrows in Fig. 2.4 (a) illustrates the horizontal strain at the surface and shows that when the reservoir contracts, or "caves in", there is compression of the subsurface above and below the reservoir, whereas the flanks at the surface experiences extension.

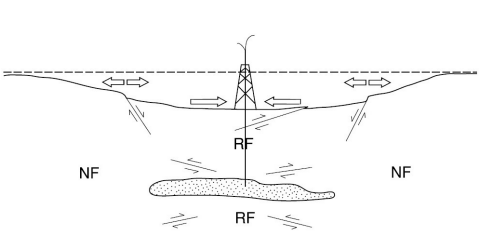

(a) Fault activation developing around a depleting reservoir (from Segall [101]).

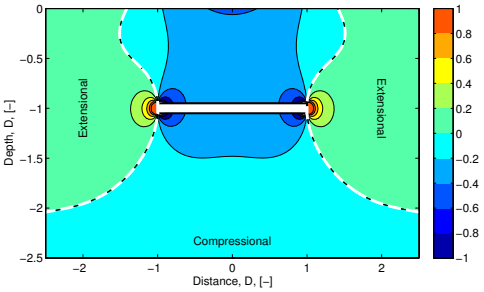

(b) Change in horizontal stress due to depletion. Depth and distance in units of reservoir depth. Stress contours in MPa. White dashed line separates areas of extension and compression.

Figure 2.4: (a) During depletion, the stress above and below a reservoir is compressive; promoting reverse/strike-slip faulting and reactivation of shallowly dipping fractures/faults. On the flanks the stress is extensional; promoting normal faulting and reactivation of steeply dipping fractures and faults. (b) A simple model of production (that can be solved by Geertsma's nucleus of strain model, see App. C.1). White dashed line indicate zero change in horizontal stress.

A schematic poroelastic model of the depleting reservoir is shown in Fig. 2.4 (b). The reservoir (white rectangle) is depleted and the white dashed line indicate the zero-change in horizontal stress. The areas of compression and extension are indicated, noting that extensional stress is positive. In a reverse faulting stress regime, compression promotes activation of shallowly dipping fractures/faults and in a normal faulting stress regime, extension promotes steeply dipping fractures/faults. This concept has been applied to several case-studies with good correlation between theoretically and observed seismicity [101, 126]. Detailed stress analysis is the topic for the next chapter 3.

2.4 Stress approximations

Here two first order approximations of stress is described. The first method is the stress state-method, or k_0-method. The ratio k_0 between the effective minimum horizontal stress, $(\sigma_h - p)$ and the effective vertical stress $(\sigma_v - p)$ has been widely used to describe the state-of-stress in sedimentary basins [1, 44, 54, 112]:

$$\boxed{k_0 = \frac{\sigma_h - p}{\sigma_v - p}} \tag{2.14}$$

The vertical stress σ_v in a point at elevation d can often be approximated as the total weight of the overlying rock (including any formation fluids):

$$\sigma_v = g \int_d^{D_0} \rho_b(z) dz \tag{2.15}$$

where z [m] is the vertical coordinate direction, g [m/s^2] is the gravitational constant and D_0 [m] is the elevation of the surface, ρ_b [kg/m^3] is the bulk density of the overlying rock that (usually) changes with depth. Rearranging Eq. (2.14) yields:

$$\sigma_h = k_0 \sigma_v + (1 - k_0) p \tag{2.16}$$

It is known that changes in pore pressures also affects the horizontal stress while the vertical stress, which is in most cases simply the weight of overburden, is largely unaffected. This can be justified given that the earths surface is a free surface where the strain is allowed to absorb any change in pore pressure while there are constraints in lateral strains. Hence, total vertical stress is an absolute limit to pore pressure because pore pressure larger than vertical stress (and tensile strength: $p \geq \sigma_v + T_0$) will induce horizontal tensile fractures, see also Eq. 2.7.

The second approximation is often referred to as the *stress path* or *pore pressure-stress coupling*. For thin, laterally extending reservoir, and by assuming the following: horizontal strains are negligible, total vertical stress is constant and isothermal conditions, it can be derived that change in horizontal stress is proportional to the change in pore pressure according to (see e.g. [102]):

$$\boxed{\frac{\Delta\sigma_h}{\Delta p} = b\frac{1-2\nu}{1-\nu}, \quad \frac{\Delta\sigma_H}{\Delta p} = b\frac{1-2\nu}{1-\nu}} \tag{2.17}$$

where b [-] is the Biot's coefficient, or effective stress parameter, and ν [-] is the Poisson's ratio of the rock. Biot's coefficient b is often assumed to be equal to 1 and is therefore often left out of the expression. It is Eq. (2.17), which states the correlation between the change in horizontal stress to the change in pore pressure, that is often referred to as the *stress path* or *pore pressure-stress coupling*. Differentiating Eq. (2.16) with respect to pore pressure p yields:

$$\frac{d\sigma_h}{dp} = (1 - k_0) \tag{2.18}$$

Comparing Eq. (2.18) with Eq. (2.17) it can be seen that (for $b = 1$):

$$k_0 = \frac{\nu}{1-\nu} \tag{2.19}$$

which can be rearranged to $\nu = k_0/(1 + k_0)$. For Poisson's ratio $\nu = 0.25$, the ratio $\Delta\sigma_h/\Delta p = 0.67$ (and similarly from Eq. (2.18)), which is comparable to values measured in the field [44, 54, 112].

The effect of changing the pore pressure in the three typical stress regimes; normal, reverse and strike-slip faulting regimes, are shown in a Mohr diagram in Fig. 2.5. The state-of-stress value k_0 is calculated from the initial stress state (black dashed lines). Upon changing the pressure, the various stress terms can be updated to [3]:

$$\sigma'_v = \sigma'^0_v - \Delta p \tag{2.20}$$

$$\sigma'_h = \sigma'^0_h + \frac{\Delta\sigma_h}{\Delta p}\Delta p - \Delta p \tag{2.21}$$

$$\sigma'_H = \sigma'^0_H + \frac{\Delta\sigma_H}{\Delta p}\Delta p - \Delta p \tag{2.22}$$

and the resulting Mohr circles, after decreasing or increasing pressure and updating the principal stresses, are plotted in the same diagram, blue and red curves, respectively. Note that total vertical stress typically does not change with change in pressure (because the weight of the rock remains unchanged).

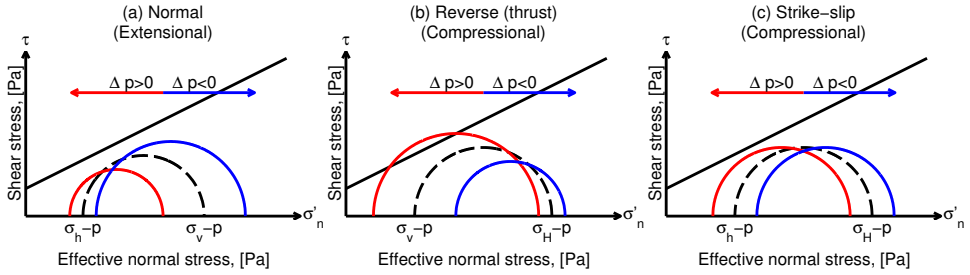

Figure 2.5: Mohr diagram for various stress regimes; normal, reverse/thrust and strike-slip faulting regimes, respectively, and the effect on the total principal stress components with a change in pore pressure p. For a given initial state of stress (black dashed line) the effective horizontal differential stresses changes with increasing pore pressure (red line) and decreasing pore pressure (blue line) according to Eqs. (2.20)-(2.22). Figures are modified from [3].

It can be seen that, for a normal faulting stress regime, the effective vertical stress decreases more rapidly (proportional to the pore pressure) than the effective minimum horizontal stress, causing the Mohr circle to become smaller as the differential stress is reduced. For decreasing pore pressure the effect is the reversed. Compared to the normal fault stress regime, the effect is the opposite for the reverse stress regime. However, for the strike-slip stress regime, both maximum and minimum principal stresses are horizontal and react equally to the pore pressure change, hence the Mohr circle simply shifts to the left or right for increasing or decreasing pore pressure, respectively.

The result of this analysis indicate that for the normal faulting stress regime, the pore pressure-stress coupling favor the formation of tensile fractures with increasing pore pressure rather than reactivation of pre-existing faults. Also, for applications of injection, normal faulting stress regimes seem beneficial, as the reverse/thrust faulting stress regime tends to approach the failure envelope more rapidly.

The range of possible principal stress magnitudes for normal, reverse/thrust and strike-slip faulting stress regimes can also be visualised in an allowable stress region diagram [126], see example in Fig. 2.6. The allowable stress conditions for a particular geographic region can be assumed to lie within an area defined by frictional limits. Frictional limits theory states that the ratio of the maximum to minimum effective stress cannot exceed the magnitude required to cause faulting on an optimally oriented, pre-existing, cohesionless fault plane. Thus the frictional limit to stress is obtained from Eq. (2.10) and the allowable stress region diagram can be drawn by using the following

relations for the various stress regimes:

$$\text{Normal faulting:} \quad \frac{\sigma_1'}{\sigma_3'} = \frac{\sigma_v - p}{\sigma_h - p} \leq \left[\sqrt{(\mu_f^2+1)} + \mu_f\right]^2 \tag{2.23}$$

$$\text{Reverse faulting:} \quad \frac{\sigma_1'}{\sigma_3'} = \frac{\sigma_H - p}{\sigma_v - p} \leq \left[\sqrt{(\mu_f^2+1)} + \mu_f\right]^2 \tag{2.24}$$

$$\text{Strike-slip faulting:} \quad \frac{\sigma_1'}{\sigma_3'} = \frac{\sigma_H - p}{\sigma_h - p} \leq \left[\sqrt{(\mu_f^2+1)} + \mu_f\right]^2 \tag{2.25}$$

The three Eqs. (2.23), (2.24) and (2.25) has five unknowns, assuming that for an average reservoir rock $\mu_f = 0.6$ [126] and by specifying one of the stress components or pore pressure, the frictional stress limits can be calculated and the allowable stress diagram can be constructed.

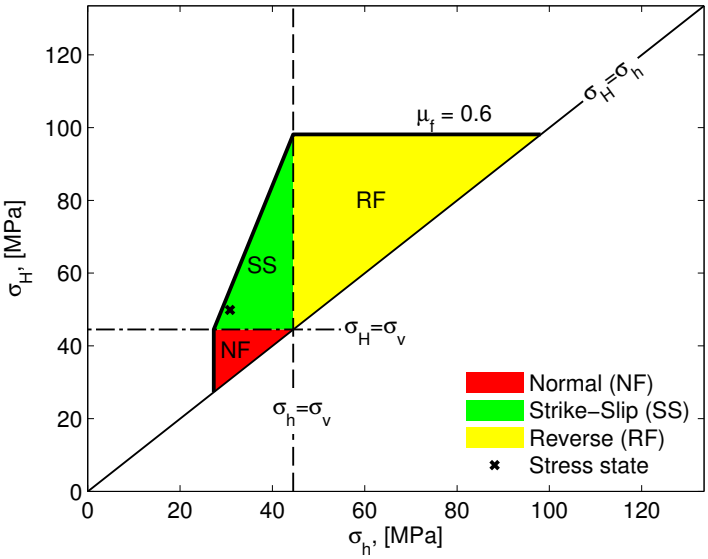

Figure 2.6: An example of on an allowable stress region diagram. σ_H and σ_h are the maximum and minimum horizontal stress, respectively. The black cross shows the stress state at In Salah, Algeria (at CO_2 injection well KB-502 [76]); $\sigma_v = 44.5$ MPa, $\sigma_H = 49.9$ MPa, $\sigma_h = 30.8$ MPa, and pore pressure (before CO_2-injection started) $p = 19.2$ MPa. From Eq. (2.14) the stress state $k_0 = 0.46$. The thick black line indicates the failure envelope for a friction coefficient $\mu_f = 0.6$. It can also be seen that the stress state is in the strike-slip faulting stress regime and within the allowable stress region of not failing.

Chapter 3

Poromechanics

3.1 Introduction

Poromechanics is the study of the mechanical deformation of a fluid-saturated porous medium. Porous media are often considered as solids permeated with interconnected pores that are saturated with a fluid. As was seen in chapter 2, stress is affected by change in pore pressure, thus fluid flow and geomechanics are coupled processes. Poroelastic behavior can be divided into primary and secondary coupling effects [96, 119]. The primary coupling effects occurs through deformation and pore fluid interactions and relate to changes in the pore volume and the volumetric strain rate, see Fig. 3.1:

(i) Change in stress causes a deformation of the pore space that affects the fluid pressure or fluid mass.

(ii) Change in fluid pressure or fluid mass changes the effective, causing the porous material to deform.

The secondary coupling considers indirect effects of change in pore volume and volumetric strain:

(iii) Change in the stress causes a change in the hydraulic properties of the rock mass.

(iv) Change in the pore fluid pressure causes a change in the mechanical properties of the rock mass.

Both primary and secondary coupled processes may be fully reversible, the secondary effects (iii) and (iv) will not be considered in this study. Note how the couplings between both processes are coupled to the pore volume change. The two processes can be de-coupled, and greatly simplify any numerical analysis, if a proper correlation for pore volume change can be defined and in the literature many material properties have also been found to correlate with pore volume or change in pore volume.

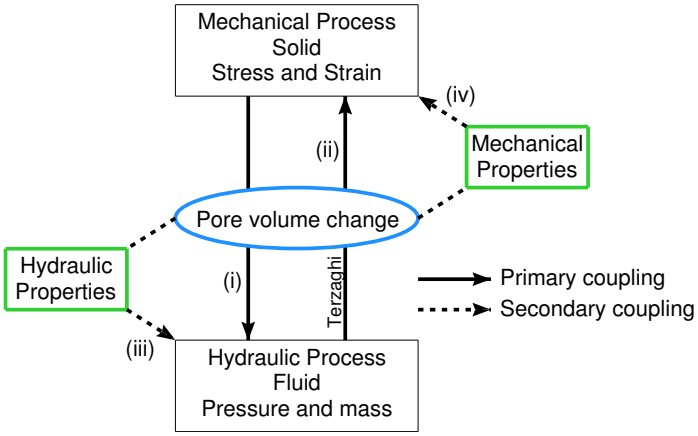

Figure 3.1: Hydromechanical couplings in geological media. (i) and (ii) are direct couplings through pore volume change, whereas (iii) and (iv) are indirect couplings through changes in material properties (modified from Rutqvist and Stephansson [96]).

The concept of poromechanics is based on early work by Karl von Terzaghi and later Maurice Anthony Biot [13–17], now known as Biot's theory of linear poroelasticity. Terzaghi assumed the mechanical and hydraulic processes could be treated uncoupled where consolidation could be determined by evaluating the pore pressure only. See App. C.3 for more details on the theory and an example. Biot's theory of linear poroelasticity follows from the combination of Hooke's law with the momentum balance equations for the pore structure, which will be reviewed in this chapter, and Darcy's law with the fluid mass conservation equations, which will be reviewed in chapter 4 for single- and two-phase flow. The theory by Biot has later been further developed, by e.g. Detournay and Cheng [40] and Rice and Cleary [93]. The theory captures the primary coupling in Fig. 3.1. Based on work by Van Der Knaap [114], who showed that the compressibility of a solid matrix in a porous media is partially linear, Biot [17] extended his theory by introducing the concept of semilinearity. Although the constitutive relations are not strictly valid for a nonlinear inelastic media, one can make the assumption that the properties are piecewise constant such that the elastic moduli are meaningful quantities at small increments of stress [8, 12, 36].

In this chapter a brief review of the concepts of linear elasticity (for small deformations) and how the constitutive relations for stress and strain are affected by temperature (thermoelasticity), pore pressure (poroelasticity) and both temperature and pore pressure (thermoporoelasticity) are given. It is important to note that rocks in general exhibit nonlinear, partly irreversible and sometimes viscous mechanical behaviour, particularly when the pore pressure is high or the rock is unconsolidated (e.g. clay or sand). Despite this, it will in the remainder of the thesis be assumed that the rock behaves perfectly elastic, and acknowledge that it only provides an approximate description of the real behavior.

3.2 Linear elasticity

By balancing all forces acting on all faces of an elementary volume the stress state in a material point as the dimensions of the cube approaches an infinitesimal value, see Fig. 3.2, can be derived.

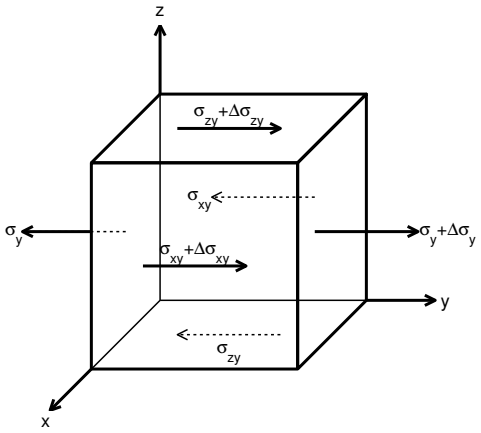

Figure 3.2: Forces acting on an elementary volume. Note that only the y-direction components of the stress are shown. σ_y is the outward pointing normal stress and σ_{xy} and σ_{zy} are shear stresses. The differences in stress magnitude between opposing faces are indicated with the addition of $\Delta\sigma_y$, $\Delta\sigma_{xy}$ and $\Delta\sigma_{zy}$.

In matrix form the stress tensor looks like:

$$\sigma = \begin{bmatrix} \sigma_x & \sigma_{xy} & \sigma_{xz} \\ \sigma_{yx} & \sigma_y & \sigma_{yz} \\ \sigma_{zx} & \sigma_{zy} & \sigma_z \end{bmatrix} \tag{3.1}$$

where the first subscript indicate the face on which the stress acts and the second subscript in which direction it is pointing, e.g. σ_{xy} [Pa] represents the stress pointing in the y-direction acting on the surface with a normal vector pointing in the x-direction. It can be shown that Eq. (3.1) holds for any orientation of the coordinate axes, e.g. Nordal [80].

Conservation of momentum (Cauchy's first law of equilibrium/motion):

$$\boxed{-\nabla \cdot \sigma = \mathbf{f}} \tag{3.2}$$

Here $\mathbf{f}$ [N/m^3] is the body load vector defined as:

$$\mathbf{f} = \rho\mathbf{g} - \rho\mathbf{a} \tag{3.3}$$

where $\mathbf{a}$ [m/s^2] is the acceleration vector in dynamic problems (for static/quasi-static

problems $\mathbf{a} = 0$[1]), $\mathbf{g}$ [m/s^2] is the gravity vector

$$\mathbf{g} = g\mathbf{e}_z = g \begin{bmatrix} 0 \\ 0 \\ -1 \end{bmatrix} \tag{3.4}$$

where $\mathbf{e}_z$ [-] is the unit vector in the vertical direction and g [m/s^2] is the gravity constant. The volume-averaged total mass density ρ [kg/m^3] is (typically) given by:

$$\boxed{\rho = (1-\phi)\rho_s + \phi \sum_{\alpha}^{n_p} s_\alpha \rho_\alpha} \tag{3.5}$$

where α denotes the fluid phase, n_p [-] is the number of fluid phases and s_α [-] is the fluid volume fraction (saturation) of fluid phase α (see Eq. (4.40), two-phase flow is introduced in chapter 4.3).

A constitutive relation is the relation between two physical quantities, in structural analysis it relates the stresses to strains and for a linear elastic problem it can be expressed as:

$$\boxed{\sigma = \lambda \varepsilon_v \mathbf{I} + 2G\varepsilon} \tag{3.6}$$

where ε_v [-] is the volumetric strain, ε [-] is the strain tensor, λ [Pa] and G [Pa] are the Lamé coefficients and $\mathbf{I}$ [-] is the identity matrix. The strains and displacements are related according to:

$$\varepsilon = \frac{1}{2}\left(\nabla \mathbf{u} + (\nabla \mathbf{u})^T\right) \tag{3.7}$$

where $\mathbf{u} = [u, v, w]^T$ and u, v and w [m] are the displacements in x-, y- and z-direction, respectively. By combining Eqs. (3.6) and (3.7) it is obtained that

$$\sigma = \lambda \left(\nabla \cdot \mathbf{u}\right)\mathbf{I} + G\left(\nabla \mathbf{u} + (\nabla \mathbf{u})^T\right) \tag{3.8}$$

where $\nabla \mathbf{u}$ can be expressed as[2]:

$$\nabla \mathbf{u} = \begin{bmatrix} \frac{\partial u}{\partial x} & \frac{\partial u}{\partial y} & \frac{\partial u}{\partial z} \\ \frac{\partial v}{\partial x} & \frac{\partial v}{\partial y} & \frac{\partial v}{\partial z} \\ \frac{\partial w}{\partial x} & \frac{\partial w}{\partial y} & \frac{\partial w}{\partial z} \end{bmatrix} \tag{3.9}$$

For small deformations, the volumetric strain ε_v in Eq. (3.6) is given as the sum of the normal strains (diagonal in Eq. (3.7)):

$$\varepsilon_v = \nabla \cdot \mathbf{u} = \frac{\partial u}{\partial x} + \frac{\partial v}{\partial y} + \frac{\partial w}{\partial z} = \varepsilon_x + \varepsilon_y + \varepsilon_z \tag{3.10}$$

[1] $\mathbf{a} = \partial^2 \mathbf{u}/\partial t^2$, where $\mathbf{u} = [u, v, w]^T$ and u, v and w [m] are the displacements in x-, y- and z-direction, respectively.

[2] The component $(\nabla \mathbf{u})_{i,j}$ in Eq. (3.9) is here defined as $\partial u_j/\partial x_i$, this is also frequently defined in the literature as $\partial u_i/\partial x_j$.

3.3 Poroelasticity

Fluid flow and geomechanics are coupled processes and a hydromechanical model describes the interaction between the solid phase of the porous media and the fluid phase in the pores. Poroelasticity describes the constitutive behavior of a fluid saturated rock and usually refers to the linearized theory of poroelasticity, in which the compressibilities and the other constitutive coefficients are independent of stress. There are many physical processes in which the stress increments are small enough that this restriction is of little consequence since the governing equations can always be linearized for small stress increments, as noted in chapter 3.1.

Central in poroelasticity is the concept of *effective stress* first proposed by [109, 110]. Effective stress, often denoted with an apostrophe, σ', is the stress carried by the solid matrix as opposed to the pore pressure, which is carried by the fluid in the pores. In other words; *the effective stress is the part of the total stress that causes deformation of the porous media* and is expressed by the constitutive relations in Eq. (3.6) for elastic deformation and Eq. (3.27) for thermoelastic deformation. Effective stress is often expressed as the difference between the total stress σ and the pore pressure p [Pa] according to:

$$\sigma' = \sigma - p\mathbf{I} \tag{3.11}$$

where positive confining stress is compressive, as illustrated in Fig. 3.3 (right). For an extensional stress regime a negative confining stress is compressive, see Fig. 3.3 (left). Note that the fluid is in a compressive state for positive fluid pressure, e.g. the density of a fluid increases when fluid pressure increases.

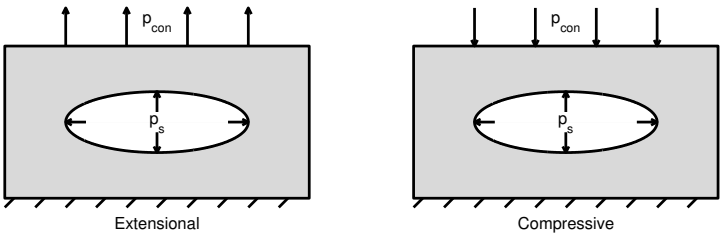

Figure 3.3: Sketch of a porous medium with sign conventions for confining pressure p_{con} [Pa] (stress) and the pore pressure acting on the solid, p_s [Pa]. (Left) Positive stress p_{con} is extensional. (Right) Positive stress p_{con} is compressional.

The definition of effective stress σ' depends on the sign convention of confining stress and pore pressure. The total stress σ of a porous medium with incompressible grains is given by:

$$\text{Compressive:} \quad \sigma = \sigma' + p_s\mathbf{I} \tag{3.12}$$

$$\text{Extensional:} \quad \sigma = \sigma' - p_s\mathbf{I} \tag{3.13}$$

where p_s [Pa] is the stress the pore fluid exerts on the solid.

For a poroelastic material where the grains are compressible, the effective stress, now denoted as σ'' (as in Lewis and Schrefler [64]), is defined in Biot's theory of linear

poroelasticity and is given by:

$$\text{Compressive:} \quad \sigma = \sigma'' + bp_s\mathbf{I} \tag{3.14}$$

$$\text{Extensional:} \quad \sigma = \sigma'' - bp_s\mathbf{I} \tag{3.15}$$

where b [-] is Biot's coefficient that is defined as[3]:

$$\boxed{b = 1 - \frac{K}{K_s}} \tag{3.16}$$

and K_s [Pa] is the bulk modulus of the grains; the solid constituents of the porous medium. It should be noted that although both σ' and σ'' are expressed by the same constitutive relations: Eq. (3.6) for elasticity and Eq. (3.27) for thermoelasticity, they are not equal in magnitude, hence the different notations. However, the total stress σ will be the same, regardless of the compressibility of the solid constituents.

In the following, and in this thesis, the extensional stress convention will be used where the stress is positive for tensile strain. Thus, by inserting the constitutive relation for linear elasticity, Eq. (3.6), for the effective stress σ'' in Eq. (3.15), the poroelastic stress tensor can be expressed as:

$$\boxed{\sigma = \lambda\varepsilon_v\mathbf{I} + 2G\varepsilon - bp_s\mathbf{I}} \tag{3.17}$$

A first order approximation and a validation model for poroelasticity is given by Geertsma [48], see App. C.1 for two examples.

A useful relation that will be used later, in deriving the equation of state (EOS) for the solid phase, is the first effective stress invariant, I_1' [Pa]: $\mathrm{I}_1' = tr(\sigma')$. From Eq. (3.13) (for an extensional stress regime):

$$\mathrm{I}_1' = tr(\sigma + p_s\mathbf{I}) \tag{3.18}$$

For a poroelastic material where the grains are compressible, the total stress is expressed by Eq. (3.15):

$$\mathrm{I}_1' = tr(\sigma'' + (1-b)p_s\mathbf{I}) \tag{3.19}$$

By using that σ'' is expressed by the constitutive relation for thermoelasticity, Eq. (3.27), the first effective stress invariant I_1' can thus be expressed as:

$$\boxed{\mathrm{I}_1' = 3K\left(\nabla\cdot\mathbf{u} + \frac{p_s}{K_s} - \beta_s T\right)} \tag{3.20}$$

[3]The Biot's coefficient b can also be interpreted as an effective stress coefficient, indicating how much of the pore pressure that can be transferred to the solid, and this depends on the contact area between the fluid and the grain. In compression, this contact area can decrease, but cementation of a rock can also reduce this area and in effect lower the value of b [2].

Pore pressure in multi-phase flow

Bishop [18] derived a general expression for the effective stress in unsaturated soil according to:

$$\sigma' = \sigma - p_a \mathbf{I} + \chi(p_a - p_w)\mathbf{I} \tag{3.21}$$

where p_a [Pa] and p_w [Pa] were the fluid pressure in air and water, respectively. $\chi = \chi(s_w)$ [-], called the Bishop parameter, depends on the water saturation s_w of the soil. A common approximation is to use that $\chi = s_w$ such that p_s can be expressed as the saturation averaged partial fluid phase pressure according to:

$$p_s = \sum_{\alpha}^{n_p} s_\alpha p_\alpha \tag{3.22}$$

where α [-] denotes the fluid phase, n_p [-] is the number of phases and s_α [-] and p_α [Pa] are the saturation and pressure of fluid phase α, respectively, and

$$\sum_{\alpha}^{n_p} s_\alpha = 1 \tag{3.23}$$

For two-phase flow this can also be justified by considering a force balance and equating the upward and downward acting forces on an idealized porous rock, as illustrated in Fig. 3.4.

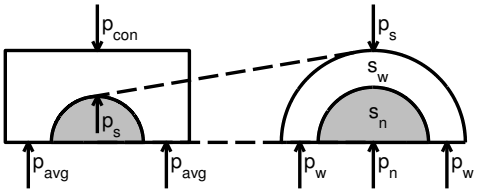

Figure 3.4: Stress on a pore pressure-grain contact. p_{con} [Pa] is the confining stress and p_{avg} [Pa] is the average effective stress acting against confining stress [modified from 125]. Note that the arrows do not represent scaled vectors, but are just indicators of stress terms and directions.

The balance of forces around an arbitrary pore (shown cut in half in Fig. 3.4 left), can be expressed as:

$$p_{con} = (1 - \phi)p_{avg} + \phi p_s \tag{3.24}$$

Similar argument can be extended to the pore pressure (Fig. 3.4, right) by decomposing the fluid in the pore space into a wetting and a non-wetting fraction (according to saturation) to obtain

$$p_s = s_w p_w + s_n p_n \tag{3.25}$$

which is the same as Eq. (3.22) for $n_p = 2$.

From the definition of the capillary pressure, which relates the phase pressures according to $p_c = p_n - p_w$ (see App. E for details and various expressions encountered in the literature), it can be seen that the capillary suction has a direct effect on the effective stress in the rock:

$$p_s = p_w + s_n p_c \tag{3.26}$$

However, for a water-wet rock or when capillary pressure can be ignored ($p_c \ll p_s$), e.g. when non-wetting saturation becomes small, a reasonable approximation can be that $p_s \approx p_w$.

3.4 Thermoelasticity

The theory of *thermoelasticity* accounts for the effect of changes in temperature on the stresses and strains in a rock. It is well described in the literature, e.g. Coussy [36] and Jaeger et al. [58], in this thesis, the description from Jaeger et al. [58] is adopted. The theory is analogous to the theory of *poroelasticity*, which is described in details in Sec. 3.3, with temperature playing a role similar to that of pore pressure. For instance, a change in temperature, or a change in pore pressure, will both give rise to change in normal strains. Despite this, the effect of mechanical deformation on the temperature field is often ignored, whereas the effect of mechanical deformation due to changes in pore pressure cannot, in most instances, be ignored [58]. Thermoelastic effects are generally concentrated around injectors/producers while poroelastic effects extends much farther and therefore affects a much larger area/volume [66].

Consider a rock that is initially unstressed and at a uniform temperature T_0 [°C]. This state can be taken as the reference state, where the strains are usually defined to be zero. If the temperature of a rock is increased, to T_1 [°C], and no other forces act on the rock, it will expand. Under the assumption of linearity, this temperature rise will induce thermal strains ε_{th} in the rock according to $\varepsilon_{th} = \beta(T_1 - T_0)$, where β [1/K] is the linear/uniaxial thermal expansivity coefficient (although β can also be a tensor). For an expanding material, β is defined to be positive number, although a minus sign is included when extensional strains are considered to be negative (typical in rock mechanics).

Thermoelastic stress can be defined as [e.g. 58]:

$$\boxed{\sigma = \lambda \varepsilon_v \mathbf{I} + 2G\varepsilon - \beta_s K T \mathbf{I}} \tag{3.27}$$

where T [K] represents the change in temperature ($T_1 - T_0$) and positive stresses are extensional, K [Pa] is the bulk modulus of the porous medium and $\beta_s = 3\beta$ [1/K] is a tensor. It can be seen that if the rock is constrained the effective stress is zero and the change in total stress σ will be equal to the thermal stress: $\sigma = -\beta_s K T \mathbf{I}$.

From Eq. (3.27) it can be seen that thermal stresses can contribute to an order of $\beta_s K T$, which can be significant. It can also be seen that thermoelastic effects increases with increasing rock mechanical stiffness. Given typical values $K = 10$ [GPa] and $\beta_s = 10^{-5}$ [1/K] (see e.g. Schön [100] for more properties of rocks), a thermal stress of approximately 0.1T MPa/°C will be induced. High temperature differences can be expected, for instance, around underground radioactive waste canisters, during cold

water injection of geothermal wells (for pressure maintenance) and in various natural geothermal processes [58] and in such systems, thermally induced stresses may be of considerable importance. An example of this on a CO_2 storage system will be described in more details and illustrated in chapter 5.

3.5 Thermoporoelasticity

Thermoporoelasticity considers the effect of both temperature and pore pressure on the mechanical behavior; combining the equations of momentum balance, mass and energy conservation for the phases. The thermoporoelasticity stress tensor is given by (for positive extensional stress):

$$\boxed{\sigma = \lambda \varepsilon_v \mathbf{I} + 2G\varepsilon - \beta_s K T \mathbf{I} - b p_s \mathbf{I}} \tag{3.28}$$

Eq. (3.28) can be obtained by inserting the constitutive relation for linear thermoelasticity in Eq. (3.27) for the effective stress σ'' in Eq. (3.15).

When injecting a cold fluid (increasing pressure p_s and reducing temperature T), e.g. CO_2 storage, it can be seen that the combined effect on the stress of the last two terms in Eq. (3.28) is reduced. Thus neglecting thermal stress in cold injection processes can be considered conservative when evaluating the geomechanical integrity by overestimating the effective stress.

3.6 Navier-Cauchy equations

The governing equations for solving displacement due to linear elastic deformation is described by the linear elasticity equation, aka. Navier-Cauchy equation. The linear elasticity equation can be derived by combining the momentum balance equation Eq. (3.2) with the constitutive relation for linear elastic materials, Eq. (3.6). In terms of the Lamé coefficients it can be expressed as (see App. G for derivation):

$$(\lambda + G)\nabla(\nabla \cdot \mathbf{u}) + G\nabla^2 \mathbf{u} + \mathbf{f} = 0 \tag{3.29}$$

Similarly, by combining the momentum balance equation Eq. (3.2) with the other (linear) constitutive relations described earlier for poroelasticity, thermoelasticity and thermoporoelasticity, Eqs. (3.17), (3.27) and (3.28), respectively, the following governing equations can be derived:

$$\text{poroelasticity:} \quad (\lambda + G)\nabla(\nabla \cdot \mathbf{u}) + G\nabla^2 \mathbf{u} - b\nabla p_s \mathbf{I} + \mathbf{f} = 0 \tag{3.30}$$

$$\text{thermoelasticity:} \quad (\lambda + G)\nabla(\nabla \cdot \mathbf{u}) + G\nabla^2 \mathbf{u} - \beta_s K \nabla T \mathbf{I} + \mathbf{f} = 0 \tag{3.31}$$

$$\text{thermoporoelasticity:} \quad (\lambda + G)\nabla(\nabla \cdot \mathbf{u}) + G\nabla^2 \mathbf{u} - b\nabla p_s \mathbf{I} - \beta_s K \nabla T \mathbf{I} + \mathbf{f} = 0 \tag{3.32}$$

Note that the material properties in the various governing equations above can also be tensors.

Decoupling momentum balance and flow equation

There are many attempts in the literature to determine if the equations for poroelasticity and porous media flow need to be solved simultaneously (fully coupled) or if they can be decoupled and solved separately (explicitly coupled) or sequentially (iteratively coupled) [39]. However, there are cases where these equations truly decouples, this is reviewed below, but in cases where they do not, solving repeatedly and/or sequentially can sometimes give a satisfactory accurate approximation. Explicitly coupled approach often means that the fluid flow is solved first, assuming some simplified mechanical behavior (e.g. using one of the decoupling strategies discussed below), and the resulting pressure profile is then used as input for solving the mechanical process at all or a selection of time steps from the flow simulation. The iteratively coupled approach often means that the two equation systems are solved in an iterative loop; paths (i) and (ii) in Fig. 3.1 in sequence. This latter approach has many possible algorithms. The goal is to save time and reduce the size of the numerical problem to be solved, partly because solving two small problems is generally faster than solving one large problem, but also because a satisfactory accuracy can sometimes be achieved even without solving for all the processes at every time step in a simulation. However, it is difficult to know when any of the two approaches will work satisfactory. Without going to deep into the literature on this, Dean et al. [39] concluded from four sample problems that no method is superior and that the choice of method comes down to ease of implementation, program availability, numerical stability and computational efficiency. However, as mentioned above there are cases where these processes truly decouple:

1. Steady state, since the mechanical coupling term in the equation for flow disappears along with all other time derivatives (single and two-phase flow equations will be introduced in chapter 4)

2. A highly compressible fluid; the compressibility of the fluid dominate the storage term and in a rigid material, e.g. a rock, the deformations can be negligible

3. An *irrotational displacement* field in an infinite or semi-infinite domain without body forces. For negligible changing body-loads it corresponds to uniaxial strain under constant vertical stress, see 4. below

4. A state of *uniaxial strain* and constant vertical stress. The horizontal deformations are assumed negligible compared to vertical deformation and the vertical total stress is constant, then the volumetric strain becomes equal to the vertical strain and the momentum balance equation simplifies to a linear relation between volumetric strain, pore pressure and temperature

Some of these decoupled cases will be evaluated and compared in section 4.2, but first, irrotational displacement and uniaxial strain (3. and 4.) will be described in more detail.

Irrotational deformation

Deformation is considered irrotational when:

$$\frac{\partial u}{\partial y} = \frac{\partial v}{\partial x}, \quad \frac{\partial u}{\partial z} = \frac{\partial w}{\partial x}, \quad \frac{\partial w}{\partial y} = \frac{\partial v}{\partial z} \tag{3.33}$$

This reduces Eq. (3.29) to:

$$(\lambda + 2G)\nabla(\nabla \cdot \mathbf{u}) + \mathbf{f} = 0 \tag{3.34}$$

In elastodynamics this leads to the three-dimensional wave equation [e.g. 52, Ch. 9.11,]. Applying Eq. (3.33) on the constitutive relation for thermoporoelasticity, Eq. (3.32), it can be obtained that

$$\nabla\left((\lambda + 2G)\varepsilon_v - bp_s - \beta_s KT\right) = 0 \tag{3.35}$$

when using that that $\varepsilon_v = \nabla \cdot \mathbf{u}$. A useful application of this is the one-dimensional case, or in uniaxial displacement (and consolidation), where the only equation left to solve is the uniaxial component, e.g. strain in z-direction.

Uniaxial displacement

An important approximation which justifies an uncoupled analysis is the uniaxial strain approximation. In this approximation, horizontal deformations are assumed negligible (compared to vertical strain) and the vertical total stress is assumed to be constant. When the horizontal deformations are set equal to zero, the volumetric strain is equal to the vertical strain and the remaining term of Eq. (3.35) is:

$$\frac{\partial}{\partial z}\left[(\lambda + 2G)\varepsilon_v - bp_s - \beta_s KT\right] = 0 \tag{3.36}$$

Assuming that the vertical momentum is negligible (due to negligible change in vertical stress), the volumetric strain can be expressed as:

$$\boxed{\varepsilon_v = \frac{bp_s + \beta_s KT}{\lambda + 2G}} \tag{3.37}$$

The assumption is widely used in analytical solution, e.g. Geertsma [48], Mandel [69], Terzaghi et al. [111] (see App. C for examples), but also in reservoir models, as an approximation when the lateral extent of the reservoir is much larger than its thickness. It is also used in controlled lab experiments, like the Oedometer test, to obtain material properties by constraining the displacements in the lateral direction with a rigid jacket. The quantity $\lambda + 2G$ is also called the Oedometer modulus.

Chapter 4

Flow equations

4.1 Introduction

The governing equations for single-phase fluid flow in a deformable porous medium are derived in Biot's theory of linear poroelasticity, described in Chapter 3, where the voids of the porous medium are assumed fully saturated by a fluid and the fluid flow in the deforming porous medium is assumed to be governed by Darcy's law. In addition to Darcy's law, the governing equations are derived from the momentum balance equation, the mass conservation equations for the solid and the fluid and the energy conservation equations for the solid and the fluid. Note that the energy conservation equation will be covered in chapter 5 and here a constant temperature will be assumed. In case of multi-phase flow there are multiple mass conservation equations for the fluid-phase, in addition some auxiliary equations is needed, e.g. the equation of state for the fluid and solid, and the details will be described in the following sections.

There are two basic underlying phenomena in poroelastic behavior, cf. Fig. 3.1:

- Solid-to-fluid coupling (i): occurs when a change in applied stress produces a change in fluid pressure or fluid mass. The magnitude of solid-to-fluid coupling depends on the porosity and the compressibility of the bulk frame of the porous material, the pores, the solid grains and pore fluid.
- Fluid-to-solid coupling (ii): occurs when a change in fluid pressure or fluid mass results in a change in volume of the porous material.

When only fluid-to-solid coupling is important, the flow field can be solved independently of the stress field. However, when the changes in stress feed back significantly to the pore pressure it is important to consider the two-way coupling, see also discussion on decoupling in section 3.6.

In this chapter the equations for fluid flow in porous media will be derived: first for a single-phase fluid, second the two-phase immiscible flow and finally two-phase partially miscible flow.

4.2 Single-phase flow

Single-phase fluid flow in a deformable porous medium can be described by considering the mass conservation equations for the fluid phase and the solid phase:

$$\text{Fluid phase:} \quad \frac{\partial\left(\rho_f \phi\right)}{\partial t} + \nabla \cdot \left(\rho_f \phi \mathbf{v}_f\right) = R_f \tag{4.1}$$

$$\text{Solid phase:} \quad \frac{\partial\left[\rho_s (1-\phi)\right]}{\partial t} + \nabla \cdot \left[\rho_s (1-\phi) \mathbf{v}_s\right] = 0 \tag{4.2}$$

where t [s] is the time, ρ_s [kg/m^3] and ρ_f [kg/m^3] are the density of the solid constituents of the porous medium and fluid, respectively, and ϕ [-] is the porosity of the porous medium. $\mathbf{v}_f$ [m/s] and $\mathbf{v}_s$ [m/s] are the local volume averaged velocities for the fluid and the solid, respectively. R_f [kg/m^3/s] is the volumetric fluid source/sink-term. The specific discharge $\mathbf{q}_f$ expresses the volumetric flux relative to the deforming porous medium and can be expressed according to Darcy's law:

$$\boxed{\mathbf{q}_f = \phi\left(\mathbf{v}_f - \mathbf{v}_s\right) = -\frac{\mathbf{k}}{\mu_f}\left(\nabla p_f - \rho_f \mathbf{g}\right)} \tag{4.3}$$

where μ_f [Pa·s] is the dynamic fluid viscosity, p_f [Pa] is the fluid pressure, $\mathbf{k}$ [m^2] is the intrinsic permeability tensor and $\mathbf{g}$ [m/s^2] is the gravity vector.

When the porous medium is moving, or deforming, the fluid (and solid) moves with it. Changes in phase properties needs to consider this movement and it is provided by the material derivative, relative to the solid phase, and is for some property $(\cdot)$ defined as:

$$\frac{d(\cdot)}{dt} = \frac{\partial(\cdot)}{\partial t} + \mathbf{v}_s \cdot \nabla(\cdot) \tag{4.4}$$

The governing equation for single-phase flow in a fully saturated porous media is a very important one in all reservoir simulations. One might consider the aquifer or reservoir of interest to be a multi-phase and/or multi-component fluid, but the rest of the formations can often be treated as single-phase flow regions. Also, far away, the driving forces for movement might be small, or even negligible, and the main contribution of the fluid is as a constituent of the porous medium, affecting its stiffness and carrying part of the stress.

In the literature there are many forms of the governing equation for single-phase fluid flow, based on various assumptions. One needs to be cautious about which one to use (which assumptions are used) since it can have a large affect on the fluid pressure. Here, the general governing equation for single-phase flow in a fully saturated, slightly deforming porous medium will be derived, then common approximations are applied to derive some of the various formulations typically encountered in the literature. Finally the various formulations are compared in a reservoir model example.

4.2.1 Governing equations

The general governing equations for single-phase flow in a fully saturated, slightly deforming porous media is well described in the literature, e.g. Chen et al. [31], Lewis and Schrefler [64], Pinder and Gray [89] and others (here the derivations by Pinder and Gray [89] is used with a modified nomenclature to fit the rest of the text).

Combining the mass conservation equations for the fluid and solid, Eqs. (4.1) and (4.2), with the specific discharge, Eq. (4.3), apply the product rule to expand the derivative terms and the material derivative, Eq. (4.4), the following conservation equations for the fluid phase and solid phase, respectively, are obtained:

$$\rho_f \frac{d\phi}{dt} + \phi \frac{d\rho_f}{dt} + \phi \rho_f \nabla \cdot \mathbf{v}_s + \nabla \cdot (\rho_f \mathbf{q}_f) = R_f \tag{4.5}$$

$$(1-\phi)\frac{d\rho_s}{dt} - \rho_s \frac{d\phi}{dt} + (1-\phi)\rho_s \nabla \cdot \mathbf{v}_s = 0 \tag{4.6}$$

Rearranging Eq. (4.6) produces an expression for the change in porosity:

$$\frac{d\phi}{dt} = \frac{1-\phi}{\rho_s}\frac{d\rho_s}{dt} + (1-\phi)\nabla \cdot \mathbf{v}_s \tag{4.7}$$

To proceed, the equation of state for the various material properties and constitutive relation for the porous medium is needed. Considering that the fluid density depends on the fluid pressure, temperature and chemical composition: $\rho_f = \rho_f(p_f, T, C)$, the following general expression for the density of a fluid can be obtained by differentiation:

$$\frac{1}{\rho_f}\frac{d\rho_f}{dt} = -\frac{1}{V_f}\frac{dV_f}{dt} = \frac{1}{\rho_f}\left(\frac{\partial \rho_f}{\partial p_f}\frac{dp_f}{dt} + \frac{\partial \rho_f}{\partial T}\frac{dT}{dt} + \frac{\partial \rho_f}{\partial C}\frac{dC}{dt}\right) \tag{4.8}$$

where the following terms can be recognised

$$\frac{1}{\rho_f}\frac{\partial \rho_f}{\partial p_f} = c_f \tag{4.9}$$

$$\frac{1}{\rho_f}\frac{\partial \rho_f}{\partial T} = -\beta_f \tag{4.10}$$

$$\frac{1}{\rho_f}\frac{\partial \rho_f}{\partial C} = \beta_{fC} \tag{4.11}$$

and c_f [1/Pa] and β_f [1/K] are the compressibility and (volumetric) thermal expansion coefficient of the fluid, respectively. β_{fC} is the concentration compressibility and has the inverse unit of C [kg/m^3] and expresses how the density of the fluid changes with change in composition[1]. Thus, the density of a fluid phase α can be expressed by the following equation of state:

$$\boxed{\frac{1}{\rho_\alpha}\frac{d\rho_\alpha}{dt} = c_\alpha \frac{dp_\alpha}{dt} - \beta_\alpha \frac{dT}{dt} + \beta_{\alpha C}\frac{dC}{dt}} \tag{4.12}$$

where the subscript α (for fluid phase α) has replaced the subscript f (for fluid) above.

Considering now the solid phase. The density depends on the pore pressure acting on the solid, temperature and the first invariant of the effective stress [64]:

[1]The density variation of a fluid can be a complex function of many dissolved species. Composition can be expressed as solute concentration, mass- and volume fractions and, in the case of CO_2, the concentration compressibility β_{fC} in Eq. (4.11) will typically vary with temperature, pressure and salinity. This is not a relevant discussion for single-phase flow and will be revisited in section 4.4 on partially miscible two-phase flow.

$\rho_s = \rho_s(p_s, T, \mathrm{I}_1')$, the following general expression for the density of the solid can be obtained by differentiation

$$\frac{1}{\rho_s}\frac{d\rho_s}{dt} = -\frac{1}{V_s}\frac{dV_s}{dt} = \frac{1}{\rho_s}\left(\frac{\partial \rho_s}{\partial p_s}\frac{dp_s}{dt} + \frac{\partial \rho_s}{\partial T}\frac{dT}{dt} + \frac{\partial \rho_s}{\partial \mathrm{I}_1'}\frac{d\mathrm{I}_1'}{dt}\right) \tag{4.13}$$

and, similar to the fluid, the following two terms can be recognised [64]:

$$\frac{1}{\rho_s}\frac{\partial \rho_s}{\partial p_s} = c_s \tag{4.14}$$

$$\frac{1}{\rho_s}\frac{\partial \rho_s}{\partial T} = -\beta_s \tag{4.15}$$

where c_s [1/Pa] is the compressibility of the solid and β_s [1/K] is the (volumetric) thermal expansion coefficient for the solid. The last term in Eq. (4.13) can be obtained by considering the following: The mean effective stress σ_m' acting on the solid results in a volume change according to $(1/\rho_s)(\partial \rho_s/\partial \sigma_m') = -c_s$, noting that a positive change in effective mean stress results in an expansion and therefore a negative change in density. The first effective stress invariant is related to the mean effective stress σ_m' [Pa] in the solid according to $\mathrm{I}_1' = 3\sigma_m'$, resulting in $\partial \sigma_m'/\partial \mathrm{I}_1' = 1/3$. Since the mean effective stress on a surface of area A on an arbitrary plane intersecting the porous media will be distributed over a smaller area equivalent to $(1-\phi)A$, the last term in Eq. (4.13) can be expressed as follows:

$$\frac{1}{\rho_s}\frac{\partial \rho_s}{\partial \mathrm{I}_1'} = \frac{1}{\rho_s}\frac{\partial \rho_s}{\partial \sigma_m'}\frac{\partial \sigma_m'}{\partial \mathrm{I}_1'} = -c_s\frac{1}{3(1-\phi)} \tag{4.16}$$

A similar discussion as above is done by Bishop [19], Selvadurai and Nguyen [103], Verruijt [117].

To proceed, a preliminary equation of state for the solid can be summarised as:

$$\frac{1}{\rho_s}\frac{d\rho_s}{dt} = \frac{1}{K_s}\frac{dp_s}{dt} - \beta_s\frac{dT}{dt} - \frac{1}{3K_s(1-\phi)}\frac{d\mathrm{I}_1'}{dt} \tag{4.17}$$

Note that K_s [Pa] is the bulk modulus of the solid grains in the porous media; $K_s = 1/c_s$. The time derivative of the constitutive relation for the first invariant of the effective stress is given by (from Eq. (3.20)):

$$\frac{d\mathrm{I}_1'}{dt} = 3K\left(\nabla\cdot\mathbf{v}_s + \frac{1}{K_s}\frac{dp_s}{dt} - \beta_s\frac{dT}{dt}\right) \tag{4.18}$$

By combining Eqs. (4.17) and (4.18), a final expression for the equation of state for the solid material is obtained [64]:

$$\boxed{\frac{1}{\rho_s}\frac{d\rho_s}{dt} = \frac{1}{1-\phi}\left[(b-\phi)\frac{1}{K_s}\frac{dp_s}{dt} - (b-\phi)\beta_s\frac{dT}{dt} - (1-b)\nabla\cdot\mathbf{v}_s\right]} \tag{4.19}$$

Inserting Eq. (4.19) into Eq. (4.7) results in the following important relation for the change in porosity:

$$\boxed{\frac{d\phi}{dt} = (b-\phi)\left[\frac{1}{K_s}\frac{dp_s}{dt} - \beta_s\frac{dT}{dt} + \nabla\cdot\mathbf{v}_s\right]} \tag{4.20}$$

Inserting Eq. (4.20) into Eq. (4.5) the final form of the non-isothermal, single-phase flow equation in a slightly deforming porous medium is obtained (noting that $p_s = p_f$ for a single-phase fluid, see Eq. (3.22)):

$$\rho_f \left[\frac{(b-\phi)}{K_s} + \frac{\phi}{K_f} \right] \frac{dp_f}{dt} + \rho_f b \nabla \cdot \mathbf{v}_s + \nabla \cdot (\rho_f \mathbf{q}_f) = \rho_f \left(\phi \beta_f + (b-\phi)\beta_s \right) \frac{dT}{dt} + R_f \tag{4.21}$$

where $\mathbf{q}_f$ is given by Darcy's law, Eq. (4.3) and noting that the concentration compressibilities $\beta_{\alpha C}$, Eq. (4.11), is ignored.

There are several ways to derive Eq. (4.21), by analyzing the compressibility of the various components of a fluid-filled porous media, e.g. [46, 58, 117] and others. Here the approach described by [64] is adopted.

Eq. (4.21) is coupled to the momentum balance through the volumetric strain rate term ($\nabla \cdot \mathbf{v}_s$) and the material derivatives, and to the heat transport equation (introduced in chapter 5) through the temperature dependency terms on the right-hand side of the equation. Assuming isothermal conditions, Eq. (4.21) simplifies:

$$\rho_f S \frac{dp_f}{dt} + \rho_f b \nabla \cdot \mathbf{v}_s + \nabla \cdot (\rho_f \mathbf{q}_f) = R_f \tag{4.22}$$

where the storage coefficient S [1/Pa] is given by:

$$S = \left[\frac{(b-\phi)}{K_s} + \frac{\phi}{K_f} \right] \tag{4.23}$$

In general, Eq. (4.21), or Eq. (4.22), will involve solving the flow equation together with equations of equilibrium, Eq. (3.2), using the poroelastic or thermoporoelastic constitutive relation for the stress, Eqs. (3.17) or (3.28), respectively.

4.2.2 Simplifying assumptions

In the literature there are various assumptions used in deriving the equations for single-phase flow in a porous media, some will be described below. These assumptions will be compared in a numerical study of an idealized two-dimensional conceptual model described in App. K.1. For simplicity, isothermal conditions are assumed.

The effect of two parameters will be investigated:

1. The injection pressure, p_{inj}, due to a constant injection rate q_{inj} = 0.05 kg/s/m.
2. The maximum sustainable injection rate, q_{max}, due to a maximum allowable injection pressure constraint, p_{max} = 15 MPa after 30 years of injection.

The latter study implies a simple inversion analysis where the injection rate is varied until the injection pressure after 30 years of injection is equal to the maximum allowable injection pressure p_{max}. The assumptions that will be compared relate to how the movement/deformation of the solid phase is treated:

1. Completely rigid solid phase
2. Solid movement is ignored, $\mathbf{v}_s = 0$, and porous medium is assumed completely rigid, but solid constituents are compressive
3. Solid movement of porous medium is considered implicitly through its compressibility
4. Solid movement is considered implicitly assuming uniaxial strain approximation

These assumptions result in the governing equations for isothermal single-phase flow, Eq. (4.22), to become decoupled from the poroelasticity equation Eq. (3.30). Therefore, the results will be compared to a fully coupled model where the solid movement is described in detail by also solving the poroelastic equation for the displacements.

Case 1: Completely rigid solid

When treating the solid as completely rigid, properties related to the solid, like porosity and density, is considered constant and the solid movement is ignored, hence it is only needed to consider the mass conservation for the fluid, Eq. (4.1), which can be simplified to:

$$S_1 \rho_f \frac{\partial p_f}{\partial t} + \nabla \cdot (\rho_f \mathbf{q}_f) = R_f \tag{4.24}$$

and the effective storage coefficient S_1 is given as:

$$S_1 = \frac{\phi}{K_f} \tag{4.25}$$

It can be seen that the rate of change of the fluid mass per unit volume is only related to the change in density of the fluid, in general this is a good approximations for (highly) compressible fluids (relative to the porous media).

Case 2: No solid movement, rigid frame

No solid movement; $\mathbf{v}_s = 0$. All deformation is simply assumed negligible. The change in porosity is solely due to (de-) compression of the solid constituent. This assumption simplifies the mass conservation equation for the fluid to:

$$S_2 \rho_f \frac{\partial p_f}{\partial t} + \nabla \cdot (\rho_f \mathbf{q}_f) = R_f \tag{4.26}$$

where the effective storage coefficient S_2 is given as:

$$S_2 = \frac{b - \phi}{K_s} + \frac{\phi}{K_f} \tag{4.27}$$

Often it is further assumed that the density of solid is only depending on the pore pressure, and not effective stress, such that $S_2 = (1-\phi)/K_s + \phi/K_f$, which is equivalent to treating the porous media as a suspension of rigid particles and contradictory to the assumption of completely rigid solid where $b = 1 \Rightarrow K_s \to \infty \Rightarrow S_2 = \phi/K_f$ (see Eq. (3.16)).

Case 3: Implicit bulk movement

The $\mathbf{v}_s$ is eliminated from the mass conservation equation of the fluid by using the mass conservation equation of the solid. After careful rearrangement of the resulting equation, following the procedure by Pinder and Gray [89, ch. 3.6.3], it is obtained:

$$\rho_f \left[\frac{1-\phi}{K_s} + \frac{\phi}{K_f} \right] \frac{dp_f}{dt} - \frac{\rho_f}{(1-\phi)\rho_s} \frac{d\left[(1-\phi)\rho_s\right]}{dt} + \nabla \cdot (\rho_f \mathbf{q}_f) = R_f \tag{4.28}$$

Assuming that the stress exerted on the solid is the pore pressure p_f, the bulk compressibility c_b [1/Pa] is defined as:

$$c_b = -\frac{1}{(1-\phi)\rho_s} \frac{d\left[(1-\phi)\rho_s\right]}{dp_f} \tag{4.29}$$

Resulting in the mass conservation equation for the fluid (the solid velocity is negligible such that the material derivatives may be approximated as partial derivatives):

$$S_3 \rho_f \frac{\partial p_f}{\partial t} + \nabla \cdot (\rho_f \mathbf{q}_f) = R_f \tag{4.30}$$

where the bulk modulus of the porous medium $K = 1/c_b$, and the effective storage coefficient S_3 is thus given by:

$$S_3 = \frac{1-\phi}{K_s} + \frac{\phi}{K_f} + \frac{1}{K} \tag{4.31}$$

Case 4: Uniaxial strain approximation

By assuming that the horizontal strains are negligible, compared to the vertical strain, and that the change in vertical stresses are negligible, the volumetric strain can be expressed by Eq. (3.37) (remembering that temperature is constant and pore pressure $p_s = p_f$):

$$\varepsilon_v = \frac{b p_f}{\lambda + 2G} \tag{4.32}$$

Inserting this expression into Eq. (4.21), and again assuming that the solid velocity is negligible such that the material derivatives may be approximated as partial derivatives:

$$S_4 \rho_f \frac{\partial p_f}{\partial t} + \nabla \cdot (\rho_f \mathbf{q}_f) = R_f \tag{4.33}$$

where the effective storage coefficient S_4:

$$S_4 = \frac{b-\phi}{K_s} + \frac{\phi}{K_f} + \frac{b^2}{\lambda + 2G} \tag{4.34}$$

Note that S_4 is the same as the effective storage coefficient in the modified Terzaghi one dimensional consolidation equation described in App. C.3.

Results

For linear elastic materials the storage coefficients S_i can be calculated from the Young's modulus E [Pa], Poisson's ratio ν [-] and Biot's coefficient b [-] using the following relations:

$$K_f = \frac{1}{c_f} \tag{4.35}$$

$$K = \frac{E}{3(1-2\nu)} \tag{4.36}$$

$$\lambda = \frac{E\nu}{(1+\nu)(1-2\nu)} \tag{4.37}$$

$$G = \frac{E}{2(1+\nu)} \tag{4.38}$$

$$K_s = \frac{K}{1-b} \tag{4.39}$$

From these expressions, and the material properties in Table K.1, the storage terms S_i for the various cases are calculated and given in Table 4.1.

Table 4.1: Storage coefficients S_i for the various cases.

	Fully Coupled (Biot)	Case 1 Rigid solid	Case 2 Rigid frame	Case 3 Implicit	Case 4 Uniaxial
S_i (S_1, S_2, S_3 and S_4), [1/GPa]	0.067	0.043	0.067	0.37	0.20

In the first comparison a constant injection rate q_{inj} is applied and the concomitant injection pressure, p_{inj}, for various storage coefficients S_i are compared. Results are shown in Fig. 4.1 (left). The solution from the reference model (fully coupled poroelastic model) is shown in thick, black dashed line. Due to the layered structure of the model, it can be seen that the uniaxial strain approximation solution (magenta line) compares, as expected, almost perfectly to the reference model. For the other cases it can be seen that the decoupling of the groundwater flow equation from the poroelasticity equation gives very different pressure responses, see Fig. 4.1 (center). Note that in case 2 (for completely rigid solid), the deformation is simply ignored. After long injection times the solutions converge as the models approach steady state.

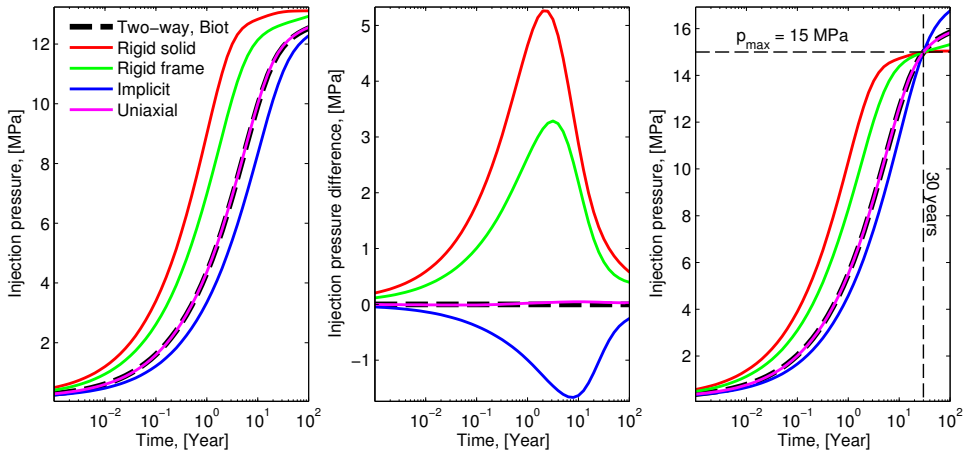

Figure 4.1: Results from the comparison study of simplifying assumptions for single-phase flow. Left: Pore pressure profile at injection well for a constant injection rate. Center: Deviation in injection pore pressure profile compare to a fully coupled model (two-way, Biot). Right: Pore pressure profile at injection well for a constant injection rate such that pore pressure is constrained to p_{max} = 15 MPa after 30 years of injection. See App. K.1 for model description.

In the second comparison, the maximum sustainable injection rate, q_{max}, due to a maximum allowable injection pressure constraint after 30 years, p_{max} = 15 MPa, is evaluated. The resulting pressure profile is given in Fig. 4.1 (right), and the corresponding injection rates and total injected amounts are given in Table. 4.2 together with the deviation from solution from the reference model (two-way, Biot).

Table 4.2: Injection rates and total mass injected after 30 years of constant injection rates constrained to maximum injection pressure p_{max} = 15 MPa.

	Fully coupled (Biot)	Rigid solid Case 1	Rigid frame Case 2	Implicit Case 3	Uniaxial Case 4
Injection rate, [kg/s/m]	0.063	0.0573	0.0591	0.0682	0.0629
Total injection, [ktons/m]	59.6	54.1	55.8	64.5	59.6
Deviation from ref. model (Biot), [%]	NA	-9.2	-6.4	8.3	0.0

It is obvious that the difference in the solution of the models are due to the differences in the storage coefficients S_i, see table 4.1, which is a property that expresses the aquifers capacity to release a fluid. The only difference between model case 1-4 is the way the displacement of solid material, and thereby also porosity, is interpreted, resulting in the various expressions for the storage coefficient. Most of the assumptions used here are obviously not good, the exception being case 4 (uniaxial). Case 2 illustrates very well the importance of considering deformation, simply ignoring deformation completely can underestimate the pore pressure dissipation, resulting in too

high pore pressure estimates. It is seen how a simple approximation of uniaxial deformation, as in case 4, improves the results substantially. Thus, depending on the purpose of the model, the examples serves as a reminder that for simplified, yet realistic calculations, special attention should be on obtaining representative values for the storage coefficient.

4.3 Two-phase immiscible flow

When multiple fluids with different material properties are occupying the pore space in a porous medium, the mass conservation equations for the various fluids becomes more complex. The fluids coexist in the pores; sharing the pore space, where they mix and dissolve and they can even react with each other. They can also react chemically with the porous media itself, depending on the chemical composition, to form new species. Particularly in the case of injecting CO_2 into a brine saturated porous medium, the CO_2 will partially dissolve in the brine, forming carbonic acid and a subsequent lowering of the pH. In particular, carbonic acid can potentially react with metal-oxide bearing materials in the porous medium, forming corresponding carbonates and solid byproducts, e.g. calcite, magnesite, dolomite, and siderite [106]. The products of mineral carbonation are naturally occurring, stable solids that would provide storage capacity on a geological time scale, aka. *mineral sequestration* [74]. However, these are often considered slow processes and assumed to play a long-term role in CO_2 sequestration as the carbonates are thermodynamically stable for millions of years [106]. This complex interaction of dissolution of the porous medium and precipitation can for instance change the porosity and affective the hydraulic and mechanical properties of the porous medium [122]. In the short-term, it has been shown that the permeability can increase up to an order of magnitude due to chemical reactions between CO_2-rich water and minerals commonly found in caprocks [7]. On the other hand, the chemical reaction between the porous medium and the fluid occurs in the vicinity of the fluid-rock interface and the dissolved minerals may be precipitated further downstream of the flow, clogging the pores. Hence, the caprock integrity is not necessarily compromised due to dissolution alone, but it can be an important mechanism in reactivating faults and fractures that may act as conduits and therefore emphasizes the need for further site specific investigations of geochemical interactions in future sequestration projects.

Here the discussion on multi-phase flow is limited to two non-reacting fluid phases. Partial miscibility of the fluid phases will be considered in section 4.4.

4.3.1 Governing equations

Two-phase immiscible flow implies that the two fluids do not dissolve in each other, thus the three phases, the solid phase and the two fluid phases, occupying different volumes. The pores are assumed fully saturated with one or both of the fluids such that the sum of the fluid volume fractions, saturation s_α for fluid phase α, equals unity, see Eq. (3.23). For $n_p = 2$:

$$\sum_{\alpha}^{n_p} s_\alpha = s_w + s_n = 1 \tag{4.40}$$

where s_w [-] and s_n [-] are the volume fractions of the wetting- and non-wetting fluid[2], respectively. The mass conservation equation for each phase component is derived in App. D and for immiscible phases it is obtained from Eq. (D.17) that:

$$\frac{d(\phi s_w \rho_w)}{dt} + \nabla \cdot (\rho_w \mathbf{q}_w) + \phi s_w \rho_w \nabla \cdot \mathbf{v}_s = R_w \tag{4.41}$$

$$\frac{d(\phi s_n \rho_n)}{dt} + \nabla \cdot (\rho_n \mathbf{q}_n) + \phi s_n \rho_n \nabla \cdot \mathbf{v}_s = R_n \tag{4.42}$$

where the R_w [kg/m^3/s] and R_n [kg/m^3/s] are the volumetric source/sink terms of the wetting and non-wetting phases, respectively. The mass balance equation for the solid phase is given by Eq. (4.2), and the multi-phase extension of Darcy's law is given by:

$$\boxed{\mathbf{q}_\alpha = s_\alpha \phi (\mathbf{v}_\alpha - \mathbf{v}_s) = -\frac{\mathbf{k}\mathbf{k}_{r\alpha}}{\mu_\alpha} (\nabla p_\alpha - \rho_\alpha \mathbf{g}), \quad \alpha = w,n} \tag{4.43}$$

where $\mathbf{k}_{r\alpha}$ [-] is the relative permeability (for single-phase flow $\mathbf{k}_{r\alpha} = 1$). Various forms of relative permeability are given in App. E. In addition, the phase pressures relate to each other through the capillary pressure function p_c [Pa]:

$$\boxed{p_c = p_n - p_w = p_c(s_\alpha)} \tag{4.44}$$

Assuming that the capillary pressure is not hysteretic (see App. E), the capillary pressure is considered a unique function of saturation that can be inverted to give the capillary effective saturation:

$$\boxed{s_{e\alpha}^{cap} = p_c^{-1}(s_\alpha)} \tag{4.45}$$

noting that although the capillary pressure p_c is a function of saturation, it only varies with effective saturation $s_{e\alpha}$ [-]. The effective saturation depends on the irreducible saturation $s_{r\alpha}$ of the phases present. The mobility of a phase is zero if the saturation is less than the residual saturation; $s_\alpha \leq s_{r\alpha}$. Hence, sometimes the mobile part of a phase corresponds to a saturation $s_{rw} \leq s_w \leq 1$, but if the non-wetting phase is present, in sufficient amount ($s_n \geq s_{rn}$), the mobile part can correspond to $s_{rw} \leq s_w \leq (1 - s_{rn})$ and the effective saturation can be defined as (depending on the circumstances):

$$\boxed{\begin{aligned} s_{e\alpha} &= \frac{s_\alpha - s_{rw}}{1 - s_{rw}}, \quad s_{rw} \leq s_w \leq 1 \\ s_{e\alpha} &= \frac{s_\alpha - s_{r\alpha}}{1 - s_{rw} - s_{rn}}, \quad s_{rw} \leq s_w \leq (1 - s_{rn}) \end{aligned}} \tag{4.46}$$

where s_{rw} and s_{rn} [-] are the residual saturations for wetting phase and non-wetting phase, respectively.

Using the material derivative, Eq. (D.6), and expand the resulting derivatives, the mass conservation equation for the fluid phase α can be expressed as:

$$\phi \rho_\alpha \frac{ds_\alpha}{dt} + s_\alpha \rho_\alpha \frac{d\phi}{dt} + \phi s_\alpha \frac{d\rho_\alpha}{dt} + s_\alpha \phi \rho_\alpha \nabla \cdot \mathbf{v}_s + \nabla \cdot (\rho_\alpha \mathbf{q}_\alpha) = R_\alpha \tag{4.47}$$

[2]Wetting phase "wets" the porous media.

Using Eq. (4.20) for the change in porosity, and the equation of state for fluid phase α, Eq. (4.12) (ignoring the dependence on chemical composition), the governing, non-isothermal mass balance equation for fluid phase α is obtained:

$$\phi\rho_\alpha\frac{ds_\alpha}{dt}+s_\alpha\rho_\alpha\left[\frac{b-\phi}{K_s}\frac{dp_s}{dt}+\frac{\phi}{K_\alpha}\frac{dp_\alpha}{dt}+b\nabla\cdot\mathbf{v}_s\right]+\nabla\cdot(\rho_\alpha\mathbf{q}_\alpha)=s_\alpha\rho_\alpha\left[\phi\beta_\alpha+(b-\phi)\beta_s\right]\frac{dT}{dt}+R_\alpha \tag{4.48}$$

where $\mathbf{q}_\alpha$ is given by Eq. (4.43) and K_α [Pa] is the inverse of the fluid phase α compressibility. Note that similarly to single-phase flow, Eq. (4.48) can be decoupled from the momentum balance equation by approximating the volumetric strain rate-term, $b\nabla\cdot\mathbf{v}_s$, using the concepts introduced in chapter 4.2.2. For uniaxial strain approximation the following substitution can be made:

$$b\nabla\cdot\mathbf{v}_s=\frac{b^2}{\lambda+2G}\frac{\partial p_s}{\partial t} \tag{4.49}$$

where the pore pressure acting on the solid, p_s, is defined by Eq. (3.22) (for $n_p=2$):

$$p_s=s_w p_w+s_n p_n \tag{4.50}$$

Note that other expressions for p_s can be encountered in the literature, e.g. the sum of the phase pressures (Dalton's law for total pressure in a mixture of gases): $p_s=p_w+p_n$, and in fractional flow formulations: $p_s=p_n-\int_S(f_w\frac{dp_c}{dS})(\xi)d\xi=p_w+\int_S(f_n\frac{dp_c}{dS})(\xi)d\xi$, see e.g. [31]. However, it seems that Eq. (4.50) is the typical choice.

4.3.2 Various formulations

The governing equations for immiscible, two-phase flow is described by the fluid phase conservation equation, Eq. (4.48), containing the unknowns; s_w, s_n, p_w, p_n, temperature T and displacement velocity $\mathbf{v}_s$. However, in the remainder of this chapter $\mathbf{v}_s$ and T will be neglected. By using the auxiliary equations for saturation, capillary pressure and total pressure (Eqs. (4.40), (4.44) and (4.50), respectively), and rearrange, various formulations in terms of dependent variables can be obtained. There are two main groups of dependent variable combinations. The first group is the pressure based formulations, where the dependent variables can be any pair-combination of p_w, p_n, p_s and p_c (12 possible combinations) and the saturations are solved for implicitly using the capillary pressure p_c and pore pressure p_s (Eqs. (4.44) and (4.50), respectively). The second group is the saturation based formulations where the dependent variables can be any combination of either s_w or s_n together with any of the pressure variables p_w, p_n or p_s (6 possible combinations). Some examples that will be evaluated are given in table 4.3.

Table 4.3: Various two-phase flow formulations: dependent variable pairs.

Pressure based formulations:	Saturation based formulations:
1. p_s-p_c	5. p_w-s_n
2. p_w-p_n	6. p_n-s_w
3. p_n-p_c	7. p_s-s_w
4. p_w-p_c	8. p_s-s_n

When considering two-phase isothermal, incompressible and immiscible displacement in a rigid homogeneous porous medium, the governing equations reduces substantially. By using that:

$$\frac{\partial s_w}{\partial t} = \frac{\partial s_w}{\partial p_c}\frac{\partial p_c}{\partial t} \tag{4.51}$$

$$\frac{\partial s_n}{\partial t} = \frac{\partial s_n}{\partial s_w}\frac{\partial s_w}{\partial p_c}\frac{\partial p_c}{\partial t} \tag{4.52}$$

the mass conservation equations for the wetting- and non-wetting phase can be described as (here shown for the $(p_w - p_n)$-formulation):

$$\phi \frac{\partial s_w}{\partial p_c}\frac{\partial p_c}{\partial t} - \nabla \cdot \left(\frac{\mathbf{k}\mathbf{k}_{rw}}{\mu_w} \nabla p_w \right) = R_w \tag{4.53}$$

$$-\phi \frac{\partial s_w}{\partial p_c}\frac{\partial p_c}{\partial t} - \nabla \cdot \left(\frac{\mathbf{k}\mathbf{k}_{rn}}{\mu_n} \nabla p_n \right) = R_n \tag{4.54}$$

where it can be obtained from Eq. (4.40) that $\partial s_w/\partial s_n = \partial s_n/\partial s_w = -1$ and recognizing that the $\partial p_c/\partial t$-term can be expressed by the dependent variables p_w and p_n through:

$$\frac{\partial p_c}{\partial t} = \frac{\partial p_n}{\partial t} - \frac{\partial p_w}{\partial t} \tag{4.55}$$

When including compressibility of the fluid phases, the conservation equations can be described as:

$$\phi \rho_w \frac{\partial s_w}{\partial p_c}\frac{\partial p_c}{\partial t} + s_w \rho_w \phi c_w \frac{\partial p_w}{\partial t} - \nabla \cdot \left(\rho_w \frac{\mathbf{k}\mathbf{k}_{rw}}{\mu_w} \nabla p_w \right) = R_w \tag{4.56}$$

$$-\phi \rho_n \frac{\partial s_w}{\partial p_c}\frac{\partial p_c}{\partial t} + s_n \rho_n \phi c_n \frac{\partial p_n}{\partial t} - \nabla \cdot \left(\rho_n \frac{\mathbf{k}\mathbf{k}_{rn}}{\mu_n} \nabla p_n \right) = R_n \tag{4.57}$$

In the pressure-based formulations, the saturations can be calculated from the capillary effective saturation $s_{e\alpha}^{cap}$ in Eq. (4.45), and from Eq. (4.46) it follows that:

$$\begin{aligned} s_\alpha &= s_{e\alpha}^{cap}(1 - s_{rw}) + s_{r\alpha} \\ s_\alpha &= s_{e\alpha}^{cap}(1 - s_{rw} - s_{rn}) + s_{r\alpha} \end{aligned} \tag{4.58}$$

where $0 \leq s_{e\alpha}^{cap} \leq 1$. Thus the conservation equations for the pressure based formulations can get an additional, artificial source-term from the residual saturation term on the left-hand side in Eqs. (4.56) and (4.57) when $s_w < s_{rw}$ and/or $s_n > 1 - s_{rn}$.

Known solutions

There are two well known mathematical solutions to two-phase flow in porous media; the Buckley-Leverett equation [28], and the McWhorter-Sunada equation (MSE) by McWhorter and Sunada [72]. The former ignores capillary pressure, allowing the governing equation to be reduced to a hyperbolic partial differential equation that can be solved analytically using similarity transform and the method of characteristics, see for instance Orr [85].

However, the analogue solution to the Buckley-Leverett equation for viscous dominated flow, where capillary pressure is significant, is diffusive and not generally self-similar. One of the more general exception is when the boundary flux is inversely proportional to the square

root of time, and McWhorter and Sunada [72] showed that the governing equation could be effectively reduced to a single non-linear, second order ordinary differential equation (see for instance Schmid and Geiger [98] for other examples). They demonstrated an exact solution in the form of an iterative integral equation to a boundary value problem and proposed an iterative procedure to solve it. But, the method proved to be exceptionally sensitive to several model parameters (especially the relative permeability, the fluid viscosity and for large wetting saturations at the inlet) resulting in convergence problems and often in failure, strongly limiting the applicability of the solution.

As an analogue to the Buckley-Leverett equation, to evaluate for instance the impact of capillary pressure, and as a semi-analytical solution to two-phase flow with capillarity it is important that the solution to the MSE is not only fast, but also robust. Therefore, Bjørnarå and Mathias [22] proposed an alternative approach using a pseudospectral method and Chebyshev differentiation matrices [88, 121] that offers not only a fast and accurate, but also a robust solution to the MSE. In the following section this approach will be used in a numerical code validation for various formulations for two-phase flow.

Comparing various formulations

The various formulations in table 4.3 are compared in terms of performance and validated against the semi-analytical solution for a one-dimensional, horizontal (thus ignoring gravity), two-phase incompressible and immiscible displacement in a rigid and homogeneous porous medium as described by Bjørnarå and Mathias [22]. The equations that are solved are Eqs. (4.53) and (4.54), but formulated in terms of the various combinations of dependent variables given in table 4.3.

The reservoir is initially close to fully saturated with a non-wetting phase, $s_n^0 = 0.9$, and a wetting phase is injected ($q_{inj} = A/\sqrt{t}$, where $A = 0.0114$, see Bjørnarå and Mathias [22] for details), displacing the non-wetting phase. The material properties used are given in table 4.4 and the relative permeability and capillary pressure functions are given by Brooks and Corey [27] (see App. E).

Table 4.4: Hydraulic properties of the aquifer in two-phase immiscible flow validation model.

	Property	Value
Permeability, [m^2]	k	10^{-10}
Porosity, [-]	ϕ	0.3
Entry pressure, [Pa]	p_d	10^5
Pore size distribution parameter, [-]	λ	2
Viscosity, wetting phase, [mPa·s]	μ_w	1
Viscosity, non-wetting phase, [mPa·s]	μ_n	0.5

The resulting saturation of the wetting phase, s_w, for the various formulations are plotted in Fig. 4.2.

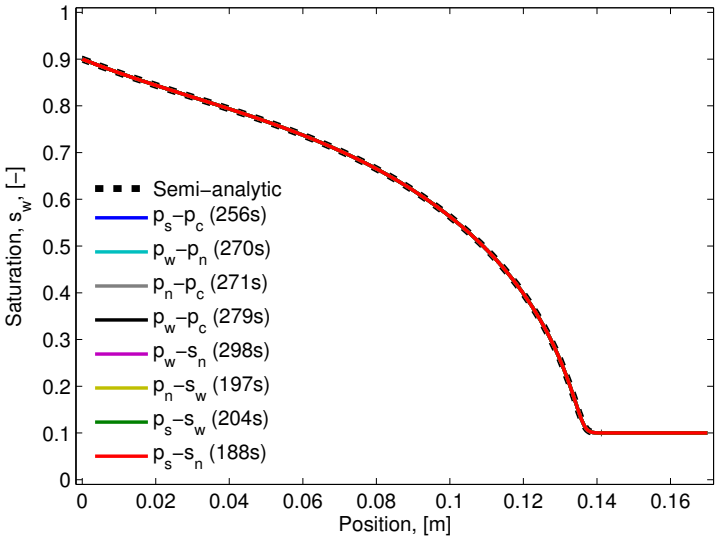

Figure 4.2: Wetting phase saturation profiles for one-dimensional, horizontal (ignoring gravity), two-phase incompressible and immiscible displacement in a rigid and homogeneous porous medium for the various two-phase flow formulations in table 4.3. The semi-analytical solution from Bjørnarå and Mathias [22] are given by the thick dotted black line. The simulation time for the various formulations are given in brackets.

As expected, Fig. 4.2 shows that all the formulations give the same result and are equal to the semi-analytical solution (thick, black dashed line), but an interesting result is the solution times indicated in brackets in Fig. 4.2 and this is commented further in chapter 7.

As mentioned, there are many possibilities to derive equations for two-phase flow, there are four pressure variables and two saturation variables that will behave differently from case to case depending on the hydraulic and mechanical properties and it can be useful to have some choices when faced with a particular problem. In general, the saturation-based formulations are more applicable because they solve for the saturation and can therefore handle correctly saturations outside the mobility range, e.g. when wetting saturation is below residual saturation. Also, in terms of heterogeneity in the entry pressure (in the capillary pressure function), the saturation-based formulations can handle the resulting discontinuity in saturation.

4.4 Two-phase partially miscible flow

Now the assumption that the phases are immiscible is relaxed and the components are allowed to mutually dissolve; i.e. a fraction of the non-wetting phase can dissolve in the wetting phase, and vice versa. Here we will consider a two-component, two-phase system.

4.4.1 Two-component, two-phase flow

The mass conservation equation of each component is given by Eq. (D.11). To derive the governing equations for two-component, two-phase flow, two assumptions will be emphasized: (1) Instantaneous local chemical equilibrium will be assumed, such that the components will

mutually dissolve and immediately satisfy equilibrium composition conditions. (2) Ideal mixing will be assumed, where the component densities are independent of composition, resulting in a simple expression for the phase density (harmonic average):

$$\rho_\alpha = \left(\sum_i^{n_c} \frac{X_{i\alpha}}{\rho_i} \right)^{-1} \tag{4.59}$$

where ρ_i [kg/m^3] is the mass density of component i, n_c [-] is the number of components (here $n_c = 2$) and $X_{i\alpha}$ [-] is the mass fraction of component i in fluid phase α.

Under the assumption of ideal mixing, i.e. constant total volume on mixing, a volume fraction of component i in phase α, $c_{i\alpha}$ can also be defined, expressed as [e.g. 85]:

$$c_{i\alpha} = \frac{\frac{X_{i\alpha}}{\rho_i}}{\sum_i^{n_c} \frac{X_{i\alpha}}{\rho_i}} \tag{4.60}$$

where $c_{i\alpha}$ [-] are the tie-line volume fractions corresponding to the chemical equilibrium compositions in the phases [85]. Comparing Eqs. (4.59) and (4.60) it can be seen that:

$$\rho_i c_{i\alpha} = \rho_\alpha X_{i\alpha} \tag{4.61}$$

Using Eq. (4.61), Eq. (D.11) can be expressed as:

$$\boxed{\frac{d(\phi s_\alpha \rho_i c_{i\alpha})}{dt} + \nabla \cdot (\rho_i c_{i\alpha} \mathbf{q}_\alpha) + \phi s_\alpha \rho_i c_{i\alpha} \nabla \cdot \mathbf{v}_s - \nabla \cdot (\mathbf{D}_\alpha \nabla (\rho_i c_{i\alpha})) = R_{i\alpha}} \tag{4.62}$$

Before deriving the governing equations for two-component, two-phase flow, some useful relations will be introduced. Firstly, the volume fractions of components i in phase α sum up to unity:

$$\sum_i^{n_c} c_{i\alpha} = 1 \tag{4.63}$$

As a consequence of Eq. (4.63) it follows that

$$\sum_i^{n_c} \nabla c_{i\alpha} = 0 \tag{4.64}$$

The overall volume fraction of component i in all the phases:

$$\boxed{c_i = \sum_\alpha^{n_p} c_{i\alpha} s_\alpha} \tag{4.65}$$

and from Eqs. (4.63), (4.65) and using the saturation constraint in Eq. (4.40) it follows that

$$\sum_i^{n_c} c_i = 1 \tag{4.66}$$

The expressions for the saturation can now be found by rearranging Eq. (4.65) (and again using the saturation constraint in Eq. (4.40)):

$$s_n = \frac{c_n - c_{nw}}{c_{nn} - c_{nw}}, \quad s_w = \frac{c_w - c_{wn}}{c_{ww} - c_{wn}} \tag{4.67}$$

4.4.2 Governing equations

The continuity equation is obtained by summing the conservation equation Eq. (4.62) for all components i in all the phases:

$$\sum_{i}^{n_c}\sum_{\alpha}^{n_p}\left[\frac{d(\phi s_\alpha \rho_i c_{i\alpha})}{dt}+\nabla\cdot(\rho_i c_{i\alpha}\mathbf{q}_\alpha)+\phi s_\alpha \rho_i c_{i\alpha}\nabla\cdot\mathbf{v}_s-\nabla\cdot(\mathbf{D}_\alpha\nabla(\rho_i c_{i\alpha}))-R_{i\alpha}\right]=0 \quad (4.68)$$

For two-component, two-phase flow this can be expressed as:

$$\begin{aligned}\frac{d\left[\phi(\rho_n c_n+\rho_w c_w)\right]}{dt}&+\nabla\cdot\left[\rho_n\left(c_{nn}\mathbf{q}_n+c_{nw}\mathbf{q}_w\right)+\rho_w\left(c_{wn}\mathbf{q}_n+c_{ww}\mathbf{q}_w\right)-\mathbf{D}\right]\\&+\phi\left(\rho_n c_n+\rho_w c_w\right)\nabla\cdot\mathbf{v}_s=R\end{aligned} \quad (4.69)$$

where

$$R=\sum_{\alpha}^{n_p}\sum_{i}^{n_c}R_{i\alpha} \quad (4.70)$$

and the dispersion-term $\mathbf{D}$ is expressed by:

$$\mathbf{D}=\mathbf{D}_n\left[\rho_n\nabla c_{nn}+c_{nn}\nabla\rho_n+\rho_w\nabla c_{wn}+c_{wn}\nabla\rho_w\right]+\mathbf{D}_w\left[\rho_n\nabla c_{nw}+c_{nw}\nabla\rho_n+\rho_w\nabla c_{ww}+c_{ww}\nabla\rho_w\right] \quad (4.71)$$

where the phase diffusion/dispersion-terms $\mathbf{D}_n$ and $\mathbf{D}_w$ are defined by Eq. (D.13). The mass conservation for component i is expressed in terms of the overall volume fraction, c_i in all the fluid phases:

$$\sum_{\alpha}^{n_p}\left[\frac{d(\phi s_\alpha \rho_i c_{i\alpha})}{dt}+\nabla\cdot(\rho_i c_{i\alpha}\mathbf{q}_\alpha)+\phi s_\alpha \rho_i c_{i\alpha}\nabla\cdot\mathbf{v}_s-\nabla\cdot(\mathbf{D}_\alpha\nabla(\rho_i c_{i\alpha}))-R_{i\alpha}\right]=0 \quad (4.72)$$

For two-phase, two-component flow, this can be expressed as:

$$\frac{d(\phi\rho_i c_i)}{dt}+\nabla\cdot\left[\rho_i(c_{in}\mathbf{q}_n+c_{iw}\mathbf{q}_w)-\mathbf{D}_n\nabla(\rho_i c_{in})-\mathbf{D}_w\nabla(\rho_i c_{iw})\right]+\phi\rho_i c_i\nabla\cdot\mathbf{v}_s=R_i \quad (4.73)$$

where

$$R_i=\sum_{\alpha}^{n_p}R_{i\alpha} \quad (4.74)$$

By rearranging Eq. (4.69), the continuity equation can be expressed in terms of known quantities as:

$$\begin{aligned}&\phi\left[(\rho_n-\rho_w)\frac{dc_n}{dt}+c_n\frac{d\rho_n}{dt}+c_w\frac{d\rho_w}{dt}\right]+(\rho_n c_n+\rho_w c_w)\left(\frac{d\phi}{dt}+\phi\nabla\cdot\mathbf{v}_s\right)+\\&\nabla\cdot\left[\rho_n\left(c_{nn}\mathbf{q}_n+c_{nw}\mathbf{q}_w\right)+\rho_w\left(c_{wn}\mathbf{q}_n+c_{ww}\mathbf{q}_w\right)-\mathbf{D}\right]=R\end{aligned} \quad (4.75)$$

Similarly, Eq. (4.73) can be rearranged and expressed in terms of known quantities (here the non-wetting component):

$$\begin{aligned}&\phi\left[\rho_n\frac{dc_n}{dt}+c_n\frac{d\rho_n}{dt}\right]+(\rho_n c_n)\left(\frac{d\phi}{dt}+\phi\nabla\cdot\mathbf{v}_s\right)+\\&\nabla\cdot\left[\rho_n(c_{nn}\mathbf{q}_n+c_{nw}\mathbf{q}_w)-\mathbf{D}_n\nabla(\rho_n c_{nn})-\mathbf{D}_w\nabla(\rho_n c_{nw})\right]=R_n\end{aligned} \quad (4.76)$$

The change in porosity, $d\phi/dt$, can be expressed by Eq. (4.20) and the change in density of the fluids are given by the equation of state for the fluid component, Eq. (4.12). Note that in the governing equations for partially miscible two-phase flow, Eqs. (4.75) and (4.76), it can be seen from Eq. (4.65) that:

$$\nabla c_{i\alpha} = \frac{dc_{i\alpha}}{dc_i}\nabla c_i = \frac{1}{s_\alpha}\nabla c_i \tag{4.77}$$

4.4.3 Validation

The set of equations for two-phase partially miscible flow, Eqs. (4.75) and (4.76) is validated by comparing the solution to an analytical, two-component, two-phase flow extension to Buckley-Leverett, see e.g. Orr [85]. The hydraulic and material properties in the validation model are given in Table 4.5. The model is one dimensional and horizontal (ignoring gravity) with mutual dissolution of the two components, brine and CO_2, in a rigid and homogeneous porous medium. Fluid density is assumed constant for both phases and the relative permeability and capillary pressure functions are defined by Brooks and Corey [27] (see App. E). Since the analytical model assumes negligible capillary pressure, a low value is used for the capillary pressure in the numerical model: entry pressure $p_d = 10$ [Pa].

Table 4.5: Properties in two-phase partially miscible flow validation model.

	Property	Value
Porous media:		
Permeability, [m^2]	k	10^{-10}
Porosity, [-]	ϕ	0.3
Diffusion coefficient (Eq. (D.13)), [m^2/s]	d_α	0
Longitudinal dispersion coefficient (Eq. (D.13)), [mm]	$d_{l\alpha}$	5
Residual wetting saturation, [-]	s_{rw}	0.2
Residual non-wetting saturation, [-]	s_{rn}	0
Initial wetting saturation, [-]	s_w^0	0.95
Fluid phases:		
Viscosity, wetting phase, [mPa·s]	μ_w	1
Viscosity, non-wetting phase, [mPa·s]	μ_n	0.5
Dissolution of CO_2 in water, [-]	c_{nw}	0.24
Dissolution of water in CO_2, [-]	c_{wn}	0.012
Injection fluid:		
Non-wetting phase fraction, [-]	s_n^{inj}	0.99
Wetting phase fraction, [-]	s_w^{inj}	0.01
Total injection rate, [1/s]	q_t	0.74709
Non-wetting phase injection rate, [1/s]	q_n	$0.988q_t$
Wetting phase injection rate, [1/s]	q_w	$q_t - q_n$
Brooks-Corey parameters (see App. E):		
Entry pressure, [Pa]	p_d	10
Relative permeability parameter, [-]	λ	2

The dissolution of CO_2 in water ($c_{nw} = 0.24$) and dissolution of water in CO_2 ($c_{wn} = 0.012$) are somewhat exaggerated compared to a real case CO_2 storage scenario. Dissolution of CO_2 and water/brine depend on temperature, pressure and salinity of the water. It is typically assumed that dissolving CO_2 in water increases the density of water. However, this is highly

depending on the salinity and temperature, and for high salinity brines at high temperature the density is actually reduced [123]. Therefore, for more precise modeling of partially miscible phases, expressions for phase and component density with temperature and pressure variations should be obtained. Approximate values for the dissolution of the phases are given in Table 4.6 for a temperature range of 50-100°C, pressure range of 10-30 MPa and at high salinity (from Yan et al. [123], see also Duan and Sun [42] for a mathematical model to calculate the solubility of CO_2 in water and brine at various temperatures (0-260 °C) and pressure (0-2000 bar)) and App. B.

The values for dissolution used in the validation model (specified in Table 4.5) are four times the approximated dissolution numbers in Table 4.6. See also Fig. B.13 for more values of volume fraction c_{nw} at various salinity, pressure and temperature. Note also that dissolution of the phases can also affect the viscosity [77], an effect that is not considered in this thesis.

Table 4.6: Volume fraction of mutual dissolution of brine and CO_2 (assuming a temperature range of 50-100 °C and pressure range of 10-30 MPa and high salinity, numbers are approximated from Yan et al. [123]).

	Volume fraction
CO_2 dissolved in brine, c_{nw}, [-]	0.06
Brine dissolved in CO_2, c_{wn}, [-]	0.003

The saturation profiles (total and effective) and the overall volume fraction of the non-wetting phase are plotted in Fig. 4.3.

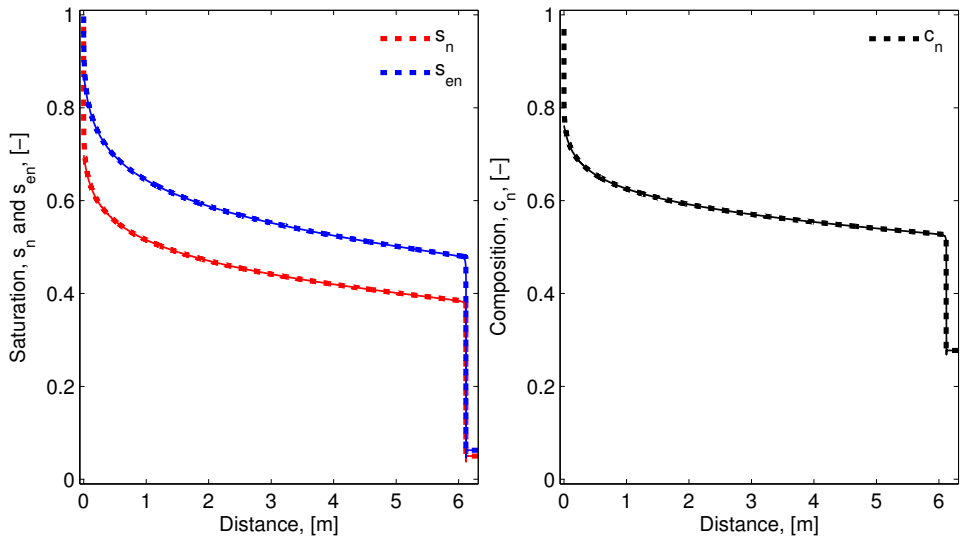

Figure 4.3: (Left) Saturation and (right) overall volume fraction of non-wetting phase for partially miscible two-phase flow after 1 second. Numerical solution (thin lines) is compared with the analytical solution (thick, dashed lines) which is a two-component, two-phase flow extension of the Buckley-Leverett model after Orr [85].

Due to diffusion through the capillary pressure-term and dispersion, the profiles in Fig. 4.3

show some discrepancy close to the injection well, but the effect of dissolution and residual saturation is well captured as well as the leading front.

Analysis of the pressure and effect of various dispersion coefficients $d_{l\alpha}$ and dissolution on a modified model is discussed in Chapter 7, Figs. 7.3 and 7.4, respectively.

Chapter 5

Consideration of non-isothermal effects

5.1 Introduction

Temperature is a very important property, in reservoir simulations it affects material properties such as density and viscosity, but also mechanical properties and even thermal properties. Some properties vary less than others with changing temperature and can be considered constant. Temperature dependency in density of the fluid and solid phase was addressed in chapter 4 in relation to the equation of state, Eqs. (4.12) and (4.19), respectively. Effects of temperature change on stresses and strains have been addressed in chapter 3, and particularly in chapter 3.4 on thermoelasticity. When temperature is expected to change significantly, an additional equation that describes the spatial and temporal variations in temperature is required. This equation, the heat transport equation, can be obtained by considering the conservation of energy and will be described in this section.

The focus in this thesis is how to simplify geomechanical considerations, although thermoporoelasticity is part of this, it will not be evaluated in detail. This chapter is meant to complement the description of the main processes affecting the reservoir and caprock when injecting CO_2 and give some insight into the consequences of spatial and temporal temperature variations. Analysis by Gor et al. [49], Luo and Bryant [68], Preisig and Prévost [90] suggest that thermoporoelasticity is an important factor to consider when evaluating safety of CO_2 storage, particularly when large temperature differences are expected between the injected fluid and the injection formation, and this is discussed further in chapter 7.4.

5.2 Heat transport equation

There are several modes of heat transport. The main modes, that will be considered here, are heat conduction in the fluid(s) and solid phase and convective transport by advection of fluid(s) in the pores. By ignoring heat convection by the solid and by assuming that the phases are in a local state of equilibrium (temperature T is the same in all the phases), then the energy conservation equations for all the phases can be added to obtain the overall heat transport equation [64]:

$$(\rho C_p)_{\text{eff}} \frac{\partial T}{\partial t} + \left(\sum_{\alpha}^{n_p} \rho_\alpha C_\alpha \mathbf{q}_\alpha \right) \cdot \nabla T - \nabla \cdot (\chi_{\text{eff}} \nabla T) = R_q \tag{5.1}$$

Here $(\rho C_p)_{\text{eff}}$ [J/m^3/K] and χ_{eff} [W/m/K] are the effective volumetric heat capacity and the effective thermal conductivity tensor, respectively. $\mathbf{q}_\alpha$ [m/s] is the Darcy flux given by Eq. (4.43) (where $\mathbf{v}_s = 0$ since heat transport due to solid movement is ignored) and R_q [W/m^3] is the difference between the volumetric energy sources and sinks in the fluids and solids. In Eq. (5.1), terms related to radiation, mixing of fluids, chemical reactions, phase transition and dispersion are also ignored. Despite all these assumptions, Eq. (5.1) is appropriate for many practical applications, including CO_2 storage. The effective volumetric heat capacity at constant pressure, $(\rho C_p)_{\text{eff}}$, and the effective thermal conductivity tensor, χ_{eff}, can be expressed by [64]:

$$(\rho C_p)_{\text{eff}} = (1-\phi)\rho_s C_s + \phi \sum_{\alpha}^{n_p} (\rho_\alpha s_\alpha C_\alpha) \tag{5.2}$$

$$\chi_{\text{eff}} = (1-\phi)\kappa_s + \phi \sum_{\alpha}^{n_p} s_\alpha \kappa_\alpha \tag{5.3}$$

where C_s [J/kg/K] and C_α [J/kg/K] are the specific heat capacity (evaluated at constant pressure) and κ_s [W/m/K] and κ_α [W/m/K] are the thermal conductivity tensors of the solid and fluid phases α, respectively.

In order to illustrate the non-isothermal effects, a CO_2 storage scenario based on conditions at the CO_2 storage project at In Salah, Algeria, is defined.

5.3 The non-isothermal effect: Case study

The temperature of the injected fluid at In Salah is about 40°C lower than the temperature in the reservoir [20]. Here a slightly less conservative value of 30°C lower temperature is used. Two models will be evaluated and compared (See App. K.2 for details on model and parameters):

1. THM: Thermo-hydro-mechanical coupling
2. HM: Hydro-mechanical coupling (thermal effects are ignored)

In both models the material properties for the fluids (water and CO_2) are evaluated from the equations of state from the online NIST database [65] using a constant temperature profile (30°C at the surface and 30°C/km gradient) and the initial pore pressure profile based on estimated in situ pore pressure at the reservoir in the area of injection well KB-502 at In Salah from Morris et al. [76]. Note also that the fluid properties are considered constant (in time).

Table 5.1: In situ stress state and pore pressure at the reservoir in the area of injection well KB-502 at In Salah. Values are from Morris et al. [76].

Property	Parameter	Value
Vertical stress	σ_v^0	44.5 MPa
Maximum horizontal stress	σ_H^0	49.9 MPa
Minimum horizontal stress	σ_h^0	30.8 MPa
Initial pore pressure	p_s^0	19.2 MPa

In situ stress state and pore pressure at the reservoir in the area of injection well KB-502 at In Salah is given in table 5.1, and it can be seen that the reservoir is in a strike-slip stress

regime where the vertical stress σ_v is the intermediate principal stress; $\sigma_H > \sigma_v > \sigma_h$. The stresses and pore pressure in table 5.1 is extrapolated to the rest of the over- and underlying formations of the reservoir with a fixed, constant gradient that is obtained by assuming zero stress at the surface and the stress- and pore pressure-state in table 5.1 at 1820 meter depth. The stress state and pore pressure can thus be approximated as:

$$p_s^0 = 1055gD \tag{5.4}$$
$$\sigma_H^0 = 2742gD \tag{5.5}$$
$$\sigma_v^0 = 2445gD \tag{5.6}$$
$$\sigma_h^0 = 1692gD \tag{5.7}$$

where D [m] is the elevation relative to the surface and g is the gravity constant. The models (THM and HM) are assuming plane-strain conditions where the minimum horizontal principal stress σ_h is acting in the out-of-plane direction, according to the stress orientation at In Salah (injection well is parallel with σ_H [94]).

5.3.1 Results

The first observation is the limited dissipation of the temperature compared to the migration of the injected CO_2, see Fig. 5.1. After 12 years a temperature change can be observed up to 100 meters laterally into the reservoir, and in the vertical direction it extends about 60 meters into the caprock and underburden. On the other hand, the injected CO_2 migrates almost 1700 meters, thus illustrating the local effect of the temperature. Since the material properties of the fluids are constant, the volume of the injected fluid is the same in the two models and thus the saturation distribution are almost the same, which is illustrated by the black dashed lines from the HM-model superimposed on the solution of the THM-model, colored contours in Fig. 5.1 (b).

How far the temperature dissipates into the formation depends on the magnitude of the effective volumetric heat capacity $(\rho C_p)_{\text{eff}}$ and the effective heat conductivity χ_{eff}, Eqs. (5.2) and (5.3), respectively, which expresses how much heat can be transport with the fluid through the pores. The water has a much greater heat capacity than the injected CO_2 and the solid phase, see table K.4, thus much of the energy difference between the injected fluid and the residing fluid (brine) is effectively neutralized by the formation water. It can also be seen in Eq. (5.3) that the effective heat conductivity will be largely dominated by the solid material, both in magnitude compared to the fluids (see table K.4) and due to the porosity (water occupies only 17 % of the rock volume). The usually low thermal conductivity exhibited by rocks [e.g. 99] implies little heat transport by conduction. Heat capacity C_p for rocks are typically in the order of 800-1000 [J/kg/K] (at temperatures 50-150 °C) and thermal conductivity κ_s is typically in the order of 3 [W/m/K] [99].

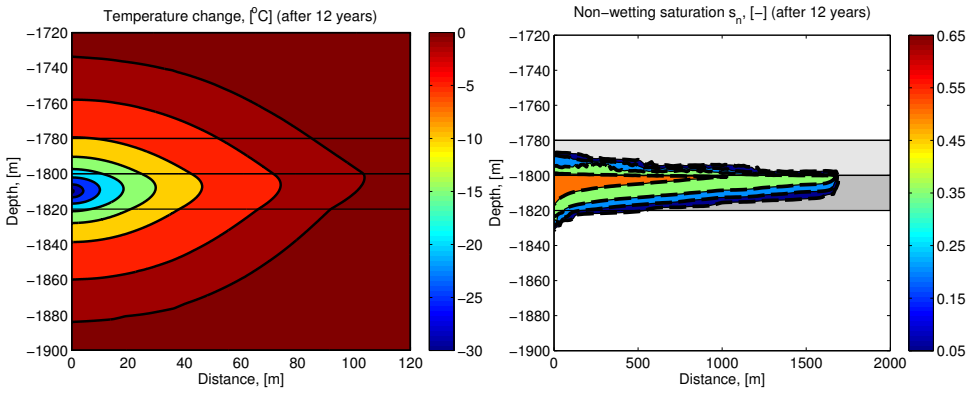

(a) Temperature distribution around the injection well after 12 years of injection.

(b) Non-wetting (CO_2) saturation in the reservoir after 12 years of injection. Black dashed lines are from the HM-model.

Figure 5.1: Temperature distribution (a) and non-wetting phase saturation distribution (b) in the reservoir after 12 years of injection. The reservoir (between 1800-1820 meters depth), overlying caprock layers and underburden are outlined by the thin, black lines.

Temperature is affecting the geomechanics of the system through thermal strains, see chapter 3.4. Excess pore pressure causes the reservoir to expand, resulting in a positive (extensional) volumetric strain, while cooling of the reservoir due to injection of colder CO_2 causes the solid rock phase to contract. The net result of these two processes is that the reservoir is expected to expand less in the THM-model compared to the HM-model. This is illustrated well in Fig. 5.2, showing the deformation of the reservoir after 1, 3.4 and 12 years of injection. The grey shaded area is the initial (undeformed) location of the reservoir and the red and blue lines show the deformed position of the top and bottom boundaries of the reservoir (exaggerated 5000 times). The inserted axis illustrate the absolute difference in the displacement (in mm) of the boundaries for the THM- and HM-models. It can be seen that the difference is local and due to the thermal strains resulting from the cooling. A similar result is shown in Fig. 5.3 where the ratio of volumetric strain ε_v between the two models are shown. The negative ratio indicates that the volumetric strain in the THM-model is less compared to the HM-model, thus ignoring the thermal effects, here cooling, overestimates the deformation.

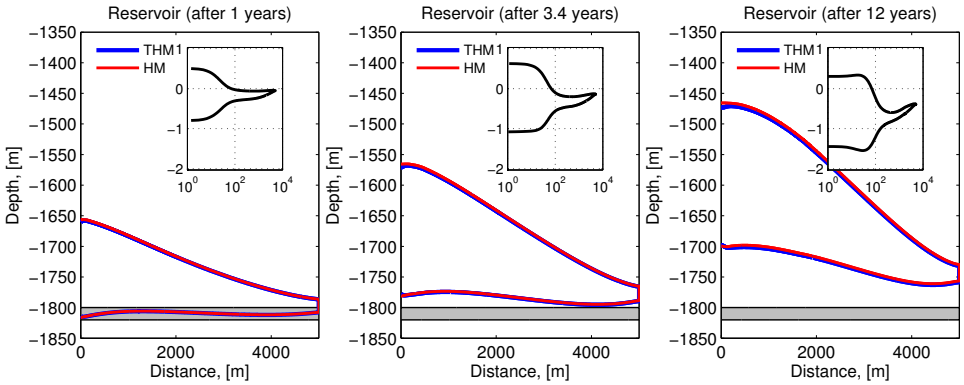

Figure 5.2: Deformation of the reservoir due to cooling by injecting cold CO_2 into a reservoir after 1, 3.4 and 12 years of constant injection. The grey shaded area is the initial (undeformed) location of the reservoir, the red and blue lines show the deformed position of the outer boundaries (exaggerated 5000 times). The inserted axis illustrate the absolute difference in the displacement (in mm) of the boundaries, between the THM- and HM-models.

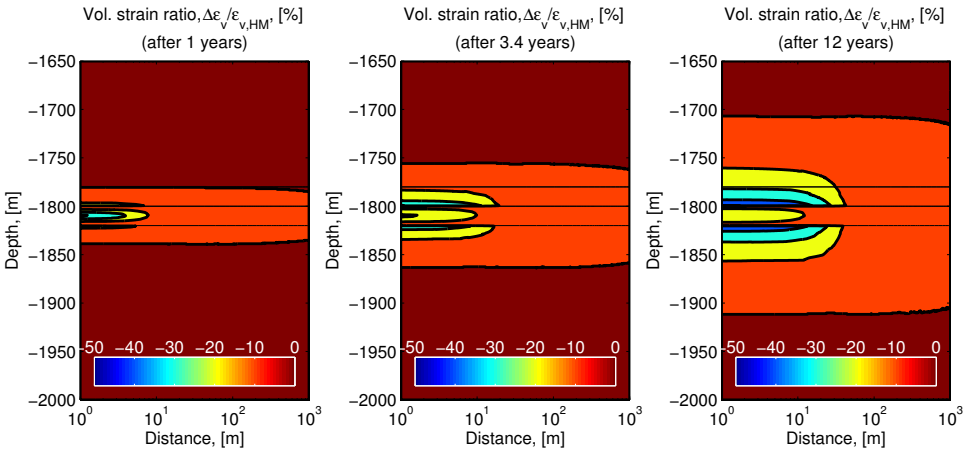

Figure 5.3: Ratio of volumetric strain, ε_v, between the THM- and HM-model after 1, 3.4 and 12 years of injection. Note that the distance is in logarithmic scale. The reservoir (between 1800-1820 meters depth), overlying caprock layers and underburden are outlined by the thin, black lines.

Inspecting the mass conservation equation for the fluid phases, Eq. (4.48), there are two terms that couple the geomechanics to the flow. But, since Biot's coefficient $b = 1$, making the solid compressibility $c_s = 0$ (see Eq. (3.16)), the remaining non-zero coupling term is the volumetric strain rate (which becomes positive due to expansion):

$$s_\alpha \rho_\alpha \nabla \cdot \mathbf{v}_s > 0 \tag{5.8}$$

The thermal expansion terms couple the temperature to the flow (which becomes negative due

to cooling):

$$s_\alpha \rho_\alpha \left[\phi \beta_\alpha + (b-\phi)\beta_s\right] \frac{dT}{dt} < 0 \tag{5.9}$$

The net effect of these two processes is that the fluids have more space to occupy and the mass conservation equations yields a mass "sink", with the result of a lower pore pressure increase. However, when comparing the magnitude of the injection pressure in the two models, they are almost undistinguishable, see for instance the comparison of the injection pressure in Fig. 5.5 (right). But, when comparing the spatial differences, it can be seen clearly that there is an effect and it is indeed local and related to the temperature change, see Fig. 5.4.

The big difference in pore pressure is predominantly directly above and below the reservoir and it indicates that the cooling has an expected positive effect on pore pressure in the sense that the pressure increase is reduced and a lower pore pressure decreases the poroelastic effective stress σ'' (see Eq. (3.15)) and inhibit failure. Thus not considering thermal effects, here cooling, overestimates the pressure increase by up to 0.35 MPa in the caprock/underburden.

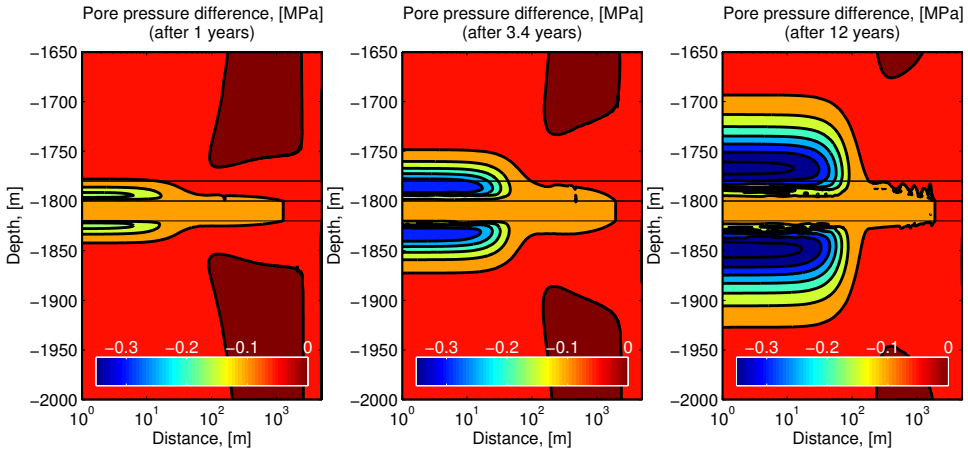

Figure 5.4: Pore pressure difference between THM- and HM-model after 1, 3.4 and 12 years of injection. Note that the distance is in logarithmic scale. The reservoir (between 1800-1820 meters depth), overlying caprock layers and underburden are outlined by the thin, black lines.

Despite the limited and local nature of the temperature effect, it is significant. The differences in displacement and strain are small, see Figs. 5.2, 5.3 and the comparison of surface elevation in Fig. 5.5 (Left), and less deformation means less stress transfer to the surrounding formation. But cooling also introduces thermal stress in the vicinity of the injection well and the critical area, the caprock. Analysis of the stress differences in the two models, compared to failure criteria, will be discussed in chapter 7.4.

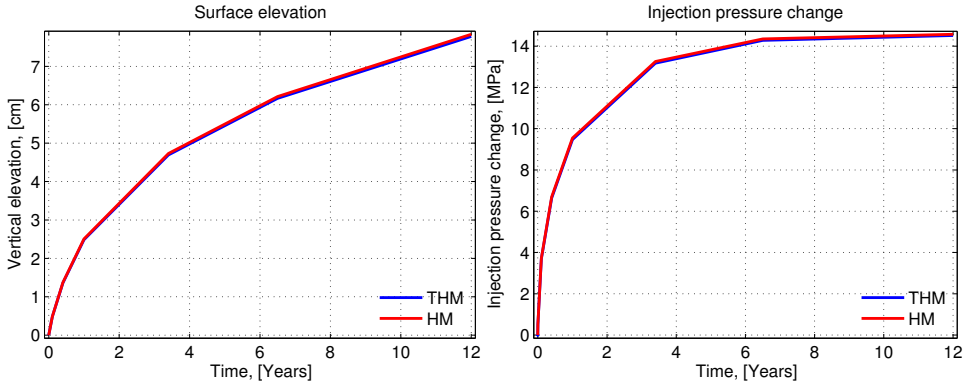

Figure 5.5: (Left) Vertical elevation at the surface directly above the injection well and (right) injection pressure.

Chapter 6

Dimensionally reduced models

6.1 Introduction

When modeling two-phase flow and poroelasticity we are faced with solving a three dimensional problem. Sometimes the variability in one dimension/direction can be ignored, for instance along one of the principal directions or angular direction, allowing the model to be reduced to a two-dimensional problem or an axially symmetric problem, respectively. In rare cases the variability can even be ignored in two dimensions to allow the model to be reduced to a one dimensional problem. However, ignoring variabilities in one or two directions/dimesions are often not a good approximation for real scenarios. Here an alternative simplification will be described; dimensional reduction, where the variability across one of the dimensions is approximated explicitly. A fine scale n-dimensional model is defined whereas the corresponding coarse scale model is the dimensionally reduced, $(n-1)$-dimensional model. The governing equations describing the fine scale model is then integrated along a path where, by making appropriate assumptions, the variability of the solution (dependent variable(s)) can be explicitly expressed to obtain the corresponding governing equations for the, now, dimensionally reduced coarse scale model. The details on when and how this can be applied to two-phase flow and poroelasticity in an aquifer/reservoir is described in the following sections.

First, some general considerations that apply to dimensionally reduced models will be described. Then, the dimensionally reduced models for single-phase flow and two-phase immiscible flow under vertical equilibrium and momentum balance for elasticity (LVD; Linear Vertical Deflection) and poroelasticity (PLVD; Poroelastic Linear Vertical Deflection) will be derived in detail along with illustrative examples. An extension to include thermal effects and miscibility of the phases have not been investigated here, although, miscibility in dimensionally reduced models for two-phase flow have been documented by other authors, see e.g. Gasda et al. [47], Mykkeltvedt and Nordbotten [79], Nordbotten and Celia [81].

6.2 Dimensionally reduced aquifer/reservoir models

Due to the often layered nature of reservoirs, aquifers and aquitards, the horizontal extent is often much larger than the vertical extent and they can be referred to as large aspect ratio geological features. This high aspect ratio property permits justification of the assumptions on the local vertical variability in the solution of the dependent variables because the variability across the thickness is smaller compared to the variability in the horizontal direction. A conceptual sketch of such a system is shown in Fig. 6.1 where the aquifer is located between an

over- and underburden and shows topographic behavior. The bounding surfaces of the aquifer are denoted F_B and F_T, where the location of surface F_n can be expressed as

$$F_n(x,y,z) = z - \zeta_n(x,y) = 0 \tag{6.1}$$

and $\zeta_n(x,y)$ [m] is the vertical position of surface F_n. This notation allows the normal vector $\mathbf{n}$ of a surface to be defined as $\mathbf{n} = \nabla F_n$. For an aquifer with a top and bottom surface, F_T and F_B, as shown in Fig. 6.1, it will be used in the following derivations that the normal vectors are defined as:

$$\mathbf{n}_T = \nabla F_T = \left[-\frac{\partial \zeta_T}{\partial x}, -\frac{\partial \zeta_T}{\partial y}, 1\right]^T, \quad \mathbf{n}_B = \nabla F_B = \left[-\frac{\partial \zeta_B}{\partial x}, -\frac{\partial \zeta_B}{\partial y}, 1\right]^T \tag{6.2}$$

Note that these normal vectors are scaled such that the vertical extent equals 1, thus $|\mathbf{n}| \geq 1$ and pointing (upwards) in positive z-direction; $\partial F_n / \partial z = 1$.

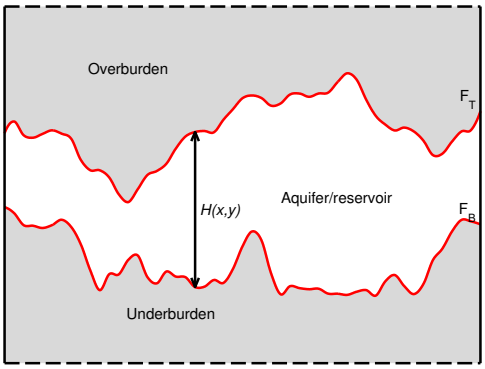

Figure 6.1: Example of an aquifer/reservoir with varying thickness located between an over- and underburden. Note that the vertical dimension has been exaggerated severely and the maximum slopes are typically only a few degrees for geological formations considered for CO_2 storage.

In order to complete the formulations for dimensionally reduced models, some assumptions on the variability, or structure, of the solution within the aquifer is needed. This is specifically required to obtain explicit expressions, or closure relationships, for fluid flux, fluid pressure and geomechanical strain across the thickness of the aquifer. These closure relationships will be introduced when required.

In the following sections it will be shown how the equations for single-phase flow and immiscible two-phase flow, including capillary pressure, can be converted to the equivalent dimensionally reduced formulation using the vertical equilibrium (VE) assumption. For the two-phase flow, this assumption implies a strong buoyant drive in the system that leads to vertical segregation of the phases on a time scale that is fast compared to the time scale of the simulation. The simplest dimensionally reduced formulation for two-phase flow is obtained when assuming the phases are immiscible and the capillary pressure can be completely ignored. This results in the sharp interface model and is well described by Nordbotten and Celia [81]. But here the capillary pressure will be included.

To keep the notation simple, vertical variability in the material or fluid properties within the dimensionally reduced domain will not be considered, but note that the following integrated

conservation equations are valid without regard to any assumptions on the parameters. It is possible to derive the constitutive laws for stress and strains and fluid fluxes with greater generality than what will be done here. However, this can add significant complexity in the definitions of the effective parameters in the integrated equations, for instance for variable fluid density, see e.g. Andersen et al. [5].

6.3 Flow in porous media

6.3.1 Single-phase flow

The mass conservation equation for single-phase flow is given by Eq. (4.21). When ignoring non-isothermal terms, it can be expressed as:

$$\rho_f \left[\frac{(b-\phi)}{K_s} + \frac{\phi}{K_f} \right] \frac{dp_f}{dt} + \rho_f b \nabla \cdot \mathbf{v}_s + \nabla \cdot (\rho_f \mathbf{q}_f) = R_f \tag{6.3}$$

When integrating Eq. (6.3) in the vertical direction, assuming a rigid porous medium such that the material derivatives can be written as partial derivatives and the volumetric strain becomes zero, the integral becomes:

$$\int_{\zeta_B}^{\zeta_T} \left(\rho_f \left[\frac{(b-\phi)}{K_s} + \frac{\phi}{K_f} \right] \frac{\partial p_f}{\partial t} + \nabla \cdot (\rho_f \mathbf{q}_f) - R_f \right) dz = 0 \tag{6.4}$$

In order to be able to perform the integration, the parameters that are not constant in the equation needs to be expressed in terms of the variable of integration, here the vertical position z. This is described in more detail in App. H and is referred to below. After integration, upon using Leibniz' integral rule, the following dimensionally reduced equation for single-phase flow is obtained:

$$\boxed{\rho_f \left[\frac{(b-\Phi)}{K_s} + \frac{\Phi}{K_f} \right] \frac{\partial P_f}{\partial t} H + \tilde{\nabla} \cdot (\rho_f \mathbf{Q}_f) + (\rho_f \mathbf{q}_f \cdot \mathbf{n})\big|_T - (\rho_f \mathbf{q}_f \cdot \mathbf{n})\big|_B = \tilde{R}_f} \tag{6.5}$$

where P_f is the representative fluid pressure defined at the datum $z = \zeta_p$; $P_f = p_f(\zeta_p)$, and is given by Eq. (H.14). The datum is typically the top or bottom boundary of the aquifer but can in principle be chosen freely. $H = H(x,y)$ [m] is the thickness of the aquifer:

$$H = \zeta_T(x,y) - \zeta_B(x,y) \tag{6.6}$$

$\tilde{R}_f$ is the integrated volumetric source/sink term:

$$\tilde{R}_f = \int_{\zeta_B}^{\zeta_T} R_f dz \tag{6.7}$$

and the notation for the resulting horizontal gradient after integration has been introduced:

$$\boxed{\tilde{\nabla} = \left[\frac{\partial}{\partial x}, \frac{\partial}{\partial y}, 0 \right]^T} \tag{6.8}$$

Φ [-] is the average porosity expressed by Eq. (H.4). The integrated Darcy flux $\mathbf{Q}_f$ is derived in App. H.5, Eq. (H.57). For fluid phase mobility $\Lambda_f = 1$ and when assuming that the material properties are constant, it can be expressed as:

$$\mathbf{Q}_f = -\frac{\mathbf{K}H}{\mu_f}\left(\nabla P_f + \rho_f g \nabla \zeta_P\right) \tag{6.9}$$

Note that since vertical variability in the material or fluid properties is not considered within the dimensionally reduced domain, their respective notation is also used in the reduced form.

Validation: Compare with fully resolved model

To illustrate the solution of Eq. (6.5), two examples with an over- and an underburden and a caprock that is overlying a topographic aquifer is solved, see App. K.3 for a detailed description of the model parameters and geometries that will be evaluated. The geometry of the caprock and aquifer is also indicated together with the vertical pressure profiles in Figs. 6.2a and 6.2b.

In the first example, the bottom of the aquifer is flat and the top is sine-shaped, in the second example the bottom of the aquifer is sine-shaped. For both examples, the solution of Eq. (6.5) is compared to a reference solution which is obtained by solving a fully resolved, full-dimensional, model. Vertical crossections of the normalized pore pressure is shown in Fig. 6.2. The location of the profiles are indicated by the corresponding, colored vertical dashed lines across the aquifer and caprock.

The gain in performance when solving for single-phase flow in the aquifer is limited since the diffusive single-phase flow equation is already efficient to solve, but it is still apparent, see a comparison of solver convergence rates in Fig. 6.3 and solver performance in Tab. 6.1.

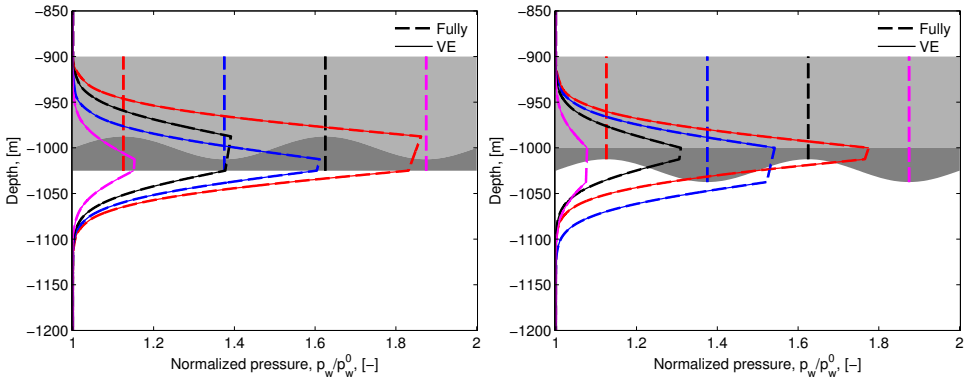

(a) Results from validation example 1.

(b) Results from validation example 2.

Figure 6.2: Results from validation examples (see App. K.3 for model description). Normalised vertical pore pressure profiles from the dimensionally reduced single-phase flow equation compared to a fully resolved, full-dimensional, model. The thick dashed lines are from the fully resolved model and the corresponding thin lines are from the dimensionally reduced model using the vertical equilibrium assumption for the pore pressure.

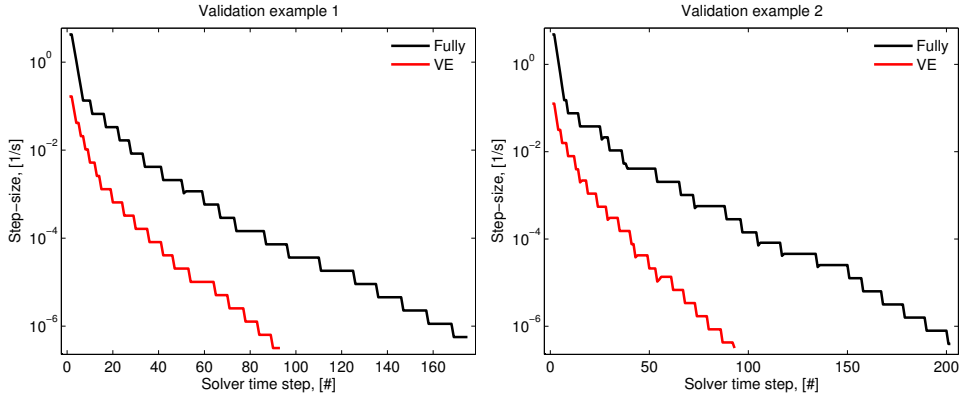

(a) Solver performance of validation example 1.

(b) Solver performance of validation example 2.

Figure 6.3: Output from the solver-log for the two single-phase flow validation models.

Table 6.1: A summary of performance of single-phase flow simulations considering a dimensionally reduced aquifer, assuming VE, and a fully resolved aquifer.

	VE		Fully resolved	
	No. dofs, [#]	Solving time, [s]	No. dofs, [#]	Solving time, [s]
Model 1	12866	5	19119	10
Model 2	13222	5	19475	12

6.3.2 Immiscible two-phase flow

In this section the governing equations for immiscible two-phase flow, including capillary pressure, in porous media using the vertical equilibrium (VE) assumption will be described and the implementation in a numerical code will be validated by comparing the results with a fully resolved (full-dimensional) model.

Governing equation

The governing equations are derived following the approach by Nordbotten and Dahle [83] and Nordbotten and Celia [81]. Similar to previous section (on single-phase flow), it is assumed, for now, that the porous medium is fully rigid, such that the material derivative can be expressed by partial derivatives, and non-isothermal effects are ignored (extension to poroelasticity and deforming media will be described in chapter 6.4 and 6.5). The mass conservation equation for fluid phase α, Eq. (4.48), can then be expressed as:

$$\phi\rho_\alpha\frac{\partial s_\alpha}{\partial t}+s_\alpha\rho_\alpha\left[\frac{b-\phi}{K_s}\frac{\partial p_s}{\partial t}+\frac{\phi}{K_\alpha}\frac{\partial p_\alpha}{\partial t}\right]+\nabla\cdot(\rho_\alpha\mathbf{q}_\alpha)=R_\alpha \tag{6.10}$$

where $\mathbf{q}_\alpha$ is given by Eq. (4.43). Integrating the mass conservation equation in the vertical direction,

$$\int_{\zeta_B}^{\zeta_T}\left(\phi\rho_\alpha\frac{\partial s_\alpha}{\partial t}+s_\alpha\rho_\alpha\left[\frac{b-\phi}{K_s}\frac{\partial p_s}{\partial t}+\frac{\phi}{K_\alpha}\frac{\partial p_\alpha}{\partial t}\right]+\nabla\cdot(\rho_\alpha\mathbf{q}_\alpha)-R_\alpha\right)dz=0 \tag{6.11}$$

and using Leibniz' integral rule, the following dimensionally reduced equation for two-phase flow, including capillary pressure, it is obtained:

$$\Phi\rho_\alpha \frac{\partial S_\alpha}{\partial t} H + S_\alpha \rho_\alpha \left[\frac{b-\Phi}{K_s}\frac{\partial P_s}{\partial t} + \frac{\Phi}{K_\alpha}\frac{\partial P_\alpha}{\partial t} \right] H + \tilde{\nabla}\cdot(\rho_\alpha \mathbf{Q}_\alpha) + (\rho_\alpha \mathbf{q}_\alpha \cdot \mathbf{n})|_T - (\rho_\alpha \mathbf{q}_\alpha \cdot \mathbf{n})|_B = \tilde{R}_\alpha \tag{6.12}$$

where $\tilde{R}_\alpha$ is the integrated volumetric source/sink term of fluid phase α:

$$\tilde{R}_\alpha = \int_{\zeta_B}^{\zeta_T} R_\alpha dz \tag{6.13}$$

Eq. (6.12) and the various upscaled quantities are described in detail in App. H. Note that since vertical variability in the material or fluid properties is not considered within the dimensionally reduced domain, their respective notations in also used in the reduced form.

Validation: Compare with fully resolved model

To illustrate the solution of Eq. (6.12), two example models are defined with a topographic aquifer, see App. K.4 for detailed description of model parameters and the geometries. In both models the aquifer is assumed to be confining and the solution is compared to a reference solution obtained from an identical, but fully resolved, full-dimensional, model.

Results of the comparison are shown in Figs. 6.4 and 6.5. The figures show some selected saturation contours (Figs. 6.4a and 6.5a), the change in pore pressure at the top and bottom of the aquifer (Figs. 6.4b and 6.5b, left) and the non-wetting saturation at top and bottom of aquifer (Figs. 6.4b and 6.5b, right), respectively, at various times.

A summary of the performance is given in Table 6.2.

Table 6.2: A summary of performance of two-phase flow, confined aquifer.

	VE		Fully resolved	
	No. dofs, [#]	Solving time, [s]	No. dofs, [#]	Solving time, [s]
Model 1	798	105	19926	1128
Model 2	798	83	19926	1095

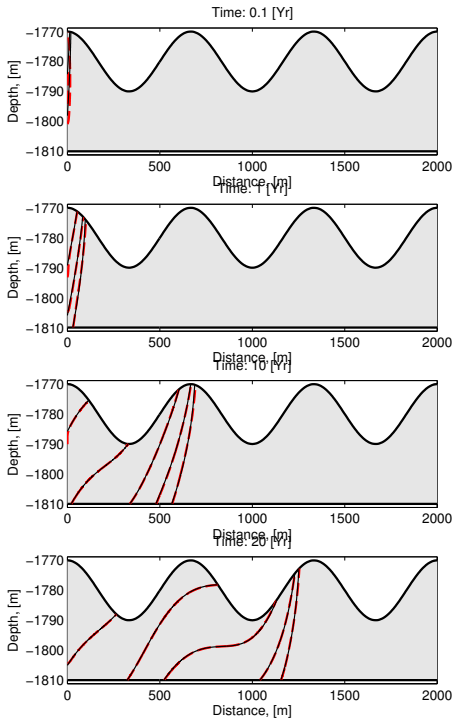

(a) Comparison of saturation contours at various times of fully resolved model (red dashed line) and dimensionally reduced model (thin black line).

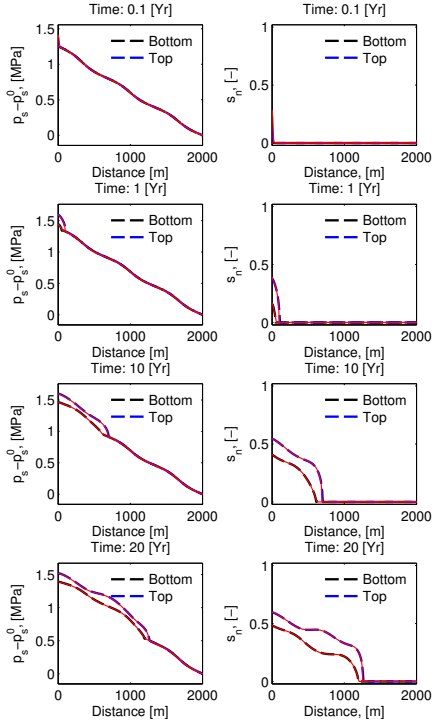

(b) Comparing solution at top and bottom face of the reservoir of fully resolved model (thick dashed lines) and dimensionally reduced model (thin red line). Left: Change in pore pressure. Right: Non-wetting saturation.

Figure 6.4: Results of validation model 1 for two-phase flow using the VE assumption in a confined aquifer. See App. K.4 for details on model.

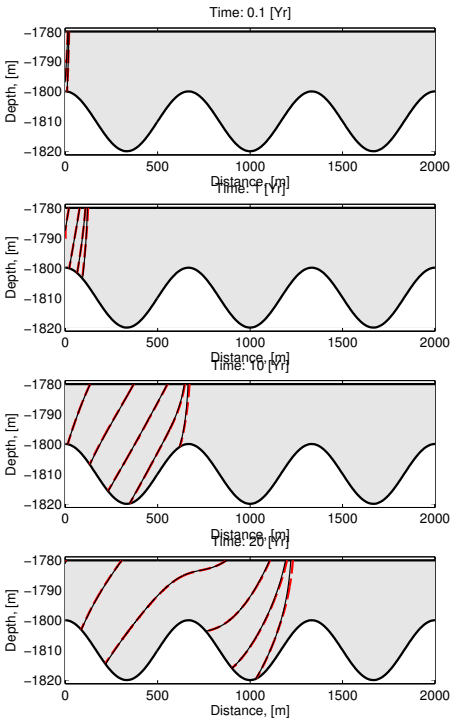

(a) Comparison of saturation profiles at various times of fully resolved model and dimensionally reduced model.

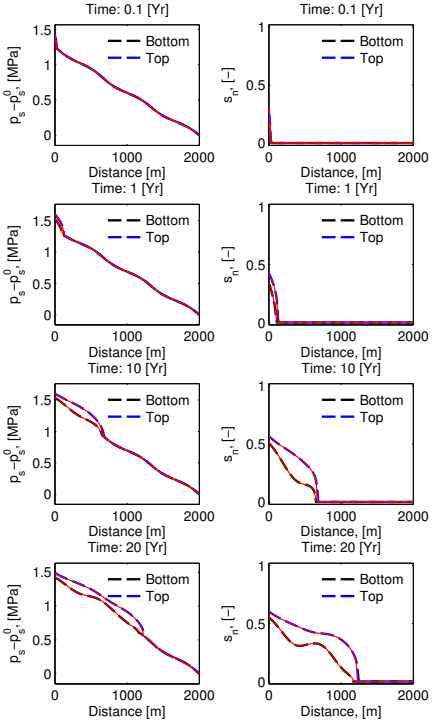

(b) Comparing solution at top and bottom face of the reservoir of fully resolved model (thick dashed lines) and dimensionally reduced model (thin red line). Left: Change in pore pressure. Right: Non-wetting saturation.

Figure 6.5: Results of validation model 2 for two-phase flow using the VE assumption in a confined aquifer. See App. K.4 for details on model.

6.4 LVD: Linear Vertical Deflection

The theory of linear elasticity was presented in chapter 3. In order to derive an approximate, yet accurate, description of linear elasticity appropriate for large aspect ratio formations, e.g. thin aquifers, the momentum balance equation, Eq. (3.2), is integrated across the thickness of the aquifer to obtain an upscaled, dimensionally reduced, formulation. The requirements to dimensionally reduce the momentum balance equation is to assert certain assumptions on the variablility of the solution (displacement) in the direction of integration. The assumption of the Linear Vertical Deflection (LVD) equation is that the displacements across the thickness of a large aspect ratio formation can be approximated by linear functions. The acronym LVD comes from the assumption of linear displacements across the integration path which is (typically) vertical. First these assumptions will be introduced and discussed and the LVD-equation will be derived in detail. In the following section, an extension to the LVD equation to include poroelastic effects will be presented: Poroelastic Linear Vertical Deflection (PLVD) equation, along with some illustrative examples.

6.4.1 LVD: Assumptions

The main assumptions that is used in the derivation of the LVD equation is linearity in the displacements across the integration path of the aquifer (here in the vertical z-direction):

$$u_R = u_B + \frac{u_T - u_B}{H}(z - \zeta_B) \tag{6.14}$$

$$v_R = v_B + \frac{v_T - v_B}{H}(z - \zeta_B) \tag{6.15}$$

$$w_R = w_B + \frac{w_T - w_B}{H}(z - \zeta_B) \tag{6.16}$$

where u [m], v [m] and w [m] are the displacement in x-, y- and z-direction, respectively, and the subscripts R, T and B indicate reservoir/aquifer and top and bottom of reservoir/aquifer, respectively. Using these linear relationships, the strains (derivatives for the displacements components) can be derived, here just shown for u-component; displacement in x-direction:

$$\frac{\partial u_R}{\partial x} = \frac{\partial u_B}{\partial x} + \left(\frac{\partial u_T}{\partial x} - \frac{\partial u_B}{\partial x}\right)\frac{z-\zeta_B}{H} - \frac{u_T - u_B}{H}\left(\frac{\partial \zeta_B}{\partial x} + \left(\frac{\partial \zeta_T}{\partial x} - \frac{\partial \zeta_B}{\partial x}\right)\frac{z-\zeta_B}{H}\right) \tag{6.17}$$

$$\frac{\partial u_R}{\partial y} = \frac{\partial u_B}{\partial y} + \left(\frac{\partial u_T}{\partial y} - \frac{\partial u_B}{\partial y}\right)\frac{z-\zeta_B}{H} - \frac{u_T - u_B}{H}\left(\frac{\partial \zeta_B}{\partial y} + \left(\frac{\partial \zeta_T}{\partial y} - \frac{\partial \zeta_B}{\partial y}\right)\frac{z-\zeta_B}{H}\right) \tag{6.18}$$

$$\frac{\partial u_R}{\partial z} = \frac{u_T - u_B}{H} \tag{6.19}$$

6.4.2 LVD: Governing equations

To obtain the governing equation for LVD, the equilibrium equation, Eq. (3.2), is integrated between the bottom and top of the reservoir (defined by the surfaces F_B and F_T in Fig. 6.1):

$$\int_{\zeta_B}^{\zeta_T} (\nabla \cdot \sigma + \mathbf{f})\, dz = 0 \tag{6.20}$$

The critical part is integrating the divergence-term. Applying Leibniz' rule on the first (horizontal) component of σ, the integral of the divergence can be expressed as:

$$\begin{aligned}
&\int_{\zeta_B}^{\zeta_T} \frac{\partial \sigma_x}{\partial x} dz + \int_{\zeta_B}^{\zeta_T} \frac{\partial \sigma_{yx}}{\partial y} dz + \int_{\zeta_B}^{\zeta_T} \frac{\partial \sigma_{zx}}{\partial z} dz = \\
&\frac{\partial}{\partial x}\int_{\zeta_B}^{\zeta_T} \sigma_x dz - \left[\sigma_x|_T \frac{\partial \zeta_T}{\partial x} - \sigma_x|_B \frac{\partial \zeta_B}{\partial x}\right] + \frac{\partial}{\partial y}\int_{\zeta_B}^{\zeta_T} \sigma_{yx} dz - \left[\sigma_{yx}|_T \frac{\partial \zeta_T}{\partial y} - \sigma_{yx}|_B \frac{\partial \zeta_B}{\partial y}\right] + [\sigma_{zx}|_T - \sigma_{zx}|_B] = \\
&\frac{\partial}{\partial x}\int_{\zeta_B}^{\zeta_T} \sigma_x dz + \frac{\partial}{\partial y}\int_{\zeta_B}^{\zeta_T} \sigma_{yx} dz - \left(\left[\sigma_x|_T \frac{\partial \zeta_T}{\partial x} - \sigma_x|_B \frac{\partial \zeta_B}{\partial x}\right] + \left[\sigma_{yx}|_T \frac{\partial \zeta_T}{\partial y} - \sigma_{yx}|_B \frac{\partial \zeta_B}{\partial y}\right] - [\sigma_{zx}|_T - \sigma_{zx}|_B]\right)
\end{aligned} \tag{6.21}$$

Similarly, the integrated $(\nabla \cdot \sigma)$-term for the other two components can be obtained to obtain on tensor form:

$$\int_{\zeta_B}^{\zeta_T} (\nabla \cdot \sigma)\, dz = \tilde{\nabla} \cdot \Sigma + [\sigma \cdot \mathbf{n}|_T - \sigma \cdot \mathbf{n}|_B] \tag{6.22}$$

where the stress-terms on the upper and lower surfaces of the aquifer in Eq. (6.22), $\sigma \cdot \mathbf{n}|_T$ and $\sigma \cdot \mathbf{n}|_B$, are the traction forces acting on the over- and underburden, respectively, and

$$\Sigma = \int_{\zeta_B}^{\zeta_T} \sigma dz \tag{6.23}$$

To derive Eq. (6.23) for linear elasticity, the stress tensor defined by Eq. (3.8) is integrated:

$$\int_{\zeta_B}^{\zeta_T} \sigma dz = \int_{\zeta_B}^{\zeta_T} \left[\lambda \left(\nabla \cdot \mathbf{u} \right) \mathbf{I} + \mu \left(\nabla \mathbf{u} + (\nabla \mathbf{u})^T \right) \right] dz \tag{6.24}$$

The detailed step by step derivation to solve the integral is shown in App. I and the final result is given by Eq. (I.8):

$$\boxed{\Sigma = \lambda \left[\tilde{\nabla} \cdot \mathbf{U} \right] \mathbf{I} + \mu \left[\tilde{\nabla} \mathbf{U} + (\tilde{\nabla} \mathbf{U})^T \right] + \left[\lambda \left(\mathbf{u} \cdot \mathbf{n}|_T - \mathbf{u} \cdot \mathbf{n}|_B \right) \mathbf{I} + \mu \left(\mathbf{nu}|_T - \mathbf{nu}|_B \right) + \mu \left(\mathbf{un}|_T - \mathbf{un}|_B \right) \right]} \tag{6.25}$$

where

$$\mathbf{U} = \int_{\zeta_B}^{\zeta_T} \mathbf{u} dz \tag{6.26}$$

which, from the assumptions of linear displacements (Eqs. (6.14)-(6.16)) can be expressed, on tensor form, as:

$$\mathbf{U} = \frac{1}{2} \left(\mathbf{u}_T + \mathbf{u}_B \right) H \tag{6.27}$$

The governing equation for LVD can finally be expressed, in a similar structure as the original momentum balance equation, Eq. (3.2), as:

$$\boxed{-\tilde{\nabla} \cdot \Sigma = \mathbf{F}} \tag{6.28}$$

where

$$\boxed{\mathbf{F} = \left[\sigma \cdot \mathbf{n}|_T - \sigma \cdot \mathbf{n}|_B \right] + \int_{\zeta_B}^{\zeta_T} \mathbf{f} dz} \tag{6.29}$$

The last term, the integral of the body load $\mathbf{f}$ from Eq. (6.20), is case dependent and can be integrated once it is defined.

6.5 PLVD: Poroelastic Linear Vertical Deflection

When considering the pore pressure from the fluid in a porous medium, an additional term is added to the stress tensor; $-bp_s\mathbf{I}$, see constitutive relation in Eq. (3.17). Similarly, an additional term is added to the LVD-equation to obtain the Poroelastic Linear Vertical Deflection (PLVD) equation, and from Eq. (3.17) the constitutive relation for a poroelastic medium can be expressed as:

$$\sigma = \lambda \left(\nabla \cdot \mathbf{u} \right) \mathbf{I} + \mu \left(\nabla \mathbf{u} + (\nabla \mathbf{u})^T \right) - bp_s \mathbf{I} \tag{6.30}$$

The pore pressure for two-phase flow in a porous medium is given by Eq. (4.50). In the dimensionally reduced form (using the vertical equilibrium assumption for the fluid pressure), the pore pressure is integrated across the thickness of the aquifer/reservoir, when assuming constant Biot's coefficient b, the integrated effective stress can be expressed as (for positive extensional stress):

$$\boxed{\Sigma = \Sigma'' - bP_s \mathbf{I}} \tag{6.31}$$

where the integrated effective stress Σ'' is now given by Eq. (6.25) and P_s is given by the integral in Eq. (H.37) (see section H.4 for details).

6.6 Validation of LVD- and PLVD-equation

To validate the LVD- and the PLVD-equations (Eq. (6.28) where the constitutive relations are described by Eqs. (6.25) and (6.31), respectively) two example cases are defined:

1. Static pore pressure, no flow
2. Dynamic pore pressure, two-phase flow

The models in the study are two-dimensional assuming plain strain conditions for more accurate assessment of computational performance.

6.6.1 Example 1: Static pore pressure, no flow

The first example is a static (non-transient) case where an over- and underburden is separated by an aquifer with various topography. The reservoir thickness $H = 30 \pm 10$ meters thick, see App. K.5 for detailed description of model parameters and the geometries. A linearly varying pore pressure change Δp_s is prescribed in the aquifer according to:

$$\Delta p_s = \left(\frac{\mathrm{W} - x}{\mathrm{W}} \right) 10^7 \tag{6.32}$$

where W [m] is the width of the aquifer and x [m] is the horizontal position.

The results for various stress components (σ_x, σ_y and σ_{xy}) for the two geometries are shown in Figs. 6.6, 6.7 and 6.8 and the displacement components (u and v, horizontal and vertical, respectively) are shown in Figs. 6.9 and 6.10. Note that the deformation in the plots is exaggerated 5000 times. Note also that the contours are somewhat arbitrary chosen to give a fairly uniform distribution of the contours in the plots. The filled colored contours with thick dashed lines show the solution of the fully resolved, full-dimensional model and the thin black lines are the corresponding solution from the dimensionally reduced PLVD-model.

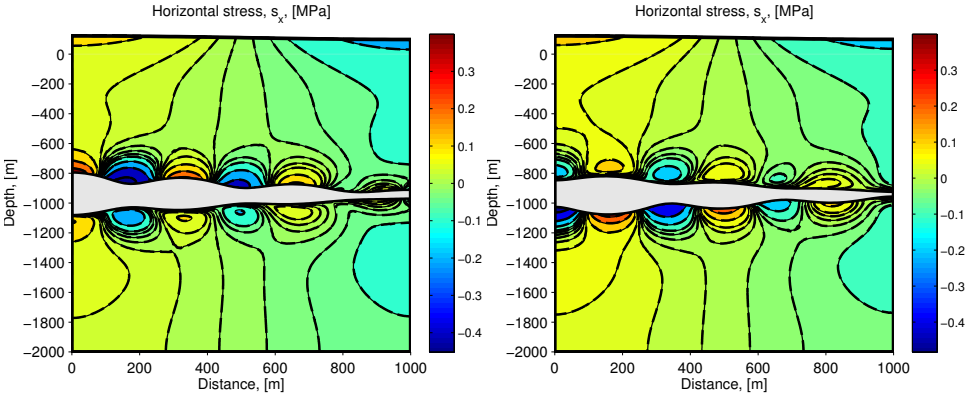

(a) Model 1, flat bottom aquifer boundary.

(b) Model 2, flat top aquifer boundary.

Figure 6.6: PLVD validation case; static pore pressure. The figures show horizontal stress contours of the two different geometries modelled for the aquifer. The filled contours and dashed lines are from the fully resolved model and the thin lines are the corresponding solution from the PLVD-model.

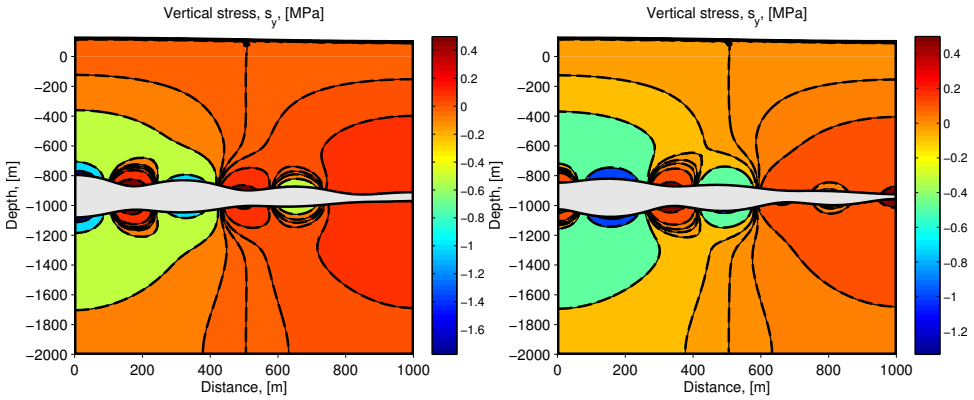

(a) Model 1, flat bottom aquifer boundary.

(b) Model 2, flat top aquifer boundary.

Figure 6.7: PLVD validation case; static pore pressure. The figures show vertical stress contours of the two different geometries modelled for the aquifer. The filled contours and dashed lines are from the fully resolved model and the thin lines are the corresponding solution from the PLVD-model.

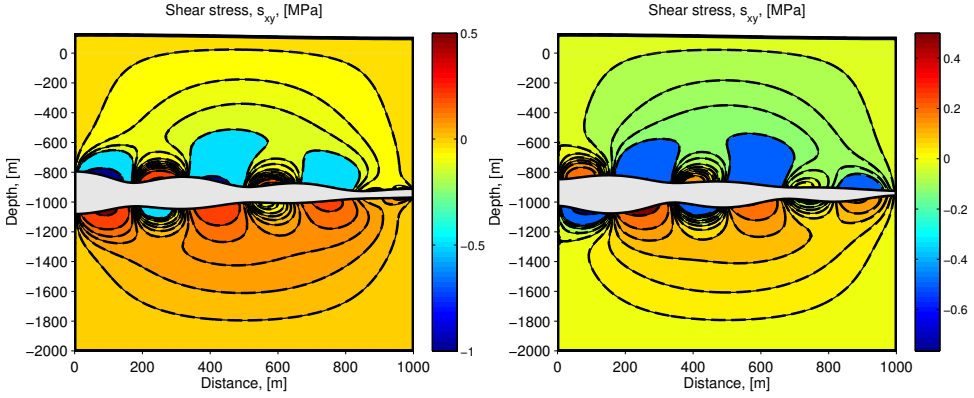

(a) Model 1, flat bottom aquifer boundary.

(b) Model 2, flat top aquifer boundary.

Figure 6.8: PLVD validation case; static pore pressure. The figures show shear stress contours of the two different geometries modelled for the aquifer. The filled contours and dashed lines are from the fully resolved model and the thin lines are the corresponding solution from the PLVD-model.

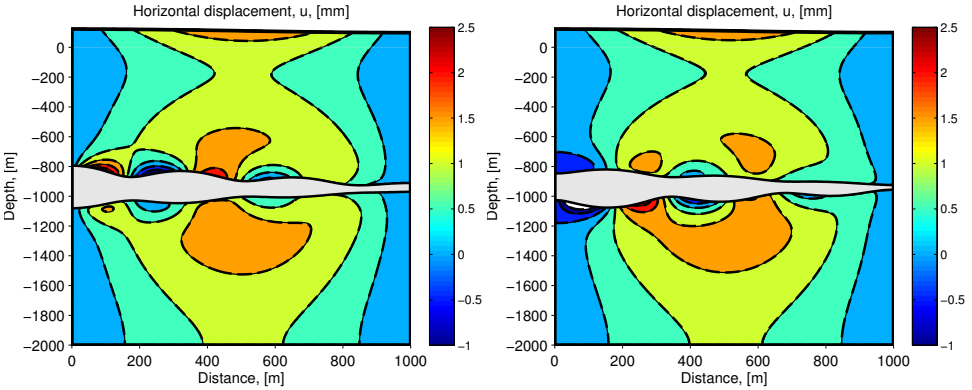

(a) Model 1, flat bottom aquifer boundary.

(b) Model 2, flat top aquifer boundary.

Figure 6.9: PLVD validation case; static pore pressure. The figures show horizontal displacement contours of the two different geometries modelled for the aquifer. The filled contours and dashed lines are from the fully resolved model and the thin lines are the corresponding solution from the PLVD-model.

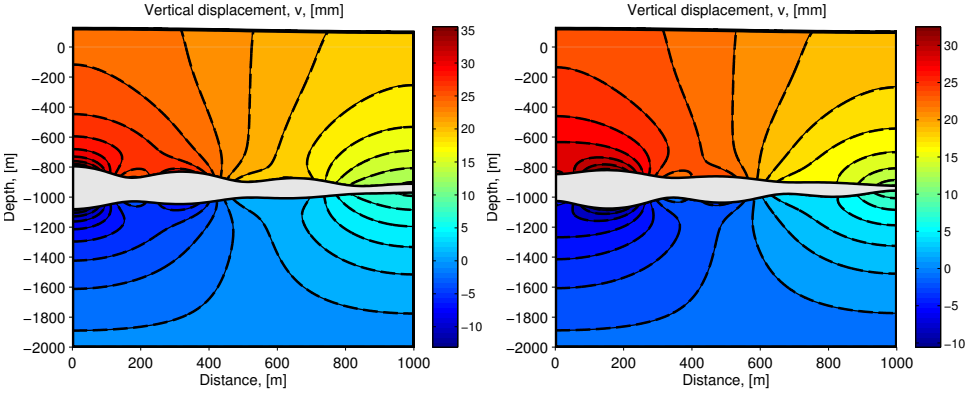

(a) Model 1, flat bottom aquifer boundary.

(b) Model 2, flat top aquifer boundary.

Figure 6.10: PLVD validation case; static pore pressure. The figures show vertical displacement contours of the two different geometries modelled for the aquifer. The filled contours and dashed lines are from the fully resolved model and the thin lines are the corresponding solution from the PLVD-model.

6.6.2 Example 2: Dynamic pore pressure, two-phase flow

In the second example case, the porous medium is fully saturated with a wetting phase (here water) and a non-wetting phase (here CO_2) is injected through a long horizontal pipe located in the middle of the reservoir, see App. K.4 for detailed description of model parameters and the geometries evaluated. Note that this is the same model that was evaluated in chapter 6.3.2 for single-phase flow.

The aquifer is assumed to be semi-confining: the non-wetting phase is confined in the aquifer while the wetting phase is allowed to enter/leave the aquifer. For both geometries, the solution is compared to a reference solution obtained from an identical but fully resolved model.

Some plots of the comparison is given in Figs. 6.11-6.16, showing some selected contours for the stress components (σ_x, σ_y and σ_{xy}), displacement (u and v) and pore pressure (p_s) after 20 years of injection. The figures to the left are for a flat, 30 meter thick reservoir, the center figures are for an aquifer with a flat bottom boundary and the figures to the right are for an aquifer with a flat top boundary. The inserted plots show the relative deviation of the respective quantities evaluated in a point located in the middle of the caprock (indicated by the small black circle in the figures) as a function of time and the color indicates a positive (blue) and negative (red) deviation. The relative deviation is a measure of the difference between the solution of dimensionally reduced and full-dimensional models divided by the solution of the full-dimensional model for the quantities evaluated.

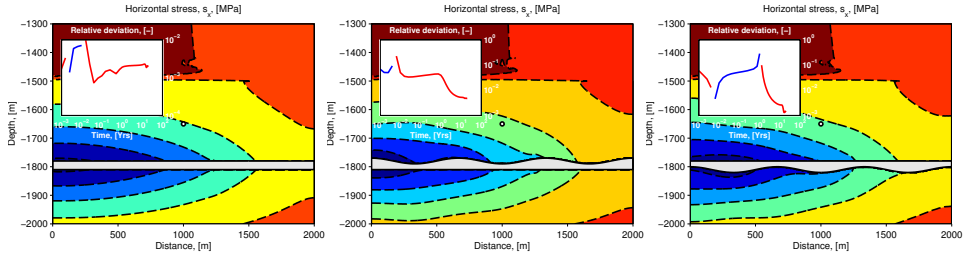

(a) Flat aquifer.

(b) Flat bottom aquifer surface.

(c) Flat top aquifer surface.

Figure 6.11: PLVD validation case; transient pore pressure. The figures show horizontal stress contours. The filled contours are from the fully resolved model and the thick dashed lines are the corresponding solution from the PLVD-model. The Inserted axis show the relative deviation between the dimensionally reduced model and full-dimensional model.

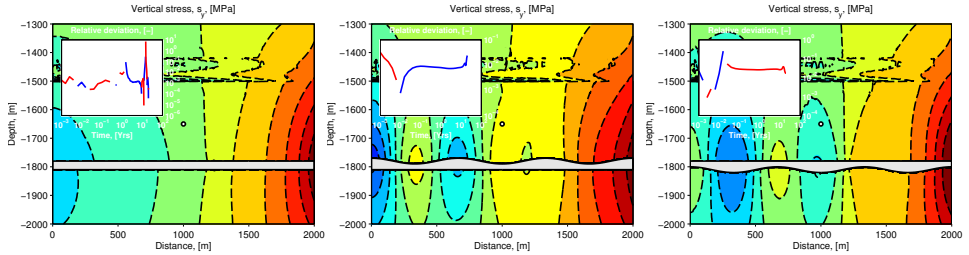

(a) Flat bottom aquifer surface.

(b) Flat bottom aquifer surface.

(c) Flat top aquifer surface.

Figure 6.12: PLVD validation case; transient pore pressure. The figures show vertical stress contours. The filled contours are from the fully resolved model and the thick dashed lines are the corresponding solution from the PLVD-model. The Inserted axis show the relative deviation between the dimensionally reduced model and full-dimensional model.

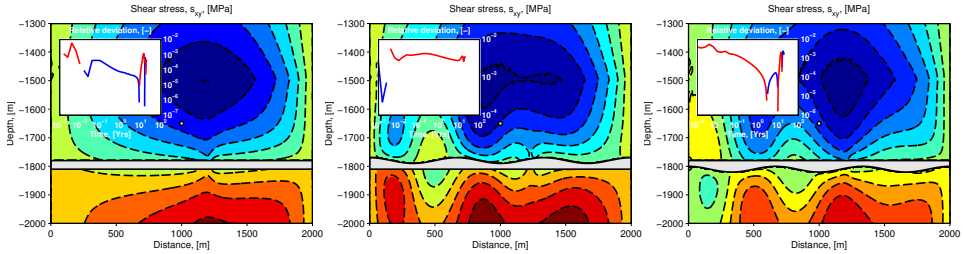

(a) Flat bottom aquifer surface.

(b) Flat bottom aquifer surface.

(c) Flat top aquifer surface.

Figure 6.13: PLVD validation case; transient pore pressure. The figures show shear stress contours. The filled contours are from the fully resolved model and the thick dashed lines are the corresponding solution from the PLVD-model. The Inserted axis show the relative deviation between the dimensionally reduced model and full-dimensional model.

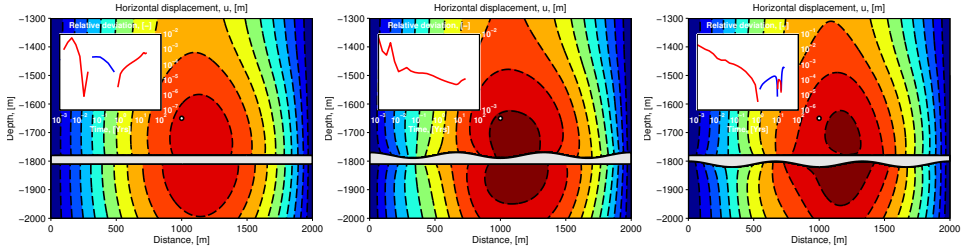

(a) Flat bottom aquifer surface.

(b) Flat bottom aquifer surface.

(c) Flat top aquifer surface.

Figure 6.14: PLVD validation case; transient pore pressure. The figures show horizontal displacement contours. The filled contours are from the fully resolved model and the thick dashed lines are the corresponding solution from the PLVD-model. The Inserted axis show the relative deviation between the dimensionally reduced model and full-dimensional model.

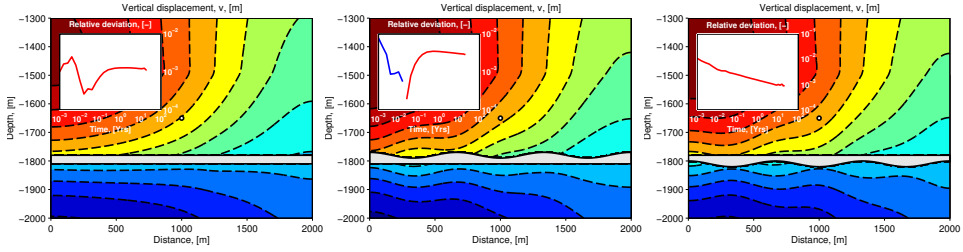

(a) Flat bottom aquifer surface.

(b) Flat bottom aquifer surface.

(c) Flat top aquifer surface.

Figure 6.15: PLVD validation case; transient pore pressure. The figures show vertical displacement contours. The filled contours are from the fully resolved model and the thick dashed lines are the corresponding solution from the PLVD-model. The Inserted axis show the relative deviation between the dimensionally reduced model and full-dimensional model.

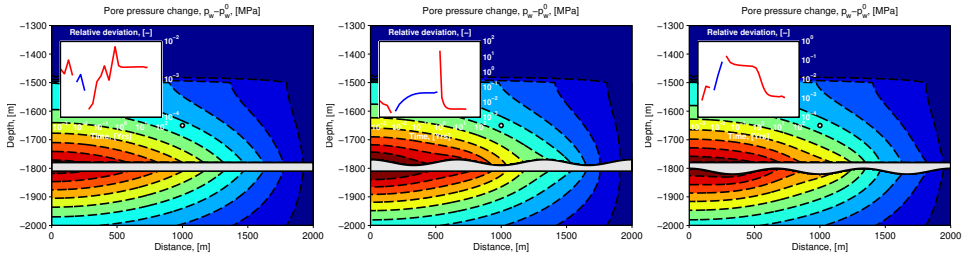

(a) Flat bottom aquifer surface.

(b) Flat bottom aquifer surface.

(c) Flat top aquifer surface.

Figure 6.16: PLVD validation case; transient pore pressure. The figures show pore pressure change contours. The filled contours are from the fully resolved model and the thick dashed lines are the corresponding solution from the PLVD-model. The Inserted axis show the relative deviation between the dimensionally reduced model and full-dimensional model.

A summary of the performance is given in Table 6.3.

Table 6.3: A summary of performance of two-phase flow in a confined aquifer.

	VE, PLVD		Fully resolved	
	No. dofs, [#]	Solving time, [s]	No. dofs, [#]	Solving time, [s]
Flat	62556	1047	99216	23360
Model 1	62382	1873	99042	21278
Model 2	62232	1653	98892	19634

Chapter 7

Discussion

The preceding chapters have covered several topics and relevant processes for CO_2 storage and injection, leading up to a simplified model. Successful storage of CO_2 depends on the ability to contain the CO_2 in the storage formation, and successful containment of CO_2 relies on not compromising the confining rock. Therefore various failure mechanisms and criteria were reviewed in chapter 2 where the evaluation of principal stress and effective principal stress are important parts of the analysis, and the constitutive relations for elasticity, poroelasticity, thermoelasticity and thermoporoelasticity were given in chapter 3.

Next, the various modeling results from chapters 4, 5 and 6 will be discussed, together with some extended analysis from the respective chapters.

7.1 Single-phase flow

The effective stress is an important concept when evaluating the integrity of the storage formation and surrounding formations and it plays a major role in deriving the fluid flow equations, as shown in chapter 4. The mass conservation equation for a single-phase fluid was carefully derived in chapter 4.2. Although seemingly trivial, the single-phase flow equation is very important in reservoir simulations because the flow in a large part of the reservoir and surrounding formations can be described by this equation. In chapter 4.2.2 various simplifying assumptions on the solid-phase movement were compared for single-phase fluid flow. The results illustrate the importance of treating the mechanics of the solid phase properly. It was also seen that the uniaxial strain approximation is a good first order approximation in simplified analysis.

7.2 Two-phase, immiscible flow

In chapter 4.3 the equations for two-phase immiscible flow were reviewed, various formulations of different pairs of dependent variables were solved and compared to a semi-analytical solution as shown by Bjørnarå and Mathias [22]. The performance (which depends on many factors such as the number of degrees of freedom, time-stepping in the numerical solver, etc.) of the various formulations were compared (see Fig. 4.2) and the fastest being the $p_s - s_n$-formulation and the slowest was the $p_w - s_n$-formulation, with a factor 1.6 difference in performance. A preferred formulation can not be concluded based on the validation model because it will depend on a number of factors, such as initial property values and capillary pressure and relative permeability functions. In the examined model the number of degrees of freedom

were the same, hence the performance depended on how efficient the time-stepping in the numerical solver is for the various formulations. The results of a similar extended test is shown in Figs. 7.1 and 7.2 where in the first test-case a wetting phase is displacing a non-wetting phase (Fig. 7.1) and in the second test-case a non-wetting phase is displacing a wetting phase (Fig. 7.2). Material- and model parameters are described in table 7.1.

Table 7.1: Properties in two-phase immiscible flow validation model. Relative permeability and capillary pressure functions are defined by Brooks and Corey [27] (see App. E for details). Fluids and solid are incompressible and isothermal conditions are applied. Results are shown in Figs. 7.1 and 7.2.

Description	Property	Value	Model 1 (Fig. 7.1)	Model 2 (Fig. 7.2)
Permeability, [m^2]	k	10^{-10}		
Porosity, [-]	ϕ	0.3		
Injection rate, wetting phase, [m/s]	q_w^{inj}	-	0.018295	0
Injection rate, non-wetting phase, [m/s]	q_n^{inj}	-	0	0.018295
Viscosity, wetting phase, [mPa·s]	μ_w	1		
Viscosity, non-wetting phase, [mPa·s]	μ_n	0.5		
Initial wetting saturation, [-]	s_w^0	-	0.05	0.95
Residual wetting saturation, [-]	s_{rw}	0		
Residual non-wetting saturation, [-]	s_{rn}	0		
Entry pressure, [Pa]	p_d	10^5		
Pore size distribution parameter, [-]	λ	2		
Diffusion coefficient (Eq. (D.13)), [m^2/s]	d_α	0		
Longitudinal dispersivity, [mm]	$d_{l\alpha}$	0.1		
Dissolution of CO_2 in water, [-]	c_{nw}	0.0		
Dissolution of water in CO_2, [-]	c_{wn}	0.0		

In the first test-case, Fig. 7.1, the $p_w - s_n$ formulation showed the poorest performance of the immiscible, two-phase flow formulations, by a factor of 2.4 compared to the fastest, but in general the saturation-based formulations seem to perform better compared to the pressure-based formulations. This general trend is comparable to the previous results shown in Fig. 4.2. However, this is reversed in the second test case, Fig. 7.2, although the difference in performance is slightly less. In Figs. 7.1 and 7.2 the solution time for the compositional flow model ($p_w - C_n$-formulation, described in chapter 4.4) is also shown. It is interesting to note that the performance is better compared to the immiscible flow formulations, and this is due to the added diffusion and dispersion that stabilizes the solution by "smearing" out the sharp leading saturation front of the injected phase, but as can be seen on both the saturation profile and injection pressure evolution, the impact on the solution is negligible. However, this also depends on the phase being injected as it can be seen that the trend is opposite when injecting non-wetting phase, compare performance in Figs. 7.1 and 7.2 for $p_w - C_n$-formulation, and further emphasizes that different mathematical formulations can have a numerical advantage in different scenarios.

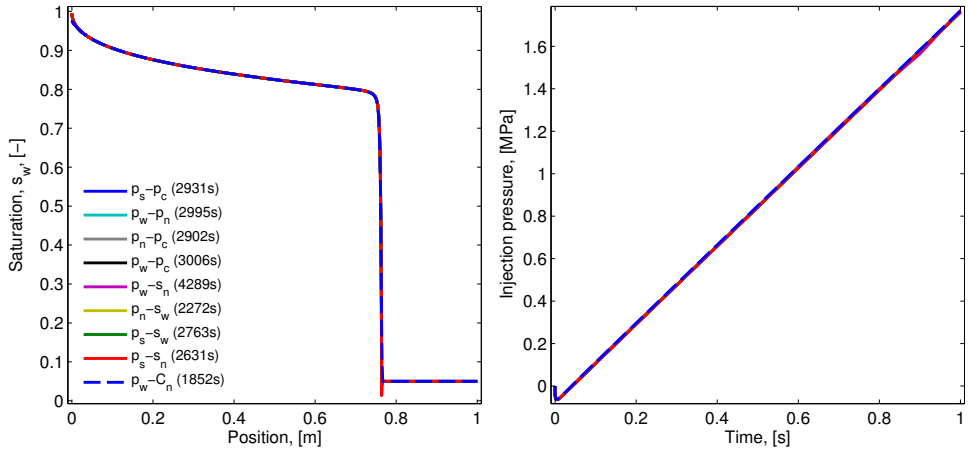

Figure 7.1: Comparing performance of various formulations of two-phase flow when injecting a wetting phase into a non-wetting phase saturated domain ($s_w^0 = 0.05$). (Left) Saturation profile of the wetting phase s_w at end of simulation (1 sec.). The legends indicate which formulation is used and the solving time. (Right) Injection pressure p_s. See table 7.1 for material- and model parameters. See Box 7.2 for a note on the undershoot in saturation profile (left figure) around 0.75 m.

Box. 7.2. Note on overshoots/undershoots in numerical solutions

Overshoots or undershoots, typically close to areas of high gradients in solution, can look like oscillations/wiggles in a numerical solution and are due to numerical errors in the numerical discretization scheme. It is important to note that this is not a matter of numerical method (e.g. finite difference method, finite element method or finite volume method), but a matter of numerical discretization. These errors can grow uncontrollably and completely deteriorate the solution, but a less severe instability occurs when the solution is locally unbounded (small oscillations/wiggles that do not grow uncontrollably), yet globally stable, and the solution is locally inaccurate but globally accurate to the allowable numerical error. More specifically it can be said that the local oscillations where the dependent variable shows a large gradient are due to too locally large *Pe*clet numbers. For a stable solution it is generally required that

$$Pe = \frac{|v|h}{D_h} < 2$$

where v [m/s] is the local velocity, h [m] is the local mesh size and D_h [m^2/s] is the local diffusion coefficient. Localized oscillations occurs because the numerically discretized solution does not have enough diffusion compared to the actual problem. For simple problems the amount of (artificial) diffusion that needs to be added can be determined exactly. However, for higher dimension models and more complicated equations this is normally not possible and the problem can be solved by (1) refining the numerical grid (reducing h) until the actual diffusion can be properly resolved or (2) the problem can be remedied by adding "sufficient" amount of artificial diffusion to the equation, or numerical diffusion by changing the discretization scheme, or both.

Note that $Pe < 2$ is not an absolute and decisive limit for stability, e.g. according

to Hirsch [55] the limit for stability also depends on the time-stepping, thus "sufficient" amount is problem dependent and makes it difficult to determine. Adding too little artificial diffusion will still give oscillations/wiggles and local inaccuracies in the solution (even though it may be reduced), while adding too much may alter the original problem and result in a wrong solution. Thus, the amount of artificial diffusion should always be subject to a sensitivity analysis to determine the optimum amount.

In some numerical schemes so-called slope (or flux) limiters can be used to avoid over-/under-shoots in the solution by limiting the spatial derivatives to physically meaningful quantities (make the solution total variation diminishing). These limiters are applicable in numerical schemes that are locally conservative and this is why the finite volume method is often the preferred method of choice for solving flow problems.

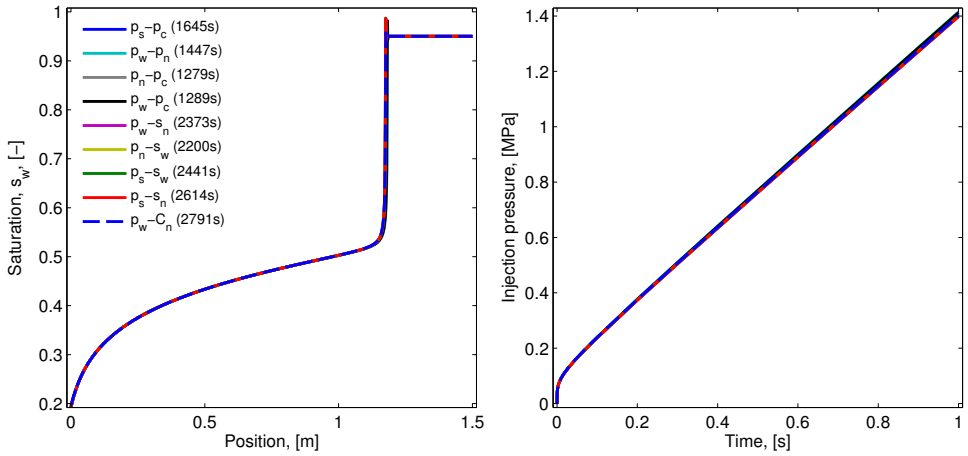

Figure 7.2: Comparing performance of various formulations of two-phase flow when injecting a non-wetting phase into a wetting phase saturated domain ($s_w^0 = 0.95$). (Left) Saturation profile of the wetting phase s_w at end of simulation (1 sec.). The legends indicate which formulation is used and the solving time. (Right) Injection pressure p_s. See table 7.1 for material- and model parameters. See Box 7.2 for a note on the overshoot in saturation profile (left figure) around 1.15 m.

7.3 Two-phase, miscible flow

To investigate the effect of miscibility on the pore pressure, a similar model (as above) was defined and compared for various contributions of dispersion and dissolution, see table 7.2 for material- and model parameters.

Table 7.2: Properties in a partially miscible two-phase flow model used in the parameter sensitivity analysis. Relative permeability and capillary pressure functions are defined by Brooks and Corey [27], (see App. E). Fluids and solid are incompressible and isothermal conditions are applied. Results are shown in Figs. 7.3 and 7.4.

Description	Property	Value	Model 1 (Fig. 7.3)	Model 2 (Fig. 7.4)
Permeability, [m^2]	k	10^{-10}		
Porosity, [-]	ϕ	0.3		
Injection rate, wetting phase, [m/s]	q_w^{inj}	0.00012		
Injection rate, non-wetting phase, [m/s]	q_n^{inj}	0.00988		
Viscosity, wetting phase, [mPa·s]	μ_w	1		
Viscosity, non-wetting phase, [mPa·s]	μ_n	0.5		
Initial wetting saturation, [-]	s_w^0	0.99		
Residual wetting saturation, [-]	s_{rw}	0.2		
Residual non-wetting saturation, [-]	s_{rn}	0		
Entry pressure, [Pa] (App. E.1.1)	p_d	10^5		
Pore size distribution parameter, [-]	λ	2		
Diffusion coefficient (Eq. (D.13)), [m^2/s]	d_α	0		
Longitudinal dispersivity, [mm]	$d_{l\alpha}$	0.5	0.05-100	
Dissolution of CO_2 in water, [-]	c_{nw}	0.06		0.03-0.36
Dissolution of water in CO_2, [-]	c_{wn}	0.003		0.0015-0.018

The results from the compositional flow model is compared to immiscible two-phase flow. In Fig. 7.3 the saturation and injection pressure profiles are compared for various values of dispersivity $d_{\alpha l}$ (in Eq. (D.13) which defines the diffusion/dispersion tensor in the governing Eqs. (4.75) and (4.76)). It can be seen how the saturation profile is increasingly "smeared" out with increasing dispersion, Fig. 7.3, and the injection pressure is affected by dissolution, Fig. 7.4. For a longitudinal dispersivity up to 5 [mm][1] the affect on pore pressure is modest; less than 1 % compared to immiscible flow. At this value the solving time is also comparable to immiscible case, see summary of performance in Table 7.3.

In Fig. 7.4 the results for various levels of dissolution of the phases is compared to immiscible flow. The dissolution has an effect on the saturation close to the injection well, but the migration is almost identical compared to immiscible two-phase flow.

[1] Following the procedure in App. J, the shape of the immiscible flow profile compares to a dispersivity $d_{l\alpha}$ of 0.03 mm.

Table 7.3: Summary of performance of partial miscibility two-phase flow models.

Model 1		Model 2	
Dispersivity [mm], $d_{l\alpha}$	Solving time [s]	Solubility [-], (c_{nw},c_{wn})	Solving time [s]
0.05	2570	(0.0015,0.03)	1838
0.5	2320	(0.003,0.06)	1980
5	1381	(0.006,0.12)	1717
50	339	(0.012,0.24)	1638
100	201	(0.018,0.36)	858
Immiscible ($p_n - s_w$)	1295		

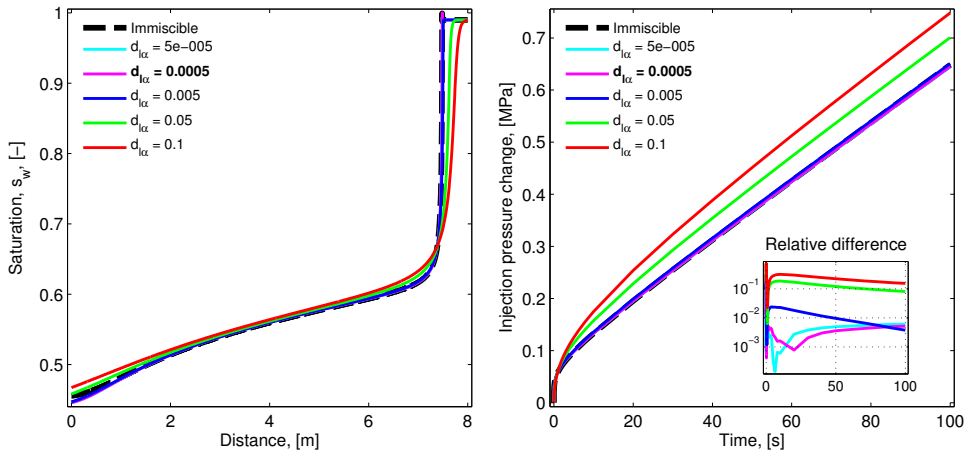

Figure 7.3: Comparing saturation profiles and injection pressure for various values of longitudinal dispersion coefficient, $d_{l\alpha}$ [m], in the compositional flow model. The inserted figure shows the relative difference in the pressure compared to immiscible two-phase flow. See table 7.2 for material- and model parameters. See Box 7.2 for a note on the overshoot in saturation profile (left figure) around 7.5 m.

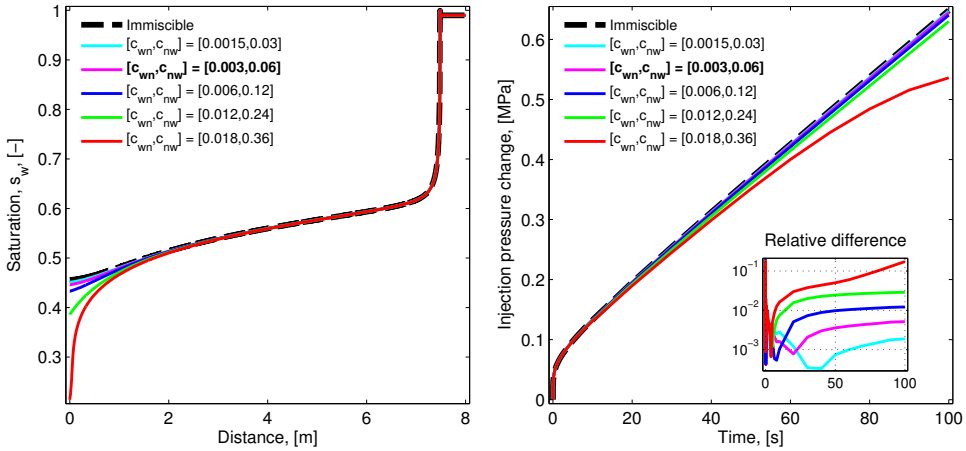

Figure 7.4: Comparing saturation profiles and injection pressure for various equilibrium compositions in the fluid phases: c_{wn} is the volume fraction of wetting phase that dissolve in the non-wetting phase and c_{nw} is the volume fraction of non-wetting phase that dissolve in the wetting phase. The inserted figure shows the relative difference in the pressure compared to immiscible two-phase flow. See table 7.2 for material- and model parameters. See Box 7.2 for a note on the overshoot in saturation profile (left figure) around 7.5 m.

Dissolution has a limited effect on the pressure and saturation distribution, especially when reasonable amounts of dissolution is considered compared to what can be expected in typical CO_2 storage projects, see also table 4.6. The main exception is for extreme dissolution values.

This simple analysis has tried to address the issue of how the pressure is affected by considering partial miscibility and in turn the effective stress in the reservoir and surrounding formations. It can be seen that for the expected solubility of the, and moderate dispersion, CO_2 injection can with sufficient accuracy capture the migration and pressure evolution by assuming immiscible flow.

It has been shown that the governing equations for two-phase flow can be formulated in numerous ways by considering the mass conservation of the two phases using the auxiliary equations for capillary pressure, Eq. (4.44), the constraint on the saturation, Eq. (4.40), and rearranging. The underlying assumption is (normally) that both phases are present, at least in a small enough amount so that it does not cause numerical instabilities. When considering two-phase immiscible flow, it is not unreasonable to assume that a small amount of both phases is present and it is often assumed that some amount of formation water is always present such that the wetting pressure is continuous throughout the whole domain of interest. The typically used capillary pressure functions are also defined such that, once present, the wetting saturation will never become zero (as the pressure required to do so approaches infinity, see App. E). However, when considering partially miscible flow, in practice it is possible that one phase can completely disappear as it becomes dissolved in the other phase. This is particularly crucial when for instance CO_2 is displacing the formation brine. In order to avoid this, a small amount of wetting phase is injected with the non-wetting phase, in sufficient amounts, to make sure that both phases are present at the injection well. This can pose a practical problem as dry-out of brine due to CO_2 injection can cause the dissolved salt to precipitate, which in turn can have a negative effect on the permeability/porosity and lead to increased injection pressure, and/or lower injectivity. Interestingly, it has been proposed as a means of sealing

abandoned/abandoning wells to inject high salinity brine followed by CO_2 [120].

7.4 Non-isothermal effects

An often overlooked aspect in reservoir modeling is heat transport, as coupled flow and geomechanics is more frequently encountered in the literature. Here the effect of considering non-isothermal processes in the context of CO_2 storage is illustrated. It is is not a thorough analysis, but points out some significant effects. Consider the thermoporoelastic constitutive relation in Eq. (3.28), by comparing the thermoelastic stress-term to the poroelastic stress-term, temperature effects can often be ignored when

$$b\Delta p_s \gg \beta_s K \Delta T \tag{7.1}$$

However, non-isothermal effects might be very relevant for high-permeable reservoirs when pore pressure change is presumably small.

Considering the contribution of thermal expansivity of fluids q_T for fluid phase α, in the fluid conservation equation for immiscible flow, Eq. (4.48):

$$q_T = s_\alpha \rho_\alpha \left[\phi \beta_\alpha + (b-\phi)\beta_s\right] \frac{dT}{dt} \tag{7.2}$$

It can often be ignored when dT/dt is small. It can be seen that temperature change can be a key factor, temporally (for fluid mass conservation, Eq. (7.2)) and spatially (for stress, Eq. (7.1)), but the change must be significant enough to make a difference.

In general it is difficult to compare the various rate terms in the flow equation, heat transport equation and momentum balance equation because they have very different spatial and temporal variations. Volumetric strain rate, for instance, will have two time-scales: one for pressure dissipation (fast) and one for temperature dissipation (slow). Before continuing the analysis, remember the two models that were solved in Chapter 5.3:

1. THM: Thermo-hydro-mechanical coupling, model is considering two-phase flow, poroelasticity and energy transport.

2. HM: Hydro-mechanical coupling, model is considering two-phase flow and poroelasticity and temperature is assumed constant in time.

In both models the initial material properties for the fluids (water and CO_2) were evaluated from the equations of state from the online NIST database [65] using an initial temperature gradient (30°C at the surface and 30°C/km gradient) and an initial pore pressure profile that was based on estimated in situ pore pressure. Remember that in the example presented in chapter 5, the material properties of the fluid phases (density, viscosity and compressibility) are based on initial pressure and temperature conditions and are considered constant in time. It was seen that the effect of the temperature was very local in nature and had very little effect on the saturation distribution, deformation and pore pressure beyond the temperature signature. In a modified example, where the fluid properties (density, viscosity and compressibility) are functions of pressure and temperature and not constant in time, the same effect is observed. This is illustrated in Figs. 7.5 and 7.6 where the contours of the density and viscosity of water and CO_2 [from 65] are plotted for various temperatures and pore pressures. The diagonal white lines represents the initial condition for temperature and pore pressure and the white dots in Fig. 7.5 represents the pressure and temperature combinations in all the degrees of freedom in

the HM-model, after 12 years of injection, superimposed on the EOS-plots, and illustrate that the density and viscosity increases with time as the pore pressure is increasing in a small part of the model corresponding to the reservoir.

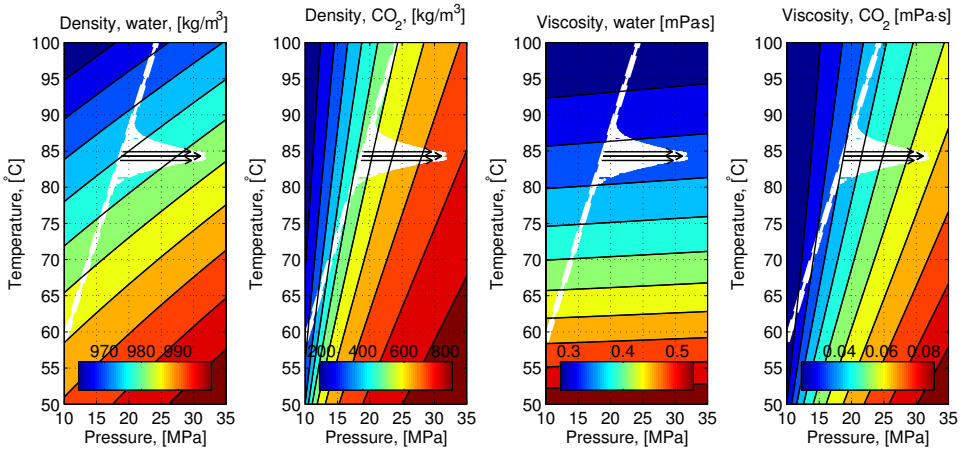

Figure 7.5: The density and viscosity variations in the HM-model (temperature is assumed constant but varies with depth). The diagonal white lines indicate the initial state. The white dots are the PT-data points of all the degrees of freedom in the model after 12 years of injection. The black lines show how the temperature and pore pressure in selected points around the injection well evolves in time. Since temperature is constant in time, the black arrows are horizontal: density/viscosity increases as pore pressure increases.

In the HM-model, Fig. 7.5, the temperature profile is constant, linearly varying with depth, and the white area is gradually extended in time towards higher pressure values. This is illustrated by the black lines in Fig. 7.5 where the pressure and temperature evolution is tracked in time in a few selected locations around the injection well. Since the temperature is constant in time the lines are horizontal as the pressure increase with time.

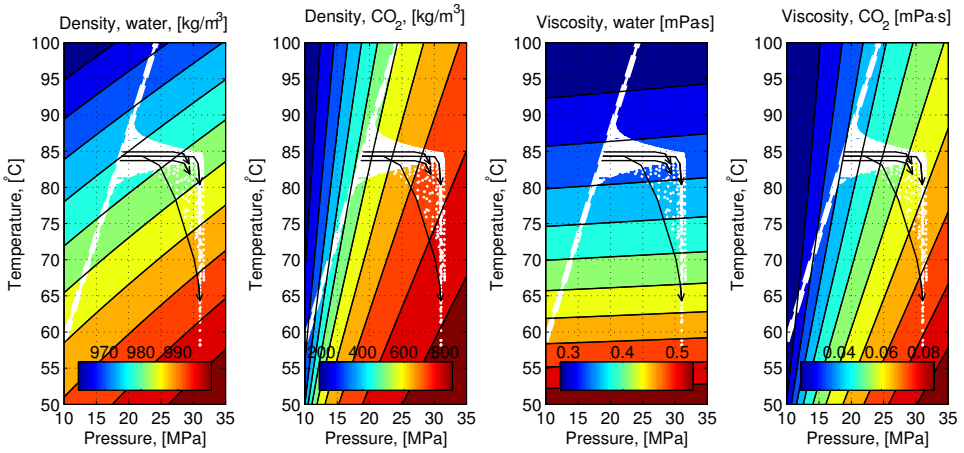

Figure 7.6: The density and viscosity variations in the THM-model. The diagonal white lines indicate the initial state. The white dots are the PT-data points of all the degrees of freedom in the model after 12 years of injection. The black lines show how the temperature and pore pressure in selected points around the injection well evolves in time: density/viscosity increases as pressure increases and temperature reduces.

Similarly, in Fig. 7.6 the pressure and temperature combinations in all the degrees of freedom in the THM-model, after 12 years of injection, is superimposed on the EOS-plots.

In the THM-model, Fig. 7.6, the high pore pressure points that is cooled down close to the injection well is shown as a vertical trail of white points. This is also illustrated by the black lines which track the temperature and pressure evolution in time in a few selected locations around the injection well. The reduction in temperature results in a higher increase in density and viscosity.

In Fig. 7.7 the results from this modified model is compared with the results from Fig. 5.5 and it can be seen that the temperature effect is very modest. In Fig. 7.7 there are two dashed lines and two solid lines. The difference between the two solid lines is that the material properties are updated with temperature and pressure in the THM-model and only pressure in the HM-model. The difference between the solid lines and the dashed lines is that in the dashed lines the material properties are constant in time (not changing with neither pressure nor temperature). In all cases the initial pressure and temperature are varying with depth.

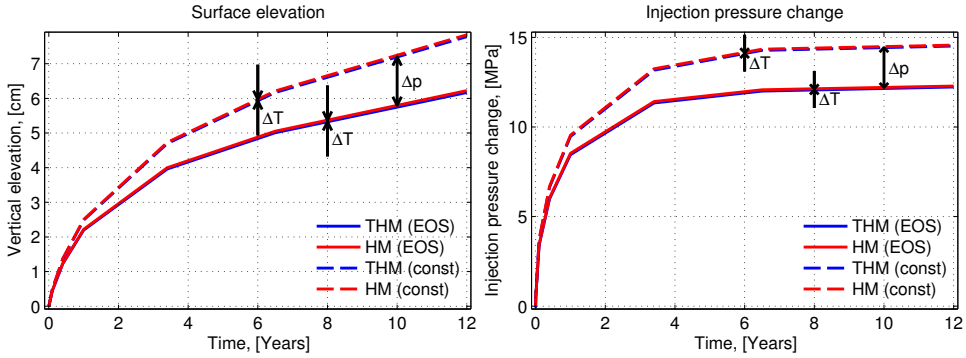

Figure 7.7: (Left) Vertical elevation at the surface directly above the injection well and (right) injection pressure. The dashed lines are the results from Fig. 5.5 where the material properties were constant in time and defined using initial pressure and temperature conditions (but varying with depth). The EOS-models indicate that the material properties are updated in time with pressure and temperature in the THM-model and pressure only in the HM-model. Δp and ΔT indicates the difference in the solutions when fluid properties are constant in time and when they are changing with pressure and temperature, respectively.

It is apparent from the results in Fig. 7.7 that considering the temporal change in pressure on the material properties is more important than considering the temporal change in both pressure and temperature on the material properties: the cooling effect is almost negligible compared to the pressure effect.

The pressure effect on the saturation distribution is also noticeable, compare results in Figs. 5.1 and 7.8. The migration of CO_2 plume is noticeable shorter, which is mainly because the density of CO_2 increases with increasing pressure.

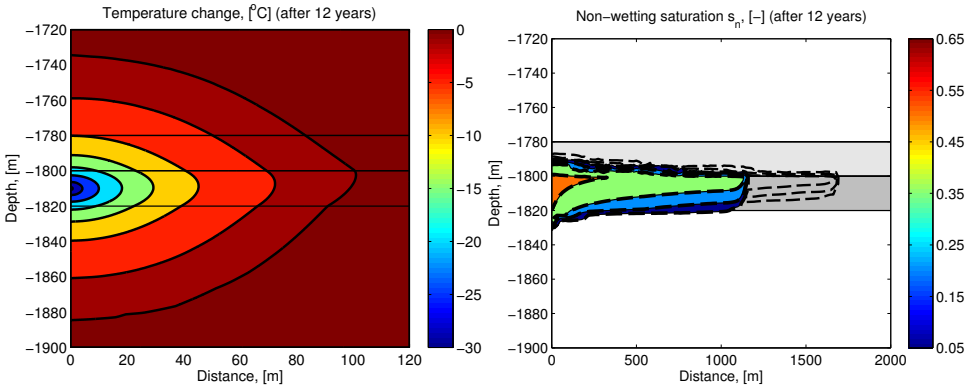

(a) Temperature distribution around the injection well after 12 years of injection.

(b) Non-wetting (CO_2) saturation in the reservoir after 12 years of injection. Black dashed lines are from solution where material properties are constant in time, see Fig. 5.1b.

Figure 7.8: (a) Temperature distribution and (b) non-wetting phase saturation distribution in the reservoir after 12 years of injection. The reservoir (between 1800-1820 meters depth), overlying caprock layers and underburden are outlined by the thin, black lines. The material properties are functions of pressure and temperature and not constant in time.

As was shown in chapter 5, and argued above, the temperature effect is local and does not affect the flow regime. Thus, when fluid flow and migration is of main concern, the temperature may (often) be assumed constant in time, but should not necessarily be considered constant in space. However, it will be shown that this does not apply to the stress-field, which will be considered next.

It was also shown in chapter 5 that the temperature effect is local in relation to strain and displacement, see Figs. 5.2 and 5.3. In Figs. 7.9 and 7.10 the differences in maximum and minimum principal stresses in the THM- and HM-model is shown, and again the local nature of the temperature effect is apparent (note that the x-axis is in logarithmic scale). The thermal stress reduces the local stress as the THM-model shows significant lower maximum and minimum principal stress directly above and below the injection well, approximately 2.5 MPa and 4 MPa, Figs. 7.9 and 7.10 respectively, compared to the HM-model. Remember the initial maximum and minimum principal stresses in Table 5.1, 49.9 MPa and 30.8 MPa, respectively. As discussed in chapter 2, the maximum and minimum principal stresses are essential when evaluating the possibility of rock failure.

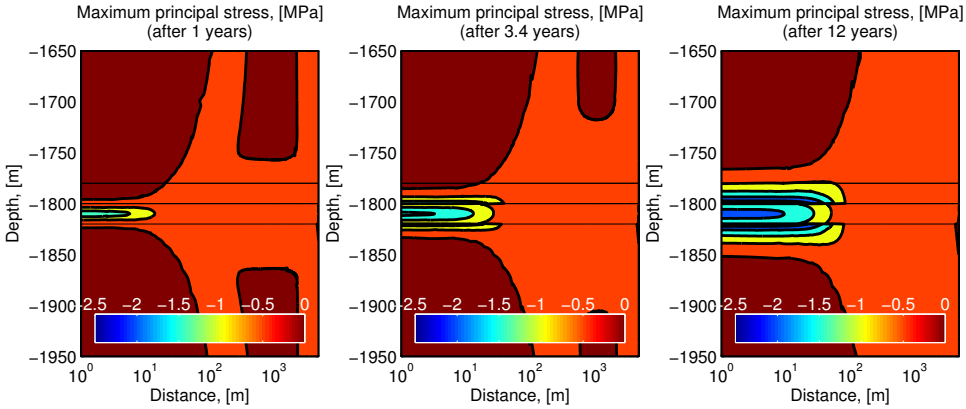

Figure 7.9: Difference in maximum principal stress between THM- and HM-model at 1, 3.4 and 12 years after start of injection. Note that the distance is in logarithmic scale. The reservoir (between 1800-1820 meters depth), overlying caprock layers and the underburden are outlined by thin black lines.

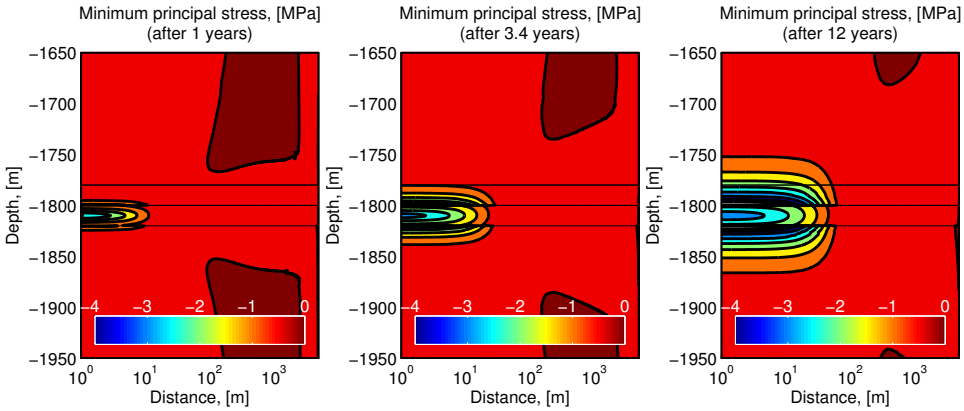

Figure 7.10: Difference in minimum principal stress between THM- and HM-model at 1, 3.4 and 12 years after start of injection. Note that the distance is in logarithmic scale. The reservoir (between 1800-1820 meters depth), overlying caprock layers and the underburden are outlined by thin black lines.

The initial and resulting (after 12 years of injection) Mohr circle with failure envelope (for fault/fracture reactivation in the caprock 20 m above the injection well) for the two models are shown in Fig. 7.11 (left). It can be seen that due to the strike-slip stress regime, the differential stress (difference between the maximum and minimum principal stresses) in the HM-model is almost constant after 12 years of injection, resulting in an almost pure shift of the Mohr circle to the left (blue curve compared to dashed, black line representing initial stress). In the THM-model, the Mohr circle is also shifted to the left, but the differential stress is increased, resulting in the Mohr circle crossing the failure envelope (red curve). This is also illustrated in Fig. 7.11 (right), the initial state is the same in the two models, but the current stress state (after 12 years of injection) in the THM-model (red curve) is outside the allowable stress region

(which is enclosed by the solid black line), while the stress state in the HM-model (blue line) is just within the allowable stress state region.

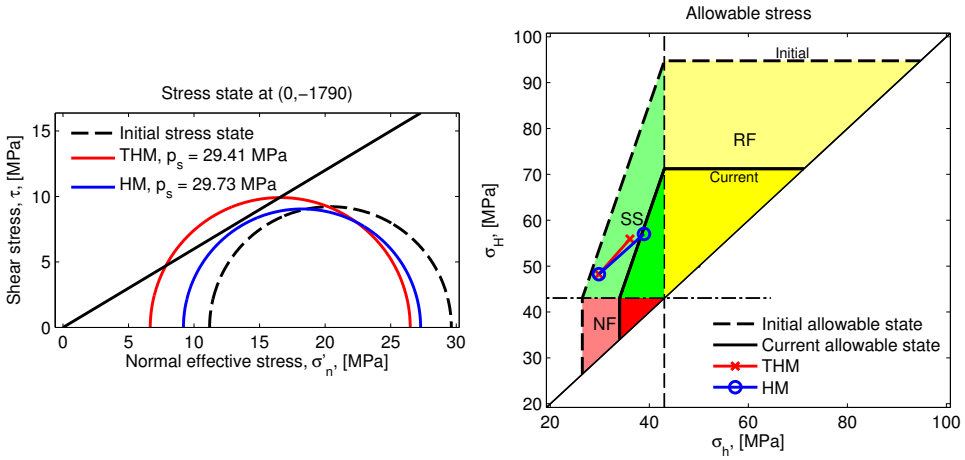

Figure 7.11: (Left) Stress state evaluated in point $[0, -1790]$ (middle of caprock above injection well) for THM- (red curve) and HM-model (blue curve), after 12 years of injection. Black dashed curve indicates initial stress state conditions, the pressure increase 10 m above the top reservoir has shifted the initial Mohr-circle towards the left. The Coulomb failure envelope is expressed by Eq. (2.9) (for cohesionless faults) and assuming a sliding friction coefficient $\mu_f = 0.6$. (Right) Allowable stress region. As the pore pressure is increased after 12 years of injection the allowable stress area becomes smaller (compare area inside thick dashed and solid lines). The red (THM) and blue (HM) lines indicate the change in stress state.

It has been shown that injecting cold CO_2 into a hot reservoir results in increased risk of failure. In Fig. 7.11 the risk of failure was evaluated in a point above the injection well, in the middle of the lower caprock. In Fig. 7.12 the frictional limit failure criteria given by Eq. (2.10) is evaluated (again using that $\mu_f = 0.6$), where positive values indicate risk of failure. It can be seen that in the THM-model (Fig. 7.12, left), the risk of failure (dark red region) is apparent around the injection well in the reservoir and the first 20 meter into the lower caprock and underburden, while the HM-model shows a lower risk of failure and no risk of failure outside the reservoir (relative to the frictional limit failure criteria).

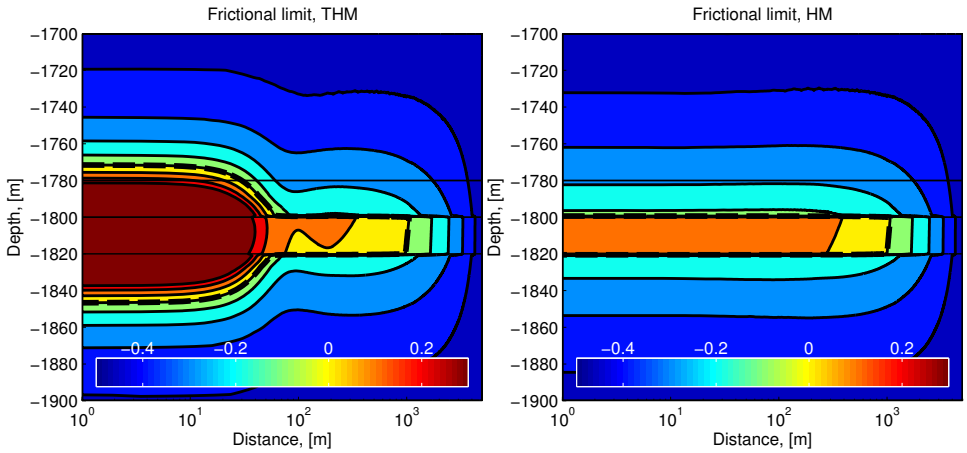

Figure 7.12: Frictional limit criteria evaluated after 12 years of injection for THM-model (left) and HM-model (right). The values are calculated after Eq. (2.10), where positive values indicate risk of failure and negative values indicate safe stress state. Note that the distance in logarithmic scale. The dashed lines indicate failure limit.

Temperature has an effect on flow and the pressure, but the initial spatial temperature profile is more important than considering the temporal changes. The temperature effect is very local, the conductive and convective energy transport is too small to affect the flow. For the stress, the temperature change significantly increases the risk of failure in the caprock above the injection well in the illustrative example based on conditions at the CO_2 storage site at In Salah, Algeria.

7.5 Simplifying geomechanics

It is tempting to find ways to eliminate the need to calculate the momentum balance equation to evaluate the stress state. Two methods were highlighted in chapter 2.4: the k_0-method expressed by Eq. (2.16), and the stress-path method with equations relating the change in stress to change in pore pressure, Eqs. (2.20), (2.21) and (2.22). In Fig. 7.13 the difference between the calculated and the approximated minimum horizontal stress (σ_h) for the stress-path method (using Eq. (2.21), left figure) and the k_0-method (using Eq. (2.16), right figure).

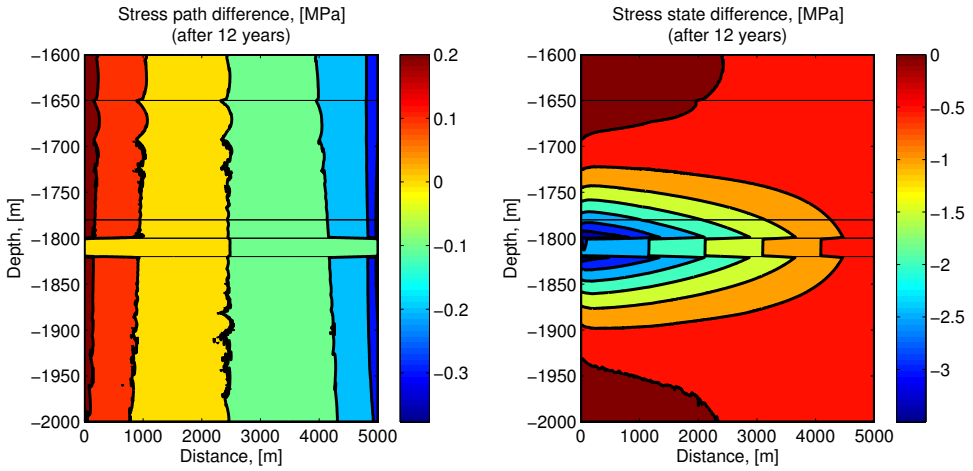

Figure 7.13: The difference between approximated and simulated minimum horizontal principal stress σ_h. The approximated stress is evaluated using the stress-path method (left, Eq. (2.21)) and the k_0-method (right, Eq. (2.16)).

Both methods approximates the change in stress solely due to changes in pore pressure. It can be seen that the stress path method gives a reasonably good approximation in the reservoir. However, outside the reservoir the stress transfer due to deformation of the reservoir is completely ignored and can not be used.

The k_0-method does not consider the change in horizontal stress with change in pore pressure, $d\sigma_h/dp$, and fails even worse. Altmann et al. [4] also showed that the ratio expressed in Eq. (2.21) represents the long-term limit ($t \to \infty$) thus none of the approximations handle dynamics accurately and are strictly valid for steady-state conditions only. Stress analysis is therefore needed to accurately predict spatio-temporal distribution of failure risk [4].

7.6 Dimensionally reduced models

It is not always desirable, nor feasible, to model in full-dimension because of the computational cost and long simulation times. By integrating the governing equations for the leading order processes, many degrees of freedom can, in effect, be eliminated, allowing a numerically smaller problem to be solved, and faster. This was explored in chapter 6. The mass conservation equations were integrated to obtain the dimensionally reduced form of the single-phase flow equation, Eq. (6.5), and the two-phase flow equation (including capillary pressure effects), Eq. (6.12). Both dimensionally reduced models were compared to a fully resolved, full-dimensional model for two different geometries of the reservoir (reservoir thickness of 30 ± 10 meters) and the results are shown in Fig. 6.2 for single-phase flow and Figs. 6.4 and 6.5 for two-phase flow. The dimensionally reduced models compare excellent with the reference models for both saturation and pressure.

The underlying assumption for the derivation of the dimensionally reduced flow equations implies that the pressure gradient in the vertical direction has reached a steady state: vertical equilibrium (VE). In high permeable aquifers the pressure propagates quickly, thus this assumption is close to the real behavior for the pressure. Yortsos [124] examined the validity of

the VE assumption and identified a key dimensionless variable R_L defined as:

$$R_L = \frac{L}{H}\sqrt{\frac{k_v}{k_h}} \tag{7.3}$$

where L [m] is a characteristic length, H [m] is the height (length of integration path) and k_v [m^2] and k_h [m^2] are the vertical and horizontal permeability in the aquifer, respectively. The VE assumption was found to be valid in the limit of large R_L^2. In a validation model presented by Bjørnarå et al. [25] based on realistic CO_2 storage conditions at In Salah, Algeria, it was found that it holds even for reservoir thickness H up to at least 100 meters. The VE-assumption implies further that since the pressure is in vertical equilibrium, then so is the phase distribution, or saturation. In practice, the phase segregation is much slower than the propagation of the pressure and the VE-assumption on the saturation is not valid at early times. However, this is mainly an issue for the vertical distribution of the phases and to a little degree the phase pressure. This quick pressure equilibrium is particularly important, and fortunate, when evaluating effective stress because the pore pressure is normally less dependent on the saturation, but mainly on the wetting pressure, see Eq. (3.26).

The performance of the dimensionally reduced model compared to a full-dimensional model is given in table 6.2 and show a speed-up of more than 10 times. it is interesting to note that a high vertical resolution in the fully resolved full-dimensional model is required to get a comparable saturation profile. This is particularly the case of high permeability reservoirs because the thickness of the plume, which will be thin at high permeability, needs to be resolved.

The concept of vertical equilibrium (VE) for flow was applied to the momentum balance, Eq. (3.2). For the flow, VE implies a constant vertical pressure gradient (e.g. from Eq. (H.14) when fluid density can be assumed constant across the thickness of the reservoir): $\partial p_\alpha/\partial z = -\rho_\alpha g$. In the dimensionally reduced form of the momentum balance equation the underlying assumption is constant vertical strain component: linearly varying displacement across the thickness of the reservoir as expressed in Eqs. (6.14)-(6.16). Integration of the momentum balance equation, using these assumptions, results in a dimensionally reduced form of the equation for linear elasticity that is therefore referred to as the Linear Vertical Deflection equation (LVD). It was shown that the LVD equation can be expressed on a similar form as the full-dimensional momentum balance equation: $-\tilde{\nabla}\cdot\Sigma = \mathbf{F}$ (Eq. (6.28)). The LVD stress tensor Σ and body-load vector $\mathbf{F}$ contains several boundary-terms that are well defined when the dimensionally reduced domain is embedded by surrounding formations.

To account for effective stress, the pore pressure is included in the constitutive relation for the stress, see Eq. (3.17). The LVD equation is the dimensionally reduced form of the momentum balance equation, and the equivalent form of the dimensionally reduced poroelasticity equation is simply termed the Poroelastic Linear Vertical Deflection (PLVD) equation. To validate the PLVD equation, as well as the implementation into a finite element code, two validation models were defined. The first model was a static case with a constant load; here a constant pore pressure profile across the width of the reservoir as expressed by Eq. (6.32). The aim was to compare the accuracy of various stress-terms and displacement variables and it can be seen that the two solutions coincide almost perfectly, see Chapter 6.6.1 for results. Note also that the topography causes large stress contrasts related to the slope of the reservoir. In the second model, the PLVD-model was also compared to a fully resolved, full-dimensional model, but with a transient pore pressure arising from the injection of CO_2 into a water saturated reservoir. Thus, the PLVD-form of the momentum balance equation was coupled with a

dimensionally reduced form of the two-phase flow equation under vertical equilibrium conditions as described in chapter 6.3.2 (and App. H).

As with the dimensionally reduce two-phase flow models under VE assumptions, there is a significant gain in performance. Three different model geometries was solved for and the speed-up of the simulations showed 11-22 times faster calculation times, see table 6.3. Due to the dimensional reduction, the numerical size of the problems was reduced by 35-40 %. The difference in improved performance (speed-up) and computational cost (number of degrees of freedom) are very different. By reducing the numerical size of a problem, the calculation becomes faster. In a time dependent problem the linear system of equations are solved many times, to capture the transient behavior. Solving a smaller problem many times (for every time step) can accumulate to significant savings in total computational time. However, the large speed-up (11-22) compared to the (modest) reduction (35-40 %) in cost is also due to a less stiff non-linear system of equations in the dimensionally reduced models, allowing the numerical solver to use larger time-steps. This is illustrated in Fig. 7.14, showing the output from the solver log of one of the models.

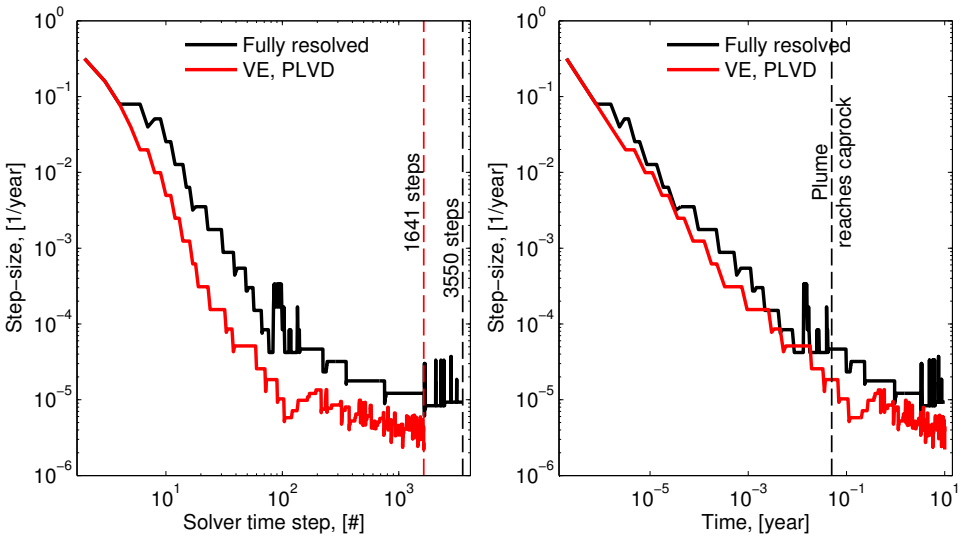

Figure 7.14: Output from the solver-log for the two-phase flow problem in table 6.3 (flat reservoir) for the fully resolved model (black curve) and dimensionally reduced model (red curve). (Left) Step-size as a function of the number of time steps taken by the solver. The dimensionally reduced model requires 1641 time steps by the solver to solve 10 years of injection while the fully resolved model requires 3550 time steps. (Right) Step-size as function of simulated time (10 years of injection). Vertical black dashed line indicate when the plume reaches the caprock.

The non-linear system of equations in a dimensionally reduced model is less stiff, allowing longer time-steps to be taken by the time dependent solver and resulting in fewer time steps (calculations) and therefore shorter calculation time, see Fig. 7.14 (left). The dimensionally reduced model requires 1641 time steps by the solver to solve 10 years of injection while the fully resolved model requires 3550 time steps. Also, the numerical cost for every time step is lower (35-40%) for the dimensionally reduced models.

The benefit of the dimensionally reduced model is, as pointed out previously, that the dimensionally reduced domain can in effect be eliminated from the model. This is particularly beneficial for large-aspect ratio domains, e.g. very thin but laterally extensive domains, which can be challenging, or even impossible, to discretize (mesh).

Lu et al. [67] compared fully resolved numerical simulations to simple analytical solutions based on the vertical-equilibrium and sharp-interface assumptions (two-phase flow without capillary pressure) of a simplified and radially symmetric problem. They concluded that the vertical-equilibrium, sharp-interface analytical approaches were unable to accurately predict the CO_2 front position and further that these simplified models were not appropriate to model CO_2 injection. [35] extended this analysis and looked at conditions under which vertical-equilibrium models are appropriate and the conditions under which the sharp-interface models are appropriate. They showed that in many cases the vertical-equilibrium models are reasonable. Naturally, by making simplifying assumptions the range of validity may be reduced. In that sense, the sharp-interface model may have limited use, but at the same time it is extremely efficient to solve compared to a fully resolved model and can therefore be absolutely necessary to use, particularly when large numbers of realisations are required. However, it has been shown here, and by Bjørnarå et al. [25], that application of dimensionally reduced models can give accurate results when applied to realistic scenarios.

Chapter 8

Conclusion

In order to continue to use fossil fuels for energy, storing the bi-product CO_2 is the only sustainable option. In CO_2 storage, the main concern is containment of the stored gas. Any safe storage is constrained by how much gas can be injected while not exceeding a pressure that can compromise the storage and in particular the integrity of the surrounding formation and caprock.

The overall objective of this project was to *"derive the mathematical description of the main relevant processes involved in CO_2 injection and storage to assess the geomechanical integrity of the storage reservoir and the surrounding formations and analyze how these can be simplified for a faster numerical evaluation while keeping an acceptable level of accuracy"*. To this end, several processes, and the interaction between them, were investigated: single-phase and two-phase (immiscible and partially miscible) fluid flow in porous media, energy transport and poroelasticity, to derive a reduced-dimensional model for coupled single- and two-phase fluid flow and geomechanical deformation within the context of CO_2 storage.

For single-phase flow, many formulations from various simplifying assumptions are encountered in the literature, but it is not always clear what these assumptions or justifications are. The various formulations originate from various simplifying assumptions on the mechanical behavior (deformation) of the porous media (e.g. rock or soil) under consideration, resulting in different formulations for the fluid storage term. In a comparison test in this study, it was shown that the various simplifications can give significantly different results and it is therefore important to be aware of what they imply. In one case the deformation was simply ignored (completely rigid solid), and while the fluid flow equation was the same as in the fully coupled reference model (which solves for both fluid flow and geomechanics, simultaneously), the resulting pore pressures were very different. On the other hand, in the case of a relatively thin reservoir, a simple consideration of deformation (uniaxial strain approximation) improved the results substantially. These various formulations were also the topic of the paper by [23] and, although seemingly trivial, it was pointed out that the single-phase flow equation is very important in reservoir simulations because it is typically applied to a larger part of the reservoir and the surrounding formations.

From the governing equations for multi-phase flow and the auxiliary equations (capillary pressure functions and the saturation constraint), as much as eighteen formulations for immiscible two-phase flow can be derived. Eight of these formulations were compared to a new semi-analytic solution of the McWhorter-Sunada equation (MSE, originally proposed by McWhorter and Sunada [72]) for two-phase flow in porous media including capillary pressure. The originally proposed algorithm to solve MSE is exceptionally sensitive to hydraulic properties and the new solution procedure by Bjørnarå and Mathias [22] provided a fast, robust and

accurate alternative using a pseudospectral method. The comparison revealed some preferred formulations in terms of solving time, depending on the process, e.g. if a wetting-phase was invading a non-wetting phase saturated medium, or vice versa. The difference in calculation time for the various formulations was up to a factor two between the fastest and the slowest calculation. However, an optimal formulation or a detailed guideline to which formulation will be the fastest is difficult to assess, if even possible, as it is problem dependent. However, the saturation-based formulations (six possible formulations) are in general more applicable because they can handle situations where the saturation is below the residual saturation as well as discontinuities in the saturation due to heterogeneity in capillary pressure in the formations.

The partially miscible (soluble) two-phase flow formulation was validated to an analytical two-component, two-phase flow extension to the Buckley-Leverett equation [28]. The model was further used to evaluate the effect of solubility of CO_2 on the migration and the pore pressure that in turn will affect the stresses in the reservoir and surrounding formations. CO_2 has a low solubility in water, in the order of a few percent in mass ratio (noting that the exact ratio depends on temperature, pressure and salinity), and it was shown that when considering moderate dispersion, the assumption of immiscible two-phase flow is a good approximation, both in terms of CO_2 migration, pore pressure and solving time.

Non-isothermal effects were illustrated in a well-documented case study of CO_2 storage from In Salah, Algeria. To isolate the non-isothermal effect, the difference between a hydromechanical (HM) model and a thermohydromechanical (THM) model was analyzed. In the HM-model, fully coupled fluid flow (two-phase) and poroelasticity were considered and in the THM-model, the energy balance was also considered. It was shown that the temperature effect is very local due to limited heat transport that results in a slow dissipation of temperature compared to the migration of the injected CO_2 and the pressure dissipation. This means that the thermal effect on the material properties is local and spatially limited to the injection well. Thus, from a regional-scale point of view, when the fluid migration and pore pressure are important aspects, the initial spatial temperature profile is more important to consider than the temporal changes.

The non-isothermal effect on stress is a different matter. In general, cold injection (relative to formation temperature) lowers the fracture pressure and the limit for maximum sustainable injection rate. However, how significant this effect is, depends on: the magnitude of the thermal expansion coefficient, the stiffness of the formations in question and the magnitude of the temperature change. Thus, for cold injection, ignoring non-isothermal effects can underestimate the risk of failure, and vice versa. In the illustrative example based on conditions at the CO_2 storage site at In Salah, Algeria, the temperature change is significant enough to cause failure in the caprock above the injection well.

To provide capacity estimates and to analyze long-term storage safety and potential risk factors in CO_2 injection and storage, it is necessary to have a consistent mathematical description of the main relevant processes involved: fluid flow, energy transport and geomechanics. However, the numerical models quickly become large, requiring a huge computational effort. For instance, knowing how far the pressure footprint extends is crucial when comparing models to measured data, implying that large models may need to be considered, to the extent that a full three-dimensional model can become unfeasible to solve. When geometrical simplifications are not possible (no spatial symmetries), another approximation was exploited: dimensional reduction. This approximation has been found particularly attractive in modeling of CO_2 injection and storage due to: strong buoyant segregation of the lighter CO_2 phase compared to the resident brine, the relatively long time-scales associated with storage and the typically large aspect ratios of the storage formations (flat/thin with large lateral extent). Since

stress is particularly essential to consider when evaluating the integrity of the caprock, the concept of dimensional reduction was extended to also include the geomechanical processes. A fully coupled dimensionally reduced model for multiphase flow and geomechanics in an aquifer being of lower dimension while the surrounding formations (e.g. caprock and over- and underburden) are of full dimension, was developed. The model is derived from the general mathematical description of immiscible two-phase fluid flow with capillary pressure and poroelasticity. In deriving the dimensionally reduced formulation, the following assumptions (within the dimensionally-reduced domain) were applied: the fluid is in Vertical Equilibrium (VE), implying here that the vertical pressure gradient is constant, and the Linear Vertical Deflection (LVD) for the momentum balance equation, implying that the vertical strains are constant (displacement components are linearly varying in the vertical direction). These choices of closure relationship (VE and LVD) allow for an efficient and accurate reconstruction of fluid saturation, fluid pressure and deformation that works just as well on flat, horizontal aquifers as topographic aquifers.

The dimensionally reduced model was thoroughly tested and it successfully captures the main processes investigated. The model also retains all the benefits of reduced-dimensional models for flow, including less stiff non-linear systems of equations, allowing longer time-steps to be taken by the numerical solver and requiring fewer degrees of freedom. This provides significant savings in computational time when faced with a large number of simulations, up to more than twenty times faster calculation times compared to a full-dimensional model. The new model was validated for single- and two-phase flow coupled to poroelasticity in practical examples, with various topography of the aquifer, in both two and three dimensions. The model was also the main topic of the papers by Bjørnarå et al. [24] and Bjørnarå et al. [25] and it was applied to real field data from the CO_2 storage site at In Salah, Algeria, [21].

Chapter 9

Papers

Paper I: *A Pseudospectral Approach to the McWhorter and Sunada Equation for Two-Phase Flow in Porous Media with Capillary Pressure*

When deriving and implementing a numerical code for two-phase fluid flow it is important to have an analytical solution to verify that it behaves as expected and the solution is correct. McWhorter and Sunada [72] defined a nonlinear second-order ordinary differential equation to solve one-dimensional immiscible two-phase flow in porous media with capillary pressure (MSE). This equation, MSE, can be considered a capillary effect-analog to the analytical Buckley-Leverett solution [28] which neglects the capillary pressure. However, the convergence of the original solution procedure by McWhorter and Sunada [72] has proven to be extremely sensitive to the model parameters, thus we proposed a fast and robust solving procedure using Chebyshev spectral collocation (pseudospectral) method. The equations by McWhorter and Sunada [72] were re-derived and the final formulation is slightly more flexible, supporting both co-current and counter-current flow. This procedure and formulation is used to validate various two-phase, immiscible flow formulations in chapter 4.3.

Paper II: *Vertically Integrated Models for Coupled Two-Phase Flow and Geomechanics in Porous Media*

This paper contains the main contribution of this thesis: the first complete model including a consistent, vertically integrated approach for fully coupled multi-phase flow and mechanical deformation. Typical CO_2-storage reservoirs have large aspect ratios and are relatively flat. By making reasonable assumptions on the structure of the solution across the thickness of the reservoir, the governing equations can effectively be reduced to a lower dimension, e.g. the processes (multi-phase flow and mechanical deformation) in a 3D reservoir volume can be described on a surface, while the surrounding overburden and underburden are of full dimension. The reduced-dimensional model has less degrees of freedom compared to the full-dimensional model (since the high grid resolution in the vertical direction can be avoided) and the resulting system of equations are less stiff (since the upscaled constitutive functions are closer to linear), allowing longer time steps by the numerical solver. The computational example, based on the In Salah CO_2-storage site, showed that the solution was accurate up to the order of 0.1% for reservoirs up to 100 meter thick compared to a full-dimensional computation.

Paper III: *Field data analysis and hydromechanical modeling of CO_2 storage at In Salah, Al-*

geria

Here we apply the dimensionally reduced model defined in the previous paper [25] on real field data from the CO_2 storage site at In Salah, Algeria. The In Salah storage reservoir is approximately 20 m thick and located about 1.8 km below ground, about 3.8 Mtons of CO_2 has been injected into three wells (KB501, KB502 and KB503) between 2004 and 2011. The injection pressure has frequently exceeded the fracture pressure, thus fracture injection is an important transport mechanism for the injected CO_2 and a static geomodel cannot adequately capture the geomechanical processes. A pressure dependent correlation for the reservoir permeability was suggested based on an analysis of the field data (pressure decay in wellhead pressure data from the injection) and shows a good fit for the measured surface heave above all the wells and for the pressure response at two of the three wells (KB501 and KB503). The field data at KB502 suggest a strong dependency on the behavior of a large and intersecting fault system (F12) with highly uncertain material properties, but this was not analyzed in details since the focus of the paper was the reservoir permeability and the utilization of shut-in curves (pressure decay curves following a shut-in). The modeling work consisted of fitting two parameters in the pressure dependent correlation for the reservoir permeability and benefitted largely from the use of the dimensionally reduced model described in this thesis and in the previous two papers [24, 25].

9.1 A Pseudospectral Approach to the McWhorter and Sunada Equation for Two-Phase Flow in Porous Media with Capillary Pressure

Authors: **Tore I. Bjørnarå** and Simon A. Mathias.
Journal: Computational Geosciences.

9.2 Vertically Integrated Models for Coupled Two-Phase Flow and Geomechanics in Porous Media

Authors: **Tore I. Bjørnarå**, Jan M. Nordbotten and Joonsang Park.
Journal: Water Resources Research.

AGU PUBLICATIONS

Water Resources Research

RESEARCH ARTICLE
10.1002/2015WR017290

Vertically integrated models for coupled two-phase flow and geomechanics in porous media

Tore I. Bjørnarå[1,2], Jan M. Nordbotten[1], and Joonsang Park[2]

[1]Department of Mathematics, University of Bergen, Bergen, Norway, [2]NGI, Oslo, Norway

Key Points:
- Dimensionally reduced equations for multiphase flow and poroelasticity
- Efficient and accurate hydromechanical analysis of high aspect ratio aquifers
- Vertical Equilibrium and Linear Vertical Deflection assumptions in dimensionally reduced models

Correspondence to:
T. I. Bjørnarå,
tore.ingvald.bjornara@ngi.no

Citation:
Bjørnarå, T. I., J. M. Nordbotten, and J. Park (2016), Vertically integrated models for coupled two-phase flow and geomechanics in porous media, *Water Resour. Res.*, *52*, 1398–1417, doi:10.1002/2015WR017290.

Received 24 MAR 2015
Accepted 30 JAN 2016
Accepted article online 5 FEB 2016
Published online 28 FEB 2016

Abstract Models of reduced dimensionality have been found to be particularly attractive in simulating the fate of injected CO_2 in supercritical state in the context of carbon capture and storage. This is motivated by the confluence of three aspects: the strong buoyant segregation of the lighter CO_2 phase above water, the relatively long time scales associated with storage, and finally the large aspect ratios that characterize the geometry of typical storage aquifers. However, to date, these models have been confined to considering only the flow problem, as the coupling between reduced dimensionality models for flow and models for geomechanical response has previously not been developed. Herein, we develop a fully coupled, reduced dimension, model for multiphase flow and geomechanics. It is characterized by the aquifer(s) being of lower dimension(s), while the surrounding overburden and underburden being of full dimension. The model allows for general constitutive functions for fluid flow (relative permeability and capillary pressure) and uses the standard Biot coupling between the flow and mechanical equations. The coupled model retains all the simplicities of reduced-dimensional models for flow, including less stiff nonlinear systems of equations (since the upscaled constitutive functions are closer to linear), longer time steps (since the high grid resolution in the vertical direction can be avoided), and less degrees of freedom. We illustrate the applicability of the new coupled model through both a validation study and a practical computational example.

1. Introduction

The coupling of flow and deformation of geological porous media is important in a range of applications such as groundwater withdrawal, geothermal energy extraction, shale gas extraction, and CO_2 storage. The two latter applications require attention to multiphase flow, while all examples (perhaps with the exception of groundwater extraction) include features of high aspect ratios. These may take the form of fractures (in the case of geothermal energy or shale gas extraction) or the presence of relatively thin storage units in the case of CO_2 storage [*Celia and Nordbotten*, 2009]. Our attention is therefore drawn to modeling and simulation of multiphase flow in deformable porous media with high aspect ratios.

The combined presence of multiphase flow and thin storage layers for CO_2 storage makes models of reduced complexity attractive for large-scale simulation [*Lake*, 1989; *Nordbotten and Celia*, 2012]. This has led to the development of both simple immiscible two-phase flow models [*Hesse et al*., 2008; *Nordbotten et al*., 2005] and more elaborate models including both explicit consideration of capillary forces and hysteresis [*Nordbotten and Dahle*, 2011], partially soluble fluids with upscaled convective mixing [*Gasda et al*., 2011], as well as models including careful treatment of effective fluid properties such as spatially varying fluid density [*Andersen et al*., 2014]. Such upscaled, or vertically integrated, models, have been applied to assess real field data [*Celia et al*., 2011; *Mykkeltvedt and Nordbotten*, 2012; *Nilsen et al*., 2011] and participated in benchmark studies [*Class et al*., 2009; *Nordbotten et al*., 2012], while their range of validity has been established by several authors both numerically [see e.g., *Court et al*., 2012] and analytically [see e.g., *Yortsos*, 1995].

Reduced models for coupled flow and mechanics have received comparatively less attention, with little work appearing after the early work of Bear and Corapcioglu [*Bear and Corapcioglu*, 1981a,b; *Corapcioglu and Bear*, 1983]. In particular, no work has shown how to couple the vertically integrated multiphase flow models of the previous paragraph to mechanical deformation.

In this work, we show the first complete model including a consistent, vertically integrated approach for coupled multiphase flow and mechanical deformation. We consider the setting of thin porous layers, such

as aquifers, embedded in a larger physical domain (typically denoted overburden and underburden). Our interest is thus in the case where the thin layer can be upscaled to a lower dimensional surface, on which vertically integrated equations govern the physics, while we will retain the full-dimensional formulation outside the thin layer.

Throughout this paper, we consider the context of CO_2 storage, wherein CO_2 in supercritical state is injected into an underground geological formation, e.g., a saline aquifer or an abandoned oil or gas reservoir [*Celia et al.*, 2015]. Our interest herein is safe storage, and in particular the mechanical integrity of the reservoir and overlying caprock. In this context, hydromechanical models are essential in order to evaluate induced stresses with respect to failure envelopes or strengths of reservoir and surrounding seals. These models describe the interaction between the porous media and the fluid, linking the stress and the pore pressure. We consider this coupling within the theory of poroelasticity. A general description of this theory was first considered by *Biot* [1935] and his later works [*Biot*, 1941, 1955, 1972, 1973], and later this initial work has been given a more rigorous theoretical foundation [see for instance *Rice and Cleary*, 1976; *Ferrín and Mikelić*, 2003; E. Detournay and A. H.-D. Cheng, Fundamentals of poroelasticity, unpublished data, 1993].

There is an extensive literature on the subject of hydromechanical coupling. More particularly, in relation to CO_2 storage, the industrial-scale projects have been subject to numerous modeling studies. At the Sleipner CO_2 storage site off the shore of Norway, flow analysis has been the main focus due to the excellent injectivity, large storage capacity, and the availability of 4-D seismic that images the extent of the injected CO_2 plume. However, at the In Salah storage site in Algeria, the unusual upheaval patterns at the surface that was detected by satellite surveys (InSAR), particularly around one of the three injection wells, attracted much attention to the hydromechanical coupling. Indeed, early studies suggested the presence of a high-permeable fault system intersecting one of the injection wells [*Vasco et al.*, 2008] which was also later confirmed by updated seismic (in 2009) [*Ringrose et al.*, 2013] and further supported by several additional modeling studies [e.g., *Durucan et al.*, 2011; *Gemmer et al.*, 2012; *Rinaldi and Rutqvist*, 2013; *Rutqvist et al.*, 2010; *Shi et al.*, 2012]. The thermohydromechanical coupling at In Salah has been studied by *Preisig and Prévost* [2011] and *Gor et al.* [2013], suggesting that nonisothermal effects and thermal stress can be important to consider when evaluating the integrity of a CO_2 storage site, particularly when significant temperature variations are expected. Despite this, the isothermal approximation is a common simplification in the context of CO_2 storage modeling. Most often isenthalpic conditions are assumed, implying that temperature conditions are considered in determining the material properties, but heat transport due to fluid flow is not.

Our emphasis throughout this manuscript therefore lies on the context of vertically integrated hydromechanical models, and in particular the novel treatment of mechanical deformation, which we term Linear Vertical Deflection (LVD). The LVD equations are the dimensionally reduced (integrated) equations for linear elasticity. We see this model in the broader setting of a hierarchy of models with different complexity [*Celia and Nordbotten*, 2009]. Such a hierarchy is particularly valuable, as the different stages of operation (screening, ranking, planning, and operation) have very different data availability and computational objectives. As such, it is both infeasible and undesirable to make a full 3-D simulation in the screening stage of operations, and at this stage, simplified models have particular value. At the same time, we point out that fully resolved 3-D simulations may be computationally infeasible even for relatively simple problems in the presence of coupled processes, as was emphasized both in a recent benchmark study [*Nordbotten et al.*, 2012], and in subsequent work [*Elenius et al.*, 2015].

We structure the rest of this manuscript as follows: in section 2, we give a brief review of hydromechanical coupling in the context of CO_2 storage. In section 3, we derive the vertically integrated model of interest herein. To demonstrate the applicability of the method, we consider a prototypical storage simulation, which is presented in section 4 and analyzed numerically in section 5. We conclude the paper in section 6.

2. Governing Equations

The basic concepts of poroelastic behavior can be divided into primary and secondary coupling [*Rutqvist and Stephansson*, 2003; *Wang*, 2000]. The primary coupling occurs through deformation and pore fluid interactions and relates to changes in the pore volume and the volumetric strain rate. A change in stress produces a change in fluid pressure or fluid mass (solid-to-fluid coupling) and a change in the pore fluid pressure or fluid mass produces a change in the volume of the porous material (fluid-to-solid coupling). The

secondary coupling considers indirect effects where a change in the stress causes a change in the hydraulic properties of the rock mass (solid-to-fluid) and a change in the pore fluid pressure causes a change in the mechanical properties of the rock mass (fluid-to-solid). Herein, we will for simplicity of exposition consider only the primary coupling; however, the results extend also to the secondary coupling phenomena.

In the following, we give the relevant components of the theory of the multiphase extension of Biot's theory. While the equations for fluid flow and mechanical deformation are coupled, it is natural to present them separately. Throughout this section, we will consider only small deformations, and the coordinate system is Lagrangian with respect to the solid.

2.1. Fluid Flow Equations

For notational simplicity, to focus on the problem of coupling vertical equilibrium two-phase flow models with larger geomechanical models, some simplifying assumptions will be made. First, only two phases will be considered: wetting and nonwetting phase. The wetting phase is the resident aqueous phase which is assumed to mainly consist of water, and the nonwetting phase is CO_2 in a supercritical state due to the pressure and temperature conditions (approximately 90°C and 18–19 MPa, see e.g., *Morris et al*. [2011], *Preisig and Prévost* [2011], and *Deflandre et al*. [2011], compared to the critical point of CO_2 at 31°C and 7.4 MPa [*Lide*, 2003]). Second, mutual dissolution of the phases is ignored. For a temperature range of 50°C–100°C, a pressure range of 10–30 MPa, and high salinity (formation water is typically saline), the volume fraction of CO_2 that can dissolve in brine and the volume fraction of brine that can dissolve in CO_2 is typically in the order of 0.06 and 0.003, respectively [*Yan et al*., 2011]. Miscibility can be an important effect to consider when evaluating long-term CO_2 storage efficiency, but this has previously been explored in the nondeformable setting, e.g., by *Gasda et al*. [2011]. Last, thermodynamic effects are ignored. When large temperature differences are expected, thermodynamic effects can be important to consider, but this has also been explored in the nondeformable setting, e.g., by *Andersen et al*. [2014]. Therefore, within the aquifer formation, the relevant governing equations for the two-phase immiscible flow system can be written as follows:

$$\frac{\partial(\phi\rho_\alpha s_\alpha)}{\partial t} = -\nabla\cdot(\rho_\alpha\phi s_\alpha \mathbf{v}_\alpha) \tag{1}$$

where ϕ is the porosity and ρ_α (kg/m^3) and s_α are the density and saturation of the fluid phase α, respectively. The phase velocity $\mathbf{v}_\alpha$ (m/s) is related to the Darcy flux $\mathbf{q}_\alpha$ (m/s) in a deforming media by the following relation:

$$\mathbf{q}_\alpha = \phi s_\alpha(\mathbf{v}_\alpha - \mathbf{v}_s) = -\frac{\mathbf{k}}{\mu_\alpha}k_{r\alpha}(\nabla p_\alpha - \rho_\alpha \mathbf{g}) \tag{2}$$

where $\mathbf{v}_s$ (m/s) is the velocity of the solid deformation, $\mathbf{k}$ (m^2) is the material permeability tensor, $\mathbf{g}$ (m/s^2) is the gravity vector and μ_α (Pa s), $k_{r\alpha}=k_{r\alpha}(s_\alpha)$, and p_α (Pa) are the dynamic viscosity, relative permeability, and fluid pressure for phase α, respectively. With the focus on CO_2 injected into a water-filled aquifer, we need only consider a nonwetting (n) and wetting phase (w), respectively, where $\alpha=n$ for the supercritical gas phase consisting mainly of CO_2 and $\alpha=w$ for the resident water. The capillary pressure, p_c (Pa), is defined by

$$p_c(s_\alpha) = p_n - p_w \tag{3}$$

Furthermore, it can be understood that since no other phases are present, the phase fractions of water and CO_2 satisfy

$$s_w + s_n = 1 \tag{4}$$

Considering the mass conservation of the solid phase:

$$\frac{\partial[\rho_s(1-\phi)]}{\partial t} + \nabla\cdot[\rho_s(1-\phi)\mathbf{v}_s] = 0 \tag{5}$$

where ρ_s (kg/m^3) is the density of the solid constituents of the porous medium. Using the equation of state for the solid, acknowledging that the density depends on the pore pressure acting on the solid, p_s (Pa), temperature T (°C), and the first invariant of the effective stress, I_1' (Pa); $\rho_s=\rho_s(p_s, T, I_1')$, the following expression for the change in porosity can be obtained, following *Lewis and Schrefler* [1998]:

$$\frac{d\phi}{dt}=(b-\phi)\left[c_s\frac{dp_s}{dt}-\beta_s\frac{dT}{dt}+\nabla\cdot\mathbf{v}_s\right] \tag{6}$$

where b is the Biot's coefficient and c_s (1/Pa) and β_s (1/K) are the compressibility and the volumetric thermal expansion coefficient for the solid phase, respectively. When assuming isothermal conditions and using equations (2), (5), and (6), equation (1) can finally be expanded to

$$\begin{aligned}\phi\rho_\alpha\frac{\partial s_\alpha}{\partial t}+\phi s_\alpha\rho_\alpha c_\alpha\frac{\partial p_\alpha}{\partial t}+\nabla\cdot(\rho_\alpha\mathbf{q}_\alpha)\\ +s_\alpha\rho_\alpha\left[(b-\phi)c_s\frac{\partial p_s}{\partial t}+b\frac{\partial\varepsilon_v}{\partial t}\right]=0\end{aligned} \tag{7}$$

where c_α (1/Pa) is the compressibility of fluid phase α obtained from the equation of state (for isothermal conditions and immiscible phases):

$$c_\alpha=\frac{1}{\rho_\alpha}\frac{\partial\rho_\alpha}{\partial p_\alpha} \tag{8}$$

and we have used that the rate of change of volumetric strain ε_v can be expressed as $\partial\varepsilon_v/\partial t=\nabla\cdot\mathbf{v}_s$.

The pore pressure, p_s, is typically defined as the sum of the saturation averaged phase pressures according to [e.g., *Bishop*, 1959; *Jaeger et al*., 2007; *Lewis and Schrefler*, 1998]:

$$p_s=\sum_\alpha s_\alpha p_\alpha \tag{9}$$

Using the capillary pressure in equation (3), equation (9) can be rearranged to

$$p_s=p_w+s_n p_c \tag{10}$$

Under many typical reservoir conditions, the last term $s_n p_c$ is small compared to p_w, such that $p_s\approx p_w$ is often used. We note that this already suggests that the fluid-to-solid coupling will primarily be through the fluid pressures, while more weakly dependent on saturation.

2.2. Geomechanical Equations

Under quasi-static conditions, the balance of momentum leads to the equation of equilibrium. In differential form, we then obtain (assuming static initial conditions):

$$\nabla\cdot(\sigma'-b\Delta p\mathbf{I})+\Delta\mathbf{f}=0 \tag{11}$$

where σ' (Pa) is the effective stress tensor, Δp (Pa) is the change in pore pressure relative to initial, steady state pore pressure, $\mathbf{I}$ is the identity matrix, and $\Delta\mathbf{f}$ (N/m^3) is the change in volumetric bodyload vector, again, relative to steady state conditions. Note that we use a stress convention where positive stress is extensional. The effective stress σ' is defined as the part of the total stress that governs the deformation of a rock, or soil. In rocks, the Biot coefficient describes the difference between the pore volume change and the bulk volume change during hydrostatic deformation and can be defined as $b=1-K/K_s$, where K (Pa) is the dry (drained) bulk modulus of the porous media and $K_s=1/c_s$ (Pa) is the solid bulk modulus (of the solid material/mineral in the porous media).

In addition, a constitutive equation relates stresses and strains, for isotropic materials they relate linearly according to

$$\sigma'=\lambda\varepsilon_v\mathbf{I}+2G\varepsilon \tag{12}$$

where the mechanical properties are here given by the Lamé parameters λ (Pa) and G (Pa). The volumetric strain is defined as $\varepsilon_v=\nabla\cdot\mathbf{u}$, where $\mathbf{u}$ (m) is the displacement vector and the full strain tensor ε is defined as

$$\varepsilon=\frac{1}{2}\left[\nabla\mathbf{u}+(\nabla\mathbf{u})^T\right] \tag{13}$$

We note again that in this convention the stresses and strains are positive for elongation and negative for compression.

The initial vertical stress is equal to the weight of the overburden; both the porous media and the pore fluids:

$$\sigma_v(z) = p_{atm} + \int_0^z \rho g dz \tag{14}$$

$$\rho = (1-\phi)\rho_s + \phi \sum_\alpha s_\alpha \rho_\alpha \tag{15}$$

where z (m) is the vertical elevation. When modeling under the assumption of steady state initial conditions, we are only interested in the change of stress, thus from equation (15) we see that a change in saturation s_α may change the buoyancy of the pore fluid and thereby alter the vertical stress through the $\Delta\mathbf{f}$-term in equation (11).

3. Dimensionally Reduced Model

Due to the often layered nature of reservoirs, aquifers, and aquitards, the horizontal extent is often much larger than the vertical extent and we can refer to them as large aspect ratio geological features. This property allows us to justify assumptions on the local vertical structure of the solution. In this section, we exploit these ideas in order to derive approximations to the governing equations for two-phase flow and poroelasticity.

In Figure 1, a conceptual sketch of such a system is shown. An aquifer is located between an overburden and underburden and shows topographic behavior. Note that in this figure, the vertical dimension has been exaggerated severely; for geological formations considered for CO_2 storage, the maximum slopes are typically only at most a few degrees.

With reference to the figure, the bounding surfaces of the aquifer are denoted F_B and F_T, where the function for surface F_n is defined as

$$F_n(x,y,z) = z - \zeta_n(x,y) = 0 \tag{16}$$

and $\zeta_n(x,y)$ (m) is the vertical position of the surface. This notation allows us to define the normal vector $\mathbf{n}$ of surface n as

$$\mathbf{n} = \nabla F_n \tag{17}$$

Note that these normal vectors are scaled such that the vertical extent equals 1, thus the vectors satisfy $||\mathbf{n}|| \geq 1$.

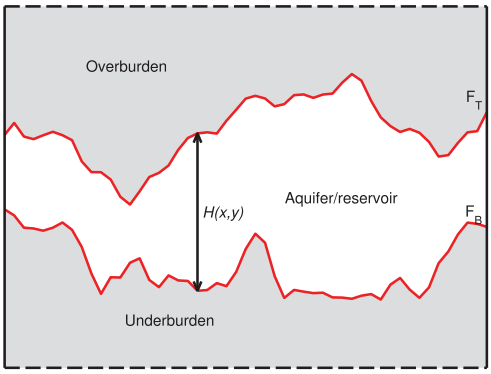

Figure 1. Example of an aquifer/reservoir of varying thickness H, located between an overburden and underburden.

In this section, we will first recall the integrated fluid flow model for immiscible two-phase flow [*Nordbotten and Dahle*, 2010; *Yortsos*, 1995], and subsequently consider the analogue model for mechanical deformation. To keep notation simple, we will not consider vertical variability in the material or fluid parameters within an aquifer. Thus, some properties will keep the same notation in both the full-dimensional formulation and the dimensionally reduced formulation.

3.1. Vertically Integrated Flow Model

We first consider the integrated form of mass conservation that will be obtained from equation (7). By assuming constant material properties in the vertical/integration direction and applying

Leibniz' rule when integrating each term in equation (7) from $z=\zeta_B$ to $z=\zeta_T$, the following dimensionally reduced form of the mass conservation for fluid phase α is obtained:

$$\begin{aligned}\phi\rho_\alpha\frac{\partial S_\alpha}{\partial t}H+\phi S_\alpha\rho_\alpha c_\alpha\frac{\partial P_\alpha}{\partial t}H+\bar{\nabla}\cdot(\rho_\alpha\mathbf{Q}_\alpha)\\+S_\alpha\rho_\alpha\left((b-\phi)c_s\frac{\partial P_s}{\partial t}+b\frac{\partial E_v}{\partial t}\right)\\+\rho_\alpha(\mathbf{q}_\alpha\cdot\mathbf{n})|_T-\rho_\alpha(\mathbf{q}_\alpha\cdot\mathbf{n})|_B=0\end{aligned}\tag{18}$$

where $H=H(x,y)$ (m) is the thickness of the aquifer and we have introduced the notation for the horizontal gradient

$$\bar{\nabla}=\left[\frac{\partial}{\partial x},\frac{\partial}{\partial y},0\right]^T\tag{19}$$

and the integrated volumetric strain is defined as

$$E_v=\int_{\zeta_B}^{\zeta_T}\varepsilon_v dz=\int_{\zeta_B}^{\zeta_T}\nabla\cdot\mathbf{u}dz\tag{20}$$

which is discussed further in equation (30) and section 3.3.3. Recall from equation (16) that ζ_B and ζ_T are the vertical positions of the bottom and top of the aquifer, respectively. Furthermore, we have introduced the representative pressure P_α (Pa) as the fluid pressure for fluid phase α at a specified datum $z=\zeta_P$; $P_\alpha=p_\alpha(x,y,\zeta_P,t)$. From the assumptions of constant density in the vertical direction, the fluid phase pressure can be expressed as

$$p_\alpha(x,y,z,t)=P_\alpha(x,y,t)-\rho_\alpha g[z-\zeta_P(x,y)]\tag{21}$$

Thus, we have for the integrated pore pressure:

$$P_s=\int_{\zeta_B}^{\zeta_T}\sum_\alpha\hat{s}_\alpha[P_\alpha-\rho_\alpha g(z-\zeta_P)]dz\tag{22}$$

where the datum ζ_P is typically chosen as the top or bottom surface of the aquifer and the integrated Darcy flux and average saturation S_α of phase α can be expressed as

$$\mathbf{Q}_\alpha=\int_{\zeta_B}^{\zeta_T}\mathbf{q}_\alpha dz\tag{23}$$

$$S_\alpha=\frac{1}{H}\int_{\zeta_B}^{\zeta_T}\hat{s}_\alpha dz\tag{24}$$

We will return to how to obtain explicit expressions for the integrated flux $\mathbf{Q}_\alpha$ and the reconstructed inverted capillary saturation $\hat{s}_\alpha$ in section 3.3 on closure relationships. Terms including the normal vector $\mathbf{n}$ in equation (18) represent the mass flux of fluid phase α across the top and bottom boundaries of the aquifer and are derived directly from the integration of the divergence term in equation (7) upon applying the Leibniz' rule.

3.2. Integrated Deflection Model

In the context of regional land subsidence due to ground water pumping, a series of papers on regional scale vertically averaged models for deformation were developed by Bear and Corapcioglu in 1981 and 1983 [*Bear and Corapcioglu*, 1981a,b; *Corapcioglu and Bear*, 1983]. There they developed a mathematical model for the areal distribution of drawdown, land subsidence, and horizontal displacement. The horizontal two-dimensional model was derived by averaging the three-dimensional model over the vertical thickness of the aquifer and taking into account the continuous variation in total stress as a result of water table fluctuations. The total stress is due to water and soil overburden weight and the vertical compaction and horizontal displacement is assumed to occur only in the reservoir where the pore pressure changes. In reality, most often the poroelastic effect extends far beyond the reservoir. For instance, the displacements will attenuate in the vertical direction as the pore pressure change also dissipates into the overburden and

underburden. This earlier work further assumed that the horizontal displacement was constant across the thickness of the aquifer and the vertical displacement varied linearly across the thickness of the reservoir.

Herein, we deviate from earlier work by treating the reservoir as an embedded region in a full three-dimensional domain, thus accounting fully for the full stress tensor in the overburden and underburden. Furthermore, we extend the fluid description to allow for multiple phases, here two phases, and consider linearly varying displacement across the thickness of the aquifer in both the horizontal and the vertical direction. Also considering linearly varying horizontal displacement across the aquifer thickness can be particularly important when noncorrelated displacement at the top and bottom of the aquifer is expected, for instance when the reservoir of interest shows topographical behavior, is inclined and/or the surrounding formations exhibit significant contrasts in mechanical properties. The effect of topography is illustrated and discussed further in section 5.3.

To obtain the compatible momentum balance equation to the VE formulations for two-phase flow, the equilibrium equation in equation (11) is integrated across the thickness of the aquifer in the vertical z direction between two surfaces F_B and F_T to obtain (in analogy to equation (18)):

$$\tilde{\nabla}\cdot\Sigma+(\sigma\cdot\mathbf{n})|_T-(\sigma\cdot\mathbf{n})|_B=\Delta\mathbf{F} \tag{25}$$

where we have introduced the integrated stress

$$\Sigma=\int_{\zeta_B}^{\zeta_T}\sigma dz \tag{26}$$

and the change in the integrated bodyload vector, $\Delta\mathbf{F}$. We recall that the total stress σ can be expressed as

$$\sigma=\lambda(\nabla\cdot\mathbf{u})\mathbf{I}+\mu\left(\nabla\mathbf{u}+(\nabla\mathbf{u})^T\right)-b\Delta p\mathbf{I} \tag{27}$$

Thus, the integral in equation (26) can be evaluated by inserting equation (27) and using Leibniz' integral rule, to obtain:

$$\begin{aligned}\Sigma=&\lambda\left[\tilde{\nabla}\cdot\mathbf{U}\right]\mathbf{I}+\mu\left[\tilde{\nabla}\mathbf{U}+(\tilde{\nabla}\mathbf{U})^T\right]-b\Delta P_s\mathbf{I}\\&+\lambda(\mathbf{u}\cdot\mathbf{n}|_T-\mathbf{u}\cdot\mathbf{n}|_B)\mathbf{I}\\&+\mu(\mathbf{nu}|_T-\mathbf{nu}|_B)\\&+\mu(\mathbf{un}|_T-\mathbf{un}|_B)\end{aligned} \tag{28}$$

where we have introduced the integrated displacement vector

$$\mathbf{U}=\int_{\zeta_B}^{\zeta_T}\mathbf{u}dz \tag{29}$$

and have that the volumetric strain E_v in equation (20) can now be expressed as

$$E_v=\tilde{\nabla}\cdot\mathbf{U}+(\mathbf{u}\cdot\mathbf{n})|_T-(\mathbf{u}\cdot\mathbf{n})|_B \tag{30}$$

Together, equations (25) and (28) form the governing Poroelastic Linear Vertical Deflection (PLVD) equations for the geomechanical system. The PLVD equations are thus the dimensionally reduced (integrated) equations of equilibrium for a poroelastic medium. How to obtain the explicit expression for the integrated displacement in equation (29) is described in section 3.3.3.

3.3. Closure Relationships

In order to complete the description of the vertically integrated model, it is necessary to make modeling assumptions regarding the structure of the solution within the aquifer [*Nordbotten and Celia*, 2012]. Specifically, this is required in order to obtain explicit expressions for $\mathbf{Q}_\alpha$ and to relate P_α and $\mathbf{U}$ to the values at the top and bottom of the aquifer.

Two main categories of closure relationships can be postulated for the main variables: (A) The internal structure is in a certain sense constant across the thickness of the aquifer. (B) The internal structure varies linearly across the thickness of the aquifer.

3.3.1. Pressure

It is common for the fluid equations to use closure form (A), wherein the fluid potential (pressure and hydrostatic effects; $p_\alpha+\rho_\alpha gz$) is assumed to be vertically uniform within the aquifer. In order to be consistent with previous studies, we will adopt this convention here. This implies that the fluid pressures are close to being in vertical equilibrium, and thus the vertical gradients are proportional to the specific gravity of the fluid. The term VE model refers to models where this assumption is applied. For each phase, the hydrostatic fluid pressure can thus be expressed by equation (21), this is schematically illustrated for the wetting phase pressure for $\zeta_P=\zeta_B$ in Figure 2.

When significant fluid flow occurs through the aquifer, the approximation of constant vertical potential may be questioned [*Guo et al.*, 2014; *Nordbotten and Celia*, 2006]. However, due to the permeability contrast between the aquifer and overburden, the dominant vertical variation in fluid potential is within the overburden and underburden [*Hunt*, 1985]. The use of constant fluid potential within the aquifer has the modeling advantage that the saturation reconstruction equation in Appendix A, equation (A1), does not depend on vertical flux.

3.3.2. Saturation and Flux

The choice of constant fluid potential across the aquifer thickness allows us to exploit the capillary pressure curve to derive the nonlinear structure of the variable $\hat{s}_\alpha$ as a function of the vertical elevation z [*Nordbotten and Dahle*, 2010]. When ignoring hysteresis in the capillary pressure function, the saturation can be solved for by inverting equation (3) such that $s_\alpha=p_c^{-1}(p_n-p_w)$, thus, since the capillary pressure is in vertical equilibrium, the saturation also becomes a distribution over the vertical elevation; $\hat{s}_\alpha=p_c^{-1}(z)$, see Figure 3. We detail an explicit expression on this form in Appendix A. Together with the definition of the fluid flux, we can then derive explicit expressions for the integrated flux in the form:

$$\mathbf{Q}_\alpha=-\frac{\mathbf{k}\Lambda_\alpha H}{\mu_\alpha}(\nabla P_\alpha-\rho_\alpha G) \tag{31}$$

where G (m/s^2) is the gravity contribution in the horizontal direction due to the topography of the datum ζ_P.

The average fluid mobility term is defined as

$$\Lambda_\alpha \equiv \frac{1}{H}\int_{\zeta_B}^{\zeta_T}\lambda_\alpha(\hat{s}_\alpha)dz \tag{32}$$

where $\lambda_\alpha(\hat{s}_\alpha)$ is a function of the reconstructed inverted capillary saturation. Explicit expressions for Λ_α when λ_α can be expressed by Corey-type power law functions, e.g., equations (38) and (39), can be obtained from equations (A2) and (A3), respectively.

Note that when the capillary pressure is ignored, the mobility simplifies and is directly proportional to the saturation [see e.g., *Nordbotten and Celia*, 2012, chapter 3.7; *Nordbotten and Dahle*, 2010].

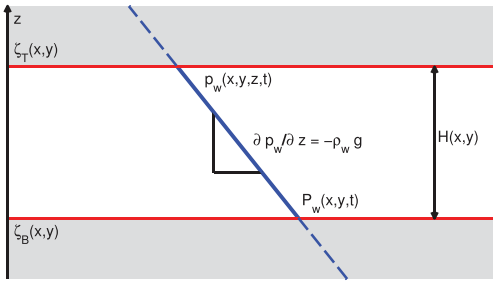

Figure 2. Vertical equilibrium pressure profile for the wetting phase (blue line). The white area represents the aquifer and the red lines are the upper and lower bounds of the aquifer. The dashed blue lines indicate continuity in wetting phase pressure into the overburden and underburden.

3.3.3. Displacement

It is important to note that it is not sufficient to use an assumption of constant vertical displacement across the aquifer thickness for our application, since the vertical expansion of the aquifer itself is an important feature of the solution. In addition, for aquifers with general topography, the overburden and underburden may have noncorrelated displacement, and standard reduced models with constant horizontal displacement may be qualitatively wrong. Thus, we are led to consider a closure relationship in the form (B). The term LVD (Linear Vertical Deflection) for the dimensionally

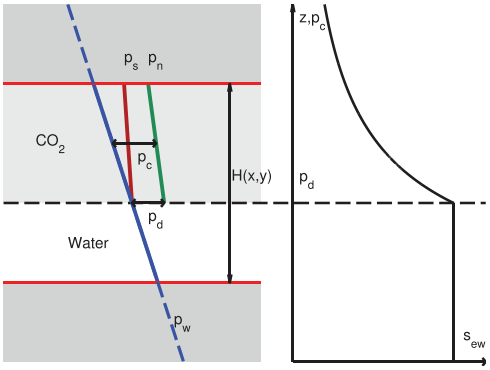

Figure 3. Schematic comparison of the phase pressure and pore pressure profiles across an aquifer in vertical equilibrium with the capillary pressure function. p_d (Pa) is the entry pressure in the capillary pressure function. The horizontal dashed line indicates where effective nonwetting saturation $s_{en} = 0$ and the light grey area indicates the two-phase flow region. Here the aquifer is assumed to be confining for the nonwetting phase and the dashed blue lines indicate the continuity in the wetting phase pressure.

reduced form of the equation of equilibrium and its poroelastic extension, PLVD (Poroelastic Linear Vertical Deflection), have already been introduced. The names reflect the assumed structure of the displacement vector $\mathbf{u}$ which varies linearly in the vertical direction across the thickness of the aquifer according to

$$\mathbf{u} = \mathbf{u}_B + \frac{\mathbf{u}_T - \mathbf{u}_B}{H}(z - \zeta_B) \tag{33}$$

where the subscripts T and B indicate top and bottom of the aquifer, respectively. The integrated displacement in equation (29) can now be evaluated to

$$\mathbf{U} = \frac{\mathbf{u}|_T + \mathbf{u}|_B}{2} H \tag{34}$$

This is, however, not sufficient to form a closed system of equations, and we need to complement equation (34) with a consistency requirement on the vertical stresses. From equation (28), we know that the vertical component of integrated stress is given by Hooke's law and the displacement at the top and bottom of the aquifer. Furthermore, we require that this integrated stress is compatible with the stress at the aquifer top and bottom, e.g.,

$$\boldsymbol{\Sigma} \cdot (\mathbf{n}|_T + \mathbf{n}|_B) = [(\sigma \cdot \mathbf{n})|_T + (\sigma \cdot \mathbf{n})|_B]H \tag{35}$$

3.4. Comments on Generality

In the preceding sections, we have consciously suppressed several nuances in the interest of obtaining a relatively concise presentation. We note a few of them here.

Saturation within an aquifer. We have suppressed to some extent explicit notation regarding the vertical structure of saturation [*Nordbotten and Celia*, 2012]. It is implied in all vertically integrated flow models that the saturation structure can be reconstructed from the integrated saturation, and we have denoted this reconstructed saturation, where needed, as $\hat{s}_\alpha$. Note that this reconstructed saturation can be obtained analytically or numerically; however, these nuances have been explored in earlier work [*Doster et al*., 2013].

Shape of pressure profile. In the preceding, we have in the interest of being compatible with the majority of earlier work on vertically integrated flow models used the convention from vertically integrated models wherein the vertical distribution of pressure is hydrostatic. However, it is possible to use also for the flow equation a nonhydrostatic vertical distribution, although this has received less attention [*Nordbotten and Celia*, 2006].

Assumptions on physical parameters. The general integrated conservation equations (18) and (25) are valid without regard to any assumptions on parameters. It is also possible to derive the constitutive laws in equations (28) and (31) with greater generality; however, this typically comes at the price of significant added complexity in the definitions of the effective parameters for the integrated equations [*Andersen et al*., 2014; *Nordbotten and Celia*, 2012].

4. Validation Model

The validation model is inspired by the study on CO_2 injection and ground deformations at In Salah, Algeria, by *Rutqvist et al*. [2010]. In this example, CO_2 is injected into a 20 m thick, flat, and horizontal reservoir with a 900 m thick caprock layer, see Figure 4. The hydromechanical material properties are given in Table 1. The pressure and temperature conditions at reservoir level (approximately 90°C and 18–19 MPa) imply that the CO_2 is in supercritical state and the fluid properties that are used are given in Table 2. In the present paper,

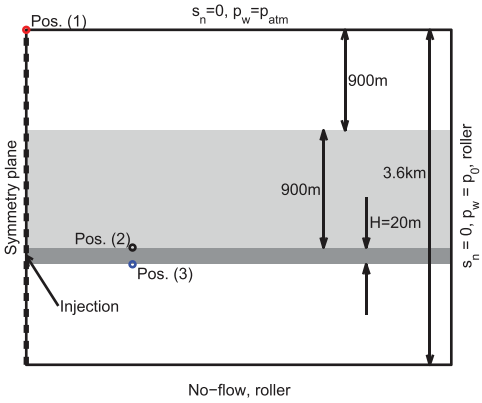

Figure 4. Sketch of model geometry of validation model and boundary conditions. Position (1)–(3) indicate the location where the values in the convergence plot in Figure 13 are obtained. Positions (2) and (3) are located at top and bottom of the aquifer, respectively, at $x = 500$ m. Initial pressure p_0 is hydrostatic with a constant vertical gradient and the pores are initially fully water saturated, $s_n = 0$.

we choose to work with dimensional variables, due to the large number of parameters associated with defining poroelastic formulations in the geometric setting of multilayered geological materials. For this problem, there is no clearly preferred choice of characteristic scales, and we find that using a nondimensional formulation for this problem would give an undue emphasis to the somewhat arbitrary choice of scaling.

It is assumed that initially the pores are fully water saturated and the initial pore pressure p_0 (Pa) is hydrostatic with atmospheric pressure at the surface, see Figure 4. The right boundary is defined as an open boundary where the pressure is equal to the initial pressure, the bottom is a no-flow boundary and the left boundary has symmetry conditions.

The aquifer is considered partially leaky where the injected CO_2 is confined to the aquifer. The water, however, is allowed to escape/enter the aquifer and we have a continuity in both the wetting phase flux and pressure across the interface between top and bottom of the aquifer and the caprock and underburden, respectively: $q_{w,u}=q_{w,d}$ and $p_{w,u}=p_{w,d}$ [*Helmig*, 1997], where u and d indicate upside and downside of both the top and bottom aquifer boundaries, respectively.

The numerical implementation was within the framework of the commercially available software COMSOL Multiphysics, which utilizes finite elements and standard linear and nonlinear solvers.

The validation model is two-dimensional, under plane strain conditions. Note that although the equations, as presented and derived in sections 2 and 3, are applicable to three-dimensional problems, a two-dimensional validation model is chosen for greater flexibility in terms of assessing computational performance. The validation model is also consistent with an approximation to a horizontal well, such as was in use at In Salah, and here the injection is at constant rate equivalent to a total yearly sequestration of 0.133 Mt of CO_2 through a horizontal, 1.5 km long injection well perpendicular to the model plane. The horizontal injection well therefore reduces to a point in the validation model and is located in the middle of the aquifer on the axial symmetry line at $x = 0$.

4.1. Capillary Pressure and Relative Permeability Functions

The capillary pressure is described by a Brooks and Corey-type function:

$$p_c(s_n)=\alpha(1-s_{en})^{-1/2}+\beta \tag{36}$$

Table 1. Hydromechanical Material Properties Used in Validation Model

Material Property	Overburden (0–900 m)	Caprock (900–1800 m)	Reservoir (1800–1820 m)	Underburden (Below 1820 m)
Young's modulus, E (GPa)	1.5	20	6	20
Poisson's ratio, ν	0.2	0.15	0.2	0.15
Biot's coefficient, b	0.7	0.7	0.7	0.7
Porosity, ϕ	0.1	0.01	0.17	0.01
Entry pressure, γ (kPa)	NA	NA	90	NA
Permeability, k (m^2)	10^{-17}	10^{-19}	13×10^{-15}	10^{-19}
Residual saturation, wetting phase, s_{rw}	NA	NA	0.4	NA
Residual saturation, non-wetting phase, s_{rn}	NA	NA	0	NA

Table 2. Properties of Water and CO_2, Evaluated at 50°C and 20 MPa [*Linstrom and Mallard*, 2015]

	Density, ρ_α (kg/m^3)	Viscosity, μ_α (mPa s)	Compressibility, c_α (1/GPa)
Water	997	0.55	0.419
CO_2	784	0.069	15.6

where it can be seen that $\gamma \equiv \alpha + \beta$ corresponds to the entry pressure p_d (Pa) in the capillary pressure function given by *Brooks and Corey* [1964] and we use that $\gamma = 90$ kPa, $\alpha = 0.9\gamma$, and $\beta = 0.1\gamma$. For an initial water saturated porous medium, and since there is no residual nonwetting saturation, the effective saturation s_{en} is related to the saturation s_n by

$$s_{en} = \frac{s_n}{1 - s_{rw}} \tag{37}$$

where s_{rw} is the residual wetting saturation. The relative permeability functions are given as Corey-type power law functions:

$$\lambda_n(s_n) = s_{en}^p \tag{38}$$

$$\lambda_w(s_n) = (1 - s_{en})^q \tag{39}$$

where the exponents p and q are fitting parameters, here $p = 2$ and $q = 3$.

5. Results and Discussion

A two-dimensional, fully resolved poroelastic model with two-phase flow, including capillary pressure, under plane strain assumption is compared to the equivalent dimensionally reduced model using Vertical Equilibrium (VE) assumption to describe the two-phase flow in the aquifer and Poroelastic Linear Vertical Deflection (PLVD) equation to describe the poroelastic behavior in the aquifer.

As CO_2 is injected into the aquifer, the water is displaced and the pore pressure increases, resulting in increased effective stress (remembering that stress is here positive in extension) and in turn causing the formation to deform. Figure 5 shows an exaggerated deformation plot of the model, except the aquifer, where the filled contours represent the vertical displacement and the values indicate the magnitude in centimeters. The solution is taken from the fully resolved model and the black contours show the corresponding solution from the dimensionally reduced model. The white space is the aquifer and is not plotted to emphasize its expansion as the CO_2 is injected.

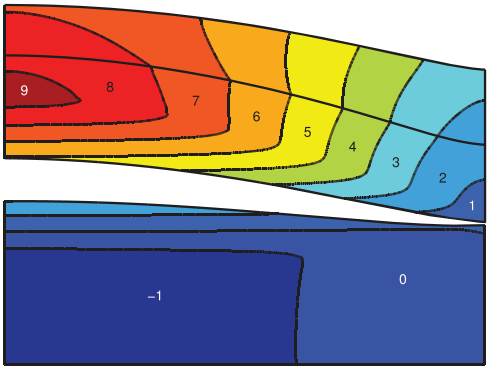

Figure 5. Exaggerated (20,000 times) deformation plot of the displacement of the overburden, caprock, and underburden after 40 years of injection. The filled contours represent the vertical displacement and the values give the vertical displacement in centimeters. The white space is the aquifer and emphasizes its expansion as the CO_2 is injected. The deformation and the colors are from the solution of the fully resolved model and the black contours are the corresponding solution from the dimensionally reduced model.

In the aquifer, the dimensionally reduced model assumes that the fluid phases are in vertical equilibrium such that the vertical flux is negligible compared to the horizontal flux. At early times, this is not a valid assumption, as is well illustrated in Figure 6 (top left) where the injected CO_2 spreads in all directions. As time progresses, the assumption becomes increasingly more appropriate and the saturation distributions of the two solutions coincide.

The main driving force for deformation is the change in stress, see equation (27). The stress depends on the pore pressure and despite the differences in the phase distribution at early time, see Figure 6, the pressure is little affected by this assumption. When comparing the injection pressure (taken as the pore pressure in the middle of the

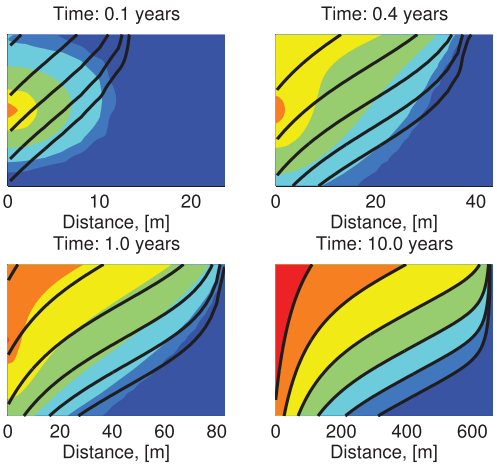

Figure 6. Saturation distribution of the CO_2 in the aquifer at various times. The filled contours are evenly distributed saturation levels ranging from 0 to 0.41. The black contours represent the corresponding distribution from the dimensionally reduced model. Note the difference in scale.

aquifer), Figure 7, it can be seen that even at early times the pressure profiles match within a small fraction. To emphasize any difference in the pressure profile, the time scale is logarithmic and the inserted axis shows the relative difference.

This weak dependency on the saturation can be explained by considering the value of the pore pressure. The initial pore pressure is approximately 18 MPa in the aquifer. For typical values of nonwetting saturation, the second term in equation (10), $s_n p_c$, becomes in the order of 0.1 MPa. Hence, it can be seen from equation (10) that $p_s \approx p_w$ and the saturation has negligible impact on the pore pressure.

The change in wetting phase pressure p_w is illustrated in Figure 8 along vertical cross sections 100 m away from the injection point. It shows how the pressure gradually dissipates out of the aquifer despite the low permeability in the caprock and underburden compared to the aquifer, and the thick dashed lines are the solution from the fully resolved model and the thin lines are from the dimensionally reduced model. The numbers indicate the time in years. Similar characteristics can be seen when looking at the change in horizontal stress σ_x, see Figure 9.

Initially, the pressure increases mainly in the aquifer, causing it to expand in all directions, and in Figure 10, it can be seen how the top and bottom of the aquifer (green and red lines, respectively) is forced apart at early times. With time, the pressure dissipates into the caprock and underburden, increasing the effective stress also here, leading eventually to the whole aquifer to heave as the underburden expands.

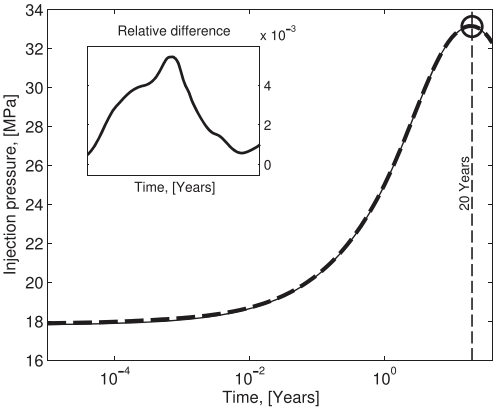

Figure 7. Evolution of the injection pressure (pore pressure in the middle of the aquifer at $x = 0$) plotted on a logarithmic time scale. Thick dashed line is the pore pressure p_s from the fully resolve model and the thin line is the pore pressure P_s from the dimensionally reduced model. The inserted axis shows the relative difference, $(p_s - P_s)/p_s$.

After 20 years of injection, the pore pressure in the aquifer reaches a maximum value, see Figure 7 and 8, but the pore pressure in the caprock and underburden continue to rise as it dissipates out of the aquifer, causing the surface to continue heaving although the aquifer has stopped expanding.

5.1. Performance and Applicability

There are two computational benefits of using a dimensionally reduced approach. First, the reduction in computational cost, which is directly related to the number of degrees of freedom that needs to be solved. Due to the two-phase flow in the aquifer, a high grid resolution may be required to resolve the distribution of phases, but in the dimensionally

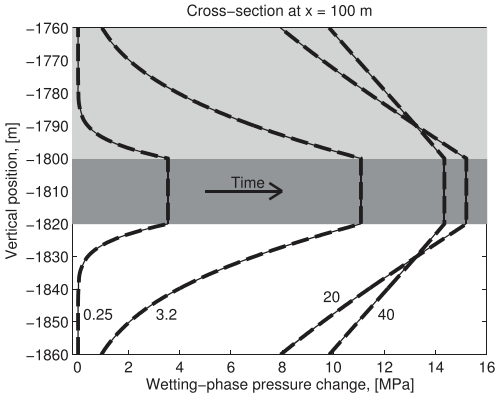

Figure 8. Vertical cross sections of the change in wetting phase pressure p_w at 100 m away from the injection point. Thick dashed lines are the solution from the fully resolved model and the thin lines are from the dimensionally reduced model. The numbers indicate the time in years.

reduced approach, the degrees of freedom inside the aquifer is eliminated altogether and the internal processes, in the aquifer, can be evaluated exactly from the upscaled variables. Second, the pressure field in flow problems is usually smooth with relatively small gradients, but two-phase and multiphase flow problems introduce volume fractions of the phases (saturation), and, depending on the hydraulic properties and the injection rate, the spatial gradients of the saturation can be very large (steeply varying saturation profile). In fact, the more convectively dominant the flow is, the steeper these gradients become. However, the dimensionally reduced model solves for the integrated mass thus the transition between the phases will be smoother and the gradients will be smaller, allowing longer time steps by the numerical solver and therefore reduced calculation time.

As indicated, in order to get physically accurate and sometimes even meaningful solutions, a numerical model usually requires a denser discretization in the two-phase flow region, and at the phase front in particular, compared to the single-phase flow region. The two-phase region is the area, or volume, where two phases are expected to sweep across in the time frame of the model. Normally, these regions are discretized differently, as illustrated in Figure 11. In the dimensionally reduced model, the two-phase flow and poroelasticity are described in the red nodes only. Hence, the reduction in computational cost is the number of degrees of freedom that can be eliminated inside the aquifer. How big this saving will be depends on the size of the two-phase region of interest.

As CO_2 displaces water, the size of the two-phase flow region will increase with times, as shown in Figure 6. To evaluate this, a study of a progressively larger two-phase flow region, allowing an increasing number of degrees of freedom to be eliminated, has been performed: eight simulations where the numerical grid in the two-phase region is dense, as in Figure 11 (left), and then gradually increase in size in the single-phase region until it looks closer to Figure 11 (right). The simulations were stopped when the CO_2 approached the extent of the more densely meshed two-phase region.

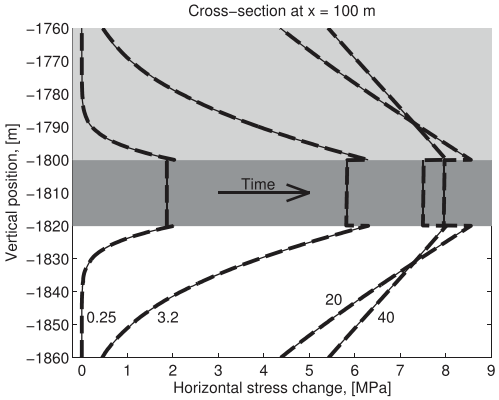

Figure 9. Vertical cross sections of the change in horizontal stress σ_x at 100 m away from the injection point. Thick dashed lines are the solution from the fully resolved model and the thin lines are from the dimensionally reduced model. The numbers indicate the time in years.

The ratio of the degrees of freedom solved for by the two models is plotted in Figure 12 (left, red line). At short times, the two-phase flow area is very small and the reduction in computational cost, by eliminating the degrees of freedom in the aquifer, is low, see for example point A in Figure 12. At longer times, the number of degrees

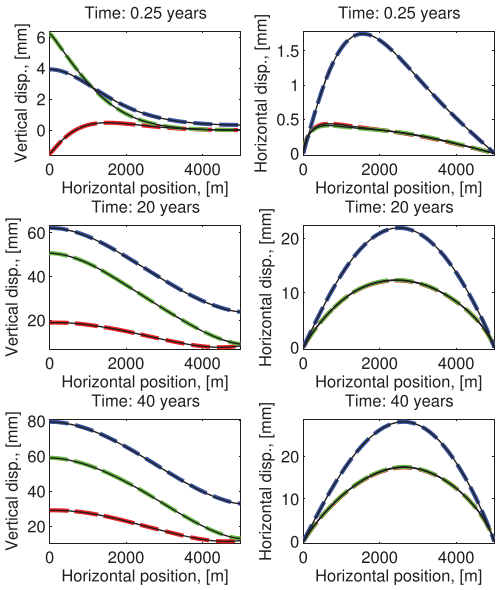

Figure 10. Plots of (left) vertical displacement and (right) horizontal displacement of the bottom and top of the aquifer and the model surface for three different times. Blue curves are at the surface of the model, green curves are at the top of aquifer and red curves are at the bottom of aquifer. Dashed lines are the solution from the fully resolved model and thin black lines are from the dimensionally reduced model. Note that in the figures to the right the horizontal displacement at the top and bottom of the aquifer (green and red curve, respectively) are almost the same and the two curves coincide.

of freedom that can be eliminated increases, see for example point B in Figure 12. The corresponding ratio of the simulation times is also shown in Figure 12 (left, blue line), and even if the reduction in degrees of freedom is modest, the reduction in calculation time becomes increasingly more significant.

In order to quantify the applicability of the dimensionally reduced model, a numerical convergence study was performed. *Yortsos* [1995] examined the validity of the VE assumption and identified the key dimensionless variable to be R_L defined as

$$R_L = \frac{L}{H}\sqrt{\frac{k_v}{k_h}} \tag{40}$$

where L is a characteristic length and k_v and k_h (m^2) are the vertical and horizontal permeability in the aquifer, respectively. The analysis showed that VE is valid in the limit of large R_L^2. In the validation model, the ratio $k_v/k_h = 1$, thus $R_L = L/H$ and the numerical convergence study is with respect to the thickness of the aquifer. The model setup was identical to the validation case, but in order to make sure that the injected CO_2 did not reach the outer boundary of the model, the injection rate was scaled with the thickness. The test was also done without any residual saturation of either phases. The large range of aquifer thickness (H varied from 2 to 100 m) required some special attention to the grid resolution in the aquifer, both in the lateral and vertical direction, to resolve the phase distribution. This affects the number of degrees of freedom in the aquifer that can be eliminated. The ratio of the computational cost (degrees of freedom) and the calculation time for the full-dimensional model versus the dimensionally reduced model for the various thicknesses are shown in Figure 12 (right).

As can be seen in both the time varying performance test of the validation model and the applicability test (convergence study) of varying aquifer thickness, Figure 12 (left and right, respectively), there are moderate

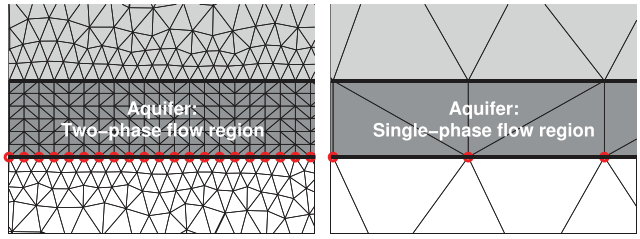

Figure 11. Example of the numerical grid in the aquifer. (left) Dense discretization in the two-phase flow region. (right) Coarse discretization in the single-phase flow region.

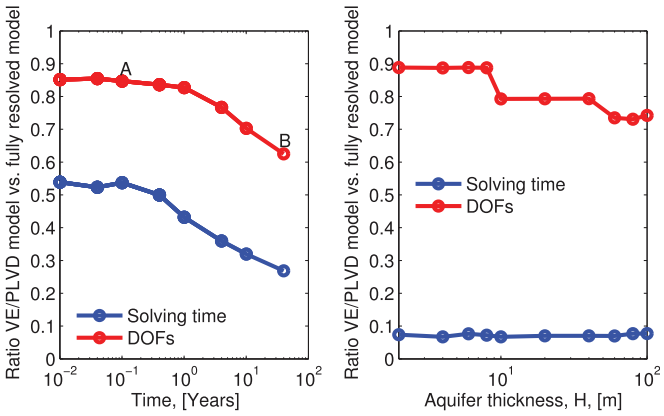

Figure 12. The ratio of numerical solving time and number of degrees of freedom (left) for various simulations times in the performance test, see text for description, and (right) for various aquifer thickness H after 20 years of injection in the convergence test.

reductions in cost, but the savings in calculation time by using the dimensionally reduced model are significant. As described earlier, this is partly the result of solving a reduced mathematical problem, but also, and more importantly, the result of solving a less stiff nonlinear system of equations in the dimensionally reduced model that allows for larger time steps by the numerical solver.

The main difference between the validation model and the convergence model is that in the latter the injection rate is scaled to the thickness and is also comparably higher (for $H = 20$ m it is 2.7 times higher, note that no residual saturation gives the injected CO_2 more pore volume to sweep across). Higher injection rates imply sharper saturation fronts, thus the applicability test further underlines the computational benefit of the dimensionally reduced form, namely that the system of equations is more efficient to solve.

5.2. Convergence

In the extreme case of a zero-thickness aquifer, the integrated equations reduce to continuity requirements on a surface, and thus the integrated model is exactly equivalent to the original full-dimensional equations. We thus expect that any modeling error will be a function of the aquifer thickness [*Yortsos*, 1995], see also equation (40). Since we are using a model with linear displacement, it is reasonable to expect the LVD model to be second-order accurate with respect to the aquifer thickness. However, due to the constant vertical potential used in the flow model, we expect the pressure to be only first-order accurate, which may impact the overall accuracy of the model. In practice, we may expect that the model accuracy lies somewhere between first and second order. We note that simpler models, with e.g., constant displacement across the aquifer thickness, are expected to be strictly less accurate. Unfortunately, a rigorous analysis of these statements is beyond the scope of this work, due to the nonlinearities present in the system, and we will therefore proceed with a purely numerical analysis of the model error as it depends on the aquifer thickness and consequently look closer at the results of the convergence study described in section 5.1.

Because analytical solutions for this problem is unavailable, we consider the full-dimensional simulation as the true model and measure the error as the relative difference in the solution obtained by the dimensionally reduced model and the fully resolved model. Furthermore, we measure the error in discrete points of interest, rather than using a spatial norm, in order to capture the accuracy exactly near the model reduction. The results are shown in Figure 13.

We note that in general a convergence between first and second order is obtained. We also remark that in all cases, the difference is small, with less than 1% in almost all cases considered. A notable feature in the convergence study is the irregularity of the plot. This stems from two cases: first, the full-dimensional grid has to be adapted to the thickness of the aquifer, and the gridding of the full model thus changes between

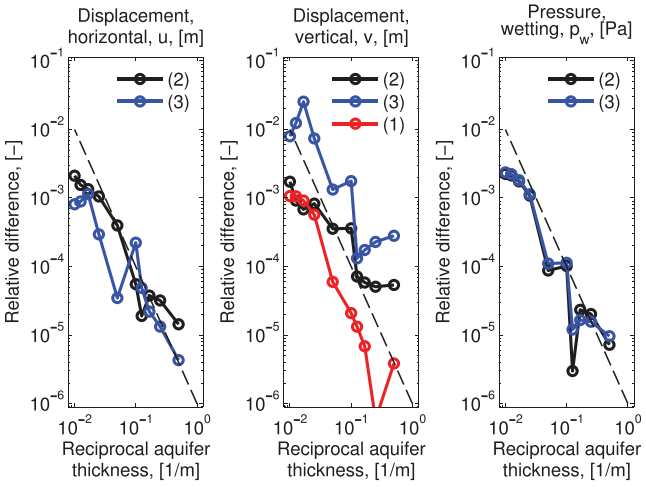

Figure 13. Convergence plot of the reciprocal of aquifer thickness *H* in various positions (position (1)–(3), as indicated in Figure 4). The thin, black dashed lines indicate second-order convergence. Thickness *H* varies from 2 to 100 m. The results are after 1 year of injection.

each case considered. Furthermore, for thin aquifers, the error is approaching the order of the tolerance of the nonlinear solver, and thus cannot be further reduced within the comparison paradigm chosen.

In sum, the convergence study indicates that the dimensionally reduced model has high accuracy for even relatively thick aquifers, and essentially second-order convergence properties compared to the fully resolved model with respect to aquifer thickness.

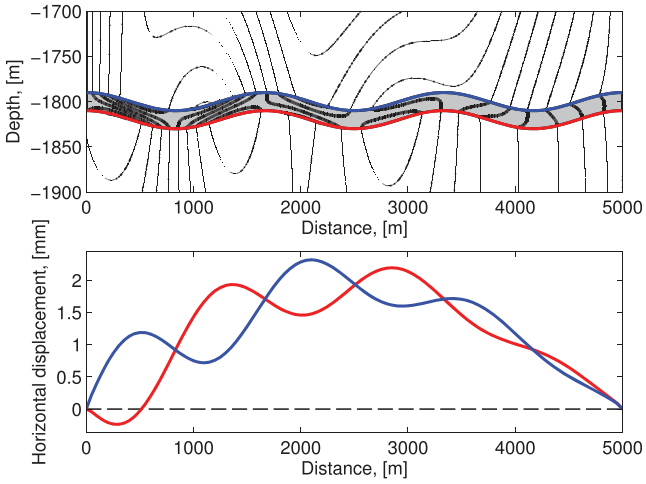

Figure 14. (top) Contours of the horizontal displacement in and around a topographic aquifer (grey, shaded area). Note the difference in scale. The overburden and underburden are assumed impermeable and a static pore pressure increase is applied to the aquifer that varies linearly from 15 MPa at the left boundary to zero at the right boundary. (bottom) Horizontal displacement along the top (blue line) and bottom (red line) surfaces of the aquifer.

5.3. Effect of Topography

As described in section 3.3.3, the assumption for the LVD and PLVD equations is linearly varying displacements across the thickness of the aquifer, see equation (33). In the validation model presented in section 4, it can be seen from the results that the horizontal displacement at the top and bottom of the aquifer is almost identical, see Figure 10 (right, green and red curves, respectively), making the assumption of constant horizontal displacement across the aquifer a good approximation. However, this is because the aquifer is flat and that the surrounding formations have the same mechanical properties. When the aquifer top and bottom topographies are variable, see example in Figure 14 (top), it can be clearly seen that there may be significant quantitative and qualitative differences in horizontal displacement across the aquifer. In this example, a 20 m thick reservoir varies sinusoidally of ± 10 m in the vertical direction. The mechanical properties are the same as in the validation model, see Table 1, but the overburden and underburden are now assumed impermeable and a static pore pressure change is applied to the aquifer that varies linearly from 15 MPa at the left boundary to zero (initial pore pressure p_0) at the right boundary. It can be seen from the horizontal displacement in Figure 14 (bottom) that it is far from constant across the aquifer, and at $x < 500$ m it even has opposite sign. This can be significant when considering the integrity of a caprock in CO_2 storage.

6. Conclusion

We have derived a reduced-dimensional model for coupled two-phase flow and geomechanical deformation within the context of CO_2 storage. The reduced-order model simplifies the complex flow and interaction within thin storage units, while retaining the full-dimensional poroelastic equations for the overburden and underburden.

Our presentation provides a general framework for reduced models; however, we emphasize our choices of closure relationship: Vertical Equilibrium (VE) for the fluid and Linear Vertical Deflection (LVD) for the solid within the aquifer. These choices allow for an efficient reconstruction of fluid saturation as well as realistic approximation of aquifer deformation, even in the presence of variable aquifer topography.

The current presentation is within the context of immiscible fluids, which couples the main fluid-mechanical coupling. We envision that recent work on advanced models for vertically integrated models for more complex processes, including fluid miscibility and accounting for vertical variation in fluid density, can be integrated with the current results. These coupled processes are important in that they are computationally demanding, and that simplified models are imperative to become computationally tractable.

In this study, the simplified model approach through dimensional reduction has proved promising in providing significant savings in computational time when faced with a large number of simulations. In general, a reduction in computational cost allows for faster calculation. However, it has been shown in both the validation model and a convergence study, see Figure 12 (left and right, respectively), that in addition to a reduction in cost, albeit modest, the dimensionally reduced formulation produces less stiff nonlinear systems of equations, allowing the numerical solver to progress with larger time steps and significantly contribute to further reduce the computational time.

It has also been demonstrated that such models can retain reasonable accuracy when applied to realistic field data, such as the conditions at CO_2 storage plant in In Salah, Algeria. The range of applicability of the dimensionally reduced model is to a leading order the thickness of the reduced domain, the aquifer. A convergence test for a range of aquifer thickness values indicates that accurate solutions in the order of 0.1% and less difference in solution compared to a full-dimensional formulation for aquifers up to 100 m thick are achieved.

The main parameter affecting the effective stress is the pore pressure that in this example is little affected by the phase distribution, hence the early-times violation of negligible vertical flow, the Vertical Equilibrium (VE) assumption, does not affect the stress. In a different scenario, for instance at lower depths where the density difference between the phases is bigger compared to the present scenario and the capillary pressure will have a bigger impact on the pore pressure, the accuracy will depend more on the validity of the Vertical Equilibrium assumption, and this has been investigated by others, see e.g., *Court et al.* [2012].

However, as illustrated here, the VE assumption becomes increasingly appropriate with time and is almost always appropriate for analysis of long-term behavior that can span many hundreds to thousands of years.

Appendix A

As the fluid phase pressures p_α can be expressed as a function of the vertical position z, so can the capillary pressure, $p_c(z)$. The average saturation S_α in equation (24) is the integral of the reconstructed inverted capillary saturation, $\hat{s}_\alpha$, which is derived from the inverted capillary pressure function $p_c^{-1}(z)$. From *Nordbotten and Dahle* [2010], we have that the reconstructed effective inverted capillary saturation for the nonwetting phase, $\hat{s}_{en}$, can be expressed by

$$\hat{s}_{en}(P_*^{cap}) = \begin{cases} 0, & 0 \le \zeta \\ 1 - \dfrac{1}{B^2\left(P_*^{cap} + \dfrac{z-\zeta_p}{H}\right)^2}, & \zeta < z \le H \end{cases} \tag{A1}$$

where B and P_*^{cap} are dimensionless constants [see *Nordbotten and Dahle*, 2010, for details], ζ (m) is the vertical location of the interface where $\hat{s}_{en}=0$, and $\hat{s}_{en}$ is related to $\hat{s}_n$ as in equation (37).

The expressions for the average phase mobilities can for simple constitutive functions (e.g., equations (38) and (39)) be calculated explicitly as

$$\Lambda_n(S_n) = \begin{cases} [Q(u_1,p) - Q(u_2,p)], & \zeta = 0 \\ [Q(u_1,p) - Q(1,p)], & \zeta > 0 \end{cases} \tag{A2}$$

and

$$\Lambda_w(S_n) = \begin{cases} \displaystyle\sum_{i=0}^{q} \binom{q}{i} (-1)^i [Q(u_1,i) - Q(u_2,i)], & \zeta = 0, \\ \displaystyle\sum_{i=0}^{q} \binom{q}{i} (-1)^i [Q(u_1,i) - Q(1,i)] + \frac{\zeta}{H}, & \zeta > 0. \end{cases} \tag{A3}$$

where

$$u_1 = BP_*^{cap} + B, \quad u_2 = BP_*^{cap} \tag{A4}$$

$$Q(u,p) = \frac{1}{B}\sum_{i=0}^{p} \binom{p}{i} \frac{(-1)^i}{1-2i} u^{1-2i} \tag{A5}$$

$$Q(u,q) = \frac{1}{B}\sum_{i=0}^{q} \binom{q}{i} \frac{(-1)^i}{1-2i} u^{1-2i} \tag{A6}$$

Acknowledgments
The authors are thankful to the following sponsors for the financial support of this work: Research Council of Norway (through the MatMoRA-II project 215641, Mathematical Modeling and Risk Assessment of CO_2 storage) and Statoil ASA and NGI in Oslo, Norway. Data used in this paper are properly cited and referred to in the reference list.

References

Andersen, O., S. E. Gasda, and H. M. Nilsen (2014), Vertically averaged equations with variable density for CO_2 flow in porous media, *Transp. Porous Media*, *107*, 1–33.
Bear, J., and M. Y. Corapcioglu (1981a), Mathematical model for regional land subsidence due to pumping: 1. Integrated aquifer subsidence equations based on vertical displacement only, *Water Resour. Res.*, *17*(4), 937–946.
Bear, J., and M. Y. Corapcioglu (1981b), Mathematical model for regional land subsidence due to pumping: 2. Integrated aquifer subsidence equations for vertical and horizontal displacements, *Water Resour. Res.*, *17*(4), 947–958.
Biot, M. A. (1935), Le problème de la consolidation de matières argileuses sous une charge, *Ann. Soc. Sci. Bruxelles, Ser. B*, *55*, 110–113.
Biot, M. A. (1941), General theory of three-dimensional consolidation, *J. Appl. Phys.*, *12*(2), 155–164.
Biot, M. A. (1955), Theory of elasticity and consolidation for a porous anisotropic solid, *J. Appl. Phys.*, *26*, 182–185.
Biot, M. A. (1972), Theory of finite deformations of porous solids, *Indiana Univ. Math. J.*, *21*, 597–620.
Biot, M. A. (1973), Nonlinear and semilinear rheology of porous solids, *J. Geophys. Res.*, 23, 4924–4937.
Bishop, A. W. (1959), The principle of effective stress, *Tek. Ukeblad*, *39*, 859–863.
Brooks, R. H., and A. T. Corey (1964), Hydraulic properties of porous media, *Hydrol. Pap. 3*, Colo. State Univ., Fort Collins.
Celia, M. A., and J. M. Nordbotten (2009), Practical modeling approaches for geological storage of carbon dioxide, *Ground Water*, *47*(5), 627–638, doi:10.1111/j.1745-6584.2009.00590.x.

Celia, M. A., J. M. Nordbotten, B. Court, M. Dobossy, and S. Bachu (2011), Field-scale application of a semi-analytical model for estimation of CO_2 and brine leakage along old wells, *Int. J. Greenhouse Gas Control*, *5*(2), 257–269, doi:10.1016/j.ijggc.2010.10.005.

Celia, M. A., S. Bachu, J. M. Nordbotten, and K. Bandilla (2015), Status of CO_2 storage in deep saline aquifers with emphasis on modeling approaches and practical simulations, *Water Resour. Res.*, *51*, 6846–6892, doi:10.1002/2015WR017609.

Class, H., et al. (2009), A benchmark study on problems related to CO_2 storage in geologic formations, *Comput. Geosci.*, *13*(4), 409–434, doi:10.1007/s10596-009-9146-x.

Corapcioglu, M. Y., and J. Bear (1983), A mathematical model for regional land subsidence due to pumping: 3. Integrated equations for a phreatic aquifer, *Water Resour. Res.*, *19*(4), 895–908.

Court, B., K. W. Bandilla, M. A. Celia, A. Janzen, M. Dobossy, and J. M. Nordbotten (2012), Applicability of vertical-equilibrium and sharp-interface assumptions in CO_2 sequestration modeling, *Int. J. Greenhouse Gas Control*, *10*, 134–147, doi:10.1016/j.ijggc.2012.04.015.

Deflandre, J.-P., A. Estublier, A. Baroni, J.-M. Daniel, and F. Adjémian (2011), In Salah CO_2 injection modeling: A preliminary approach to predict short term reservoir behavior, *Energy Procedia*, *4*, 3574–3581, doi:10.1016/j.egypro.2011.02.286.

Doster, F., J. M. Nordbotten, and M. A. Celia (2013), Impact of capillary hysteresis and trapping on vertically integrated models for CO_2 storage, *Adv. Water Resour.*, *62*, Part C, 465–474, doi:10.1016/j.advwatres.2013.09.005.

Durucan, S., J.-Q. Shi, C. Sinayuc, and A. Korre (2011), In Salah CO_2 storage JIP: Carbon dioxide plume extension around KB-502 well—New insights into reservoir behaviour at the In Salah storage site, *Energy Procedia*, *4*, 3379–3385, doi:10.1016/j.egypro.2011.02.260.

Elenius, M., D. Voskov, and H. Tchelepi (2015), Interactions between gravity currents and convective dissolution, *Adv. Water Resour.*, *83*, 77–88, doi:10.1016/j.advwatres.2015.05.006.

Ferrín, J. L., and A. Mikelić (2003), Homogenizing the acoustic properties of a porous matrix containing an incompressible inviscid fluid, *Math. Methods Appl. Sci.*, *26*(10), 831–859, doi:10.1002/mma.398.

Gasda, S. E., J. M. Nordbotten, and M. A. Celia (2011), Vertically averaged approaches for CO_2 migration with solubility trapping, *Water Resour. Res.*, *47*, W05528, doi:10.1029/2010WR009075.

Gemmer, L., O. Hansen, M. Iding, S. Leary, and P. Ringrose (2012), Geomechanical response to CO_2 injection at Krechba, In Salah, Algeria, *First Break*, *30*(2), 79–84.

Gor, G. Y., T. R. Elliot, and J. H. Prévost (2013), Effects of thermal stresses on caprock integrity during CO_2 storage, *Int. J. Greenhouse Gas Control*, *12*, 300–309, doi:10.1016/j.ijggc.2012.11.020.

Guo, B., K. W. Bandilla, F. Doster, E. Keilegavlen, and M. A. Celia (2014), A vertically integrated model with vertical dynamics for CO_2 storage, *Water Resour. Res.*, *50*(8), 6269–6284, doi:10.1002/2013WR015215.

Helmig, R. (1997), *Multiphase Flow and Transport Processes in the Subsurface: A Contribution to the Modeling of Hydrosystems*, Environ. Eng., Springer, Berlin.

Hesse, M. A., F. M. Orr, and H. A. Tchelepi (2008), Gravity currents with residual trapping, *J. Fluid Mech.*, *611*, 35–60.

Hunt, B. (1985), Flow to a well in a multiaquifer system, *Water Resour. Res.*, *21*(11), 1637–1641, doi:10.1029/WR021i011p01637.

Jaeger, J. C., N. G. W. Cook, and R. Zimmermann (2007), *Fundamentals of Rock Mechanics*, 4th ed., Wiley-Blackwell, Malden, Mass.

Lake, L. W. (1989), *Enhanced Oil Recovery*, Prentice Hall, Englewood Cliffs, N. J.

Lewis, R. W., and B. A. Schrefler (1998), *The Finite Element Method in the Static and Dynamic Deformation and Consolidation of Porous Media, Wiley Ser. Numer. Methods Eng.*, 2nd ed., John Wiley, N. Y.

Lide, D. R. (Ed.) (2003), *CRC Handbook of Chemistry and Physics*, 84th ed., CRC Press, Boca Raton, Fla.

Linstrom, P., and W. Mallard (Eds.) (2015), *NIST Chemistry WebBook, NIST Standard Reference Database Number 69*, Natl. Inst. of Stand. and Technol., Gaithersburg, Md.

Morris, J. P., Y. Hao, W. Foxall, and W. McNab (2011), A study of injection-induced mechanical deformation at the In Salah CO_2 storage project, *Int. J. Greenhouse Gas Control*, *5*(2), 270–280, doi:10.1016/j.ijggc.2010.10.004.

Mykkeltvedt, T. S., and J. M. Nordbotten (2012), Estimating convective mixing rates from commercial-scale CO_2 injection, *Environ. Earth Sci.*, *67*(2), 527–535, doi:10.1007/s12665-012-1674-3.

Nilsen, H. M., P. A. Herrera, M. Ashraf, I. Ligaarden, M. Iding, C. Hermanrud, K.-A. Lie, J. M. Nordbotten, H. K. Dahle, and E. Keilegavlen (2011), Field-case simulation of CO_2-plume migration using vertical-equilibrium models, *Energy Procedia*, *4*, 3801–3808, doi:10.1016/j.egypro.2011.02.315.

Nordbotten, J. M., and M. A. Celia (2006), An improved analytical solution for interface upconing around a well, *Water Resour. Res.*, *42*, W08433, doi:10.1029/2005WR004738.

Nordbotten, J. M., and M. A. Celia (2012), *Geological Storage of CO2: Modeling Approaches for Large-Scale Simulation*, 256 pp., John Wiley, Hoboken, N. J.

Nordbotten, J. M., and H. K. Dahle (2010), Impact of capillary forces on large-scale migration of CO_2, in *XVIII International Conference on Water Resources, CMWR 2010*, edited by J. Carrera, CIMNE, Barcelona, Spain.

Nordbotten, J. M., and H. K. Dahle (2011), Impact of the capillary fringe in vertically integrated models for CO_2 storage, *Water Resour. Res.*, *47*, W02537, doi:10.1029/2009WR008958.

Nordbotten, J. M., M. A. Celia, S. Bachu, and H. K. Dahle (2005), Semianalytical solution for CO_2 leakage through an abandoned well, *Environ. Sci. Technol.*, *39*(2), 602–611, doi:10.1021/es035338i.

Nordbotten, J. M., et al. (2012), Uncertainties in practical simulation of CO_2 storage, *Int. J. Greenhouse Gas Control*, *9*, 234–242, doi:10.1016/j.ijggc.2012.03.007.

Preisig, M., and J. H. Prévost (2011), Coupled multi-phase thermo-poromechanical effects. Case study: CO_2 injection at In Salah, Algeria, *Int. J. Greenhouse Gas Control*, *5*(4), 1055–1064, doi:10.1016/j.ijggc.2010.12.006.

Rice, J. R., and M. P. Cleary (1976), Some basic stress diffusion solutions for fluid-saturated elastic porous media with compressible constituents, *Rev. Geophys.*, *14*(2), 227–241.

Rinaldi, A. P., and J. Rutqvist (2013), Modeling of deep fracture zone opening and transient ground surface uplift at KB-502 CO_2 injection well, In Salah, Algeria, *Int. J. Greenhouse Gas Control*, *12*, 155–167, doi:10.1016/j.ijggc.2012.10.017.

Ringrose, P., A. Mathieson, I. Wright, F. Selama, O. Hansen, R. Bissell, N. Saoula, and J. Midgley (2013), The In Salah CO_2 storage project: Lessons learned and knowledge transfer, *Energy Procedia*, *37*, 6226–6236, doi:10.1016/j.egypro.2013.06.551.

Rutqvist, J., and O. Stephansson (2003), The role of hydromechanical coupling in fractured rock engineering, *Hydrogeol. J.*, *11*(1), 7–40.

Rutqvist, J., D. W. Vasco, and L. Myer (2010), Coupled reservoir-geomechanical analysis of CO_2 injection and ground deformations at In Salah, Algeria, *Int. J. Greenhouse Gas Control*, *4*(2), 225–230, doi:10.1016/j.ijggc.2009.10.017.

Shi, J.-Q., C. Sinayuc, S. Durucan, and A. Korre (2012), Assessment of carbon dioxide plume behaviour within the storage reservoir and the lower caprock around the KB-502 injection well at In Salah, *Int. J. Greenhouse Gas Control*, *7*, 115–126, doi:10.1016/j.ijggc.2012.01.002.

Vasco, D. W., A. Ferretti, and F. Novali (2008), Reservoir monitoring and characterization using satellite geodetic data: Interferometric synthetic aperture radar observations from the Krechba field, Algeria, *Geophysics*, *73*(6), WA113–WA122, doi:10.1190/1.2981184.

Wang, H. F. (2000), *Theory of Linear Poroelasticity With Applications to Geomechanics and Hydrology*, Princeton Univ. Press, Princeton, N. J.

Yan, W., S. Huang, and E. H. Stenby (2011), Measurement and modeling of CO_2 solubility in NaCl brine and CO_2 saturated NaCl brine density, *Int. J. Greenhouse Gas Control*, *5*(6), 1460–1477, doi:10.1016/j.ijggc.2011.08.004.

Yortsos, Y. C. (1995), A theoretical analysis of vertical flow equilibrium, *Transp. Porous Media*, *18*(2), 107–129, doi:10.1007/BF01064674.

9.3 Field-data analysis and hydromechanical modeling of CO_2 storage at In Salah, Algeria

Authors: **Tore I. Bjørnarå**, Bahman Bohloli and Joonsang Park.
Journal: Submitted to International Journal of Greenhouse Gas Control.

Appendix A

Papers, conference

Paper I: *Fast Evaluation of Fluid-rock Coupling in CO_2 Storage*

Fluid flow in a deforming media is a coupled process. Changes in fluid pressure affect the stress distribution in the porous media, causing it to deform, and vice versa, a deformation of the porous media affects the fluid pressure. It is not always desirable nor necessary to numerically solve both processes because of the computational cost and long solution time. How strong this coupling is, depends on the fluid pressure and fluid properties (e.g. density, viscosity and compressibility), hydraulic (e.g. porosity and permeability) and mechanical properties (e.g. stiffness and Poisson's ratio). When the coupling is weak, these processes can be considered separately, and the key to this decoupling is to implicitly capture the volumetric strain as accurately as possible without having to solve the mechanical processes. Many formulations for such decoupled equations can be found in the literature. Some of these simplifications were compared in a conceptual model that resembled the conditions of a typical CO_2-storage scenario, but with only single-phase fluid flow considered. The conceptual model illustrated an example where the mechanical process could be sufficiently captured by a uniaxial strain approximation and the two processes decoupled. A similar study is shown in chapter 4.2 to highlight the effect of various storage terms that arise from applying different assumptions on the mechanical behavior.

Paper II: *Capturing the Coupled Hydro-Mechanical Processes Occurring During CO_2 Injection - Example from In Salah*

This paper was a preview of the journal paper to follow in 2016 [25] where the theory is fully described. It was presented at the GHGT-12 conference in Austin, Texas (US).

History-matching field data from real applications with a numerical model often involve several model iterations at a high computation cost. This can be due to the complexity of the model geometry, level of details needed to accurately describe the problem, the number of unknown parameters or the parameter space can be large. To address this, a dimensionally reduced model was introduced that captures the key hydro-mechanical effects, while retaining a high accuracy when applied to realistic field data from In Salah.

The dimensional reduction implies here that the governing equations are integrated across the thickness of the reservoir (here in the vertical direction). For the fluid flow equations this means that the vertical pressure gradient is constant, hence the name vertical equilibrium (VE). To describe the poroelastic behavior, the poroelastic linear vertical deflection equations was used (PLVD) which assumes that the vertical strains are constant. This is thoroughly

described in the following paper [25], and here in this thesis, chapter 6.4 and 6.5.

The results from the dimensionally reduced model was compared to a fully resolved model to evaluate the performance. The full potential of the model was not known at the time and the reported saving in computational cost (36%) and computational speed-up factor (2.7) was very modest and conservative compared to results obtained in this thesis and by Bjørnaråa et al. [25] with speed-up of up to 20 times.

A.1 Fast Evaluation of Fluid-rock Coupling in CO_2 Storage

Authors: **Tore I. Bjørnarå**, Simon A. Mathias, Jan M. Nordbotten and Joonsang Park.
Conference paper: Fourth EAGE CO_2 Geological Storage Workshop 22-24. April 2014, Stavanger, Norway.

A.2 Capturing the Coupled Hydro-Mechanical Processes Occurring During CO_2 Injection - Example from In Salah

Authors: **Tore I. Bjørnarå**, Simon A. Mathias, Jan M. Nordbotten, Joonsang Park and Bahman Bohloli.
Conference/journal paper: GHGT-12 conference/Energy Procedia.

Available online at www.sciencedirect.com

ScienceDirect

Energy Procedia 63 (2014) 3416 – 3424

Energy Procedia

GHGT-12

Capturing the coupled hydro-mechanical processes occurring during CO_2 injection – example from In Salah

Tore Ingvald Bjørnarå[a,b,c,*], Simon A. Mathias[a], Jan M. Nordbotten[b], Joonsang Park[c], Bahman Bohloli[c]

[a]*Durham University, Dept. Earth Sciences, Durham, UK*
[b]*University of Bergen, Dept. of Mathematics, Bergen, Norway*
[c]*NGI, Dept. of Petroleum Geomechanics and Geophysics, Oslo, Norway*

Abstract

At In Salah, CO_2 is removed from the production stream of several natural gas fields and re-injected into a deep and relatively thin saline formation, in three different locations. The observed deformation on the surface above the injection sites have partly been contributed to expansion and compaction of the storage aquifer, but analysis of field data and measurements from monitoring has verified that substantial activation of fractures and faults occur. History-matching observed data in numerical models involve several model iterations at a high computation cost. To address this, a simplified model that captures the key hydro-mechanical effects, while retaining a reasonable accuracy when applied to realistic field data from In Salah, has been derived and compared to a fully resolved model. Results from the case study presented here show a significant saving in computational cost (36%) and a computational speed-up factor of 2.7.

Peer-review under responsibility of the Organizing Committee of GHGT-12

Keywords: CO_2 storage; In Salah; two-phase flow; poroelasticity; vertical equilibrium; linear vertical deflection

* Corresponding author. Tel.: +47 22023000; fax: +47 22230448.
E-mail address: tore.ingvald.bjornara@ngi.no

Peer-review under responsibility of the Organizing Committee of GHGT-12
doi:10.1016/j.egypro.2014.11.370

Nomenclature

b	Biot's coefficient, $b = 1 - K/K_s$, [-]
β, γ	fitting parameters in capillary pressure function: $p_d = \beta + \gamma$, [Pa]
c_α	compressibility of fluid phase α, [1/Pa]
ε_v	volumetric strain, [-]
$\mathbf{f}$	volumetric body load vector, [N/m^3]
ϕ	porosity, [-]
$\boldsymbol{g}$	gravity vector, [m/s^2]
$\mathbf{I}$	identity matrix, [-]
$\mathbf{k}$	permeability, [m^2]
$k_{r\alpha}$	relative permeability of phase α, [-]. Here: $k_{rn} = s_n^p$ and $k_{rw} = (1-s_n)^q$
K	bulk modulus of (drained) porous media, [Pa]
K_s	bulk modulus of solid grain, [Pa]
μ_α	viscosity of phase α, [Pa·s]
p_α	pressure of phase α, [Pa]
p_p	pore pressure, [Pa]
p_c	capillary pressure, phase pressure difference; $p_c = p_n - p_w$, [Pa]
p_d	entry pressure, pressure required for non-wetting phase to intrude wetting phase, [Pa]
p, q	fitting parameters (exponent) for the power-law relative permeability functions $k_{r\alpha}$, [-]
$\mathbf{q}_\alpha$	Darcy flux of phase α, [m/s]
ρ_α	density of phase α, [kg/m^3]
s_α	saturation of phase α, [-]
$\boldsymbol{\sigma}$	total stress tensor, [Pa]
$\boldsymbol{\sigma}'$	effective stress, [Pa]
t	time, [s]
$\mathbf{v}_\alpha$	velocity of fluid phase α, [m/s]
$\mathbf{v}_s$	velocity of solid phase, [m/s]

1. Introduction

At In Salah, CO_2 is removed from the production stream of several natural gas fields and re-injected into a deep and relatively thin saline formation, approximately 20 meters thick, at about 1800 meters below surface. CO_2 is injected into three locations; wells KB-501, -502 and -503, and the injection has been actively monitored. Of particular interest are the InSAR-surveys, that monitors the surface deformation, and tracers in the injected CO_2, that allows detection of the injected CO_2 in monitoring wells. The InSAR-data has revealed a surface heave rate of up to 5 mm/year on all the three injection wells, and a corresponding subsidence at the gas-producing wells of about 2 mm/year [11].

Due to the relatively poor hydraulic properties of the aquifer, 1-1.5 km long horizontal injection wells are used to ensure adequate injection rates and approximately 0.6 Mton CO_2 is sequestered per year all together [5]. The surface heave/subsidence is caused primarily due to expansion/compaction of the aquifer/reservoir caused by the CO_2 injection/gas production [8]. However, at injection well KB-502 there are two distinctive lobes in the heave pattern at the surface that have caught a lot of attention as to how this can be explained. It was suggested early that this was due to a long structural discontinuity; a non-sealing fault/fracture system, that is activated by tensile strains [13,15,17] due to its orientation in line with the direction of the maximum horizontal stress (a strike-slip stress regime [6,8]). Tracers in the injected CO_2 at KB-502 also showed up in a monitoring well (KB-5) about three times faster than what would have occurred with an homogeneous cylindrical plume [14], again, indicating a highly permeable pathway in line with the strike-slip stress regime. And, indeed such a fault/fracture system (labelled F12) was later confirmed by updated seismic surveys and further supported by numerical modeling studies [13,15,17]. F12 cuts through the aquifer, but how far it extends in the vertical direction is not well constrained. Modeling has suggested that it may be confined within the aquifer [13] or that it may extend into the lowermost part of the overburden [9,15].

In all the injection wells the formation bottom hole pressure (FBHP) may exceed the fracture pressure of the aquifer [3]. Analysis of the injectivity index (volumetric injection rate of CO_2 versus FBHP) indicates that fractures are activated/deactivated during injection, depending on increasing/decreasing injection rate, respectively, and this is particularly the case for KB-501 and -502 [3]. Several authors, eg. [3,13,17], have history-matched the bottom hole pressure with numerical models and have obtained very good fits with measured surface heave. However, as observed from the injectivity index analysis, for wells KB-501 and -502 it is necessary to mimic the activation of fractures by introducing a transient permeability, to the aquifer, and transmissibility of the fault system F12. This dynamic behavior is consistent with stress analysis (related to fracture pressure) and field observations [17]. Also, the subsurface at In Salah has a layered structure, but how many distinctive layers that is used in the literature varies, along with the hydraulic and mechanical properties of the aquifer, F12, caprock and over- and underburden.

This variation in model realizations encountered in the literature shows that there are many possible explanations to the observed measurements. However, it often requires many model iterations to find a good fit between modelled and measured data, which can be computationally very expensive and time consuming. To address this, we have in this study applied the assumption that the thickness of the storage aquifer is much smaller than both the lateral extent of the aquifer and the length-scale of interest, to derive a simplified model that captures the key hydro-mechanical effects. The goal is to derive a computationally efficient, yet accurate, model that can be used in analysis where large numbers of simulations are required. The simplified model is compared with a fully resolved synthetic CO_2 injection model, based on conditions in In Salah, to see how well it performs in terms of accuracy and computational cost and time.

2. Modeling approaches

The geomechanical effects related to CO_2 injection at In Salah are analyzed through fully coupled modeling approaches to simulate simultaneously CO_2 migration in the aquifer and the poroelastic stress changes during injection.

In the first approach, a fully resolved model where the complete geometry is discretized and the governing equations for two-phase immiscible fluid flow in porous media (with capillary pressure) and poroelasticity (using Biot's linear theory of poroelasticity) are solved using the finite element method. The critical area, in terms of numerical resolution, is the aquifer where the CO_2 is injected and a dense numerical discretization is required to capture its migration and distribution to a sufficient accuracy.

In the second approach, a simplified description of the physical processes in the aquifer is derived using the method of reduction of dimensionality. It involves integrating the governing equations over the thickness of the aquifer, transforming relevant variables and equations into integrated and averaged quantities and equations that are only functions of spatial variables on a plane. This reduces the computational cost by reducing the number of degrees of freedom (DOF) needed to be solved.

For two-phase flow, reduction of dimensionality involves integrating the fluid mass conservation equations to obtain the Vertical Equilibrium (VE) equations, see eg. Nordbotten and Dahle [10]. The assumption for VE is that the vertical flow can be ignored (is zero), implying that the vertical pressure gradient is static (in vertical equilibrium) and proportional to the specific gravity of the pore fluid. For the poroelasticity, it involves integrating the momentum balance equation to obtain the poroelastic Linear Vertical Deflection (PLVD) equation. The assumptions for PLVD is that (i) the vertical momentum is zero, (ii) the in-plane displacement components are constant across the thickness of the aquifer and (iii) the out-of-plane displacement component varies linearly. The PLVD equation is similar to the ones obtained by Bear and Corapcioglu [1], however, here we treat the aquifer as an embedded region in a fully three dimensional environment, accounting for the full stress tensor in the over- and underlying layers, and extend the pore fluid to also include two phases [4].

In this study, the performance of the two approaches are compared, and the applicability of the simplified model is demonstrated on realistic field data from In Salah. Wells KB-501 and -503 behaves more predictable compared to KB-502, as they do not show a similar critical feature like fault 12 at KB-502. However, KB-501 also show fracture activation [3], so the focus will be on well KB-503.

3. Governing equations

The physics related to CO_2 injection into subsurface can be described by the momentum balance equation under quasi-static conditions (neglecting inertial terms) and the mass conservation equations of two-phase fluid (brine and CO_2) which are given in the following form:

$$\nabla \cdot \boldsymbol{\sigma} + \mathbf{f} = 0 \tag{1}$$

$$\frac{\partial(\phi \rho_\alpha s_\alpha)}{\partial t} + \nabla \cdot (\phi \rho_\alpha s_\alpha \mathbf{v}_\alpha) = 0 \tag{2}$$

The Darcy flux vector $\mathbf{q}_\alpha$ in a deforming medium is defined as:

$$\mathbf{q}_\alpha = s_\alpha \phi (\mathbf{v}_\alpha - \mathbf{v}_s) = -\frac{\mathbf{k}}{\mu_\alpha} k_{r\alpha} (\nabla p_\alpha - \rho_\alpha \mathbf{g}) \tag{3}$$

The effective stress $\boldsymbol{\sigma}'$ is defined as the part of the total stress $\boldsymbol{\sigma}$ that governs the deformation, and using the concept of Terzaghi effective stress, Biot [2] modified the normal elastic stress terms in the momentum balance equation so the total stress term in Eq. (1) can be written as:

$$\boldsymbol{\sigma} = \boldsymbol{\sigma}' + b p_p \mathbf{I} \tag{4}$$

By inserting Eq. (3) into Eq. (2) and rearranging (following the procedure of Pinder [12], considering the relations for change in porosity and change in volumetric strain [18, chapter 1 and 4] and using the mass conservation equation for the solid phase) a familiar equation can be obtained for the mass conservation equation for phase α:

$$\phi \rho_\alpha \frac{\partial s_\alpha}{\partial t} + \phi s_\alpha \rho_\alpha c_\alpha \frac{\partial p_\alpha}{\partial t} + s_\alpha \rho_\alpha \left[\frac{(b - \phi)}{K_s} \frac{\partial p_p}{\partial t} - b \frac{\partial \varepsilon_v}{\partial t} \right] + \nabla \cdot (\rho_\alpha \mathbf{q}_\alpha) = 0 \tag{5}$$

It can be seen that Eq. (5) is the same flow equation obtained by Biot [2] for a single-phase fluid by inserting that $s_\alpha = 1$ and using that, in the context of multiphase flow, the pore pressure p_p in Eqs. (4) and (5) is defined as the saturation-weighted average of the phase pressure; $p_p = s_w p_w + s_n p_n$.

In Eq. (5) there are four dependent variables; s_w, p_w, s_n *and* p_n, but only two conservation equations, so two of the variables can be eliminated by applying the constraint for a fully saturated rock: $s_w + s_n = 1$, and by introducing the capillary pressure p_c defined as the difference between the phase pressures; $p_c = p_n - p_w$. Here p_c is a Brooks and Corey-type function of the non-wetting saturation s_n:

$$p_c(s_n) = \beta (1 - s_n)^{-1/2} + \gamma \tag{6}$$

Eqs. (1) and (5) are the governing equations that are solved with appropriate boundary conditions described in the next section. Since the aquifer is considered essentially horizontal, the equivalent governing equations for the dimensionally reduced model, using the VE and PLVD assumptions, are the same equations integrated in the vertical direction from the bottom to the top of the aquifer, see Bjørnarå et al. [4] for details.

4. Case study: CO_2 injection at KB-503 in In Salah, Algeria

Here we simulate numerically a simplified version of the CO_2 injection at KB-503 in In Salah, Algeria as our case study to compare the fully resolved solution with the dimensionally reduced model. The case model is inspired by Rutqvist et al. [16], but instead of solving it in three dimensions a plane strain (2D) model is solved where a symmetry plane is defined perpendicular to the horizontal injection line, see Figure 1 (left) for geometry.

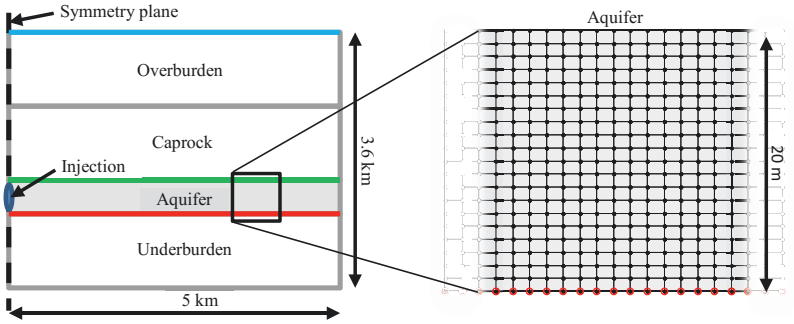

Fig. 1. Left: Geometry sketch of KB-503 injection site in In Salah, Algeria. The colored lines (red, green and blue) indicate the surfaces where the vertical displacement is plotted in Figure 2. Right: Finite element mesh in the aquifer used in the fully resolved model (black dots) and the dimensionally reduced model (red circles).

The model is 3.6 km deep and 5 km wide, which corresponds to 10 km due to the symmetry plane. The CO_2 is injected into a 20 m thick aquifer between a stiff and low permeable mudstone underburden and a carboniferous caprock. The overburden is a low permeable layer consisting of softer cretaceous sandstone and mudstone. The boundaries to the right have a constant pressure value corresponding to initial hydrostatic pressure and no horizontal displacement. The bottom boundary has no-flow conditions and no vertical displacement, and the top boundary has a constant fluid pressure and zero traction. Symmetry boundary conditions are applied to the left boundaries.

The first seven years of injection is simulated with a constant injection rate of 729 ton CO_2 /day. For a 1.5 km long horizontal injection line, this corresponds to $5.62 \cdot 10^{-3}$ kg/m/s (kg/s CO_2 per meter length of the well). It should be noted that in the fully resolved model the CO_2 is injected along the whole height of the reservoir. In the real application is it injected along a horizontal pipeline, perpendicular to the model plane and should, more appropriately, be modelled as a point source in this plane symmetric model. However, here the length scale of interest is much larger than the near well-bore scale and the aim is to compare the performance of the two approaches. Further, we assume isothermal conditions, no hysteresis in the capillary pressure function and no residual saturation of any of the phases.

Some key material properties are given in Tables 1 and 2. The density of the solid material and Biot's coefficient b is 2200 kg/m^3 and 0.7 in all layers, respectively, and the entry pressure p_d for the aquifer is $0.9 \cdot 10^5$ Pa.

Table 1. Mechanical properties used in the case study of KB-503.

Material property	Overburden (0-900m)	Caprock (900-1800m)	Aquifer (1800-1820m)	Underburden (below 1820m)
Youngs modulus, E [GPa]	1.5	20	6	20
Poisson's ratio, ν [-]	0.2	0.15	0.2	0.15
Porosity, ϕ [-]	0.1	0.01	0.17	0.01
Permeability, k [m^2]	$1 \cdot 10^{-17}$	$1 \cdot 10^{-19}$	$13 \cdot 10^{-15}$	$1 \cdot 10^{-19}$

Table 2. Fluid and fluid flow properties for brine and CO_2.

Brine			CO_2		
Density, ρ_w [kg/m^3]	Viscosity, μ_w [Pa·s]	Compressibility, c_w [1/Pa]	Density, ρ_n [kg/m^3]	Viscosity, μ_n [Pa·s]	Compressibility, C_n [1/Pa]
997	$5.5 \cdot 10^{-4}$	$4.19 \cdot 10^{-10}$	784	$6.9 \cdot 10^{-5}$	$1.56 \cdot 10^{-8}$

Here we apply the dimensional reduction approach to the aquifer, hence it is defined to be semi-confined; water is allowed to leave/enter the aquifer whereas the CO_2 is confined. Thus, the two-phase flow is limited to the aquifer, and in the rest of the model only brine is displacing.

As mention earlier, the motivation to derive an integrated poroelastic two-phase flow formulation is to save degrees of freedom and save computational time. In order to compare the performance between the fully resolved model and dimensionally reduced model a comparable mesh is used, see Figure 1 (right). In this particular case, the fully resolved model has 211 kDOFs while the reduced model has 135 kDOFs, a saving of 36% in computational cost. In computational time, the reduced model solves 2.7 times faster compared to the fully resolved model (or 36% of the solving time of the fully resolved model). Note that a lower resolution is feasible, in both cases, but for the sake of getting a nicely resolved solution, a fairly dense mesh is used.

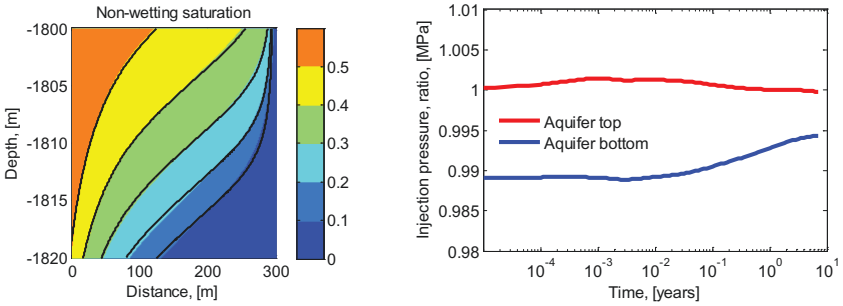

Fig. 2. Left: CO_2 saturation in aquifer after seven years of injection. Solid lines are the corresponding contour lines for the saturation calculated in the dimensionally reduced model. Note that the axis are not to scale. Right: Injection pore pressure ratio; reduced/fully resolved.

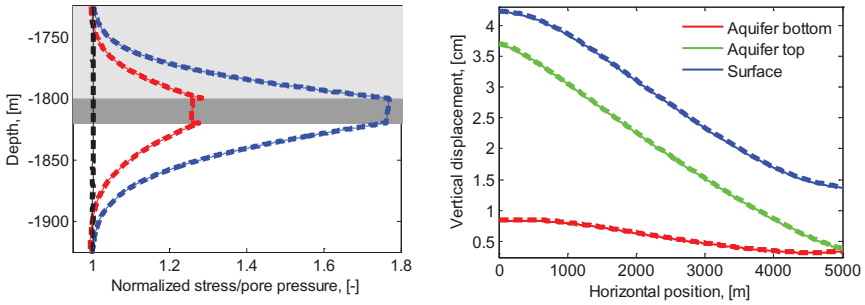

Fig. 3. Left: Vertical profiles of various normalized stress components (normalized to initial values) measured 100 meters away from the symmetry line. Black: vertical stress. Red: horizontal stress. Blue: Pore pressure. Dark gray area indicates the reservoir. Right: Vertical displacement along the bottom of the aquifer (red line), top of aquifer (green line) and surface (surface heave, blue line), cf. Figure 1 (left). In both figure the thin lines are from the simplified model and thick dashed lines are for the fully resolved model.

The saturation profile after seven years of injection for the two approaches are compared in Figure 2 (left) where the colors represent the CO_2 saturation in the fully resolved model and the black lines are the equivalent saturation contour lines for the reduced approach. It can be seen that the reduced model is capable of accurately capturing the CO_2 distribution in the aquifer. In general, the applicability of the reduced approach presented here depends on both the length- and time-scale of interest. For conditions close to the injection point/line, or at short times, the accuracy deteriorates as the underlying assumptions are violated. The match in saturation depends on how fast the phases segregate vertically, and for the dimensionally reduced model; the faster the better. Hence, for very short simulation times, in locations close to the injection point, and if the density difference between the two phases is low or the permeability in the aquifer becomes too low, the VE assumption may no longer be fully justified. However, in the realistic (and challenging) case simulated here, it is well within a very good approximate solution. In Figure 2 (right) the ratio of the pore pressure at the injection point at the top and bottom of the aquifer for the two models are shown, it is close to 1 for the entire simulation time (7 years). The results for the vertical displacement along the faces of the aquifer top and -bottom and the surface in Figure 3 (right) and the Vertical profiles of various normalized stress components (normalized to initial values) in Figure 3 (left) are coinciding for the two approaches.

The limit for the applicability of the reduced approach is case dependent and has not been investigated here. However, it appears (not shown here) that the critical assumption in the dimensionally reduced approach is the VE-assumption, as the poroelastic effect is little affected by mismatch in the saturation profile. The applicability of the VE assumption has been investigated by others, see eg. Court et al. [7].

In this study the simplified model approach through dimensional reduction has proved promising in providing significant savings in computational cost and time (2.7 times faster) when faced with a large number of simulations. It has also been demonstrated that such models can retain reasonable accuracy when applied to realistic field data, such as the conditions at In Salah.

Acknowledgements

The authors are thankful to the following sponsors for the financial support of this work: Research Council of Norway (through the MatMoRA-II project 215641, Mathematical Modeling and Risk Assessment of CO_2 storage), Statoil ASA, University of Bergen, Durham University and Norwegian Geotechnical institute (NGI).

References

[1] Bear J, Corapcioglu MY. Mathematical Model for Regional Land Subsidence Due to Pumping. 2. Integrated Aquifer Subsidence Equations for Vertical and Horizontal Displacements. Water Resources Research, 17(4):947–958, August 1981.

[2] Biot MA. General theory of three-dimensional consolidation. Journal of Applied Phsyics, 12(2):155–164, 1941.

[3] Bissell RC, Vasco DW, Atbi M, Hamdani M, Okwelegbe M, Goldwater MH. A full field simulation of the In Salah gas production and CO_2 storage project using a coupled geo-mechanical and thermal fluid flow simulator. Energy Procedia, 4(0):3290 – 3297, 2011. 10th International Conference on Greenhouse Gas Control Technologies.

[4] Bjørnarå TI, Nordbotten JM, Mathias SA, Park J, Vertically Integrated Models For Coupled Flow and Deflection in Porous Media, submitted.

[5] Cavanagh A, Ringrose P. In salah high-resolution heterogeneous simulations of CO_2 storage. Search and Discovery Article #80092, July 2010.

[6] Cavanagh A, Ringrose P. Simulation of CO_2 distribution at the In Salah storage site using high-resolution field-scale models. Energy Procedia, 4(0):3730 – 3737, 2011. 10th International Conference on Greenhouse Gas Control Technologies.

[7] Court B, Bandilla KW, Celia MA, Janzen A, Dobossy M, Nordbotten JM, Applicability of vertical-equilibrium and sharp-interface assumptions in CO_2 sequestration modeling, International Journal of Greenhouse Gas Control, 10(0):134-147, 2012

[8] Durucan S, Shi J-Q, Sinayuc C, Korre A. In salah CO_2 storage JIP: Carbon dioxide plume extension around KB-502 well-new insights into reservoir behaviour at the In Salah storage site. Energy Procedia, 4(0):3379 – 3385, 2011. 10th International Conference on Greenhouse Gas Control Technologies.

[9] Gemmer L, Hansen O, Iding M, Leary S, Ringrose P. Geomechanical response to CO_2 injection at krechba, In Salah, Algeria. First Break, 30(2):79–84, February 2012.

[10] Nordbotten JM, Dahle HK. Impact of capillary forces on large-scale migration of CO_2. In J. Carrera, editor, 18th Conference on Computational Methods for Water Resources, Barcelona, Spain, 2010.

[11] Onuma T, Okada K, Otsubo A. Time series analysis of surface deformation related with CO_2 injection by satellite-borne SAR interferometry at In Salah, Algeria. Energy Procedia, 4(0):3428 – 3434, 2011. 10th International Conference on Greenhouse Gas Control Technologies.

[12] Pinder GF, Gray WG. Essentials of Multiphase Flow and Transport in Porous Media. John Wiley & Sons, Inc., Hoboken, NJ, USA, 2008.

[13] Rinaldi AP, Rutqvist J. Modeling of deep fracture zone opening and transient ground surface uplift at KB-502 CO_2 injection well, In Salah, Algeria. International Journal of Greenhouse Gas Control, 12(0):155 – 167, 2013.

[14] Ringrose P, Atbi M, Mason D, Espinassous M, Myhrer Ø, Iding M, Mathieson A, Wright I. Plume development around well KB-502 at the In Salah CO_2 storage site. First Break, 27(1):85–89, January 2009.

[15] Rutqvist J, Liu H-H, Vasco DW, Pan L, Kappler K, Majer E. Coupled non-isothermal, multiphase fluid flow, and geomechanical modeling of ground surface deformations and potential for induced micro-seismicity at the In Salah CO_2 storage operation. Energy Procedia, 4:3542–3549, 2011.

[16] Rutqvist J, Vasco DW, Myer L. Coupled reservoir-geomechanical analysis of CO_2 injection and ground deformations at In Salah, Algeria. International Journal of Greenhouse Gas Control, 4(2):225–230, 2010. The Ninth International Conference on Greenhouse Gas Control Technologies.
[17] Shi J-Q, Sinayuc C, Durucan S, Korre A. Assessment of carbon dioxide plume behaviour within the storage reservoir and the lower caprock around the KB-502 injection well at In Salah. International Journal of Greenhouse Gas Control, 7(0):115–126, 2012.
[18] Zimmerman RW. Compressibility of Sandstones. Elsevier, Amsterdam, 1991.

Appendix B

Equation of State

Detailed data for the equation of state of water and CO_2 can be obtained from the online NIST database [65]. NIST (National Institute of Standards and Technology) was founded in 1901 and is a part of the U.S. Department of Commerce. Here we present the material properties of water and CO_2 in terms of temperature and pressure and some typically used simplifications used in the literature. Mavko et al. [71] is also a good reference for analytical expressions for brine (with varying salinity) and CO_2, but here we use the NIST-dataset.

It should be noted that the properties presented here are for pure substances and can be highly influenced by salinity (increases density of water [71]) and other impurities, e.g. methane (decreases density of supercritical CO_2 [115]). Detailed analysis should evaluate the importance of impurities.

B.1 NIST-dataset

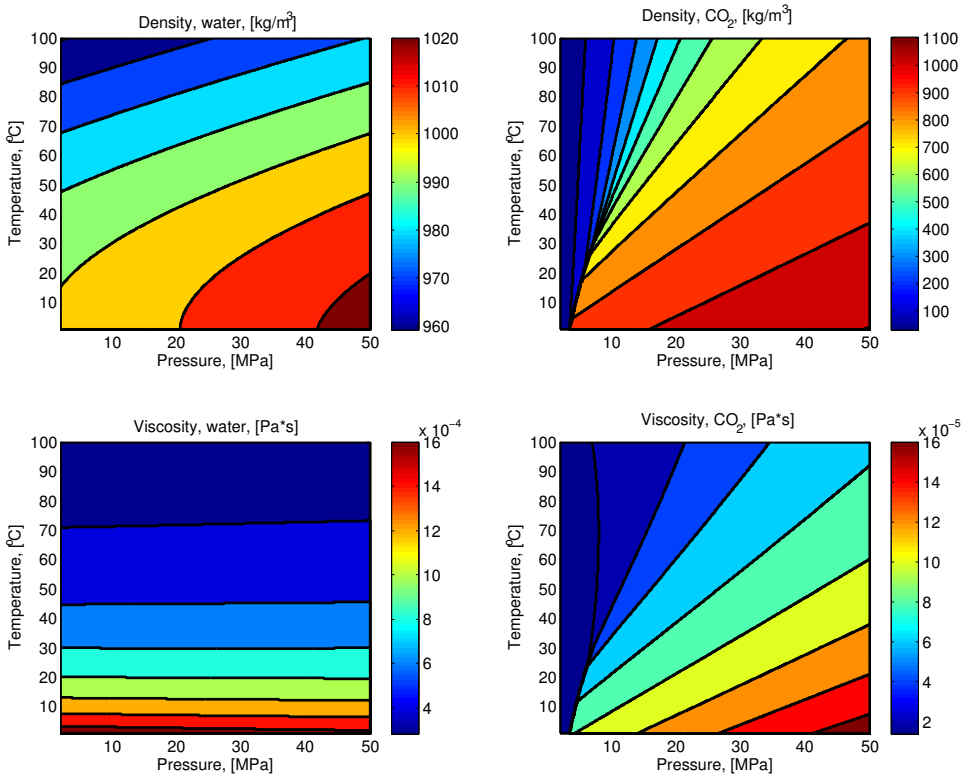

Figure B.1: Density and viscosity of water (left) and CO_2 (right) as function of pressure and temperature.

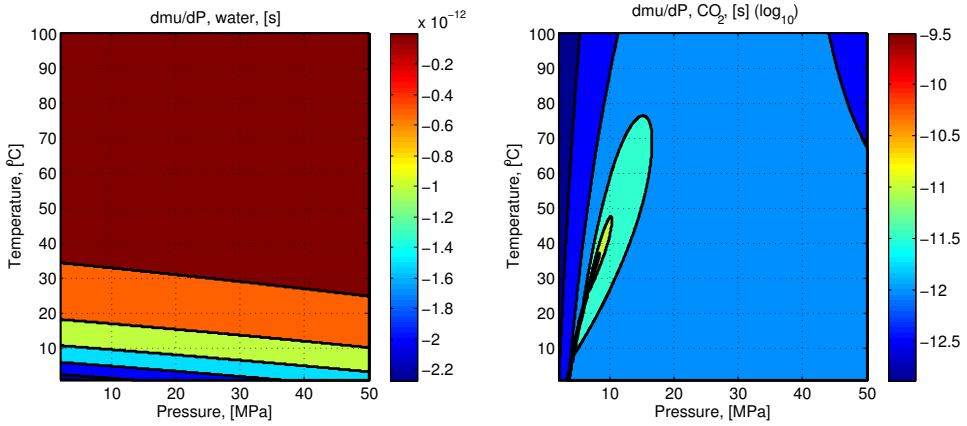

Figure B.2: Pressure dependency on viscosity of water (left) and CO_2 (right) as function of pressure and temperature.

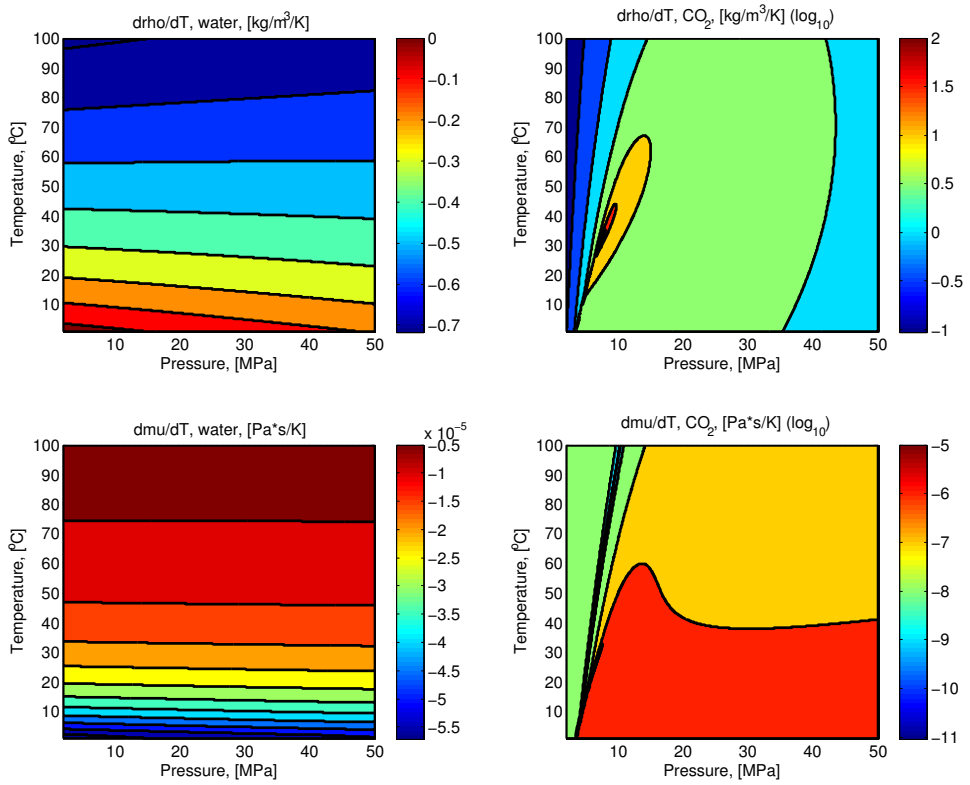

Figure B.3: Temperature dependency on density and viscosity of water (left) and CO_2 (right) as function of pressure and temperature.

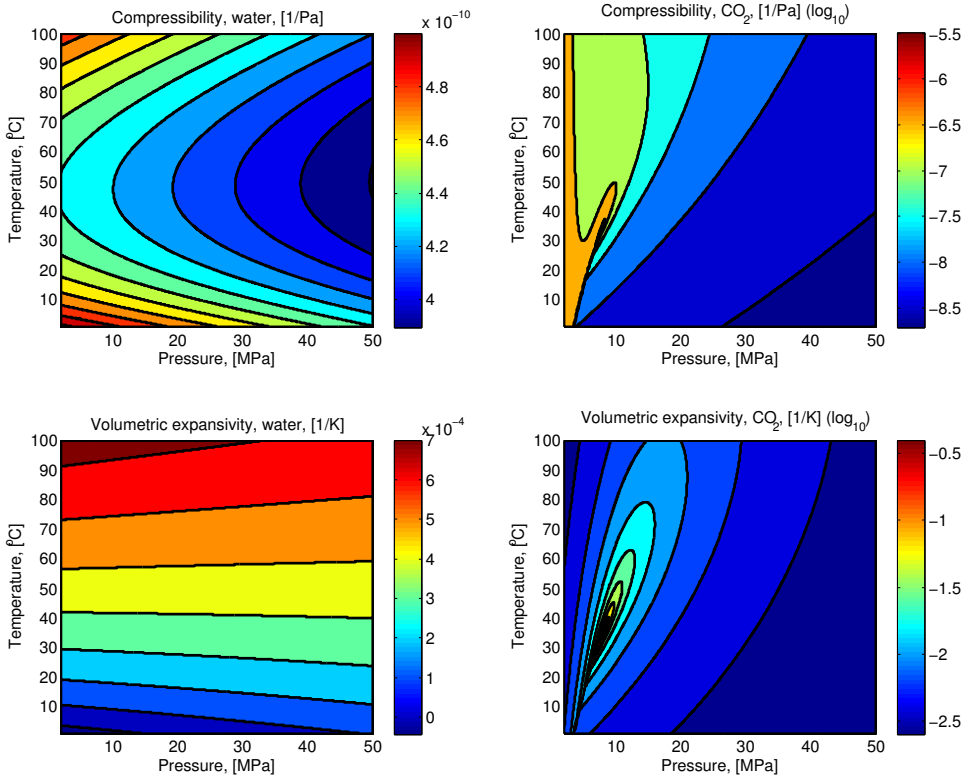

Figure B.4: Compressibility and volumetric expansivity of water (left) and CO_2 (right) as function of pressure and temperature.

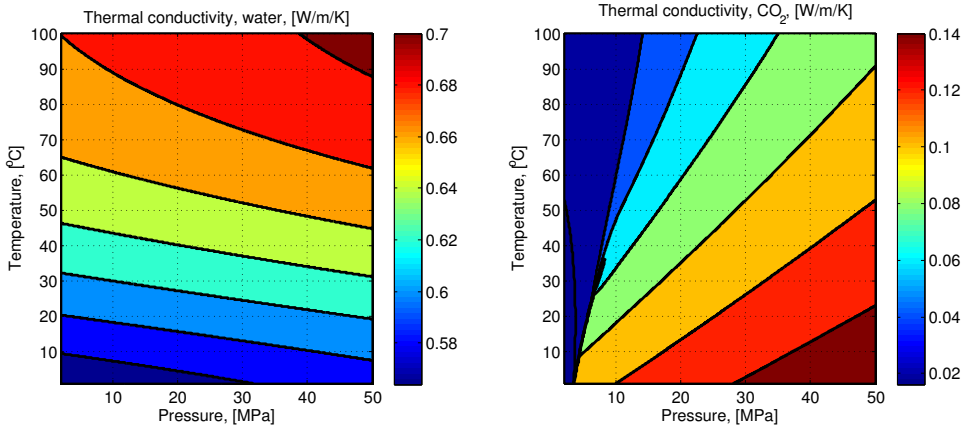

Figure B.5: Thermal conductivity of water (left) and CO_2 (right) as function of pressure and temperature.

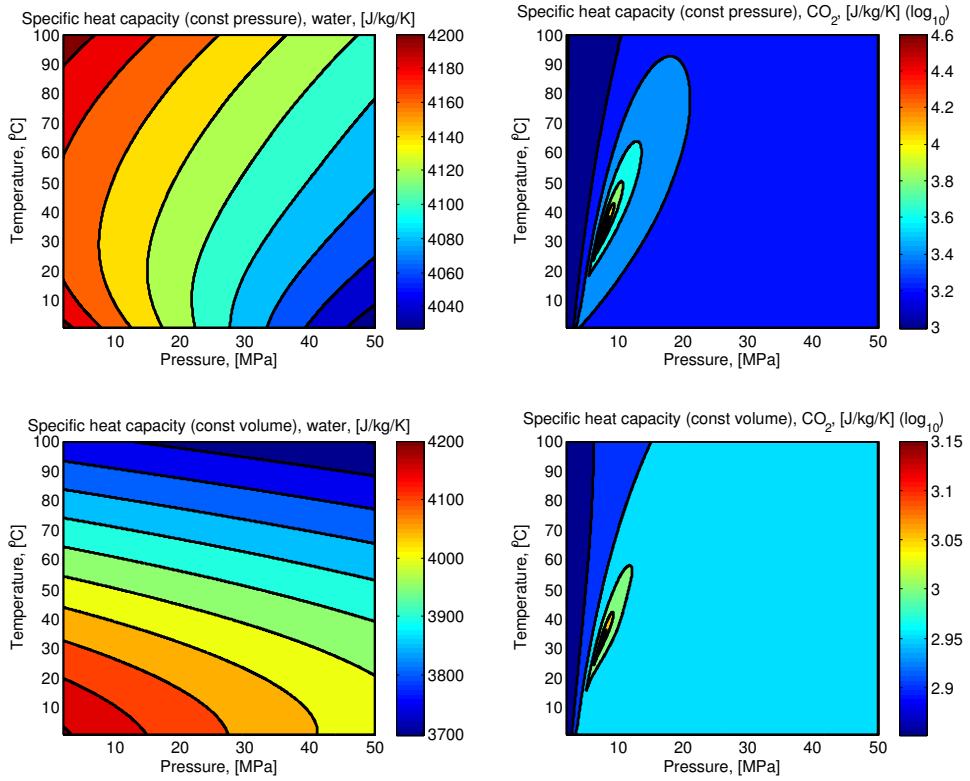

Figure B.6: Heat capacity at constant pressure and volume for water (left) and CO_2 (right) as function of pressure and temperature.

For water, a constant compressibility can often be assumed, for CO_2 it is necessary to be more cautious, see Fig. B.7.

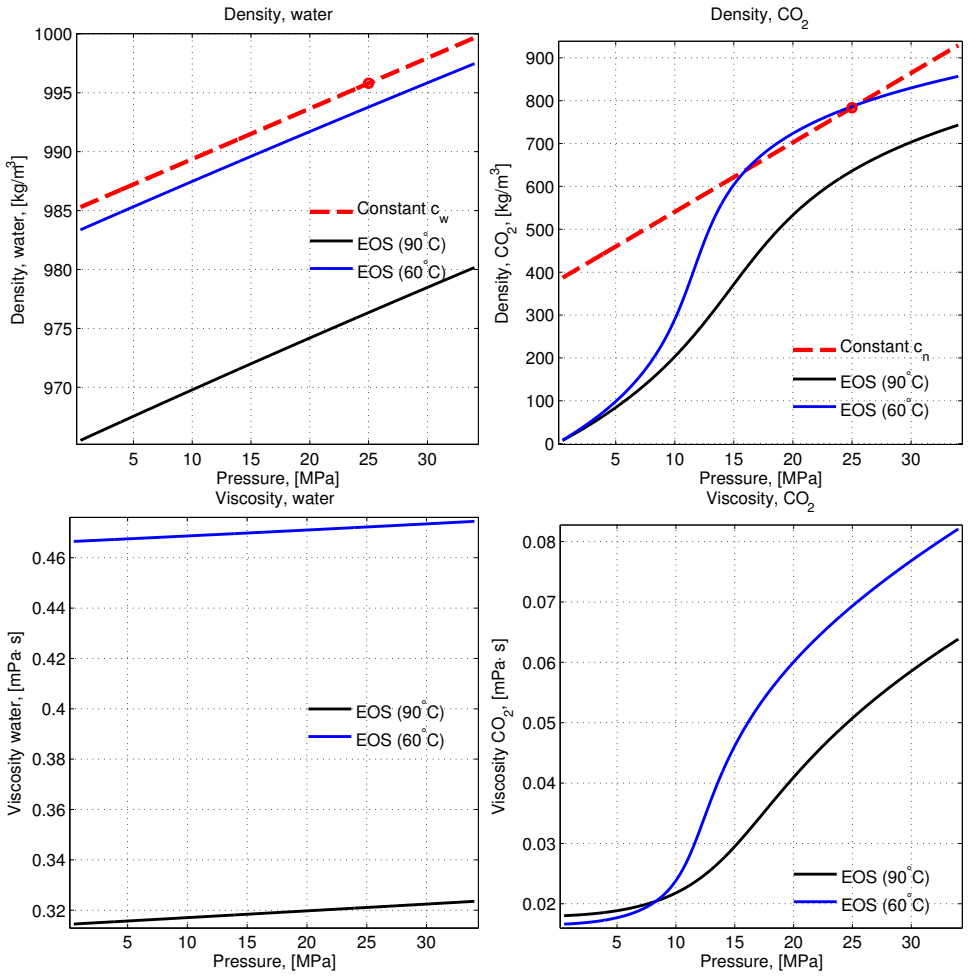

Figure B.7: Density and viscosity of water and CO_2 at 60°C and 90°C for various pressures. For density only: The red dashed lines shows the linearized density values based on compressibility ($4.39 \cdot 10^{-10}$1/Pa and $2.55 \cdot 10^{-8}$1/Pa) and thermal expansivity ($6.65 \cdot 10^{-4}$1/K and $7.73 \cdot 10^{-3}$1/K) at $p_0 = 25$MPa and $T = 90$°C for water and CO_2 (respectively), from the linearized expression for density: $\rho_\alpha = \rho_\alpha^0 (1 + c_\alpha \Delta p_\alpha - \beta_\alpha \Delta T)$. Also, the expansion coefficient is not constant with temperature, thus the approximated red-dashed line deviates slightly from the blue line. Better approximations can be obtained by using more appropriate values for compressibility and expansivity.

In Figs. B.8 and B.9 some material properties are plotted as function of depth for water and CO_2, respectively. The pressure profile is assumed to be linear with depth and with slope of $-1000g$. The surface temperature is 10°C and three profiles are shown for various constant temperature gradient. The grey shaded area indicates the location of two reservoirs: 1770-1800 m below surface (In Salah) and 800-1100 m below surface (Sleipner).

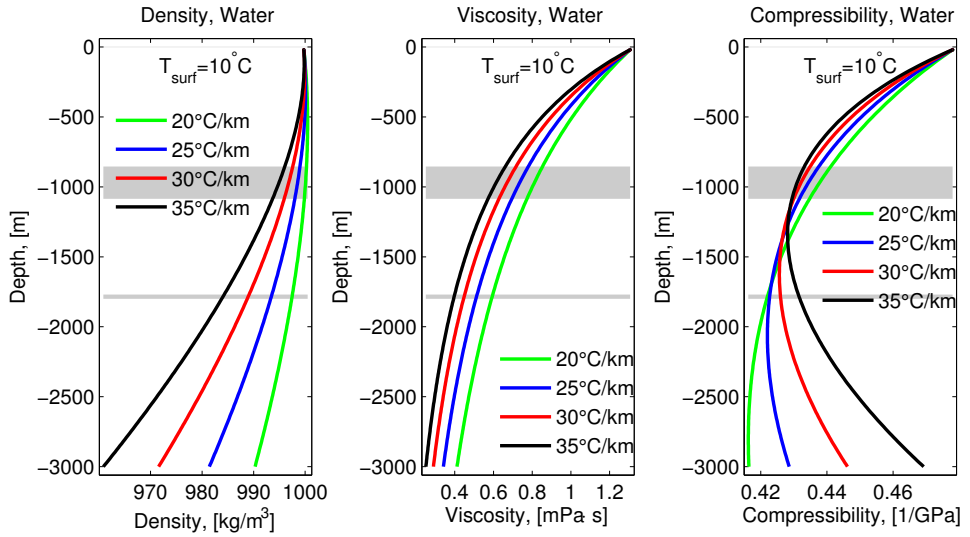

Figure B.8: Material properties for water as a function of depth, assuming a linear hydrostatic pressure profile proportional to $1000g$ and a surface temperature of $T = 10°C$. The grey shaded area indicates the location of a reservoir between 1770-1800 m below surface (In Salah) and 800-1100 m below surface (Sleipner).

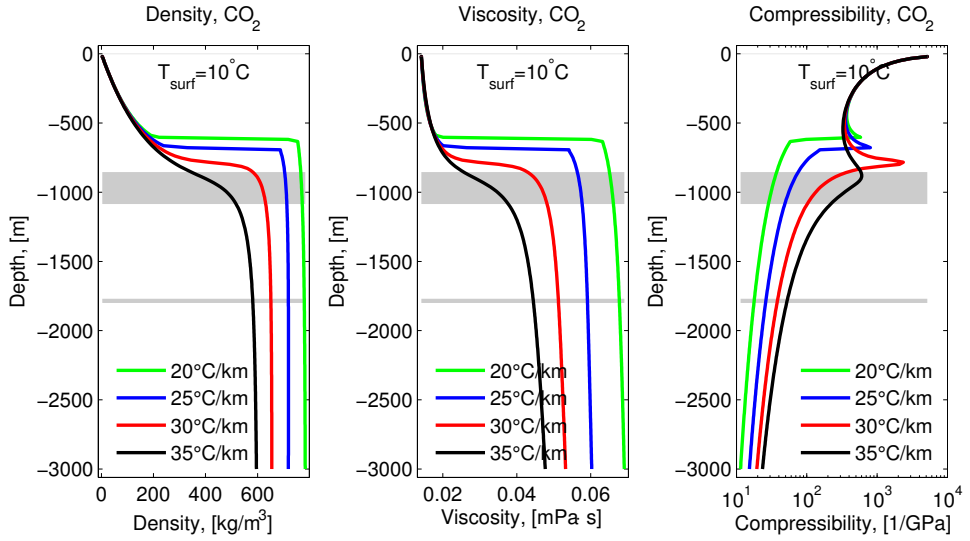

Figure B.9: Material properties for CO_2 as a function of depth, assuming a linear hydrostatic pressure profile proportional to $1000g$ and a surface temperature of $T = 10°C$. The grey shaded area indicates the location of a reservoir between 1770-1800 m below surface (In Salah) and 800-1100 m below surface (Sleipner).

B.2 Phase diagram of carbon dioxide

In Fig. B.10 a phase diagram for CO_2 is shown. Beyond the critical point (at 31.3°C and 7.39 MPa) the CO_2 is in a supercritical state where the vapor phase and liquid phase merge into one single phase: super critical phase. This is of importance to CO_2 storage, because the density and viscosity increases dramatically, allowing more CO_2 to be stored in the available pore space and the CO_2 displaces the formation water/brine more effectively (less fingering). In terms of modeling, it introduces the benefit that one only need to consider one phase; super critical, instead of a liquid and a vapor phase. Based on the critical pressure (7.39MPa), the super critical state occurs around 750 meters depth below the water table.

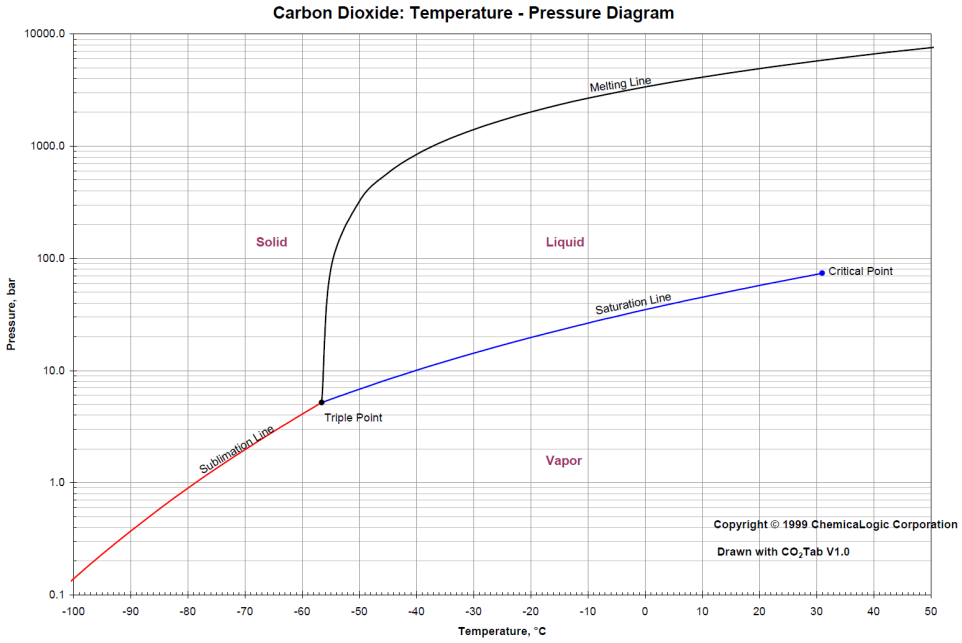

Figure B.10: Phase diagram for CO_2 (Copyright ©1999 ChemicaLogic Corporation, 99 South Bedford Street, Suite 207, Burlington, MA 01803 USA. All rights reserved). Critical point for CO_2 is 31.3°C and 7.39 MPa.

B.3 Effect of salinity

The solubility of CO_2 in water and brine varies with salinity, pressure and temperature. Duan and Sun [42] presented a mathematical model to calculate the solubility of CO_2 in water and brine at various salinity for temperatures ranging between 0-260 °C and pressure ranging between 0-2000 bar, se Fig. B.11. The figure also indicates the salinity at In Salah, Krechba formation (175 g/L water, Trémosa et al. [113]) and at Sleipner, Utsira formation (33.5 g/L water, Cavanagh [30]).

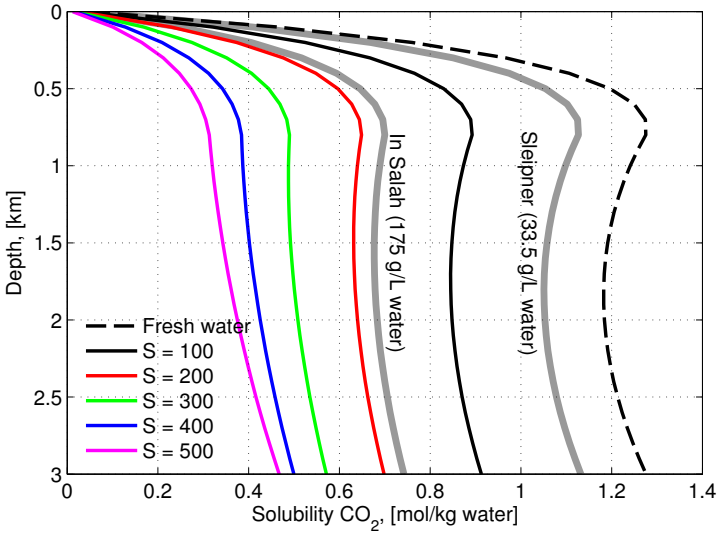

Figure B.11: Solubility of CO_2 at various salinity ([mol/kg water]). The salinity at In Salah, Krechba formation (175 g/L water (175000 ppm), Trémosa et al. [113]) and at Sleipner, Utsira formation (33.5 g/L water, 33500 ppm, Cavanagh [30]). The Solubility is calculated using the formula by Duan and Sun [42] at hydrostatic pressure with depth (using specific gravity (brine density relative to water density) $sg = 1$) and a temperature gradient of 30 °C/km and $T = 10$ °C at the surface.

Solubility of CO_2 at various salinity, pressure and temperature are shown in Fig. B.12

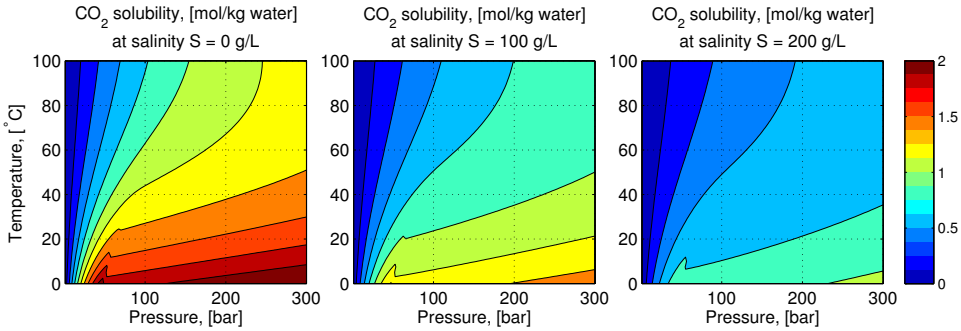

Figure B.12: Solubility of CO_2 at various salinity, pressure and temperature. The Solubility is calculated using the formula by Duan and Sun [42].

The solubility of CO_2 (obtained from the formula by Duan and Sun [42]) is converted to volume fractions using the density of water/brine (evaluated of various salinity, temperature and pressure using the formula by Mavko et al. [71]), the density of the CO_2 (evaluated at various temperature and pressure from the online NIST database [65]) and the molar masses of water and CO_2.

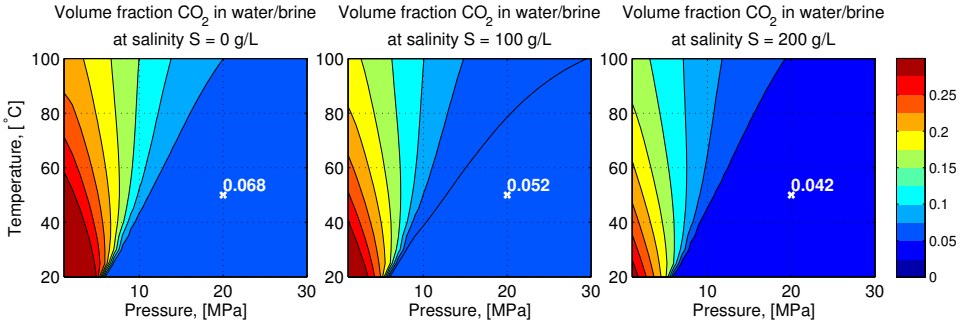

Figure B.13: Volume fraction c_{nw} of CO_2 in water/brine at various salinity, pressure and temperature.

The effect of salinity on the density and viscosity of water/brine is shown in Figs. B.14 and B.15, respectively. The properties are calculated using formula by Mavko et al. [71]. For temperatures below 250 °C the viscosity of water does not change much with pressure and is ignored [71].

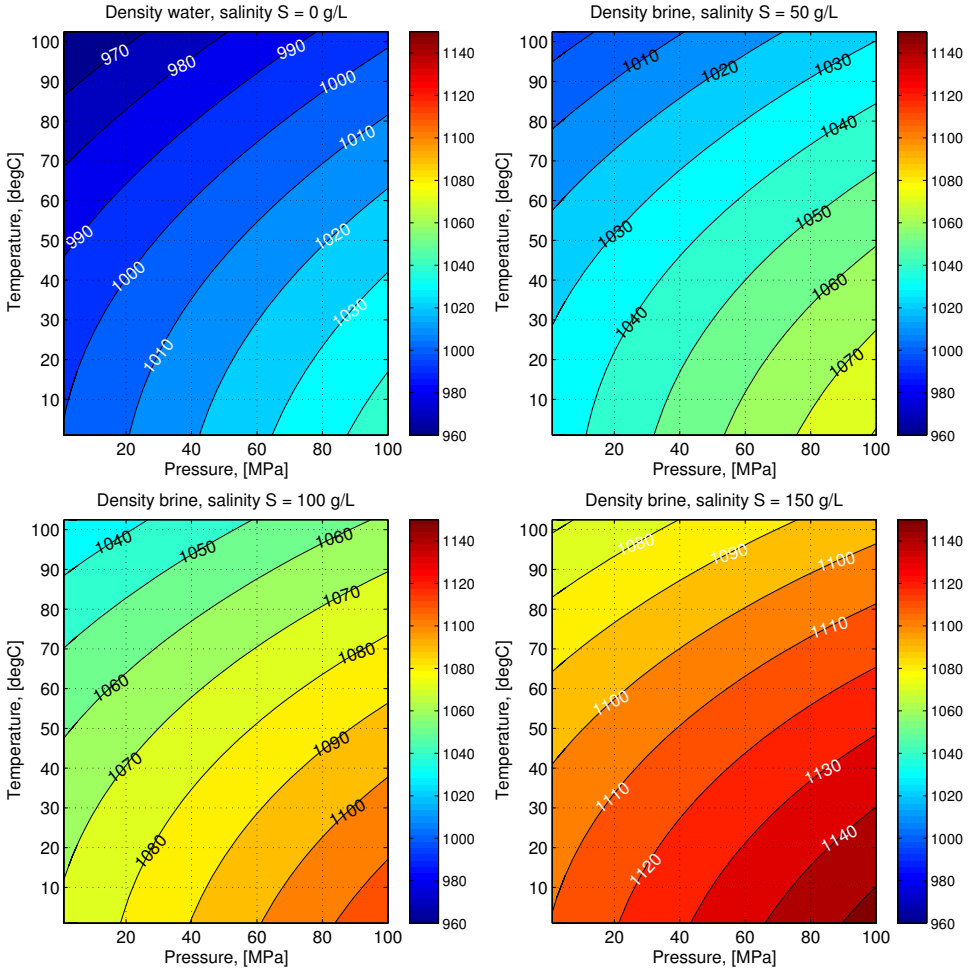

Figure B.14: Density of water/brine of various salinity at various temperature and pressure. The density is calculated using formula by Mavko et al. [71].

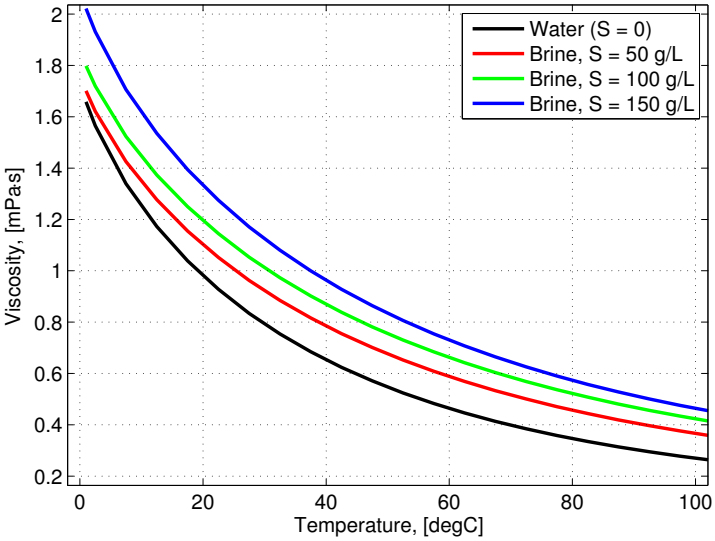

Figure B.15: Viscosity of water/brine of various salinity at various temperature. The viscosity is calculated using formula by Mavko et al. [71] (independent on pressure).

Appendix C

Elementary poroelasticity problems

Here we present some elementary problems of poroelasticity and their solutions. They serve not only as validation models for numerical codes, but also as rough estimates for quality control and evaluation of numerical solutions which should be part of any numerical study. They also demonstrate key principles of Biot's poroelasticity and effects such as the Mandel-Cryer[1]. A good source of elementary problems in poroelasticity can be found in [117].

There are many models that can be used as first-order approximate solutions, or validation models for poroelasticity, three of them are:

1. Geertsma's nucleus of strain model (no fluid flow) [48]
2. Mandels problem, with fluid flow [69]
3. One dimensional (Terzaghi) consolidation, with fluid flow [111]

Sketches of the validation models are shown in Fig. C.1. In the Geertsma model, the pressure is prescribed, thus no flow equation are solved. In the two other models; Mandels problem and Terzaghi consolidation, the transient change in pressure is captured and the mass conservation equation for a single-phase fluid is considered.

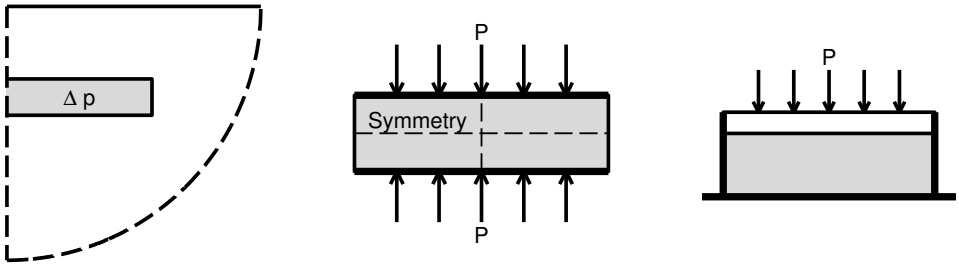

Figure C.1: Sketch of various poroelasticity validation models (from left to right): Geertsma's nucleus of strain model, mandels problem with fluid flow and one dimensional (Terzaghi) consolidation with fluid flow.

[1]Effect in consolidation where the pore pressure in a sample of soil loaded by a constant load initially increases, before it later dissipates to a final value.

C.1 Geertsma's nucleus of strain model

The nucleus of strain model by Geertsma [48] was derived to calculate how the compaction of a reservoir propagates through the surrounding over- and underburden. The idea is to calculate subsidence (or heave) resulting from compaction (or expansion) of a small sphere and then add the influence of many spheres to calculate the total effect (assuming that superposition is allowed). The model is limited to cases where there are no contrasts in elastic properties between the reservoir and the surroundings, the reservoir is assumed confined and the pressure change is assumed to be uniform. The model is axial-symmetric and the reservoir is disk-shaped and embedded into a half-space model, see Fig. C.2 (right).

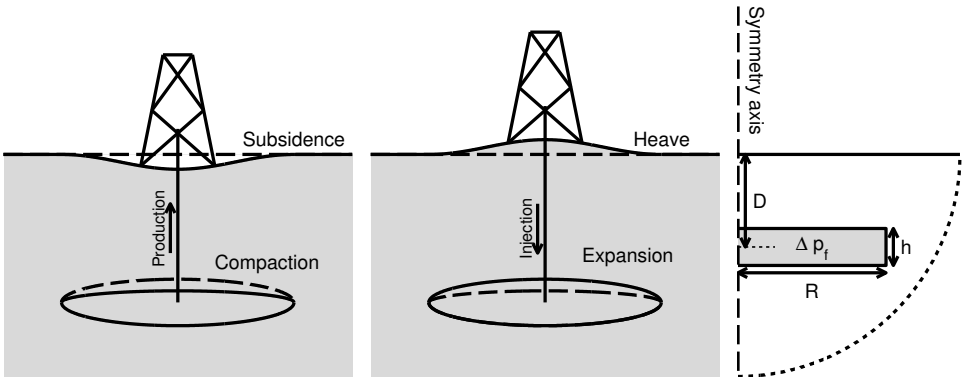

Figure C.2: Sample applications of Geertsma's nucleus strain model. Left: Depletion of a reservoir, causing subsidence at the surface. Center: Injection into a reservoir, causing the surface to heave. Right: Dimensions used in Geertsma's nucleus strain model.

The vertical displacement w along the axial symmetry line ($r = 0$) is given by (from Fjaer et al. [46]):

$$w(0,z) = -\frac{1}{2} C_m h b \Delta p_f \left(3 - 4\nu + \frac{D-z}{|D-z|} - \frac{D-z}{\sqrt{R^2+(D-z)^2}} - \frac{(D+z)(3-4\nu)}{\sqrt{R^2+(D+z)^2}} + \frac{2R^2 z}{(R^2+(D+z)^2)^{3/2}} \right) \tag{C.1}$$

and the horizontal and vertical displacement, u and w, respectively, along the surface ($z = 0$) is given by (see [48] for details):

$$u(r,0) = 2C_m(1-\nu)\Delta p_f h R \int_0^\infty e^{-D\alpha} J_1(\alpha R) J_1(\alpha r) d\alpha \tag{C.2}$$

$$w(r,0) = -2C_m(1-\nu)\Delta p_f h R \int_0^\infty e^{-D\alpha} J_0(\alpha R) J_1(\alpha r) d\alpha \tag{C.3}$$

where z [m] and r [m] are the vertical and radial dimensions, respectively, b [-] is Biot's coefficient, Δp_f [Pa] is the change in reservoir pore pressure, ν [-] is the Poissson's ratio and the dimensions D [m], R [m] and h [m] are illustrated in Fig. C.2 (right). J_0 and J_1 are the Bessel functions of zero and first order, respectively, and the compaction coefficient C_m is equal to the inverse of the Oedometer modulus H:

$$C_m = \frac{1}{\lambda + 2G} = \frac{1}{H} \tag{C.4}$$

In a uniaxial displacement, the reservoir strain corresponds to volumetric strain, comparison with Eq. (3.37) gives (neglecting temperature changes):

$$\frac{\Delta h}{h} = \varepsilon_v = \frac{b\Delta p_f}{\lambda + 2G} \tag{C.5}$$

The results of two examples (from Fjaer et al. [46]) are given in Figs. C.3-C.4. The application is depletion of a reservoir ($\Delta p_f = 10$ MPa), causing subsidence at the surface, see Fig. C.2 (left). The model parameters are given in table C.1.

Table C.1: Model parameters used in example from Fjaer et al. [46, ch. 12.3]. Results are given in Figs. C.3-C.4.

Description	Property	Value
Reservoir depth	D	2000 m
Reservoir radius	R	2000 m
Reservoir height	h	100m and 1000m
Shear modulus	G	2 GPa
Poisson's ratio	ν	0.25
Biot's coefficient	b	1
Compaction coefficient (Eq. (C.4))	C_m	6 GPa
Depletion, pressure change	Δp_f	10 MPa
Reservoir strain (Eq. (C.5))	$\Delta h/h$	0.167% (both)
Estimated (uniaxial) compaction (from Eq. (C.5))	Δh	0.167m and 1.67m
Subsidence, at $r = 0$ and $z = 0$ (Eq. (C.1))	w	7.32cm and 73.2cm

The numerical solution is a static solution of the conservation of linear momentum equation, Eq. (3.2), with the constitutive relation for the stress defined by Eq. (3.17). The solution matches almost exactly for thin reservoirs, even for thick reservoirs the match is good (see Figs. C.3-C.4).

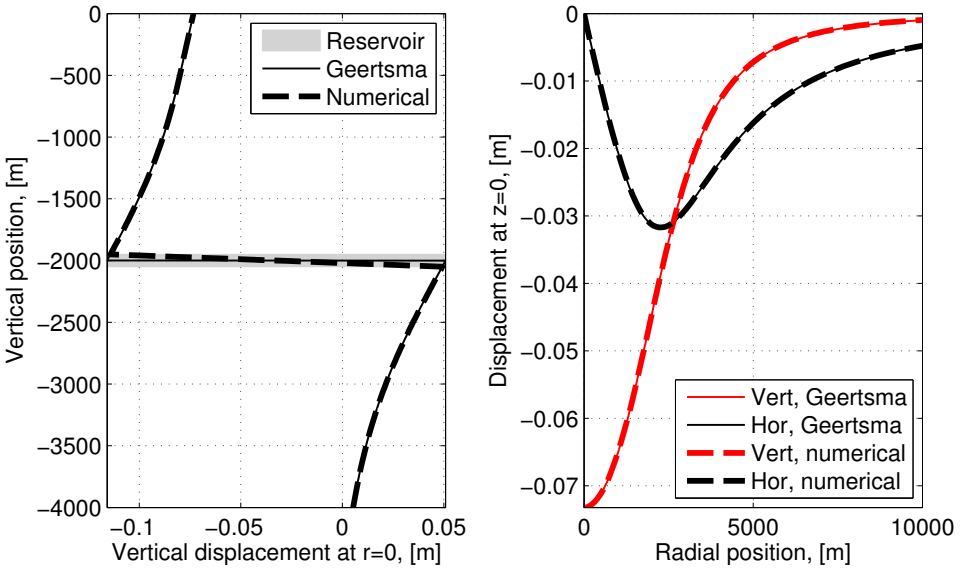

Figure C.3: Solution from Geertsma's nucleus model compared to a numerical model (using finite element method) for a 100 m thick reservoir. Left: Vertical displacement along the axial symmetry axis ($r = 0$, Eq. (C.1)). Position of the reservoir is indicated by the grey shaded area. Right: horizontal and vertical displacement at the surface (Eqs. (C.2) and (C.3)).

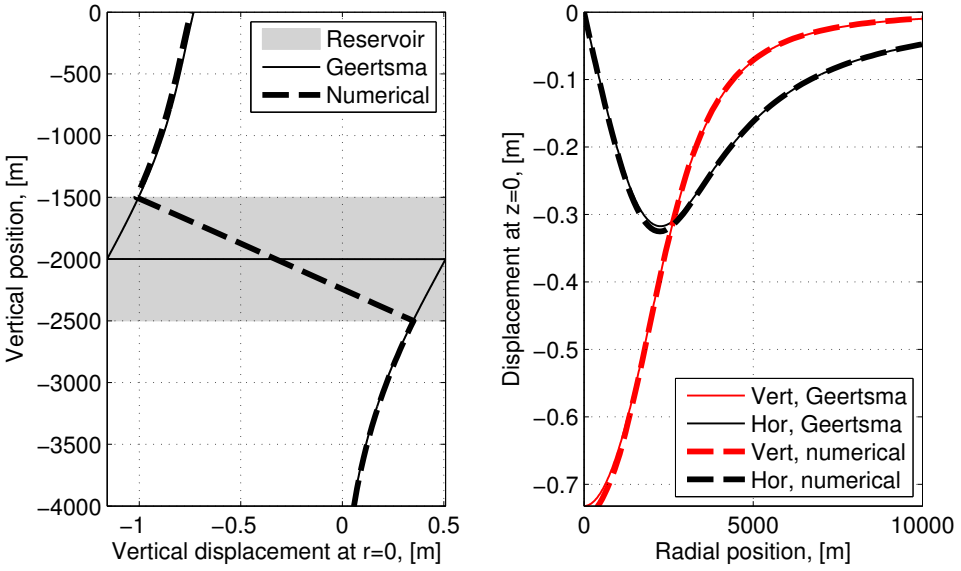

Figure C.4: Solution from Geertsma's nucleus model compared to a numerical model (using finite element method) for a 1000 m thick reservoir. Left: Vertical displacement along the axial symmetry axis ($r = 0$, Eq. (C.1)). Position of the reservoir is indicated by the grey shaded area. Right: horizontal and vertical displacement at the surface (Eqs. (C.2) and (C.3)).

C.2 Mandels problem

Mandel [69] introduced one of the first solutions to Biot's theory of linear poroelasticity. The problem that was solved was an infinitely long slab, with a rectangular crossection, of a fully saturated porous media that is clamped between to rigid and frictionless plates, see Fig. C.5.

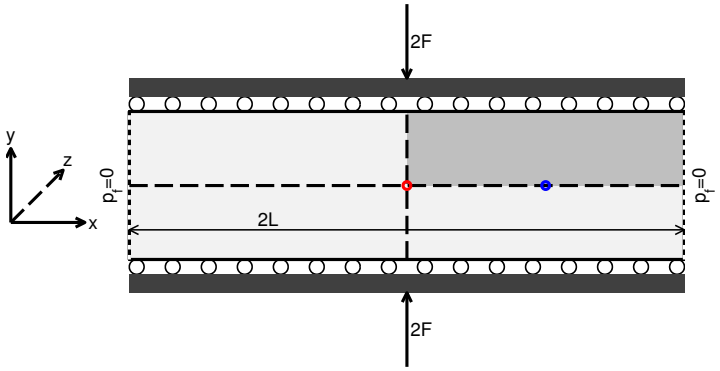

Figure C.5: Mandel's problem setup. The slab is infinite in the out-of-plane z-direction. Only a quarter of the geometry is considered due to the symmetry; shaded area.

The lateral boundaries are stress-free (no shear or normal stress) and drained (fixed fluid pressure, $p_f = 0$). An instant load $2F$ [N/m] is applied to the top and bottom plate and drainage is only allowed on the lateral sides. To derive the analytical solution, the grains in the porous media and the fluid is assumed to be incompressible, thus the transient term in the fluid flow equation, e.g. Eq. (4.22), vanishes and Biot's coefficient $b = 1$ such that the fluid flow equation becomes:

$$\nabla \cdot \mathbf{v}_s + \nabla \cdot \mathbf{q}_f = 0 \tag{C.6}$$

These assumptions also allows the initial pore pressure; immediately after the load is applied and before the fluid starts to drain, to be expressed as:

$$p_f^0 = F \tag{C.7}$$

and the normalized pore pressure can be expressed as [36][2]:

$$\frac{p_f(x,t_{nd})}{p_f^0} = 2\sum_{n=1}^{\infty} \frac{\cos(\alpha_n x/L) - \cos(\alpha_n)}{\alpha_n - \sin(\alpha_n)\cos(\alpha_n)} \sin(\alpha_n) \exp(-\alpha_n^2 t_{nd}) \tag{C.8}$$

The dimensionless time t_{nd} [-] is defined as:

$$t_{nd} = t\frac{c_v}{L^2} \tag{C.9}$$

where t [s] is time and the diffusivity coefficient c_v [m^2/s] is approximated as [36]:

$$c_v = \frac{k}{\mu_f}\frac{1}{\lambda + 2G} \tag{C.10}$$

[2]The theory presented here is from Coussy [36, ch. 5.4.3]. Other interesting references are: Mandel [69] and Lee and Gutierrez [63] (and references therein).

where k [m^2] is the permeability of the porous media, μ_f [Pa·s] is the fluid viscosity and K [Pa] and G [Pa] are the bulk and shear modulus of the porous media, respectively. The parameter α_n [-] is determined from the equation [36]:

$$\frac{\tan(\alpha_n)}{\alpha_n} = \frac{1-\nu}{\nu_u - \nu} \tag{C.11}$$

where ν [-] is the Poisson's ratio of the porous media and $\nu_u = 0.5$ [-] is the Poissons's ratio for the incompressible fluid.

Table C.2: Model properties used in Mandels problem. Results are given in Fig. C.6.

Description	Property	Value
Poisson's ratio, [-]	ν	0.2
Youngs modulus, [kPa]	E	1
Permeability, [m^2]	k	10^3
Viscosity, [mPa·s]	μ_f	0.1
Load, [N/m]	F	10^3
Slab width, [m]	L	10

The solution of Eq. (C.8) with the properties given in table C.2 is shown in Fig. C.6. The assumptions in the model are such that the storage term in the single-phase flow equation vanish, but the two processes; mechanical and hydraulic, are still fully coupled through the strain rate terms in the fluid flow equation, Eq. (C.6), and the pore pressure in the constitutive relation for the stress; Eq. (3.17).

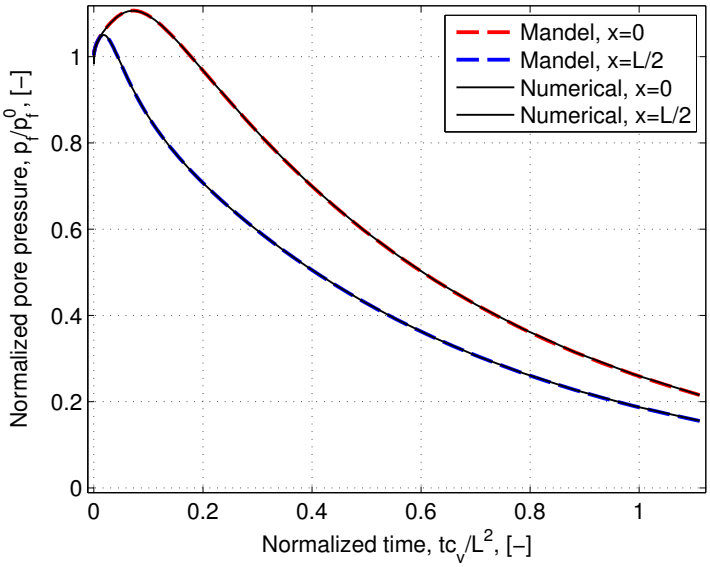

Figure C.6: Pore pressure in the middle of the slab at two horizontal locations; red and blue dot in Fig. C.5. Mandel's analytical solution is compared to a fully coupled numerical solution (using finite element method) for single-phase flow with poroelasticity.

The temporary increase in pore pressure at early-times, where $p_f > p_f^0$, is due to an effect called Mandel-Cryer; the fluid near the free surface drains faster than deeper inside the slab, causing a faster decrease in pressure at $x = L/2$ compared to the center; $x = 0$ and results in a shift in effective stress. It can also be seen in Fig. C.6 that the Mandel-Cryer is less pronounced closer to the free surface.

C.3 Terzaghi consolidation

One-dimensional consolidation is an important problem in geotechnical engineering. A load is applied on top of a soil column that starts to consolidate, or compact. How fast the soil compacts depends on the drainage which again depends on the mechanical and hydraulic properties. In one-dimensional problems, the fluid flow equation is reduced to the uniaxial form (from Eqs. (4.33) and (4.34)):

$$S\frac{\partial p_f}{\partial t} + \nabla \cdot \mathbf{q}_f = 0$$

where the Darcy flux $\mathbf{q}_f$ is given by Eq. (4.3) and the effective storage coefficient S [1/Pa] for uniaxial strain approximation is expressed by:

$$S = \frac{b-\phi}{K_s} + \frac{\phi}{K_f} + \frac{b^2}{\lambda + 2G}$$

Note that this is sometimes called the modified Terzaghi consolidation model because in the original problem the volumetric strain rate coupling term in the flow equation ($b^2/(\lambda + 2G)$) was not included and b was assumed equal to one. The poroelasticity is considered by solving the equation of equilibrium with the constitutive relation for stress defined by Eq. (3.17). Details on the solution can be found several places in the literature, e.g. Verruijt [117] and Jaeger et al. [58], here we present the solution from Jaeger et al. [58, ch. 7.6].

A validation model (of formulation and numerical code) is defined and solved both numerically (using the finite element method) and analytically using expressions from Jaeger et al. [58, ch. 7.6]. The model setup is illustrated in Fig. C.7.

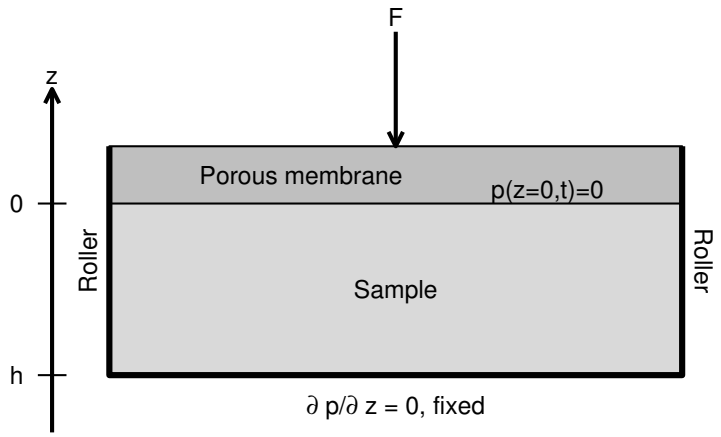

Figure C.7: Model setup of Terzaghi's one dimensional consolidation model.

The solutions that will be compared is the (vertical) consolidation at the surface of the sample and the pore pressure at the bottom of the sample as function of time and vertical pore pressure profiles at various times. The analytical expressions needed are the pore pressure (Jaeger et al. [58, Eq. 7.107]):

$$p(z,t) = \frac{bMF}{(\lambda + 2G + b^2M)} \sum_{n=1,3,\ldots}^{\infty} \frac{4}{n\pi} \sin\left(\frac{n\pi z}{2h}\right) \exp\left(\frac{-n^2\pi^2 kt}{4\mu S h^2}\right) \tag{C.12}$$

and the vertical displacement (Jaeger et al. [58, Eq. 7.111]):

$$w(z,t) = \frac{F}{(\lambda + 2G)} \left[(z-h) + \frac{b^2Mh}{(\lambda + 2G + b^2M)} \sum_{n=1,3,\ldots}^{\infty} \frac{8}{n^2\pi^2} \cos\left(\frac{n\pi z}{2h}\right) \exp\left(\frac{-n^2\pi^2 kt}{4\mu S h^2}\right) \right] \tag{C.13}$$

where z [m] and t [s] is the vertical position and time, respectively, M is given by:

$$S = \frac{1}{M} + \frac{b^2}{\lambda + 2G} \tag{C.14}$$

The rest of the properties are given in table C.3 and the results are shown in Fig. C.8.

Table C.3: Model properties used in the modified one dimensional Terzaghi consolidation model. Results are shown in Fig. C.8.

Description	Property	Value
Porosity, [-]	ϕ	0.17
Permeability, [m^2]	k	10^{-12}
Viscosity, [Pa·s]	μ_f	$3{\cdot}10^{-4}$
Poisson's ratio, [-]	ν	0.2
Youngs modulus, [GPa]	E	6
Bulk modulus, grains, [GPa]	K_s	10
Bulk modulus, fluid, [GPa]	K_f	2
Load, [N/m^2]	F	10^6
Sample height, [m]	h	500
Biot's coefficient, [-]	b	2/3

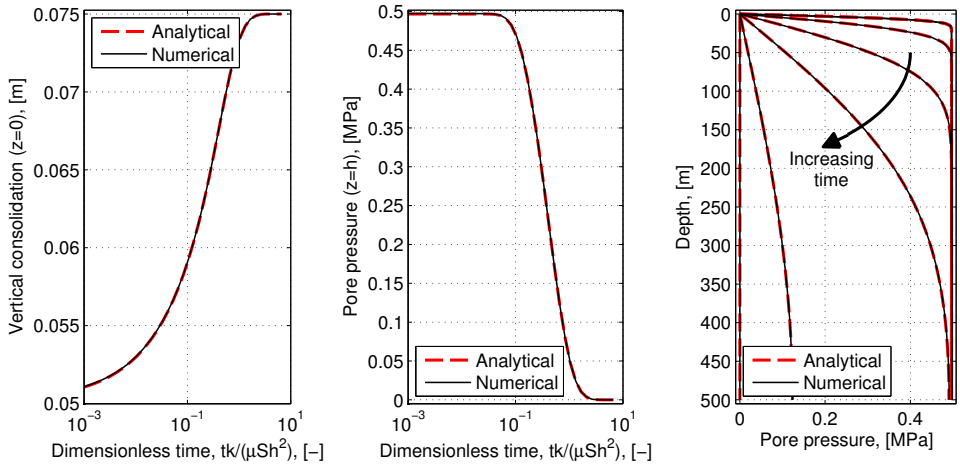

Figure C.8: Results from the analytical solution to the modified one dimensional Terzaghi consolidation model and the corresponding numerical model (using finite element method). Left: Vertical subsidence at the top surface versus time. Center: Pore pressure at the bottom of the model versus time. Right: Vertical pore pressure profile at various times: 1, 10, 100, 1000, 10^4 and 10^5 seconds.

Appendix D

Component mass conservation

The general mass conservation equation for a component i in a fluid phase α can be expressed as

$$\frac{\partial(\phi s_\alpha \rho_{i\alpha})}{\partial t} + \nabla \cdot [\phi s_\alpha \rho_{i\alpha} \mathbf{v}_{i\alpha}] = R_{i\alpha} \tag{D.1}$$

where ϕ [-] is the porosity, s_α [-] is the saturation of fluid phase α, $\rho_{i\alpha}$ [kg/m^3] is the density of component i in fluid phase α, t [s] is time, $R_{i\alpha}$ is the source/sink-term[1] [kg/m^3/s] and $\mathbf{v}_{i\alpha}$ [m/s] is the net velocity of which component i flows through a representative elementary volume (REV). This velocity is the sum of diffusion $\mathbf{j}_{i\alpha}$ [kg/m^2/s] and the bulk motion, or average phase velocity $\mathbf{v}_\alpha$ [m/s], according to:

$$\rho_{i\alpha} \mathbf{v}_{i\alpha} = \rho_{i\alpha} \mathbf{v}_\alpha + \mathbf{j}_{i\alpha} \tag{D.2}$$

By neglecting thermal diffusion, barodiffusion (diffusion due to pressure change) and effect of gravitational potential, diffusion $\mathbf{j}_{i\alpha}$ can be described by Fick's law:

$$\mathbf{j}_{i\alpha} = -\mathbf{D}_{i\alpha} \nabla \rho_{i\alpha} \tag{D.3}$$

where $\mathbf{D}_{i\alpha} = \mathbf{D}_\alpha$ [kg/(m^{2}s)] is the effective dispersion tensor of phase α and $\rho_{i\alpha}$ [kg/m^3] is the mass density of component i in phase α, according to:

$$\rho_{i\alpha} = X_{i\alpha} \rho_\alpha \tag{D.4}$$

and ρ_α [kg/m^3] is the fluid phase density. Combining Eqs. (D.1)-(D.4), we obtain the general mass conservation equation for component i in phase α:

$$\frac{\partial(\phi s_\alpha \rho_{i\alpha})}{\partial t} + \nabla \cdot [\phi s_\alpha \rho_{i\alpha} \mathbf{v}_\alpha] + \nabla \cdot (\phi s_\alpha \mathbf{j}_{i\alpha}) = R_{i\alpha} \tag{D.5}$$

The material derivative relative to an arbitrary phase α is given as (for some property denoted $(\cdot)$):

$$\frac{d^\alpha(\cdot)}{dt} = \frac{\partial(\cdot)}{\partial t} + \mathbf{v}_\alpha \cdot \nabla(\cdot) \tag{D.6}$$

Applying Eq. (D.6) on Eq. (D.5) yields [64]:

$$\frac{d^\alpha(\phi s_\alpha \rho_{i\alpha})}{dt} + \phi s_\alpha \rho_{i\alpha} \nabla \cdot \mathbf{v}_\alpha + \nabla \cdot (\phi s_\alpha \mathbf{j}_{i\alpha}) = R_{i\alpha} \tag{D.7}$$

[1] Note that the introduced general source/sink-term $R_{i\alpha}$ [kg/(m^{3}s)] can be a complex mix of inter- and intraphasial terms that account for (but not limited to) chemical reactions, adsorption and physical sources/sinks such as injection/production wells.

The relation between the material derivative of the solid and phase α is given by [64]:

$$\frac{d(\cdot)}{dt} = \frac{d^{\alpha}(\cdot)}{dt} + (\mathbf{v}_s - \mathbf{v}_{\alpha}) \cdot \nabla(\cdot) \tag{D.8}$$

where $\mathbf{v}_s$ [m/s] is the volume averaged velocity of the solid phase and the following general vector identity for velocity $\mathbf{v}$ [m/s] holds:

$$\nabla \cdot ((\cdot)\mathbf{v}) = (\cdot)\nabla \cdot \mathbf{v} + \mathbf{v} \cdot \nabla(\cdot) \tag{D.9}$$

Applying Eqs. (D.8) and (D.9) to the mass conservation equation Eq. (D.7), gives:

$$\frac{d(\phi s_{\alpha} \rho_{i\alpha})}{dt} + \nabla \cdot (\rho_{i\alpha} \mathbf{q}_{\alpha}) + \phi s_{\alpha} \rho_{i\alpha} \nabla \cdot \mathbf{v}_s - \nabla \cdot (\mathbf{D}_{\alpha} \nabla \rho_{i\alpha}) = R_{i\alpha} \tag{D.10}$$

In terms of mass fractions:

$$\boxed{\frac{d(\phi s_{\alpha} X_{i\alpha} \rho_{\alpha})}{dt} + \nabla \cdot (X_{i\alpha} \rho_{\alpha} \mathbf{q}_{\alpha}) + \phi s_{\alpha} X_{i\alpha} \rho_{\alpha} \nabla \cdot \mathbf{v}_s - \nabla \cdot (\mathbf{D}_{\alpha} \nabla (\rho_{\alpha} X_{i\alpha})) = R_{i\alpha}} \tag{D.11}$$

where $\mathbf{q}_{\alpha}$ is the Darcy flux

$$\boxed{\mathbf{q}_{\alpha} = s_{\alpha} \phi (\mathbf{v}_{\alpha} - \mathbf{v}_s) = -\frac{\mathbf{k}\mathbf{k}_{r\alpha}}{\mu_{\alpha}} (\nabla p_{\alpha} - \rho_{\alpha} \mathbf{g})} \tag{D.12}$$

and $\mathbf{k}$ [m^2] is the intrinsic permeability tensor, $\mathbf{k}_{r\alpha}$ [-], μ_{α} [Pa·s], p_{α} [Pa] and ρ_{α} [kg/m^3] are the relative permeability tensor, viscosity, pressure and mass density of fluid phase α, respectively, and $\mathbf{g}$ [m/s^2] is the gravity tensor.

Species in a solution tend to spread more than the pure convective transport can account for and this spreading is (usually) contributed to molecular diffusion (random fluctuating movements by the atoms) and mechanical dispersion (e.g. splitting and merging of flow paths through the pores). This diffusion and dispersion in single- and multi-phase flow is described by several authors, e.g. Bear [9], Chen et al. [31], Civan [33], Helmig [51], Herrera and Pinder [52], Lake [62], Pinder and Gray [89], Raffensperger [91], here we adopt the description by Chen et al. [ch. 2, 31]:

$$\boxed{\mathbf{D}_{\alpha} = \phi s_{\alpha} d_{i\alpha} \mathbf{I} + \| \mathbf{v}_{\alpha} \| \left(d_{l\alpha} \mathbf{E} + d_{t\alpha} \mathbf{E}^{\perp} \right)} \tag{D.13}$$

where $\mathbf{v}_{\alpha}$ [m/s] is the pore velocity, here defined as: $\mathbf{v}_{\alpha} = \mathbf{q}_{\alpha}/(\phi s_{\alpha})$ (from Eq. (D.12)), $d_{i\alpha}$ [m^2/s] is the molecular diffusion coefficient of component i in phase α, $d_{l\alpha}$ and $d_{t\alpha}$ [m] are longitudinal and transverse dispersivity of phase α, respectively, $\| \mathbf{v}_{\alpha} \|$ is the Euclidian norm of the pore velocity $\mathbf{v}_{\alpha}$ and

$$\boxed{\mathbf{E} = \frac{1}{\| \mathbf{v}_{\alpha} \|^2} \begin{bmatrix} v_{x\alpha}^2 & v_{x\alpha} v_{y\alpha} & v_{x\alpha} v_{z\alpha} \\ v_{y\alpha} v_{x\alpha} & v_{y\alpha}^2 & v_{y\alpha} v_{z\alpha} \\ v_{z\alpha} v_{x\alpha} & v_{z\alpha} v_{y\alpha} & v_{z\alpha}^2 \end{bmatrix}, \quad \mathbf{E}^{\perp} = \mathbf{I} - \mathbf{E}} \tag{D.14}$$

In 2D the diffusion/dispersion-coefficient in Eq. (D.13) can be expressed as:

$$\boxed{\mathbf{D}_{\alpha} = \phi s_{\alpha} d_{i\alpha} \mathbf{I} + \frac{d_{l\alpha}}{\| \mathbf{v}_{\alpha} \|} \begin{bmatrix} v_{x\alpha}^2 & v_{x\alpha} v_{y\alpha} \\ v_{y\alpha} v_{x\alpha} & v_{y\alpha}^2 \end{bmatrix} + \frac{d_{t\alpha}}{\| \mathbf{v}_{\alpha} \|} \begin{bmatrix} v_{y\alpha}^2 & -v_{x\alpha} v_{y\alpha} \\ -v_{y\alpha} v_{x\alpha} & v_{x\alpha}^2 \end{bmatrix}} \tag{D.15}$$

and in 1D the diffusion/dispersion-coefficient in Eq. (D.13) can be expressed as:

$$\boxed{\mathbf{D}_\alpha = \phi s_\alpha d_{i\alpha} \mathbf{I} + d_{l\alpha} \parallel v_{x\alpha} \parallel} \tag{D.16}$$

For immiscible fluids, the mass of all components i in a fluid phase α can be summed to obtain, from Eq. (D.11):

$$\boxed{\frac{d(\phi s_\alpha \rho_\alpha)}{dt} + \nabla \cdot (\rho_\alpha \mathbf{q}_\alpha) + \phi s_\alpha \rho_\alpha \nabla \cdot \mathbf{v}_s = R_\alpha} \tag{D.17}$$

where we have used that:

$$R_\alpha = \sum_i^{n_c} R_{i\alpha} \tag{D.18}$$

$$\sum_{i=1}^{n_c} X_{i\alpha} = 1 \tag{D.19}$$

and note that

$$\mathbf{j}_\alpha = \sum_{i=1}^{n_c} \mathbf{j}_{i\alpha} = 0 \tag{D.20}$$

and n_c is the number of components.

Appendix E

Capillary pressure and relative permeability functions

In order to describe a two-phase (or multi-phase) flow system, it is necessary to know the relationship between the phase pressures and the phase saturation. The capillary pressure is the pressure difference across the interface between two immiscible fluids, and is defined as (here for a wetting and a non-wetting fluid)[1]:

$$p_c = p_{nw} - p_w \tag{E.1}$$

This pressure difference is also proportional to the interfacial tension, γ [N/m], inversely proportional to the effective radius, r [m], of the interface, and it also depends on the wetting angle θ [rad] of the liquid on the surface of the (imagined) straight capillary tube with radius r representing a pore throat in a porous media (and equivalently for a fracture plane with aperture r) according to:

$$p_c = \frac{2\gamma\cos\theta}{r} \tag{E.2}$$

See for instance Fig. E.1 (left), the liquid is wetting the capillary tube and the capillary forces and the gravity forces equilibrate:

$$p_c = \Delta\rho g h - p_{atm} \tag{E.3}$$

where $\Delta\rho$ [kg/m^3] is the density difference of the two phases across the interface, e.g. water and air.

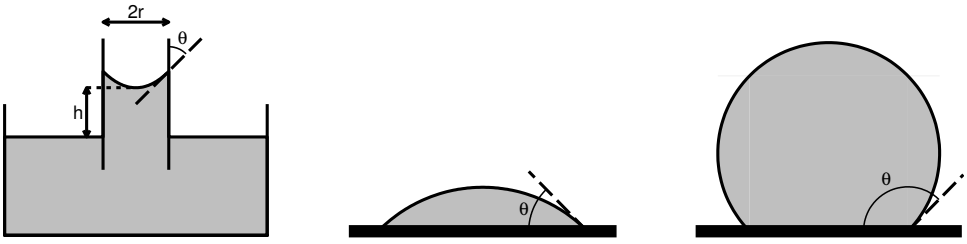

Figure E.1: Left: Balancing capillary and gravity forces in a capillary tube. Center: A wetting liquid on a solid with $\theta < 90°$. Right. A non-wetting liquid on a solid with $\theta > 90°$.

[1]The wetting-phase is the fluid phase that is the most attracted to, and sticks to, a solid.

However, a porous media does not consist of regular tubes, but rather a complex network of pores with various shapes and sizes and connectivity, resulting in a large distribution of capillary pressure values at a given average saturation of a porous media sample. Considering a representative elementary volume (REV), it is possible for a given average saturation to measure an average capillary pressure value and many mathematical relations have been proposed in the literature that fits to these measurements. They normally have one or more fitting parameters that, depending on the characteristics of the sample, can represent the capillary pressure function for a related sample. It is similar for the relative permeability, it can be obtained through laboratory tests and many mathematical relations have also been proposed in the literature that can be fitted to measured values for a given average saturation.

In the following sections some commonly used relations for capillary pressure and relative permeability will be reviewed briefly.

E.1 Capillary pressure

E.1.1 Brooks-Corey

The capillary pressure function can be related to the saturation according to the following relationship [27]:

$$p_c = \frac{p_d}{s_{ew}^{1/\lambda}} \tag{E.4}$$

$$s_{ew} = \left(\frac{p_d}{p_c}\right)^{\lambda} \tag{E.5}$$

where p_d [Pa] is related to the entry pressure of the non-wetting phase and λ [-] is a fitting parameter related to the pore size distribution where a uniform grain size corresponds to a large value and a non-uniform grain size distribution corresponds to a small value. Note the discontinuity at $s_{ew} = 0$.

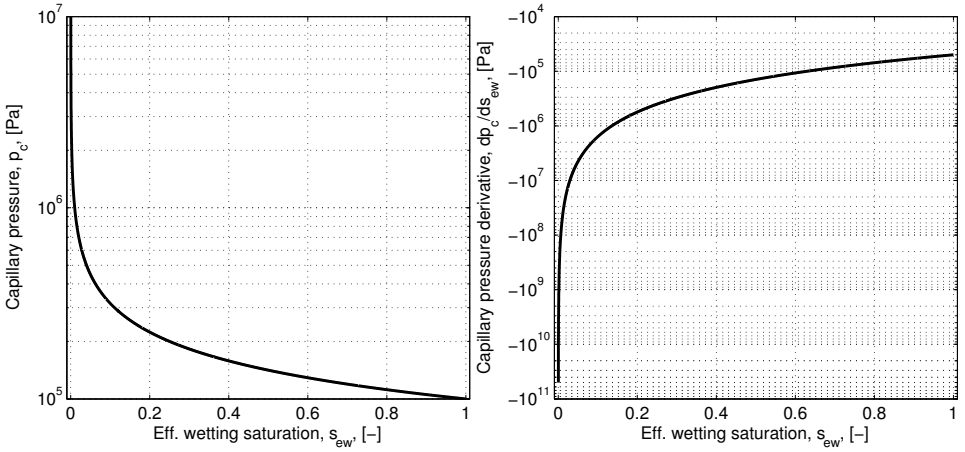

Figure E.2: Capillary pressure function as defined by Brooks and Corey [27]. Entry pressure $p_d = 10^5$ Pa and $\lambda = 2$. Left: Capillary pressure function; Eq. (E.4). Right: the derivative of the capillary pressure function.

E.1.2 van Genuchten

The capillary pressure function can be related to the saturation according to the following relationship [116]:

$$p_c = p_d \left(\frac{1}{s_{ew}^{1/m}} - 1 \right)^{1/n} \tag{E.6}$$

$$s_{ew} = \left(1 + \left(\frac{p_c}{p_d} \right)^n \right)^{-m} \tag{E.7}$$

where p_d [Pa] is related to the entry pressure of the non-wetting phase and n [-] is a fitting parameter related to the pore size distribution and m [-] is a fitting parameter related to the symmetry of the function. For $m = 1 - 2/n$ Eq. (E.6) is the same as the capillary pressure by Burdine [29], and for $m = 1 - 1/n$ Eq. (E.6) is the same as the capillary pressure by Mualem [78]. Note the discontinuity at $s_{ew} = 0$.

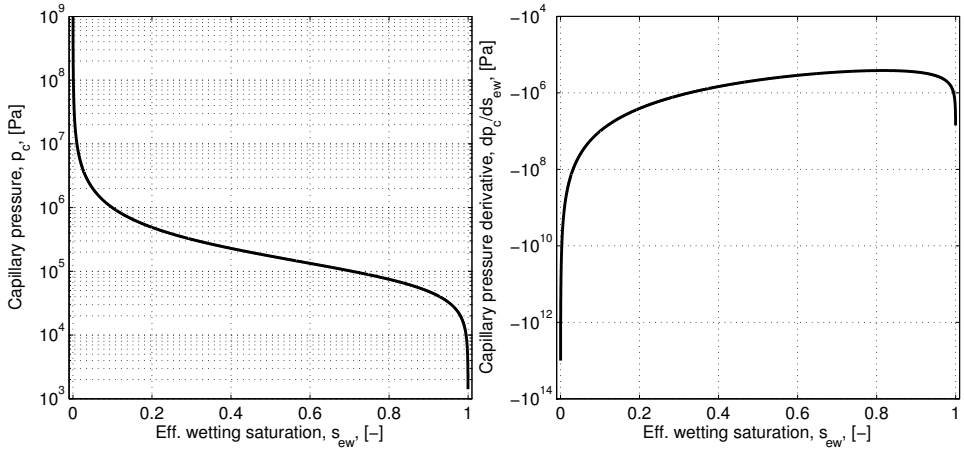

Figure E.3: Capillary pressure function as defined by van Genuchten [116]. Entry pressure $p_d = 10^5$ Pa, $n = 2$ and $m = 1 - 1/n$ [78]. Left: Capillary pressure function; Eq. (E.6). Right: the derivative of the capillary pressure function.

E.1.3 Parker

The capillary pressure function can be related to the saturation according to the following relationship [86]:

$$p_c = p_d \left(\frac{1}{s_{ew}^{1/m}} - 1 \right)^{1-m} \tag{E.8}$$

$$s_{ew} = \left(1 + \left(\frac{p_c}{p_d} \right)^{\frac{1}{1-m}} \right)^{-m} \tag{E.9}$$

where p_d [Pa] is related to the entry pressure of the non-wetting phase and $0 < m < 1$ [-] is a fitting parameter related to the pore size distribution. Note the discontinuity at $s_{ew} = 0$.

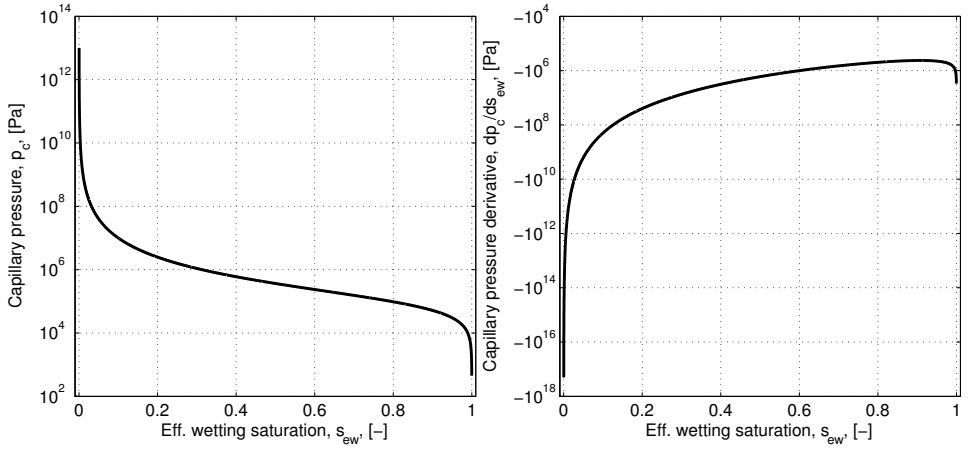

Figure E.4: Capillary pressure function as defined by Parker et al. [86]. Entry pressure $p_d = 10^5$ Pa and $m = 1/2$. Left: Capillary pressure function; Eq. (E.8). Right: the derivative of the capillary pressure function.

E.1.4 From Nordbotten and Dahle (2011)

The capillary pressure function can be related to the saturation according to the following relationship [84]:

$$p_c = \alpha(1 - s_{en})^{-1/2} + \beta \tag{E.10}$$

$$s_{en} = 1 - \left(\frac{\alpha}{p_c - \beta}\right)^2 \tag{E.11}$$

where α and β [Pa] are fitting parameters and $\alpha + \beta$ is comparable to the entry pressure in Eq. (E.4) by Brooks and Corey [27].

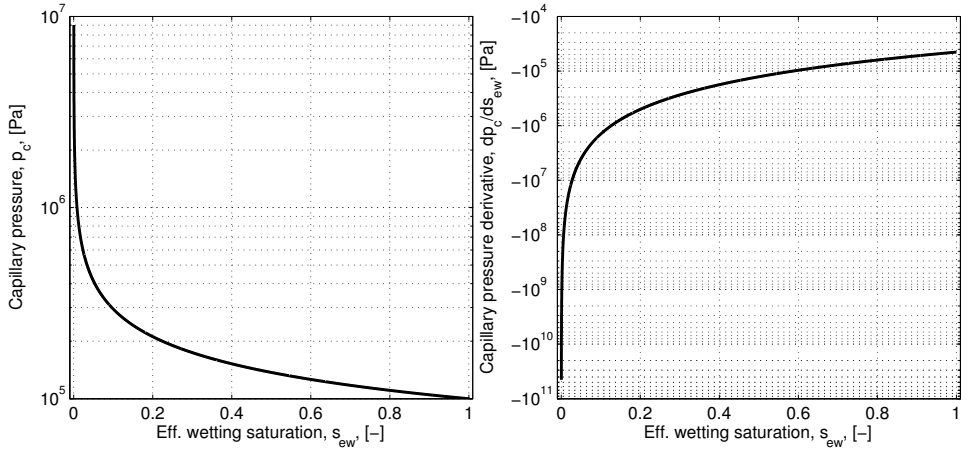

Figure E.5: Capillary pressure function as defined by Nordbotten and Dahle [84]. Entry pressure $p_d = 10^5$ Pa and $\alpha = 0.9 p_d$ and $\beta = 0.1 p_d$. Left: Capillary pressure function; Eq. (E.10). Right: the derivative of the capillary pressure function.

E.1.5 Comments on stability

An important relation to consider is how the capillary pressure p_c change with respect to change in saturation; dp_c/ds_{ew}. This is plotted in the right panels of Figs. E.2, E.3, E.4 and E.5. It can be seen that for the van Genuchten and Parker relations the derivative approaches infinity as $s_w \to 1$ and $s_w \to 0$. This can cause numerical problems, for drainage processes (such as CO_2-injection problems), as reservoirs are often considered to be initially fully water saturated, thus capillary pressure functions defined by Brooks and Corey [27] (or Nordbotten and Dahle [84]) is often preferred.

E.2 Relative permeability

E.2.1 Brooks-Corey

The relative permeability for the wetting phase and non-wetting phase can be expressed as [27]:

$$k_{rw} = s_{ew}^{(2+3\lambda)/\lambda} \tag{E.12}$$

$$k_{rn} = (1 - s_{ew})^2 (1 - s_{ew}^{(2+\lambda)/\lambda}) \tag{E.13}$$

where λ [-] is the same parameter from the capillary pressure function Eq. (E.4).

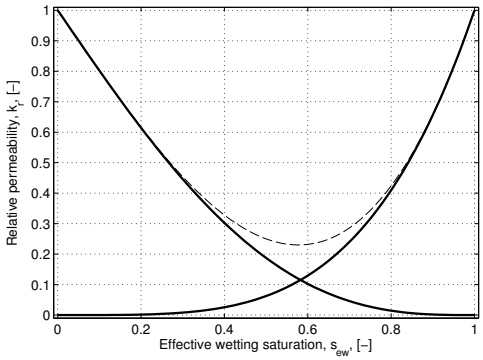

Figure E.6: Relative permeability for wetting and non-wetting phase after Brooks and Corey [27]. $\lambda = 2$.

E.2.2 van Genuchten

The relative permeability for the wetting phase and non-wetting phase can be expressed as [51]:

$$k_{rw} = s_{ew}^{\varepsilon} \left(1 - \left(1 - S_{ew}^{1/m}\right)^m\right)^2 \tag{E.14}$$

$$k_{rn} = (1 - s_{ew})^{\gamma} \left(1 - S_{ew}^{1/m}\right)^{2m} \tag{E.15}$$

where n and m are the same parameters as in the capillary pressure function Eq. (E.6), and ε [-] and γ [-] are pore connectivity parameters. Typically $\varepsilon = 1/2$ and $\gamma = 1/3$ are used [51].

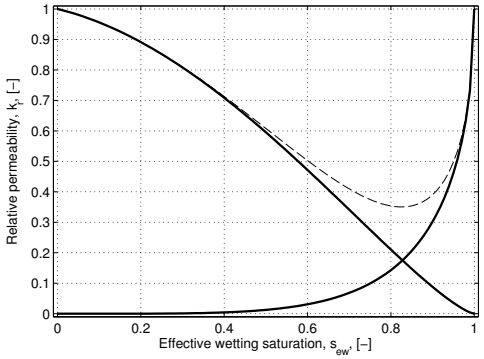

Figure E.7: Relative permeability for wetting and non-wetting phase after Helmig [51]. $n = 2$, $m = 1 - 1/n$, $\varepsilon = 1/2$ and $\gamma = 1/3$.

E.2.3 Parker

The relative permeability for the wetting phase and non-wetting phase can be expressed as [86]:

$$k_{rw} = s_{ew}^{1/2} \left(1 - \left(1 - S_{ew}^{1/m}\right)^{m}\right)^{2} \tag{E.16}$$

$$k_{rn} = (1 - s_{ew})^{1/2} \left(1 - S_{ew}^{1/m}\right)^{2m} \tag{E.17}$$

where m is the same parameters as in the capillary pressure function Eq. (E.8).

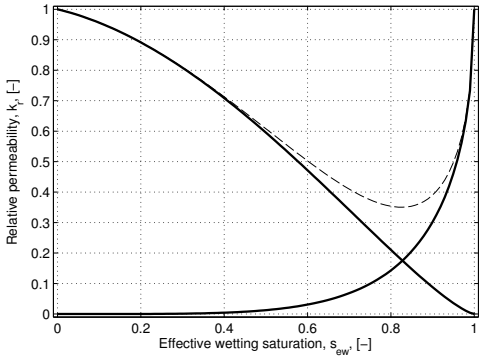

Figure E.8: Relative permeability for wetting and non-wetting phase after Parker et al. [86], $m = 1/2$.

E.3 Hysteresis

Capillary pressure and relative permeability are often considered as functions that are uniquely defined by the saturation in the pores. These correlations are found by experiments, but they depend on how the experiment is done. This is illustrated in Fig. E.9. Consider for instance a fully water saturated sample that is drained, the capillary pressure will increase until the

saturation approaches a residual value, $s_w = s_{wr}$. In the reverse process, imbibition, the water is reintroduced into the pores, but only until a certain limit where a pore volume corresponding to a residual non-wetting phase saturation. Because the large available pores are drained first, and similarly, the largest available pores are imbibed first, it results in a different correlation for the two processes. In between the main drainage and imbibition curves in Fig. E.9 there also exist an infinite number of intermediate relations, called scanning curves, depending on how far the drainage/imbibition process has come before the imbibition/drainage process is reversed. There is also a time-factor involved, such that the correlations will be different depending on how fast the experiment is performed. Thus the correlation that is used in models are often some representative correlation for a particular process of interest, e.g. drainage or imbibition.

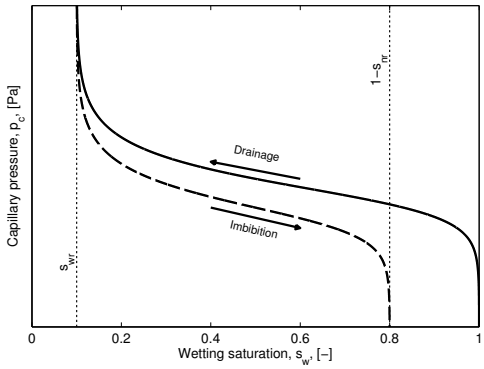

Figure E.9: Example of hysteresis in capillary pressure. Capillary pressure curves are often different in a drainage process compared to an imbibition process. Figure depicts the primary drainage curve and main imbibition curve.

Hysteresis can be considered by using $p_c = p_c(s_w, \partial s_w/\partial t)$, see e.g. Juanes et al. [60] for details on the impact of relative permeability hysteresis and Doster et al. [41] for the impact of capillary pressure hysteresis.

E.4 Heterogeneous porous media

Rocks and soils are not homogeneous materials with clearly defined properties. Instead they are often conceptualized into separate geometrical entities, e.g. layers, of materials that have similar properties, such as permeability, stiffness, porosity, etc. This can pose challenges when modeling flow, for instance, that is not confined to one particular entity. Assuming that two such entities of a porous media are in hydraulic contact but has different capillary pressure relations, this will have an affect on how the fluids are migrating across the interface. One way to handle this is to assume the following [51]:

- Continuity in mass flux across the interface
- Continuity in capillary pressure and the pressure of the mobile phases on each side of the interface (e.g. p_w)
- Discontinuity in the phase saturations

The discontinuity in saturation can be illustrated by looking at the capillary pressure of the two entities on opposite sides of the interface, see Fig. E.10. Due to a continuity in the phase pressures, and therefore also the capillary pressure, across the interface, there will be a discontinuity in the saturation. The jump in saturation can be evaluated by comparing the two capillary pressure functions.

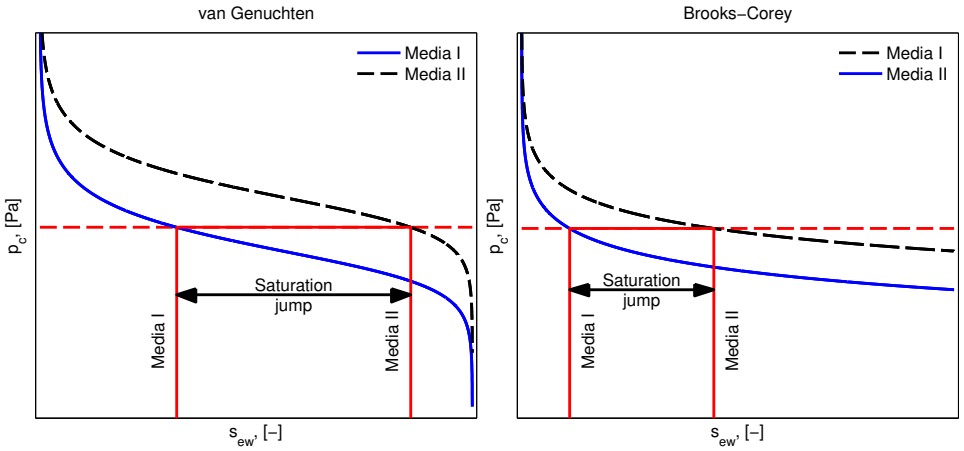

Figure E.10: Capillary pressure profiles (Left: van Genuchten, Eq. (E.6). Right: Brooks-Corey, Eq. (E.4)) for two porous medias with different entry pressure p_d. The ratio in entry pressure between the two porous media is 2.

It can be seen in Fig. E.10 that the discontinuity in the saturation is very sensitive to the entry pressure. If the difference in entry pressure is big, the non-wetting phase is often considered confined to the formation with the lowest entry pressure (if it is injected into it). This can imply that a reservoir is in effect confined when $p_d^{\text{res}} \gg p_d^{\text{conf}}$, where p_d^{res} is the entry pressure in the reservoir and p_d^{conf} is the entry pressure in the confining formations.

Appendix F

Stress invariant and principal stresses

Details on stress invariants and principal stresses can be found in the literature on elasticity. Here we refer to material from [80] and [58].

A stress invariant is a stress quantity that is reference-independent. Stress invariants are convenient for describing the actual state of stress. The principal stresses are examples of invariant stress and the first principal stress, σ_1, is the largest normal stress acting on any plane through a material particle. Principal stresses are found by rotating the basis for the stress tensor such that the shear stresses become zero, see Fig. F.1.

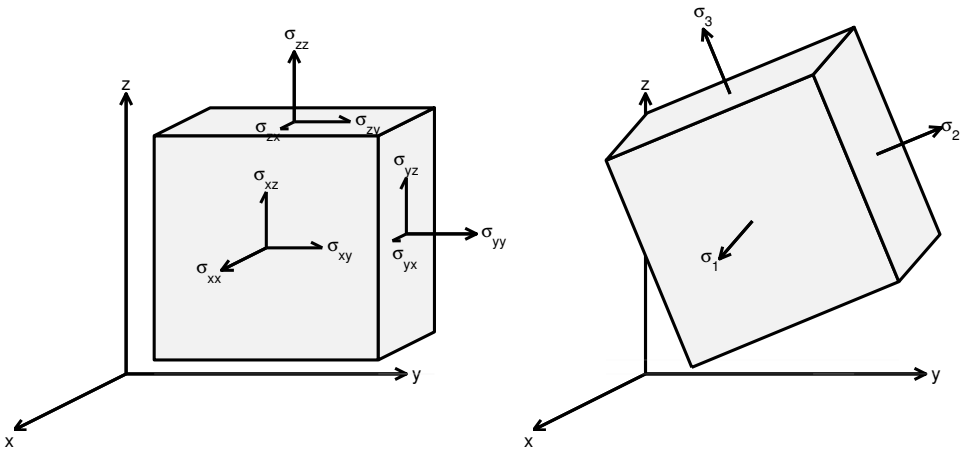

Figure F.1: Left: Normal and shear stress components on a cubic element. Right: By rotating the basis for the stress tensor, such that the shear stresses become zero, reveals the principal stresses.

In Fig. F.1 (left) we have used the cartesian notation for the various stress components. The first subscript describes the direction of the unit normal of the face that the stress component is acting on and the second subscript indicates the direction of the stress component. E.g. σ_{yx} acts on the face whos normal points in the y-direction, and the stress component itself is pointing in the x-direction. Often the notations are simplified such that the components σ_{xx}, σ_{yy} and σ_{zz} are simply expressed as σ_x, σ_y and σ_z, respectively.

In the following we will use another common notation where the axes are numbered, e.g. using 1 instead of x, 2 instead of y and 3 instead f z such that for instance σ_{xy} can be expressed

as σ_{12}.

There are three fundamental stress invariant (e.g. Davis and Selvadurai [38], Nordal [80]):

$$\mathrm{I}_1 = tr(\sigma) = \sigma_{11} + \sigma_{22} + \sigma_{33} \tag{F.1}$$

$$\mathrm{I}_2 = \frac{1}{2}\left[(tr(\sigma)^2) + tr(\sigma^2)\right] = \sigma_{11}\sigma_{22} + \sigma_{11}\sigma_{33} + \sigma_{22}\sigma_{33} - \sigma_{12}^2 - \sigma_{13}^2 - \sigma_{23}^2 \tag{F.2}$$

$$\mathrm{I}_3 = \det(\sigma) = \sigma_{11}(\sigma_{22}\sigma_{33} - \sigma_{23}^2) - \sigma_{12}(\sigma_{12}\sigma_{33} - \sigma_{13}\sigma_{23}) + \sigma_{13}(\sigma_{12}\sigma_{23} - \sigma_{13}\sigma_{22}) \tag{F.3}$$

Note that $\sigma_{13} = \sigma_{31}$ and $\sigma_{23} = \sigma_{32}$. In the case where the principal stresses coincide with the normal stresses, such that the shear stresses $\sigma_{12} = \sigma_{13} = \sigma_{23} = 0$, they simplify to:

$$\mathrm{I}_1 = \sigma_1 + \sigma_2 + \sigma_3 \tag{F.4}$$

$$\mathrm{I}_2 = \sigma_1\sigma_2 + \sigma_1\sigma_3 + \sigma_2\sigma_3 \tag{F.5}$$

$$\mathrm{I}_3 = \det(\sigma) = \sigma_1 \cdot \sigma_2 \cdot \sigma_3 \tag{F.6}$$

The principal stresses are the solution to $\sigma_i^3 - \mathrm{I}_1\sigma_i^2 + \mathrm{I}_2\sigma_i - \mathrm{I}_3 = 0$, where σ_i [Pa] is the principal stress i, and can be expressed as:

$$\sigma_1 = \frac{\mathrm{I}_1}{3} + \frac{2}{3}\left(\sqrt{\mathrm{I}_1^2 - 3\mathrm{I}_2}\right)\cos\theta \tag{F.7}$$

$$\sigma_2 = \frac{\mathrm{I}_1}{3} + \frac{2}{3}\left(\sqrt{\mathrm{I}_1^2 - 3\mathrm{I}_2}\right)\cos\left(\theta + \frac{2\pi}{3}\right) \tag{F.8}$$

$$\sigma_3 = \frac{\mathrm{I}_1}{3} + \frac{2}{3}\left(\sqrt{\mathrm{I}_1^2 - 3\mathrm{I}_2}\right)\cos\left(\theta + \frac{4\pi}{3}\right) \tag{F.9}$$

where θ [rad] is given by:

$$\theta = \frac{1}{3}\cos^{-1}\left(\frac{2\mathrm{I}_1^3 - 9\mathrm{I}_1\mathrm{I}_2 + 27\mathrm{I}_3}{2(\mathrm{I}_1^2 - 3\mathrm{I}_2)^{3/2}}\right) \tag{F.10}$$

2D approximations

In 2D we usually have either plane stress or plane strain conditions. Assuming that the in-plane stresses have the indices 1 and 2 and the out-of-plane (perpendicular direction) stress has index 3, we have for plane stress that $\sigma_{33} = \sigma_{13} = \sigma_{23} = 0$ and for plane strain that $\varepsilon_{33} = \varepsilon_{13} = \varepsilon_{23} = 0$. Under plane strain conditions we also have that $\sigma_{33} = \nu(\sigma_{11} + \sigma_{22})$ and σ_{11} and σ_{22} are both independent on σ_{33}, therefore the two (remaining) unknown principal stresses simplifies to:

$$\sigma_1 = \frac{\sigma_{11} + \sigma_{22}}{2} + \frac{1}{2}\sqrt{(\sigma_{11} - \sigma_{22})^2 + 4\sigma_{12}^2} \tag{F.11}$$

$$\sigma_2 = \frac{\sigma_{11} + \sigma_{22}}{2} - \frac{1}{2}\sqrt{(\sigma_{11} - \sigma_{22})^2 + 4\sigma_{12}^2} \tag{F.12}$$

The stresses σ_1 and σ_2 acts on planes that are perpendicular to each other. The angle the normal to these planes makes with the x-axis in a (x,y) coordinate system can be expressed as [e.g. 58]:

$$\tan 2\theta = \frac{2\sigma_{12}}{\sigma_{11} - \sigma_{22}} \tag{F.13}$$

This is also illustrated in Fig. F.2. Whether the angle 2θ belongs to σ_1 or σ_2 depends on the sign of the numerator and denominator of Eq. (F.13) and is summarized in table F.1.

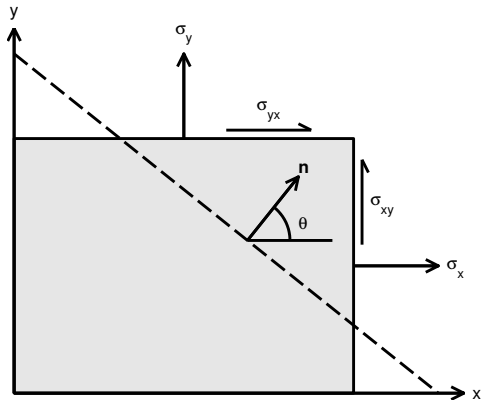

Figure F.2: Relationships between stress components and the plane the principal stresses act on in plane problems.

Table F.1: The angle the normal of the plane that σ_1 acts on relative to the x-axis, from [32, p. 10], see also Fig. F.2.

$\sigma_{xx} - \sigma_{yy} > 0$	$\sigma_{xy} > 0$	$0° < \theta < 45°$
$\sigma_{xx} - \sigma_{yy} < 0$	$\sigma_{xy} > 0$	$45° < \theta < 90°$
$\sigma_{xx} - \sigma_{yy} < 0$	$\sigma_{xy} < 0$	$90° < \theta < 135°$
$\sigma_{xx} - \sigma_{yy} > 0$	$\sigma_{xy} < 0$	$135° < \theta < 180°$

Appendix G

Navier-Cauchy momentum equation

The conservation equation for linear momentum:

$$-\nabla \cdot \sigma = \mathbf{f} \tag{G.1}$$

where σ [Pa] is the stress tensor and $\mathbf{f}$ [N/m^3] is the body load vector containing body loads (e.g. due to gravity) and inertial terms (acceleration). To derive the Navier-Cauchy momentum equations, we have for the stresses in Eq. (G.1) (here only shown for the x-component):

$$\frac{\partial \sigma_x}{\partial x} + \frac{\partial \sigma_{yx}}{\partial x} + \frac{\partial \sigma_{zx}}{\partial x} + f_x = 0 \tag{G.2}$$

where

$$\sigma_x = 2G\varepsilon_x + \lambda\left(\varepsilon_x + \varepsilon_y + \varepsilon_z\right) = 2G\frac{\partial u}{\partial x} + \lambda\left(\frac{\partial u}{\partial x} + \frac{\partial v}{\partial y} + \frac{\partial w}{\partial z}\right) \tag{G.3}$$

$$\sigma_{yx} = G\varepsilon_{yx} = G\left(\frac{\partial u}{\partial y} + \frac{\partial v}{\partial x}\right) \tag{G.4}$$

$$\sigma_{zx} = G\varepsilon_{zx} = G\left(\frac{\partial u}{\partial z} + \frac{\partial w}{\partial x}\right) \tag{G.5}$$

Substituting these stress components into Eq. (G.2), we get:

$$\begin{aligned}\frac{\partial}{\partial x}\left(2G\frac{\partial u}{\partial x} + \lambda\left(\frac{\partial u}{\partial x} + \frac{\partial v}{\partial y} + \frac{\partial w}{\partial z}\right)\right) + G\frac{\partial}{\partial y}\left(\frac{\partial u}{\partial y} + \frac{\partial v}{\partial x}\right) + \\ G\frac{\partial}{\partial z}\left(\frac{\partial u}{\partial z} + \frac{\partial w}{\partial x}\right) + f_x = 0\end{aligned} \tag{G.6}$$

Upon expanding the equation:

$$\begin{aligned}2G\frac{\partial}{\partial x}\frac{\partial u}{\partial x} + \lambda\frac{\partial}{\partial x}\left(\frac{\partial u}{\partial x} + \frac{\partial v}{\partial y} + \frac{\partial w}{\partial z}\right) + G\left(\frac{\partial}{\partial y}\frac{\partial u}{\partial y} + \frac{\partial}{\partial y}\frac{\partial v}{\partial x}\right) + \\ G\left(\frac{\partial}{\partial z}\frac{\partial u}{\partial z} + \frac{\partial}{\partial z}\frac{\partial w}{\partial x}\right) + f_x = 0\end{aligned} \tag{G.7}$$

and rearranging, it is obtained for the x-component:

$$(\lambda + G)\frac{\partial}{\partial x}\left(\frac{\partial u}{\partial x} + \frac{\partial v}{\partial y} + \frac{\partial w}{\partial z}\right) + G\left(\frac{\partial^2 u}{\partial x^2} + \frac{\partial^2 u}{\partial y^2} + \frac{\partial^2 u}{\partial z^2}\right) + f_x = 0 \tag{G.8}$$

Similarly can be done for stress in the y- and z-direction to obtain the full set of equations:

$$\begin{aligned}
(\lambda+G)\frac{\partial}{\partial x}\left(\frac{\partial u}{\partial x}+\frac{\partial v}{\partial y}+\frac{\partial w}{\partial z}\right)+G\nabla^2 u+f_x=0\\
(\lambda+G)\frac{\partial}{\partial y}\left(\frac{\partial u}{\partial x}+\frac{\partial v}{\partial y}+\frac{\partial w}{\partial z}\right)+G\nabla^2 v+f_y=0\\
(\lambda+G)\frac{\partial}{\partial z}\left(\frac{\partial u}{\partial x}+\frac{\partial v}{\partial y}+\frac{\partial w}{\partial z}\right)+G\nabla^2 w+f_z=0
\end{aligned} \tag{G.9}$$

and the Navier-Cauchy equation, in terms of λ and G:

$$(\lambda+G)\nabla(\nabla\cdot\mathbf{u})+G\nabla^2\mathbf{u}+\mathbf{f}=0 \tag{G.10}$$

Appendix H

Derivation of the VE equations

H.1 Dimensionally reduced two-phase flow equation

To derive the governing equations, the approach by Nordbotten and Dahle [83] and Nordbotten and Celia [81] is followed. Non-isothermal effects are ignored such that the mass conservation equation for fluid phase α can be described as (from Eq. (4.48):

$$\phi\rho_\alpha\frac{ds_\alpha}{dt}+s_\alpha\rho_\alpha\left[\frac{b-\phi}{K_s}\frac{dp_s}{dt}+\frac{\phi}{K_\alpha}\frac{dp_\alpha}{dt}+b\nabla\cdot\mathbf{v}_s\right]+\nabla\cdot(\rho_\alpha\mathbf{q}_\alpha)=R_\alpha \tag{H.1}$$

where $\mathbf{q}_\alpha$ is given by Eq. (4.43). Note that the source/sink term is omitted. The volumetric strain-rate term, $\nabla\cdot\mathbf{v}_s$, is only included when deformations is considered, which is relevant in section 6.5. Furthermore, the mass conservation equation is integrated in the vertical direction:

$$\int_{\zeta_B}^{\zeta_T}\left(\phi\rho_\alpha\frac{ds_\alpha}{dt}+s_\alpha\rho_\alpha\left[\frac{b-\phi}{K_s}\frac{dp_s}{dt}+\frac{\phi}{K_\alpha}\frac{dp_\alpha}{dt}+b\nabla\cdot\mathbf{v}_s\right]+\nabla\cdot(\rho_\alpha\mathbf{q}_\alpha)-R_\alpha\right)dz=0 \tag{H.2}$$

Assuming constant, or averaged, material properties in the vertical/integration direction, and applying Leibniz' rule, integrating term by term result in the following dimesionally reduced two-phase flow equation:

$$\begin{aligned}\Phi\rho_\alpha\frac{dS_\alpha}{dt}H+S_\alpha\rho_\alpha\left[\frac{b-\Phi}{K_s}\frac{dP_s}{dt}+\frac{\Phi}{K_\alpha}\frac{dP_\alpha}{dt}H+b\frac{\partial E_v}{\partial t}\right]+\tilde{\nabla}\cdot(\rho_\alpha\mathbf{Q}_\alpha)+\\ \rho_\alpha(\mathbf{q}_\alpha\cdot\mathbf{n})|_T-\rho_\alpha(\mathbf{q}_\alpha\cdot\mathbf{n})|_B=\tilde{R}_\alpha\end{aligned} \tag{H.3}$$

where the up-scaled volumetric strain E_v is defined by Eq. (I.4). The average porosity Φ [-] is defined as

$$\Phi=\frac{1}{H}\int_{\zeta_B}^{\zeta_T}\phi dz \tag{H.4}$$

and the average saturation S_α [-] of phase α is defined as

$$S_\alpha=\frac{1}{H}\int_{\zeta_B}^{\zeta_T}\hat{s}_\alpha dz \tag{H.5}$$

The up-scaled source/sink-term $\tilde{R}_\alpha$ [kg/m^2/s] is defined as:

$$\tilde{R}_\alpha=\int_{\zeta_B}^{\zeta_T}R_\alpha dz \tag{H.6}$$

The product of porosity and saturation; $s_\alpha \phi$, constitute the volume fraction of the porous media where the fluid phase α can flow, see e.g. Eq. (4.43), and here we assume that an average value is a good representative volume fraction. The integrated Darcy flux is defined as

$$\mathbf{Q}_\alpha = \int_{\zeta_B}^{\zeta_T} \mathbf{q}_\alpha dz \tag{H.7}$$

and will be derived later in section H.5. The integrated pore pressure P_s [Pa] is obtained from Eq. (4.50):

$$P_s = \int_{\zeta_B}^{\zeta_T} p_s dz = \int_{\zeta_B}^{\zeta_T} (p_w + \hat{s}_n p_c)\, dz \tag{H.8}$$

and its time derivative:

$$\frac{dP_s}{dt} = \int_{\zeta_B}^{\zeta_T} \frac{d}{dt}(p_w + \hat{s}_n p_c)\, dz \tag{H.9}$$

The pore pressure and its time derivative will be derived in section H.4. The two last terms in Eq. (H.3) are the vertically integrated net flux of the fluid phases leaving and entering the aquifer, for a confined aquifer (and if flat) these will be zero. A typically useful case that will be considered here is a partially confined aquifer where the non-wetting phase is confined to the aquifer, but the wetting phase exists in the aquifer and the surrounding formations and constitute a continuous phase with a continuous pressure profile across the aquifer. This is not always the case, but it is a very representative case and does not limit the validity of the equations derived in the following sections.

By assuming Vertical Equilibrium one can exploit the capillary pressure curve to derive the non-linear structure of the solution variable $\hat{s}_\alpha$ [84]. When ignoring hysteresis in the capillary pressure function, the inverted capillary saturation can be solved for by inverting the capillary pressure function such that $s_\alpha = p_c^{-1}(p_n - p_w)$, and, since the capillary pressure is in vertical equilibrium, the inverted capillary saturation becomes a distribution over the vertical direction z; $\hat{s}_\alpha(z)$. The details will be given in a later section.

H.2 Coarse-scale phase pressure

First we look at how the phase-pressures vary in the vertical direction. The vertical equilibrium (VE) assumption means that the vertical change in the fluid potential is negligible or constant; $\partial p_\alpha / \partial z + \rho_\alpha g \approx 0$. One interpretation is that the vertical flux is negligible and from this assumption we can thus evaluate the pressure at position z relative to a datum pressure at $z = \zeta_p$ by solving the following differential equation:

$$\int_{\zeta_p}^{z} \left(\frac{\partial p_\alpha}{\partial z} + \rho_\alpha g \right) dz = 0 \tag{H.10}$$

After integration and rearranging:

$$p_\alpha(z) - p_\alpha(\zeta_p) = -g \int_{\zeta_p}^{z} \rho_\alpha dz \tag{H.11}$$

By the definition of the coarse-scale pressure:

$$\boxed{P_\alpha = p_\alpha(\zeta_p)} \tag{H.12}$$

the fine-scale pressure can therefore be written in terms of the coarse-scale pressure according to:

$$p_\alpha(z) = P_\alpha - g\int_{\zeta_p}^{z} \rho_\alpha dz \tag{H.13}$$

For the assumption that the density is approximately constant in the vertical direction (across the direction of integration), it is simply expressed as:

$$\boxed{p_\alpha(z) = P_\alpha - \rho_\alpha g(z-\zeta_p)} \tag{H.14}$$

In more general terms of independent variables, Eq. (H.14) can be expressed as:

$$p_\alpha(x,y,z,t) = P_\alpha(x,y,t) - \rho_\alpha g(z-\zeta_p(x,y)) \tag{H.15}$$

where we have made the approximation that the datum is fixed in time (and that $P_\alpha(x,y,t)$ [Pa] is the fluid pressure of phase α at the pressure datum, see Eq. (H.12)). It has not been investigated where the datum should be, but for convenience it is used throughout this thesis that the datum is the bottom of the aquifer; $\zeta_p = \zeta_B(x,y)$. Eq. (H.15) is schematically illustrated for a continuous fluid phase α in Fig. H.1.

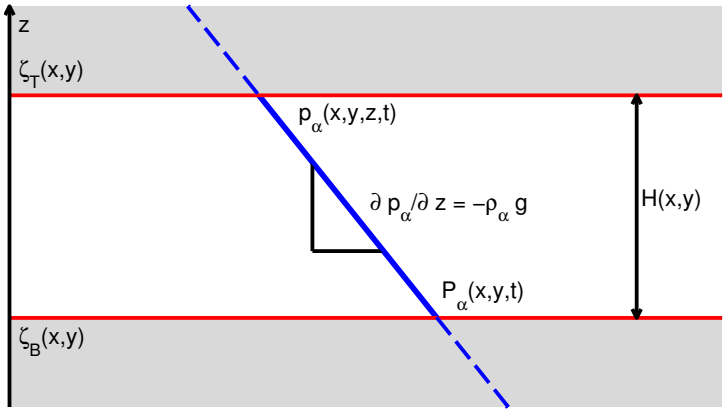

Figure H.1: Vertical Equilibrium (VE) assumption: pressure profile (blue line) of fluid phase α has a constant gradient: $\rho_\alpha g$. The white area represents the aquifer and the red lines are the upper- and lower bounds of the aquifer.

H.3 Coarse-scale capillary pressure and saturation

Due to the assumption of vertical equilibrium, the capillary pressure, $p_c = p_n - p_w$, must also be satisfied for coarse scale pressures (using Eq. (H.14) for the wetting and non-wetting phase), it can be obtained that:

$$p_c = P^{cap} + \Delta\rho g(z-\zeta_p) \tag{H.16}$$

where $\Delta\rho$ [kg/m^3] is the density difference of the phases and P^{cap} [Pa] is the coarse scale capillary pressure at the pressure datum:

$$\boxed{\Delta\rho = \rho_w - \rho_n} \tag{H.17}$$

$$\boxed{P^{cap} = P_n - P_w} \tag{H.18}$$

Assuming that the capillary pressure function p_c is a monotone function of the saturation (ignoring hysteresis, see Appendix E), the capillary pressure p_c in Eq. (H.16) can be inverted to give the capillary saturation s_α^{cap} (in terms of coarse scale variables):

$$\hat{s}_{e\alpha}(z) = s_{e\alpha}^{cap}(P^{cap}, z) = s_{e\alpha}^{cap}\left(P^{cap} + \Delta\rho g(z - \zeta_p)\right) \tag{H.19}$$

where the hat in $\hat{s}_{e\alpha}$ is used to indicate that it is expressed as a function of coarse scale variables. Note also that the capillary pressure function can only distinguish effective saturation defined by Eq. (4.46), hence the capillary saturation is an effective saturation as indicated (by the lowercase e).

The fine scale capillary pressure is defined as [83]:

$$p_c(s_n) = \alpha(1 - s_{en})^{-1/2} + \beta \tag{H.20}$$

where it can be seen that $\gamma := \alpha + \beta$ corresponds to the entry pressure in the capillary pressure function give by [27]. Other expressions for capillary pressures, e.g. van Genuchten [116] (see Appendix E for others). By equating $\hat{s}_{en}$ and s_{en}, Eqs. (H.16) and (H.20) can be compared to obtain:

$$\alpha(1 - s_{en})^{-1/2} + \beta = P^{cap} + \Delta\rho g(z - \zeta_p) \tag{H.21}$$

where the interface ζ corresponding to $s_{en} = 0$ (the bottom of two-phase region) can be defined. From Eq. (H.21) it is given that

$$\gamma = P^{cap} + \Delta\rho g(z - \zeta_p) \tag{H.22}$$

To proceed, Nordbotten and Dahle [83] define two dimensionless parameters:

$$\boxed{B = \frac{\Delta\rho g H}{\alpha}} \tag{H.23}$$

$$\boxed{P_*^{cap} = \frac{P^{cap} - \beta}{\Delta\rho g H}} \tag{H.24}$$

which can be rearranged to give the expression for the coarse-scale capillary pressure:

$$\boxed{P^{cap} = \Delta\rho g H P_*^{cap} + \beta} \tag{H.25}$$

Combining Eqs. (H.22), (H.23) and (H.24) gives for the interface where s_{en} is zero, ζ:

$$\boxed{\zeta = H\left(\frac{1}{B} - P_*^{cap}\right)} \tag{H.26}$$

where ζ [m] is the defined as the height above the bottom aquifer; $\zeta_B \leq \zeta < \zeta_T$. By inverting the capillary pressure function, Eq. (H.20), the effective capillary saturation is:

$$s_{en}^{cap} = 1 - \left(\frac{\alpha}{p_c - \beta}\right)^2 \tag{H.27}$$

Combining Eqs. (H.16) and (H.27), and the dimensionless numbers in Eqs. (H.23) and (H.24), leads to the expression for the saturation in terms of coarse-scale variables:

$$\hat{s}_{en}(P_*^{cap}) = \begin{cases} 0, & 0 \le \zeta \\ 1 - B^{-2}\left(P_*^{cap} + \dfrac{z-\zeta_p}{H}\right)^{-2}, & \zeta < z \le H \end{cases} \tag{H.28}$$

It can be seen that the saturation profile across the aquifer is now expressed as a function of the vertical position z. This is illustrated in Fig. H.2, where the phase pressures, capillary pressure and saturation can be expressed as function of z and coarse-scale variables on the datum.

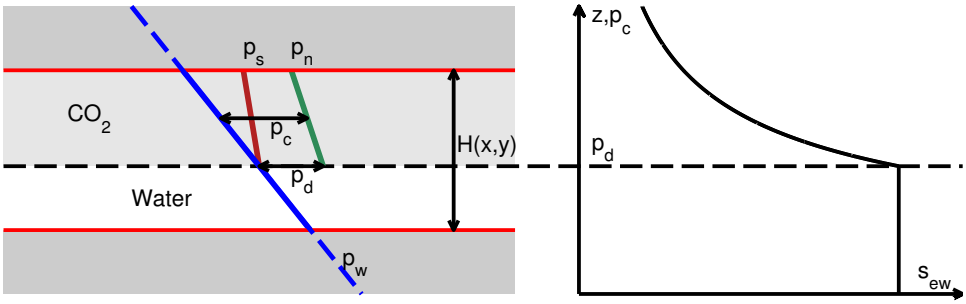

Figure H.2: Schematic comparison of the phase pressure and pore pressure profiles across an aquifer in vertical equilibrium with the capillary pressure function. p_d [Pa] is the entry pressure in the capillary pressure function. The horizontal dashed line indicates where $s_{en} = 0$ and the light grey area indicates the two-phase region where the CO_2 is. Here the aquifer is assumed to be confining for the non-wetting phase and the dashed blue lines indicate the continuity in the wetting phase pressure. Figure modified from [25].

From Eq. (H.5) the average effective saturation S_{en} can now be evaluated explicitly. Integrating across the aquifer, we have that, assuming $\zeta = 0$:

$$S_{en} = \frac{1}{H}\int_0^H \hat{s}_{en}(z)dz = \frac{1}{H}\int_0^H \left[1 - \frac{B^{-2}}{\left(P_*^{cap} + \frac{z}{H}\right)^2}\right] dz = 1 + \frac{1}{B^2}\left[\frac{1}{P_*^{cap}+1} - \frac{1}{P_*^{cap}}\right] \tag{H.29}$$

which can be inverted for P_*^{cap} to give

$$P_*^{cap} = \frac{1}{2}\left(-1 \pm \sqrt{1 + \frac{4B^{-2}}{1-S_{en}}}\right) \tag{H.30}$$

The positive root is plotted in Fig. H.3 (upper left). When $\zeta > 0$:

$$S_{en} = \frac{1}{H}\int_\zeta^H \left[1 - \frac{B^{-2}}{\left(P_*^{cap} + \frac{z}{H}\right)^2}\right] dz = 1 - \frac{\zeta}{H} + \frac{1}{B^2}\left[\frac{1}{P_*^{cap}+1} - \frac{1}{P_*^{cap}+\frac{\zeta}{H}}\right] \tag{H.31}$$

and using Eq. (H.26), it can be obtained that

$$P_*^{cap} = \frac{1}{B} + \frac{S_{en}-2}{2} \pm \frac{1}{2}\sqrt{S_{en}^2 + \frac{4S_{en}}{B}} \tag{H.32}$$

which is plotted in Fig. H.3 (upper center). Note that in both Eqs. (H.30) and (H.32) we are interested in the positive root. From Eq. (H.26), Eqs. (H.29) and (H.31) the critical dimensionless capillary pressure and critical non-wetting saturation of the fringe corresponding to $\zeta = 0$ can be derived:

$$\boxed{P_*^{crit} = \frac{1}{B}} \tag{H.33}$$

$$\boxed{S_{en}^{crit} = \frac{B}{B+1}} \tag{H.34}$$

These critical numbers are measures of when the interface ζ reaches the bottom of the aquifer. When $P_*^{cap} \geq P_*^{crit}$ or $S_{en} \geq S_{en}^{crit}$ then $\zeta \geq \zeta_B$ and the capillary fringe is within the aquifer. In Fig. H.3 (upper right) both Eqs. (H.29) and (H.31) are plotted together and the intersections are indicated with the critical numbers P_*^{crit} and S_{en}^{crit}.

Eqs. (H.30) and (H.32) are plotted in figure H.3 (upper figures), along with their derivatives (lower figures).

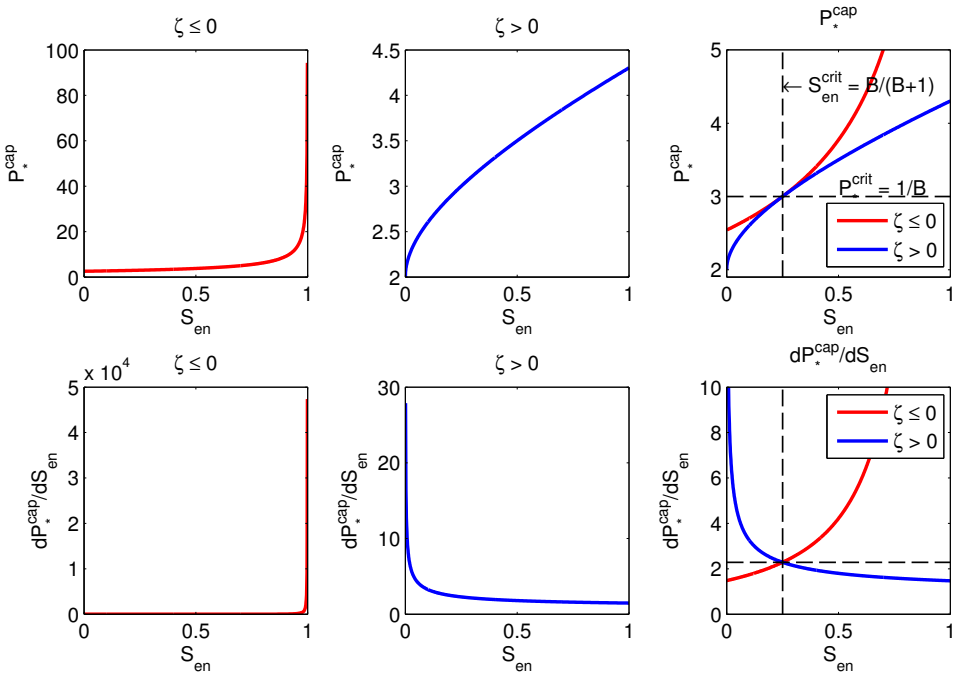

Figure H.3: Plot of P_*^{crit} as function of saturation s_{en} (upper) and their derivatives (lower). Eq. (H.30) is plotted in the upper left figure, Eq. (H.32) is plotted in the upper middle figure and in the upper right they are plotted together. The derivatives of the functions are plotted in the lower figures. The curves are calculated using $B = 1/3$.

H.4 Coarse-scale pore pressure

The coarse-scale pore pressure P_s is obtained by solving the integral in Eq. (H.8). Inserting for the coarse-scale wetting pressure from Eq. (H.14) (assuming constant density in the vertical direction) and capillary pressure Eq. (H.16), defining datum to be the bottom of the aquifer, $\zeta_P = \zeta_B$:

$$P_s = \int_{\zeta_B}^{\zeta_T} [P_w - \rho_w g(z-\zeta_B)]\,dz + \int_{\zeta_p}^{\zeta_T} \hat{s}_n \left[P^{cap} + \Delta\rho g(z-\zeta_p)\right] dz \tag{H.35}$$

Using Eq. (H.24) and rearranging

$$P_s = \int_{\zeta_B}^{\zeta_T} [P_w - \rho_w g(z-\zeta_B)]\,dz + \int_{\zeta_p}^{\zeta_T} \hat{s}_n \left[\beta + \Delta\rho g H\left(P_*^{cap} + \frac{z-\zeta_p}{H}\right)\right] dz \tag{H.36}$$

Inserting for the reconstructed fine-scale saturation $\hat{s}_n$, using Eq. (H.28) and the correlation between saturation and effective saturation (see Eq. (4.46)), and using Eq. (H.23):

$$\begin{aligned} P_s = &\int_{\zeta_B}^{\zeta_T} [P_w - \rho_w g(z-\zeta_B)]\,dz + \\ &\int_{\zeta_p}^{\zeta_T} \left[1 - \frac{1}{B^2\left(P_*^{cap} + \frac{z-\zeta_p}{H}\right)^2}\right] \left[\beta + \alpha B\left(P_*^{cap} + \frac{z-\zeta_p}{H}\right)\right] dz \end{aligned} \tag{H.37}$$

Evaluation of the first integral (of the wetting-phase pressure) gives:

$$H\left(P_w - \frac{1}{2}\rho_w g(\zeta_T + \zeta_B) + \rho_w g \zeta_P\right) \tag{H.38}$$

By expanding the second integral (the $\hat{s}_n p_c$-term in Eq. (H.8)) it is obtained that:

$$\int_{\zeta_p}^{\zeta_T} \left[\beta + \alpha B\left(P_*^{cap} + \frac{z-\zeta_p}{H}\right) - \frac{\beta}{B^2\left(P_*^{cap} + \frac{z-\zeta_p}{H}\right)^2} - \frac{\alpha}{B\left(P_*^{cap} + \frac{z-\zeta_p}{H}\right)}\right] dz \tag{H.39}$$

which can be evaluated explicitly in terms of constants and coarse-scale variables; $P_s = P_s(P_w, B, H, P_*^{cap})$.

For a water-wet rock or when capillary pressure can be ignored ($p_c \ll p_s$), e.g. when non-wetting saturation become small, a reasonable approximation is that $p_s \approx p_w$. This greatly simplifies the integration and expression for P_s. Using the same argument, the time derivative of P_s can be approximated as (here for $\zeta_P = \zeta_B$):

$$\boxed{\frac{\partial P_s}{\partial t} = \frac{\partial}{\partial t}\left(HP_w - \frac{1}{2}\rho_w g H^2\right) = H\left[\frac{\partial P_w}{\partial t} + \frac{P_w}{H}\frac{\partial H}{\partial t} - \rho_w g \frac{\partial H}{\partial t}\right]} \tag{H.40}$$

Otherwise, Eq. (H.39) needs to be evaluated and recognising that the derivative now becomes:

$$\partial P_s = \frac{\partial P_s}{\partial P_w}\partial P_w + \frac{\partial P_s}{\partial B}\partial B + \frac{\partial P_s}{\partial H}\partial H + \frac{\partial P_s}{\partial P_*^{cap}}\partial P_*^{cap} \tag{H.41}$$

This evaluates to a very large expression that is best evaluated using a symbolic math software to avoid (human) errors.

H.5 Coarse-scale flux

Here $\mathbf{Q}_\alpha$ in Eq. (H.7) will be evaluated. Starting from Eq. (4.21) in [81], and assuming that the vertical permeability is constant (or can be represented by some representative, effective value), that the phase density is constant in the vertical (integration) direction and that the mobility can be expressed by coarse-scale variables, the flux $\mathbf{Q}_\alpha$ can be expressed as:

$$\mathbf{Q}_\alpha = -\frac{\Lambda_\alpha \mathbf{K}}{\mu_\alpha} \int_{\zeta_B}^{\zeta_T} \tilde{\nabla} p_\alpha dz \tag{H.42}$$

where Λ_α [-] is the average mobility[1] (in terms of coarse-scale variables) and $\mathbf{K}$ [m·m^2] is the integrated permeability:

$$\Lambda_\alpha := \frac{1}{\mathbf{K}} \int_{\zeta_B}^{\zeta_T} \mathbf{k} \lambda_\alpha(\hat{s}_\alpha) dz \tag{H.43}$$

$$\mathbf{K} = \int_{\zeta_B}^{\zeta_T} \mathbf{k} dz \tag{H.44}$$

p_α [Pa] is the phase pressure in terms of coarse scale pressure from Eq. (H.13), or Eq. (H.14) for constant density, which will be used here.

H.5.1 Coarse mobility

The coarse-scale mobilities are derived from power-based relative permeability functions:

$$\lambda_n(s_n) = \lambda_c s_{en}^p \tag{H.45}$$

$$\lambda_w(s_n) = \lambda_b (1 - s_{en})^q \tag{H.46}$$

where λ_c and λ_b [-] are constants describing the maximum value of the relative permeability for the non-wetting and wetting phase, respectively. The phase mobility in Eq. (H.43) can now be derived by using the pseudo-capillary-pressure-saturation function, P_*^{cap}, and the reconstructed saturation $\hat{s}_{en}$ in Eq. (H.28). Assume that the effective relative permeability coefficients λ_c and λ_b are constant (in the vertical direction) and use the following simplifying notations (from [83])

$$Q(u,p) = \frac{1}{B} \sum_{i=0}^{p} \binom{p}{i} \frac{(-1)^i}{1-2i} u^{1-2i}, \quad Q(u,q) = \frac{1}{B} \sum_{i=0}^{q} \binom{q}{i} \frac{(-1)^i}{1-2i} u^{1-2i}. \tag{H.47}$$

where

$$\binom{k}{n} = \frac{n!}{k!(n-k)!} \tag{H.48}$$

it is obtained as an example for the non-wetting phase mobility when $\zeta = 0$:

$$\begin{aligned}
\Lambda_n(P_*^{cap}) &:= \frac{1}{H} \int_0^H \lambda_n(\hat{s}_n) dz = \frac{\lambda_c}{H} \int_0^H s_{en}^p dz = \frac{\lambda_c}{H} \int_0^H \left[1 - \frac{B^{-2}}{(P_*^{cap} + \frac{z}{H})^2} \right]^p dz \\
&= \lambda_c \int_0^1 \sum_{i=0}^{p} \binom{p}{i} (-1)^i (BP_*^{cap} + Bu)^{-2i} du \\
&= \lambda_c \sum_{i=0}^{p} \binom{p}{i} \frac{(-1)^i}{B(1-2i)} \left[(BP_*^{cap} + B)^{1-2i} - (BP_*^{cap})^{1-2i} \right]
\end{aligned} \tag{H.49}$$

[1] Normally mobility depends on viscosity, here the term is used for the relative permeability scaled with a maximum value.

A similar operation for $\zeta > 0$ gives for the coarse non-wetting phase mobility:

$$\Lambda_n(S_n) = \begin{cases} \lambda_c \left[Q(BP_*^{cap} + B, p) - Q(BP_*^{cap}, p) \right] & \zeta = 0, \\ \lambda_c \left[Q(BP_*^{cap} + B, p) - Q(1, p) \right] & \zeta > 0. \end{cases} \tag{H.50}$$

And similarly for the coarse wetting phase mobility:

$$\Lambda_w(S_n) = \begin{cases} \lambda_b \sum_{i=0}^{q} \binom{q}{i} (-1)^i \left[Q(BP_*^{cap} + B, i) - Q(BP_*^{cap}, i) \right] & \zeta = 0, \\ \lambda_b \sum_{i=0}^{q} \binom{q}{i} (-1)^i \left[Q(BP_*^{cap} + B, i) - Q(1, i) \right] + \left(\frac{1}{B} - P_*^{cap} \right) & \zeta > 0. \end{cases} \tag{H.51}$$

Note that to account for the mobility of the wetting phase up to the capillary fringe; $\zeta_B \leq z < \zeta$, the term $\zeta/H = 1/B - P_*^{cap}$ from Eq. (H.26) is added to the second equation for the coarse wetting phase mobility.

Example; coarse mobility

Explicit expressions for the wetting and non-wetting phase mobilities, Eqs. (H.50) and (H.51), respectively can be given for $p = 2$ and $q = 3$ as:

$$\Lambda_n(S_{en}) = \begin{cases} \lambda_c \left(\dfrac{P_*^{cap} - B^2(2(P_*^{cap})^4 + 4(P_*^{cap})^3 + 2(P_*^{cap})^2) + (P_*^{cap})^2 + 1/3}{B^4 (P_*^{cap})^3 (P_*^{cap} + 1)^3} \right) & \zeta \leq 0, \\ \lambda_c \left(\dfrac{(B + BP_*^{cap} - 1)^3 (B + BP_*^{cap} + 1/3)}{B^4 (P_*^{cap} + 1)^3} \right) & \zeta > 0. \end{cases} \tag{H.52}$$

$$\Lambda_w(S_{en}) = \begin{cases} -\lambda_b \left(\dfrac{1}{5B^6 (P_*^{cap} + 1)^5} - \dfrac{1}{5B^6 (P_*^{cap})^5} \right) & \zeta \leq 0, \\ -\lambda_b \left(\dfrac{1}{5B^6 (P_*^{cap} + 1)^5} - \dfrac{1}{5B} \right) + \dfrac{1}{B} - P_*^{cap} & \zeta > 0. \end{cases} \tag{H.53}$$

The mobilities are plotted in Fig. H.4. The solid lines are the average mobility in the aquifer that have the values $0 \geq \Lambda_w \geq \lambda_b$ and $0 \geq \Lambda_n \geq \lambda_c$ for the wetting-phase and non-wetting phase, respectively. It can be seen how the two expressions for wetting and non-wetting phase mobility tangent to one another at the critical numbers P_*^{crit} and S_{en}^{crit}.

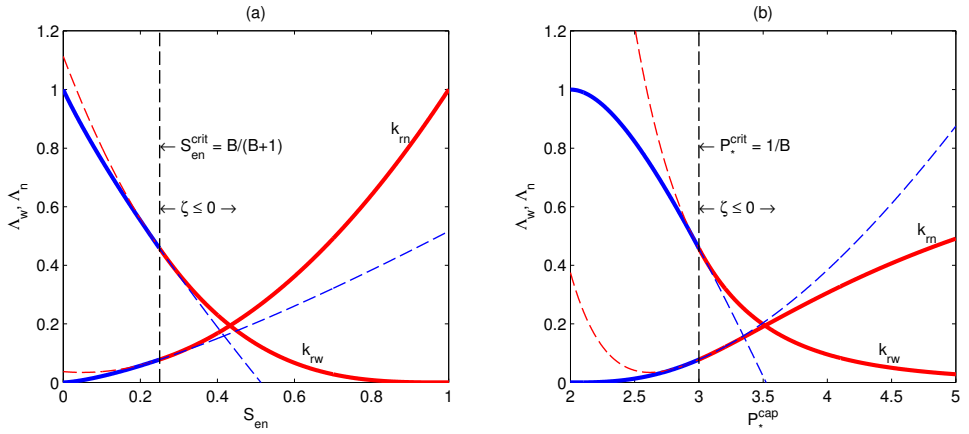

Figure H.4: Plots of wetting and non-wetting phase mobility; Eqs. (H.50) and (H.51). Parameters: $p = 2$ and $q = 3$, $\lambda_b = \lambda_c = 1$, $H = 10$ m, $\gamma = 10^5$ Pa, $\beta = 10^4$ Pa and $\Delta\rho = 300$ kg/m^3.

H.5.2 Coarse-scale flux, wetting phase

Looking at the wetting phase flux; $\mathbf{Q}_w$, and focusing on the integral in Eq. (H.42) for the wetting phase, and using Leibnitz' rule, it can be expressed as:

$$\int_{\zeta_B}^{\zeta_T} \nabla p_w dz = \nabla \int_{\zeta_B}^{\zeta_T} p_w dz - p_w \nabla \zeta_T|_T + p_w \nabla \zeta_B|_B \tag{H.54}$$

By using Eq. (H.14) for p_w, it is obtained that:

$$\begin{aligned}\int_{\zeta_B}^{\zeta_T} \nabla p_w dz =& \nabla \int_{\zeta_B}^{\zeta_T} [P_w - \rho_w g(z-\zeta_P)]\, dz - \\ & [P_w - \rho_w g(\zeta_T - \zeta_P)]\nabla\zeta_T + [P_w - \rho_w g(\zeta_B - \zeta_P)]\nabla\zeta_B\end{aligned} \tag{H.55}$$

After evaluating the integral and rearranging it reduces to:

$$\int_{\zeta_B}^{\zeta_T} \nabla p_w dz = H\,[\nabla P_w + \rho_w g \nabla \zeta_P] \tag{H.56}$$

where the change in density is ignored because $\left(1 - \frac{1}{2}\rho_w g H^2 \frac{\partial \rho_w}{\partial P_w}\right) \approx 1$. Thus, the final expressions for the coarse-scale fluxes are given as (from Eq. (H.42), and using Eq. (H.56)):

$$\boxed{\mathbf{Q}_w = -\frac{\Lambda_w \mathbf{K} H}{\mu_w}\,[\nabla P_w + \rho_w g \nabla \zeta_P]} \tag{H.57}$$

H.5.3 Coarse-scale flux, non-wetting phase

Looking at the non-wetting phase flux; $\mathbf{Q}_n$, focusing on the integral in Eq. (H.42), we have from the definition of capillary pressure that $p_n = p_w + p_c$ that it can be expressed as:

$$\int_{\zeta_B}^{\zeta_T} \nabla p_n dz = \int_{\zeta_B}^{\zeta_T} \nabla p_w dz + \int_{\zeta_B}^{\zeta_T} \nabla p_c dz \tag{H.58}$$

The first integral on the right hand side is defined in Eq. (H.56), and focusing on the capillary pressure-term (last integral):

$$\int_{\zeta_B}^{\zeta_T} \nabla p_c dz = \nabla \int_{\zeta_B}^{\zeta_T} [P^{cap} + \Delta\rho g(z-\zeta_P)]\, dz - [P^{cap} + \Delta\rho g(\zeta_T - \zeta_P)]\nabla\zeta_T + [P^{cap} + \Delta\rho g(\zeta_B - \zeta_P)]\nabla\zeta_B \tag{H.59}$$

After evaluating the integral and rearranging we obtain:

$$\int_{\zeta_B}^{\zeta_T} \nabla p_c dz = H\left[\nabla P^{cap} - \Delta\rho g \nabla\zeta_P\right] \tag{H.60}$$

where the coarse capillary pressure P^{cap} is given by Eq. (H.24) ($P^{cap} = P_*^{cap}\Delta\rho gH + \beta$) such that Eq. (H.60) can be expressed as:

$$\int_{\zeta_B}^{\zeta_T} \nabla p_c dz = H\left[\nabla(P_*^{cap}\Delta\rho gH) - \Delta\rho g\nabla\zeta_P\right] = \Delta\rho gH\left[H\nabla P_*^{cap} + P_*^{cap}\nabla H - \nabla\zeta_P\right] \tag{H.61}$$

Since $P_*^{cap} = P_*^{cap}(S_{en}, B)$ and B is defined by Eq. (H.23); $B = \Delta\rho gH/\alpha$, the gradient of the coarse pseudo-capillary-pressure-saturation function is given by:

$$\nabla P_*^{cap} = \frac{\partial P_*^{cap}}{\partial S_n}\nabla S_n + \frac{\partial P_*^{cap}}{\partial B}\frac{\partial B}{\partial H}\nabla H \tag{H.62}$$

where $\partial P_*^{cap}/\partial B$ is derived from Eq. (H.30) (for $\zeta = 0$):

$$\int_{\zeta_B}^{\zeta_T} \nabla p_c dz = H\left[\Delta\rho g\left(P_*^{cap}\nabla H + H\left(\frac{\partial P_*^{cap}}{\partial S_n}\nabla S_n + \frac{\partial P_*^{cap}}{\partial B}\frac{\partial B}{\partial H}\nabla H\right) - \nabla\zeta_P\right)\right] \tag{H.63}$$

Thus, the final expressions for the coarse-scale fluxes are given as:

$$\boxed{\mathbf{Q}_n = -\frac{\Lambda_n \mathbf{K} H}{\mu_n}\left[\nabla P_w + \rho_n g\nabla\zeta_P + \Delta\rho g\left(H\frac{\partial P_*^{cap}}{\partial S_n}\nabla S_n + H\frac{\partial P_*^{cap}}{\partial B}\frac{\partial B}{\partial H}\nabla H + P_*^{cap}\nabla H\right)\right]} \tag{H.64}$$

remembering that P_*^{cap} is defined by Eq. (H.30) for $\zeta = 0$. Note that, similar to obtaining Eq. (H.56), the compressibility terms that comes from the derivative of $\Delta\rho$ are ignored because they are usually small (and can be cancelled in the derivation).

Appendix I

Deriving the LVD equation

To derive the expression for Σ in Eq. (6.23) we solve the following integral (where the stress tensor for linear elasticity is defined by Eq. (3.8)):

$$\begin{aligned}\Sigma = \int_{\zeta_B}^{\zeta_T} \sigma dz &= \int_{\zeta_B}^{\zeta_T} \left[\lambda\left(\nabla\cdot\mathbf{u}\right)\mathbf{I} + \mu\left(\nabla\mathbf{u} + \left(\nabla\mathbf{u}\right)^T\right)\right] dz \\ &= \lambda\int_{\zeta_B}^{\zeta_T}\left(\nabla\cdot\mathbf{u}\right) dz\mathbf{I} + \mu\int_{\zeta_B}^{\zeta_T}\left(\nabla\mathbf{u}\right) dz + \mu\int_{\zeta_B}^{\zeta_T}\left(\nabla\mathbf{u}\right)^T dz\end{aligned} \tag{I.1}$$

The first integral in the right hand side of Eq. (I.1) evaluates to:

$$\begin{aligned}&\int_{\zeta_B}^{\zeta_T}\nabla\cdot\mathbf{u}dz = \int_{\zeta_B}^{\zeta_T}\left[\frac{\partial u}{\partial x}+\frac{\partial v}{\partial y}+\frac{\partial w}{\partial z}\right]dz = \left[\int_{\zeta_B}^{\zeta_T}\frac{\partial u}{\partial x}dz + \int_{\zeta_B}^{\zeta_T}\frac{\partial v}{\partial y}dz + \int_{\zeta_B}^{\zeta_T}\frac{\partial w}{\partial z}dz\right] \\ &= \left[\frac{\partial}{\partial x}\int_{\zeta_B}^{\zeta_T} u dz + \frac{\partial}{\partial y}\int_{\zeta_B}^{\zeta_T} v dz + w_T - w_B\right] - \left(\left[u\frac{\partial\zeta_T}{\partial x} + v\frac{\partial\zeta_T}{\partial y} + 0\right] - \left[u\frac{\partial\zeta_B}{\partial x} + v\frac{\partial\zeta_B}{\partial y} + 0\right]\right) \\ &= \left[\frac{\partial}{\partial x}\int_{\zeta_B}^{\zeta_T} u dz + \frac{\partial}{\partial y}\int_{\zeta_B}^{\zeta_T} v dz\right] - \left(\left[u\frac{\partial\zeta_T}{\partial x} + v\frac{\partial\zeta_T}{\partial y} - w_T\right] - \left[u\frac{\partial\zeta_B}{\partial x} + v\frac{\partial\zeta_B}{\partial y} - w_B\right]\right) \\ &= \tilde{\nabla}\cdot\mathbf{U} - \left(\left[u\frac{\partial\zeta_T}{\partial x} + v\frac{\partial\zeta_T}{\partial y} - w_T\right] - \left[u\frac{\partial\zeta_B}{\partial x} + v\frac{\partial\zeta_B}{\partial y} - w_B\right]\right) \\ &= \tilde{\nabla}\cdot\mathbf{U} + \left(\mathbf{u}\cdot\mathbf{n}|_T - \mathbf{u}\cdot\mathbf{n}|_B\right)\end{aligned} \tag{I.2}$$

where

$$\mathbf{U} = \int_{\zeta_B}^{\zeta_T}\mathbf{u}dz \tag{I.3}$$

Note that Eq. (I.2) is also equivalent to the integrated volumetric strain:

$$E_v = \tilde{\nabla}\cdot\mathbf{U} + \left(\mathbf{u}\cdot\mathbf{n}|_T - \mathbf{u}\cdot\mathbf{n}|_B\right) \tag{I.4}$$

Evaluation of the second integral in Eq. (I.1):

$$\int_{\zeta_B}^{\zeta_T}\nabla\mathbf{u}dz=\int_{\zeta_B}^{\zeta_T}\begin{bmatrix}\frac{\partial u}{\partial x} & \frac{\partial v}{\partial x} & \frac{\partial w}{\partial x}\\ \frac{\partial u}{\partial y} & \frac{\partial v}{\partial y} & \frac{\partial w}{\partial y}\\ \frac{\partial u}{\partial z} & \frac{\partial v}{\partial z} & \frac{\partial w}{\partial z}\end{bmatrix}dz=\begin{bmatrix}\int_{\zeta_B}^{\zeta_T}\frac{\partial u}{\partial x}dz & \int_{\zeta_B}^{\zeta_T}\frac{\partial v}{\partial x}dz & \int_{\zeta_B}^{\zeta_T}\frac{\partial w}{\partial x}dz\\ \int_{\zeta_B}^{\zeta_T}\frac{\partial u}{\partial y}dz & \int_{\zeta_B}^{\zeta_T}\frac{\partial v}{\partial y}dz & \int_{\zeta_B}^{\zeta_T}\frac{\partial w}{\partial y}dz\\ \int_{\zeta_B}^{\zeta_T}\frac{\partial u}{\partial z}dz & \int_{\zeta_B}^{\zeta_T}\frac{\partial v}{\partial z}dz & \int_{\zeta_B}^{\zeta_T}\frac{\partial w}{\partial z}dz\end{bmatrix}=$$

$$\begin{bmatrix}\frac{\partial}{\partial x}\int_{\zeta_B}^{\zeta_T}udz & \frac{\partial}{\partial x}\int_{\zeta_B}^{\zeta_T}vdz & \frac{\partial}{\partial x}\int_{\zeta_B}^{\zeta_T}wdz\\ \frac{\partial}{\partial y}\int_{\zeta_B}^{\zeta_T}udz & \frac{\partial}{\partial y}\int_{\zeta_B}^{\zeta_T}vdz & \frac{\partial}{\partial y}\int_{\zeta_B}^{\zeta_T}wdz\\ u_T-u_B & v_T-v_B & w_T-w_B\end{bmatrix}-\left(\begin{bmatrix}u\frac{\partial\zeta_T}{\partial x} & v\frac{\partial\zeta_T}{\partial x} & w\frac{\partial\zeta_T}{\partial x}\\ u\frac{\partial\zeta_T}{\partial y} & v\frac{\partial\zeta_T}{\partial y} & w\frac{\partial\zeta_T}{\partial y}\\ 0 & 0 & 0\end{bmatrix}-\begin{bmatrix}u\frac{\partial\zeta_B}{\partial x} & v\frac{\partial\zeta_B}{\partial x} & w\frac{\partial\zeta_B}{\partial x}\\ u\frac{\partial\zeta_B}{\partial y} & v\frac{\partial\zeta_B}{\partial y} & w\frac{\partial\zeta_B}{\partial y}\\ 0 & 0 & 0\end{bmatrix}\right)=$$

$$\begin{bmatrix}\frac{\partial}{\partial x}\int_{\zeta_B}^{\zeta_T}udz & \frac{\partial}{\partial x}\int_{\zeta_B}^{\zeta_T}vdz & \frac{\partial}{\partial x}\int_{\zeta_B}^{\zeta_T}wdz\\ \frac{\partial}{\partial y}\int_{\zeta_B}^{\zeta_T}udz & \frac{\partial}{\partial y}\int_{\zeta_B}^{\zeta_T}vdz & \frac{\partial}{\partial y}\int_{\zeta_B}^{\zeta_T}wdz\\ 0 & 0 & 0\end{bmatrix}-\left(\begin{bmatrix}u\frac{\partial\zeta_T}{\partial x} & v\frac{\partial\zeta_T}{\partial x} & w\frac{\partial\zeta_T}{\partial x}\\ u\frac{\partial\zeta_T}{\partial y} & v\frac{\partial\zeta_T}{\partial y} & w\frac{\partial\zeta_T}{\partial y}\\ -u_T & -v_T & -w_T\end{bmatrix}-\begin{bmatrix}u\frac{\partial\zeta_B}{\partial x} & v\frac{\partial\zeta_B}{\partial x} & w\frac{\partial\zeta_B}{\partial x}\\ u\frac{\partial\zeta_B}{\partial y} & v\frac{\partial\zeta_B}{\partial y} & w\frac{\partial\zeta_B}{\partial y}\\ -u_B & -v_B & -w_B\end{bmatrix}\right)=$$

$$\tilde{\nabla}\mathbf{U}-\left(\begin{bmatrix}u\frac{\partial\zeta_T}{\partial x} & v\frac{\partial\zeta_T}{\partial x} & w\frac{\partial\zeta_T}{\partial x}\\ u\frac{\partial\zeta_T}{\partial y} & v\frac{\partial\zeta_T}{\partial y} & w\frac{\partial\zeta_T}{\partial y}\\ -u_T & -v_T & -w_T\end{bmatrix}-\begin{bmatrix}u\frac{\partial\zeta_B}{\partial x} & v\frac{\partial\zeta_B}{\partial x} & w\frac{\partial\zeta_B}{\partial x}\\ u\frac{\partial\zeta_B}{\partial y} & v\frac{\partial\zeta_B}{\partial y} & w\frac{\partial\zeta_B}{\partial y}\\ -u_B & -v_B & -w_B\end{bmatrix}\right)=$$

$$\tilde{\nabla}\mathbf{U}+(\mathbf{nu}|_T-\mathbf{nu}|_B) \tag{I.5}$$

And the third integral (in Eq. (I.1)):

$$\int_{\zeta_B}^{\zeta_T}(\nabla\mathbf{u})^T dz= \tag{I.6}$$

$$\begin{bmatrix}\frac{\partial}{\partial x}\int_{\zeta_B}^{\zeta_T}udz & \frac{\partial}{\partial y}\int_{\zeta_B}^{\zeta_T}udz & 0\\ \frac{\partial}{\partial x}\int_{\zeta_B}^{\zeta_T}vdz & \frac{\partial}{\partial y}\int_{\zeta_B}^{\zeta_T}vdz & 0\\ \frac{\partial}{\partial x}\int_{\zeta_B}^{\zeta_T}wdz & \frac{\partial}{\partial y}\int_{\zeta_B}^{\zeta_T}wdz & 0\end{bmatrix}-\left(\begin{bmatrix}u\frac{\partial\zeta_T}{\partial x} & u\frac{\partial\zeta_T}{\partial y} & -u_T\\ v\frac{\partial\zeta_T}{\partial x} & v\frac{\partial\zeta_T}{\partial y} & -v_T\\ w\frac{\partial\zeta_T}{\partial x} & w\frac{\partial\zeta_T}{\partial y} & -w_T\end{bmatrix}-\begin{bmatrix}u\frac{\partial\zeta_B}{\partial x} & u\frac{\partial\zeta_B}{\partial y} & -u_B\\ v\frac{\partial\zeta_B}{\partial x} & v\frac{\partial\zeta_B}{\partial y} & -v_B\\ w\frac{\partial\zeta_B}{\partial x} & w\frac{\partial\zeta_B}{\partial y} & -w_B\end{bmatrix}\right)=$$

$$(\tilde{\nabla}\mathbf{U})^T-\left(\begin{bmatrix}u\frac{\partial\zeta_T}{\partial x} & u\frac{\partial\zeta_T}{\partial y} & -u_T\\ v\frac{\partial\zeta_T}{\partial x} & v\frac{\partial\zeta_T}{\partial y} & -v_T\\ w\frac{\partial\zeta_T}{\partial x} & w\frac{\partial\zeta_T}{\partial y} & -w_T\end{bmatrix}-\begin{bmatrix}u\frac{\partial\zeta_B}{\partial x} & u\frac{\partial\zeta_B}{\partial y} & -u_B\\ v\frac{\partial\zeta_B}{\partial x} & v\frac{\partial\zeta_B}{\partial y} & -v_B\\ w\frac{\partial\zeta_B}{\partial x} & w\frac{\partial\zeta_B}{\partial y} & -w_B\end{bmatrix}\right)=$$

$$(\tilde{\nabla}\mathbf{U})^T+(\mathbf{un}|_T-\mathbf{un}|_B) \tag{I.7}$$

Collecting the terms, and rearrange, it is obtained that:

$$\boxed{\Sigma=\lambda\left[\tilde{\nabla}\cdot\mathbf{U}\right]\mathbf{I}+\mu\left[\tilde{\nabla}\mathbf{U}+(\tilde{\nabla}\mathbf{U})^T\right]+\left[\lambda\left(\mathbf{u}\cdot\mathbf{n}|_T-\mathbf{u}\cdot\mathbf{n}|_B\right)\mathbf{I}+\mu\left(\mathbf{nu}|_T-\mathbf{nu}|_B\right)+\mu\left(\mathbf{un}|_T-\mathbf{un}|_B\right)\right]} \tag{I.8}$$

And the complete LVD-equation:

$$\boxed{\tilde{\nabla}\cdot\Sigma+[\sigma\cdot\mathbf{n}|_T+\sigma\cdot\mathbf{n}|_B]+\int_{\zeta_B}^{\zeta_T}\mathbf{f}dz=0} \tag{I.9}$$

I.1 LVD-equation: Example in 2D

Below follows the derivation of Σ in the LVD-equation, Eq. (I.9):

$$\Sigma=\int_{\zeta_B}^{\zeta_T}\left[\lambda\left(\nabla\cdot\mathbf{u}\right)\mathbf{I}+\mu\left(\nabla\mathbf{u}+\left(\nabla\mathbf{u}\right)^T\right)\right]dz \tag{I.10}$$

$$=\int_{\zeta_B}^{\zeta_T}\left[\lambda\left[\nabla\cdot\mathbf{u}\right]\mathbf{I}+\mu\left[\nabla\mathbf{u}\right]+\mu\left[\left(\nabla\mathbf{u}\right)^T\right]\right]dz \tag{I.11}$$

$$\begin{aligned}
=&\lambda\left[\tilde{\nabla}\cdot\mathbf{U}-\left(\left[u_T\frac{\partial\zeta_T}{\partial x}-w_T\right]-\left[u_B\frac{\partial\zeta_B}{\partial x}-w_B\right]\right)\right]\mathbf{I}+\\
&\mu\left[\tilde{\nabla}\mathbf{U}-\left(\begin{bmatrix}u_T\frac{\partial\zeta_T}{\partial x} & w_T\frac{\partial\zeta_T}{\partial x}\\ -u_T & -w_T\end{bmatrix}-\begin{bmatrix}u_B\frac{\partial\zeta_B}{\partial x} & w_B\frac{\partial\zeta_B}{\partial x}\\ -u_B & -w_B\end{bmatrix}\right)\right]+\\
&\mu\left[\left(\tilde{\nabla}\mathbf{U}\right)^T-\left(\begin{bmatrix}u_T\frac{\partial\zeta_T}{\partial x} & -u_T\\ w_T\frac{\partial\zeta_T}{\partial x} & -w_T\end{bmatrix}-\begin{bmatrix}u_B\frac{\partial\zeta_B}{\partial x} & -u_B\\ w_B\frac{\partial\zeta_B}{\partial x} & -w_B\end{bmatrix}\right)\right]
\end{aligned} \tag{I.12}$$

$$\begin{aligned}
=&\lambda\left(\tilde{\nabla}\cdot\mathbf{U}\right)\mathbf{I}+\mu\left(\tilde{\nabla}\mathbf{U}+\left(\tilde{\nabla}\mathbf{U}\right)^T\right)-\\
&\lambda\left(\left[u_T\frac{\partial\zeta_T}{\partial x}-w_T\right]-\left[u_B\frac{\partial\zeta_B}{\partial x}-w_B\right]\right)\mathbf{I}-\\
&\mu\left(\begin{bmatrix}u_T\frac{\partial\zeta_T}{\partial x} & w_T\frac{\partial\zeta_T}{\partial x}\\ -u_T & -w_T\end{bmatrix}-\begin{bmatrix}u_B\frac{\partial\zeta_B}{\partial x} & w_B\frac{\partial\zeta_B}{\partial x}\\ -u_B & -w_B\end{bmatrix}\right)-\\
&\mu\left(\begin{bmatrix}u_T\frac{\partial\zeta_T}{\partial x} & -u_T\\ w_T\frac{\partial\zeta_T}{\partial x} & -w_T\end{bmatrix}-\begin{bmatrix}u_B\frac{\partial\zeta_B}{\partial x} & -u_B\\ w_B\frac{\partial\zeta_B}{\partial x} & -w_B\end{bmatrix}\right)
\end{aligned} \tag{I.13}$$

$$\begin{aligned}
\Sigma=&\lambda\left(\tilde{\nabla}\cdot\mathbf{U}\right)\mathbf{I}+\mu\left(\tilde{\nabla}\mathbf{U}+\left(\tilde{\nabla}\mathbf{U}\right)^T\right)-\\
&\lambda\left(\left[u_T\frac{\partial\zeta_T}{\partial x}-u_B\frac{\partial\zeta_B}{\partial x}\right]-\left[w_T-w_B\right]\right)\begin{bmatrix}1 & 0\\ 0 & 1\end{bmatrix}-\\
&\mu\left(\begin{bmatrix}u_T\frac{\partial\zeta_T}{\partial x}-u_B\frac{\partial\zeta_B}{\partial x} & w_T\frac{\partial\zeta_T}{\partial x}-w_B\frac{\partial\zeta_B}{\partial x}\\ -u_T--u_B & -w_T--w_B\end{bmatrix}-\begin{bmatrix}0 & 0\\ 0 & 0\end{bmatrix}\right)-\\
&\mu\left(\begin{bmatrix}u_T\frac{\partial\zeta_T}{\partial x}-u_B\frac{\partial\zeta_B}{\partial x} & -u_T--u_B\\ w_T\frac{\partial\zeta_T}{\partial x}-w_B\frac{\partial\zeta_B}{\partial x} & -w_T--w_B\end{bmatrix}-\begin{bmatrix}0 & 0\\ 0 & 0\end{bmatrix}\right)
\end{aligned} \tag{I.14}$$

$$\begin{aligned}\Sigma =&\lambda\left(\tilde{\nabla}\cdot\mathbf{U}\right)\mathbf{I}+\mu\left(\tilde{\nabla}\mathbf{U}+(\tilde{\nabla}\mathbf{U})^{T}\right)-\\&\lambda\begin{bmatrix}\left[u_T\frac{\partial\zeta_T}{\partial x}-u_B\frac{\partial\zeta_B}{\partial x}-(w_T-w_B)\right] & 0\\ 0 & \left[u_T\frac{\partial\zeta_T}{\partial x}-u_B\frac{\partial\zeta_B}{\partial x}-(w_T-w_B)\right]\end{bmatrix}-\\&\mu\begin{bmatrix}u_T\frac{\partial\zeta_T}{\partial x}-u_B\frac{\partial\zeta_B}{\partial x} & w_T\frac{\partial\zeta_T}{\partial x}-w_B\frac{\partial\zeta_B}{\partial x}\\ -u_T--u_B & -w_T--w_B\end{bmatrix}-\\&\mu\begin{bmatrix}u_T\frac{\partial\zeta_T}{\partial x}-u_B\frac{\partial\zeta_B}{\partial x} & -u_T--u_B\\ w_T\frac{\partial\zeta_T}{\partial x}-w_B\frac{\partial\zeta_B}{\partial x} & -w_T--w_B\end{bmatrix}\end{aligned}\tag{I.15}$$

$$\begin{aligned}\Sigma =&\lambda\left(\tilde{\nabla}\cdot\mathbf{U}\right)\mathbf{I}+\mu\left(\tilde{\nabla}\mathbf{U}+(\tilde{\nabla}\mathbf{U})^{T}\right)-\\&\begin{bmatrix}\lambda\left[u_T\frac{\partial\zeta_T}{\partial x}-u_B\frac{\partial\zeta_B}{\partial x}-(w_T-w_B)\right] & 0\\ 0 & \lambda\left[u_T\frac{\partial\zeta_T}{\partial x}-u_B\frac{\partial\zeta_B}{\partial x}-(w_T-w_B)\right]\end{bmatrix}-\\&\begin{bmatrix}\mu\left(u_T\frac{\partial\zeta_T}{\partial x}-u_B\frac{\partial\zeta_B}{\partial x}\right) & \mu\left(w_T\frac{\partial\zeta_T}{\partial x}-w_B\frac{\partial\zeta_B}{\partial x}\right)\\ -\mu\left(u_T-u_B\right) & -\mu\left(w_T-w_B\right)\end{bmatrix}-\\&\begin{bmatrix}\mu\left(u_T\frac{\partial\zeta_T}{\partial x}-u_B\frac{\partial\zeta_B}{\partial x}\right) & -\mu\left(u_T-u_B\right)\\ \mu\left(w_T\frac{\partial\zeta_T}{\partial x}-w_B\frac{\partial\zeta_B}{\partial x}\right) & -\mu\left(w_T-w_B\right)\end{bmatrix}\end{aligned}\tag{I.16}$$

$$\begin{aligned}\Sigma =&\lambda\left(\tilde{\nabla}\cdot\mathbf{U}\right)\mathbf{I}+\mu\left(\tilde{\nabla}\mathbf{U}+(\tilde{\nabla}\mathbf{U})^{T}\right)-\\&\begin{bmatrix}\lambda\left[u_T\frac{\partial\zeta_T}{\partial x}-u_B\frac{\partial\zeta_B}{\partial x}-(w_T-w_B)\right]+2\mu\left(u_T\frac{\partial\zeta_T}{\partial x}-u_B\frac{\partial\zeta_B}{\partial x}\right) & \mu\left(w_T\frac{\partial\zeta_T}{\partial x}-w_B\frac{\partial\zeta_B}{\partial x}\right)-\mu\left(u_T-u_B\right)\\ \mu\left(w_T\frac{\partial\zeta_T}{\partial x}-w_B\frac{\partial\zeta_B}{\partial x}\right)-\mu\left(u_T-u_B\right) & \lambda\left[u_T\frac{\partial\zeta_T}{\partial x}-u_B\frac{\partial\zeta_B}{\partial x}-(w_T-w_B)\right]-2\mu\left(w_T-w_B\right)\end{bmatrix}\end{aligned}\tag{I.17}$$

$$\begin{aligned}\Sigma =&\lambda\left(\tilde{\nabla}\cdot\mathbf{U}\right)\mathbf{I}+\mu\left(\tilde{\nabla}\mathbf{U}+(\tilde{\nabla}\mathbf{U})^{T}\right)-\\&\begin{bmatrix}(\lambda+2\mu)\left(u_T\frac{\partial\zeta_T}{\partial x}-u_B\frac{\partial\zeta_B}{\partial x}\right)-\lambda\left(w_T-w_B\right) & \mu\left(w_T\frac{\partial\zeta_T}{\partial x}-w_B\frac{\partial\zeta_B}{\partial x}\right)-\mu\left(u_T-u_B\right)\\ \mu\left(w_T\frac{\partial\zeta_T}{\partial x}-w_B\frac{\partial\zeta_B}{\partial x}\right)-\mu\left(u_T-u_B\right) & \lambda\left(u_T\frac{\partial\zeta_T}{\partial x}-u_B\frac{\partial\zeta_B}{\partial x}\right)-(\lambda+2\mu)\left(w_T-w_B\right)\end{bmatrix}\end{aligned}\tag{I.18}$$

$$\Sigma = \begin{bmatrix} (\lambda+2\mu)\dfrac{\partial U}{\partial x} & \mu\dfrac{\partial W}{\partial x} \\ \mu\dfrac{\partial W}{\partial x} & \lambda\dfrac{\partial U}{\partial x} \end{bmatrix} - \begin{bmatrix} (\lambda+2\mu)\left(u_T\dfrac{\partial \zeta_T}{\partial x} - u_B\dfrac{\partial \zeta_B}{\partial x}\right) - \lambda\left(w_T - w_B\right) & \mu\left(w_T\dfrac{\partial \zeta_T}{\partial x} - w_B\dfrac{\partial \zeta_B}{\partial x}\right) - \mu\left(u_T - u_B\right) \\ \mu\left(w_T\dfrac{\partial \zeta_T}{\partial x} - w_B\dfrac{\partial \zeta_B}{\partial x}\right) - \mu\left(u_T - u_B\right) & \lambda\left(u_T\dfrac{\partial \zeta_T}{\partial x} - u_B\dfrac{\partial \zeta_B}{\partial x}\right) - (\lambda+2\mu)\left(w_T - w_B\right) \end{bmatrix} \tag{I.19}$$

$$\Sigma = \begin{bmatrix} (\lambda+2\mu)\frac{\partial U}{\partial x} - (\lambda+2\mu)\left(u_T\frac{\partial \zeta_T}{\partial x} - u_B\frac{\partial \zeta_B}{\partial x}\right) + \lambda\left(w_T - w_B\right) & \mu\frac{\partial W}{\partial x} - \mu\left(w_T\dfrac{\partial \zeta_T}{\partial x} - w_B\dfrac{\partial \zeta_B}{\partial x}\right) + \mu\left(u_T - u_B\right) \\ \mu\frac{\partial W}{\partial x} - \mu\left(w_T\frac{\partial \zeta_T}{\partial x} - w_B\frac{\partial \zeta_B}{\partial x}\right) + \mu\left(u_T - u_B\right) & \lambda\frac{\partial U}{\partial x} - \lambda\left(u_T\frac{\partial \zeta_T}{\partial x} - u_B\frac{\partial \zeta_B}{\partial x}\right) + (\lambda+2\mu)\left(w_T - w_B\right) \end{bmatrix} \tag{I.20}$$

Finally, for a two-dimensional case (plane strain assumption), the integrated stress tensor Σ can be expressed as:

$$\Sigma = \begin{bmatrix} (\lambda+2\mu)\left(\frac{\partial U}{\partial x} - u_T\frac{\partial \zeta_T}{\partial x} + u_B\frac{\partial \zeta_B}{\partial x}\right) + \lambda\left(w_T - w_B\right) & \mu\left(\frac{\partial W}{\partial x} - w_T\frac{\partial \zeta_T}{\partial x} + w_B\frac{\partial \zeta_B}{\partial x}\right) + \mu\left(u_T - u_B\right) \\ \mu\left(\frac{\partial W}{\partial x} - w_T\frac{\partial \zeta_T}{\partial x} + w_B\frac{\partial \zeta_B}{\partial x}\right) + \mu\left(u_T - u_B\right) & (\lambda+2\mu)\left(w_T - w_B\right) + \lambda\left(\frac{\partial U}{\partial x} - u_T\frac{\partial \zeta_T}{\partial x} + u_B\frac{\partial \zeta_B}{\partial x}\right) \end{bmatrix} \tag{I.21}$$

I.2 LVD-equation: 3D

$$\Sigma = \begin{bmatrix} \Sigma_x & \Sigma_{xy} & \Sigma_{xz} \\ \Sigma_{yx} & \Sigma_y & \Sigma_{yz} \\ \Sigma_{zx} & \Sigma_{zy} & \Sigma_z \end{bmatrix} \tag{I.22}$$

where

$$\Sigma_x = (\lambda+2\mu)\left(\frac{\partial U}{\partial x} - u_T\frac{\partial \zeta_T}{\partial x} + u_B\frac{\partial \zeta_B}{\partial x}\right) + \lambda\left(\frac{\partial V}{\partial y} - v_T\frac{\partial \zeta_T}{\partial y} + v_B\frac{\partial \zeta_B}{\partial y} + (w_T - w_B)\right) \tag{I.23}$$

$$\Sigma_y = (\lambda+2\mu)\left(\frac{\partial V}{\partial y} - v_T\frac{\partial \zeta_T}{\partial y} + v_B\frac{\partial \zeta_B}{\partial y}\right) + \lambda\left(\frac{\partial U}{\partial x} - u_T\frac{\partial \zeta_T}{\partial x} + u_B\frac{\partial \zeta_B}{\partial x} + (w_T - w_B)\right) \tag{I.24}$$

$$\Sigma_z = (\lambda+2\mu)(w_T - w_B) + \lambda\left(\frac{\partial U}{\partial x} - u_T\frac{\partial \zeta_T}{\partial x} + u_B\frac{\partial \zeta_B}{\partial x}\right) + \lambda\left(\frac{\partial V}{\partial y} - v_T\frac{\partial \zeta_T}{\partial y} + v_B\frac{\partial \zeta_B}{\partial y}\right) \tag{I.25}$$

$$\Sigma_{xy} = \mu\left(\frac{\partial V}{\partial x} - v_T\frac{\partial \zeta_T}{\partial x} + v_B\frac{\partial \zeta_B}{\partial x}\right) + \mu\left(\frac{\partial U}{\partial y} - u_T\frac{\partial \zeta_T}{\partial y} + u_B\frac{\partial \zeta_B}{\partial y}\right) \tag{I.26}$$

$$\Sigma_{xz} = \mu\left(\frac{\partial W}{\partial x} - w_T\frac{\partial \zeta_T}{\partial x} + w_B\frac{\partial \zeta_B}{\partial x}\right) + \mu\,(u_T - u_B) \tag{I.27}$$

$$\Sigma_{yz} = \mu\left(\frac{\partial W}{\partial y} - w_T\frac{\partial \zeta_T}{\partial y} + w_B\frac{\partial \zeta_B}{\partial y}\right) + \mu\,(v_T - v_B) \tag{I.28}$$

noting that the stress-tensor is symmetric: $\Sigma_{xy} = \Sigma_{yx}$, $\Sigma_{xz} = \Sigma_{zx}$ and $\Sigma_{yz} = \Sigma_{zy}$.

Appendix J

Dispersion properties

Hydrodynamic dispersion in porous media is often attributed to the stream splitting of a fluid flowing through the pores. As the fluid flows through a porous network it can not follow a straight line but is forced to follow the pore conduits and bypassing grain obstacles in a sequence of splitting and merging and spreading out. The various shapes and sizes of the pore throats and pore space slows down and speeds up and diverts the fluid, contributing to a complex transverse and longitudinal flow mechanism of the fluid. Longitudinal flow is the main flow direction and transverse flow is in the direction perpendicular to the main flow direction.

In the following discussion a brief review of dispersion is given. A simplified evaluation, as will be presented here, can give an indication of whether dispersion processes are important to consider or if they can be (safely) neglected. The *Pe*clet number (described later) is a useful quantity that can often give an indication if a process can be satisfactorily described by neglecting dispersion and this typically occurs at $Pe > 2500$ [85].

When considering a solute A of concentration c in a flowing system the two main transport mechanisms are convection; the bulk movement of the fluid, and dispersion; the spreading of the solute by (molecular) diffusion and hydrodynamic dispersion. Assuming a system where diffusion is negligible compared to hydrodynamic dispersion, the transport of A can, simplified, be described by the convection-dispersion equation (here ignoring any source/sink term):

$$\frac{\partial c}{\partial t} + \nabla \cdot (-\mathbf{D}\nabla c) + \mathbf{u}\nabla c = 0 \tag{J.1}$$

where c [kg/m^3] is the concentration of solute A, $\mathbf{u}$ [m/s] is the fluid velocity vector and $\mathbf{D}$ [m^2/s] is the dispersion tensor that is often defined as:

$$\mathbf{D} = \begin{bmatrix} D_L & 0 & 0 \\ 0 & D_{T1} & 0 \\ 0 & 0 & D_{T2} \end{bmatrix} \tag{J.2}$$

where D_L [m^2/s] is the longitudinal dispersion coefficient and D_{T1} and D_{T2} [m^2/s] are the two transverse dispersion coefficients. In 1D transport, Eq. (J.1) becomes:

$$\frac{\partial c}{\partial t} - D_L \frac{\partial^2 c}{\partial x^2} + u\frac{\partial c}{\partial x} = 0 \tag{J.3}$$

where u [m/s] is the velocity component in the x-direction and together with the following

boundary and initial conditions, Eq. (J.3) expresses an initial-boundary value problem:

$$c(x,0) = c^0 \tag{J.4}$$

$$c(0,t) = c_i \tag{J.5}$$

$$c(\infty,0) = c^0 \tag{J.6}$$

The solution to Eqs. (J.3)-(J.6) is given by [see e.g. 85, 87]:

$$c = \frac{c_i}{2}\left[erfc\left(\frac{x-ut}{2\sqrt{D_L t}}\right) + e^{\frac{ux}{D_L}} erfc\left(\frac{x+ut}{2\sqrt{D_L t}}\right)\right] \tag{J.7}$$

which can be approximated to

$$c \approx \frac{c_i}{2} erfc\left(\frac{x-ut}{2\sqrt{D_L t}}\right) \tag{J.8}$$

Eqs. (J.7) and (J.8) are plotted in Fig. J.1 (left) in terms of the dimensionless coordinates:

$$x_D = \frac{x}{L} \tag{J.9}$$

$$c_D = \frac{c - c^0}{c_i - c^0} \tag{J.10}$$

$$t_D = \frac{ut}{L} = \frac{qt}{\phi L} \tag{J.11}$$

where L [m] is a characteristic dimension of the particular system (here it is length L of interest), q [m/s] is the Darcy flux (volumetric flow rate per area) and ϕ [-] is the porosity of the porous domain. Notice that the thin lines (from Eq. (J.8)) in Fig. J.1 represent a good approximation to Eq. (J.7) (thick lines).

If the dimensionless concentration c_D is plotted against z_D given by

$$\boxed{z_D = \frac{x_D - t_D}{\sqrt{t_D}}} \tag{J.12}$$

it can be seen that the solution to Eq. (J.7) (and Eq. (J.8)) collapses to essentially one curve, see Fig. J.1 (right). This is true for Eq. (J.8) because the solution is symmetric and independent of scale. However, this is only partly true for the convection-dispersion equation, Eq. (J.7) and some small discrepancy from symmetry can be seen in Fig. J.1 (right). This discrepancy is amplified at large scale, e.g. reservoir scales, as heterogeneity in the porous media in reservoir scale contributes to additional dispersion [87].

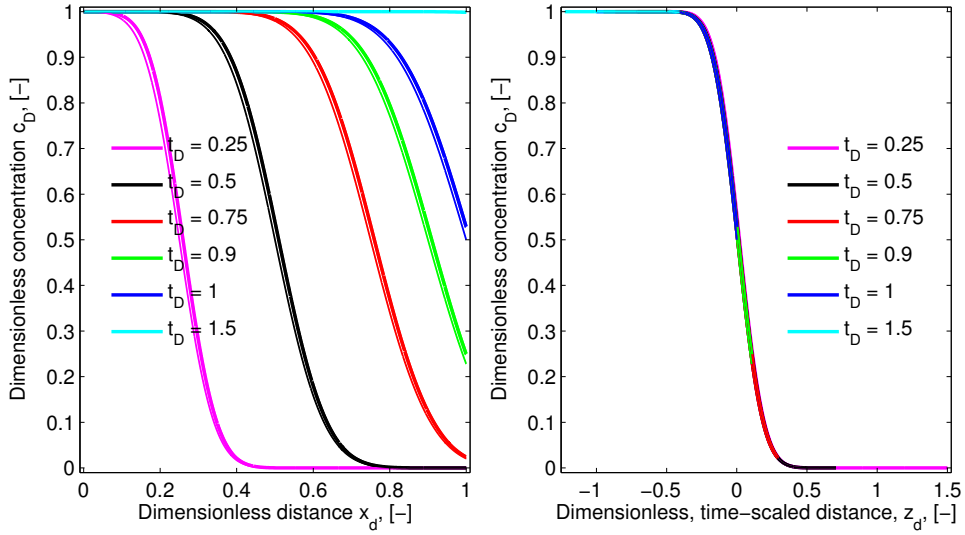

Figure J.1: Left: Plot of Eqs. (J.7) (thick lines) and (J.8) (thin lines) for scaled coordinates. Right: The curves in left figure collapse to one curve when plotted against z_D (Eq. (J.12)).

According to Peters [87], Eq. (J.8) has been shown to be related to the cumulative normal probability distribution. This is interesting because for $t_D = 0.5$ (note that t_D is also dimensionless time in pore volumes injected) some characteristic attributes of the cumulative normal probability distribution function can be applied to the convection-dispersion equation, see table J.1 and Fig. J.2. *Pe* in table J.1 is the *Pe*clet number which expresses the ratio of two transport mechanisms, here convection and dispersion, and can be expressed as

$$Pe = \frac{uL}{D_L} = \frac{qL}{\phi D_L} \tag{J.13}$$

where we have used that:

$$u = \frac{q}{\phi} \tag{J.14}$$

A high *Pe*clet number indicates that transport by convection is more significant compared to dispersion.

Table J.1: Attributes of the cumulative normal probability distribution function applied to the convection-dispersion equation approximated by (J.8) [87].

	Dimensional	Dimensionless
Mean	ut	t_D
Variance	$2D_L t$	$2t_D/Pe$
Standard deviation	$\sqrt{2D_L t}$	$\sqrt{2t_D/Pe}$

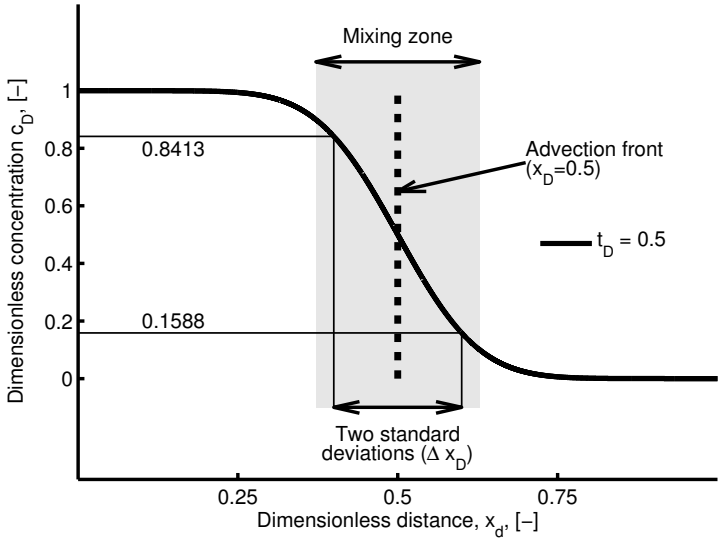

Figure J.2: Attributes of the cumulative normal probability distribution function at $t_D = 0.5$.

At $t_D = 0.5$ the advection front has moved $x_D = 0.5$. It can also be observed from Fig. J.2 that the width of the mixing zone Δx_D, caused by dispersion, at the advection front is approximately two times the standard deviation. When molecular diffusion can be neglected, it can further be shown that [87];

$$D_L = d_l u, \quad D_T = d_t u, \quad Pe = \frac{L}{d_l} \tag{J.15}$$

where d_l and d_t [m] are longitudinal and transverse dispersivity, respectively.

In the following section the method described above will be applied to an illustrative example to estimate dispersion properties from a flow experiment.

J.1 Example: Obtaining longitudinal hydrodynamic dispersion properties

In this particular example an immiscible two-phase flow problem has been solved where a wetting phase is injected into a non-wetting phase. For application to real examples see Peters [87]. The idea of the procedure is to quantify the dimensionless width Δx_D of the mixing zone at $t_D = 0.5$ at the advection front to obtain the *Pe*clet number and dispersion coefficient D_L (using the expression for the standard deviation in table J.1) and then estimate the longitudinal dispersivity d_l from Eq. (J.15).

In Fig. J.3a three profiles at different times are shown. The distance $L = 0.85$ [m], the Darcy flux $q = 0.0183$ [m/s] and porosity $\phi = 0.3$ [-]. At $t = 10$ [s] the dimensionless time $t_D = 0.72$ [-] can be obtained from Eq. (J.11), see Fig. J.3b (top). The profile that corresponds to $t_D = 0.5$ [-] is also shown. Next step is to evaluate Δx_D of the mixing zone and three values were derived by considering the gradient of the profile, Fig. J.3b (bottom). The three zones are indicated by the colored areas and the values in Fig. J.3b (top).

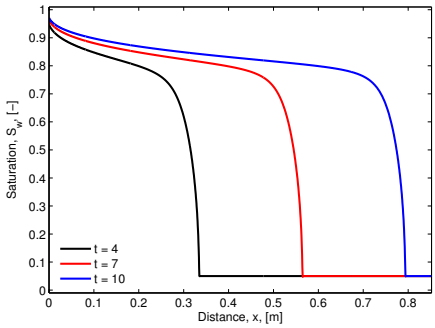

(a) Three dimensional profiles at $t = 4$ s, $t = 7$ s and $t = 10$ s. The profile at $t = 7$ s corresponds to half of the pore volume across the chosen characteristic distance $L = 0.825$ [m].

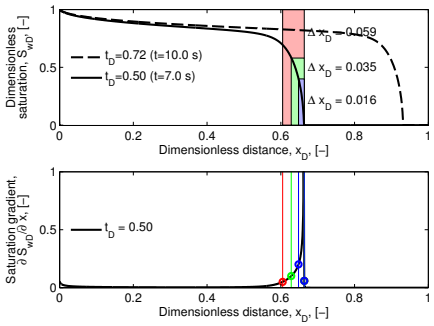

(b) Top: Two dimensionless profiles at $t_D = 0.50$ and $t_D = 0.72$. Three mixing zones are indicated (rectangles). Bottom: Gradient of profile corresponding to $t_D = 0.50$. Circles indicate the cut-off of the gradient profile to determine the mixing zones.

Figure J.3: Analyzing the mixing zone in a two-phase flow problem, Profiles of three times are given in (a). Curves from (a) in dimensionless form in shown in Fig. (b, top).

Once the width of the mixing zone Δx_D has been determined, the *Pe*clet number, dispersion coefficient D_L and dispersivity d_l can be determined using the formulas in table J.1 and using that $\Delta x_D/2$ is approximately equivalent to the standard deviation. The results are given in table J.2.

Table J.2: Dispersion properties corresponding to three mixing zones.

Width mixing zone Δx_D	Peclet number Pe, [-]	Dispersion coefficient D_L, [m^2/s]	Dispersivity d_l, [mm]
0.0586	1167	$6.131 \cdot 10^{-5}$	0.730
0.0354	3200	$2.237 \cdot 10^{-5}$	0.266
0.0155	16579	$0.432 \cdot 10^{-5}$	0.0514

J.1.1 General procedure

The general procedure to obtain the equivalent longitudinal dispersivity of a saturation profile is given below:

- Pick a simulation time t and calculate characteristic length L from Eq. (J.11) equivalent to one pore volume ($t_D = 1$): $L = qt/\phi$. It should be noted that this is assuming a well-defined saturation front and the actual characteristic length is longer because the average saturation behind the front is less than unity. But, for this estimate-calculation we assume unity.
- Plot saturation profile as a function of dimensionless distance $x_D = x/L$ and estimate mixing length Δx_D on the dimensionless length scale. If the front is "smeared" this can be difficult to determine accurately.

- Using Eq. (J.15) and that $\Delta x_D/2$ is equivalent to standard deviation in Tab. J.1, it can be obtained that the longitudinal dispersivity is:

$$d_l = \frac{L}{Pe} = \frac{L(\Delta x_D/2)^2}{2t_D} \tag{J.16}$$

Appendix K

Model definitions, from main chapters

K.1 Single-phase, comparison model

To compare the various formulations for single-phase flow in chapter 4.2, a model originally defined as a conceptual model for CO_2 storage by Rutqvist and Tsang [97] is used. The geometry is shown in Fig. K.1.

The mechanical and hydraulic properties of the various layers in the model are given in Table K.1 and the fluid properties are given in Table K.2. For simplicity the temperature is assumed constant.

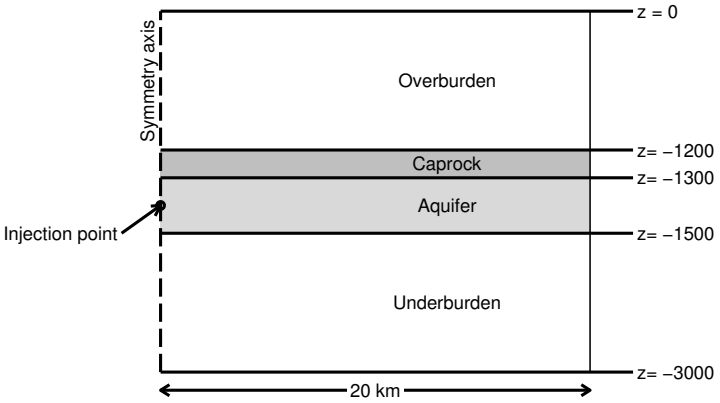

Figure K.1: Geometry of the two dimensional conceptual CO_2 injection model defined by Rutqvist and Tsang [97].

Table K.1: Mechanical and hydraulic properties in two dimensional conceptual injection model.

Property	Overburden	Caprock	Aquifer	Underburden
Permeability, [m^2]	10^{-15}	10^{-17}	10^{-13}	10^{-17}
Porosity, [-]	0.1	0.01	0.1	0.01
Youngs modulus, [GPa]	5	5	5	5
Poissons ratio, [-]	0.25	0.25	0.25	0.25
Density, [kg/m^3]	2260	2260	2260	2260
Biot's coefficient, [-]	0.9	0.9	0.9	0.9

Table K.2: Material data of water in two dimensional conceptual injection model.

Density, [kg/m^3]	Viscosity, [mPa·s]	Compressibility, [1/GPa]
1000	0.8	0.43

K.2 Non-isothermal, two-phase

Model to evaluate non-isothermal effects in a two-phase flow model, see chapter 5.3.

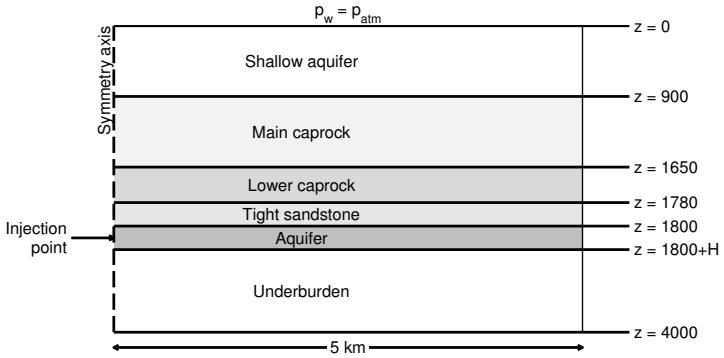

Figure K.2: Geometry of non-isothermal injection model. Note that the dimensions are not to scale. Aquifer thickness $H = 20$ m.

The injection rate is 0.0028111 kg/s/m (CO_2), equivalent to a yearly injection of 133 ktons/year along a 1.5 km long injection well, residual saturation of wetting phase is $s_{wr} = 0.25$. Initial temperature is 30°C at surface with a 30°C/km temperature gradient, such that the temperature in the reservoir is approximately 84°C:

$$T_0 = 30 + 0.03(D - D_0) \tag{K.1}$$

where D [m] is the vertical elevation and D_0 [m] is the reference elevation (surface).

Mechanical and hydraulic properties and thermal properties in the two dimensional non-isothermal injection model are given in table K.3 and K.4, respectively. Thermal properties for the solid phase are defined as typical values for rocks obtained from Schön [99]. The fluid properties are evaluated from the equation of state from the online database [65] described in

App. B. For the HM and THM models in chapter 5.3 they are obtained by using the initial pore pressure (Eq. (5.4)) and temperature gradient profiles (Eq. (K.1)). For the models in chapter 7 the initial values are also obtained from the initial pore pressure (Eq. (5.4)) and temperature gradient profiles (Eq. (K.1)), but they are updated with change in pore pressure and temperature.

Table K.3: Mechanical and hydraulic properties in the two dimensional non-isothermal injection model.

Property	Shallow aquifer	Main caprock	Lower caprock	Tight sandstone	Aquifer	Underburden
Permeability, [m^2]	10^{-17}	10^{-19}	10^{-19}	10^{-19}	$25{\cdot}10^{-15}$	10^{-19}
Porosity, [-]	0.1	0.01	0.01	0.01	0.17	0.01
Youngs modulus, [GPa]	1.5	20	20	20	6	20
Poissons ratio, [-]	0.2	0.15	0.15	0.15	0.2	0.15
Density (solid), [kg/m^3]	2200	2200	2200	2200	2200	2200
Biot's coefficient, [-]	1	1	1	1	1	1
Entry pressure, [kPa]	19.9	621	621	621	90	621

Table K.4: Thermal properties for fluids and rocks used in the non-isothermal models in chapter 5.3 and 7. Thermal properties for the fluids are approximated from App. B, assuming initial reservoir conditions, for the solid phase the values are typical values for rocks obtained from Schön [99]. Specific heat capacity is for constant pressure.

Phase α	Specific heat capacity, C_α [J/kg/K]	Thermal conductivity κ_α [W/m/K]	Thermal expansion coefficient (volumetric), β_α [1/K]
Solid	1000	2.5	$36{\cdot}10^{-6}$
Water	4200	0.67	$6.6{\cdot}10^{-4}$
CO_2	2100	0.1	$8{\cdot}10^{-3}$

K.3 VE, single-phase flow

The two geometries that are evaluated are shown in Figs. K.3 and K.4. Model and material properties are given in tables K.5 and K.5.

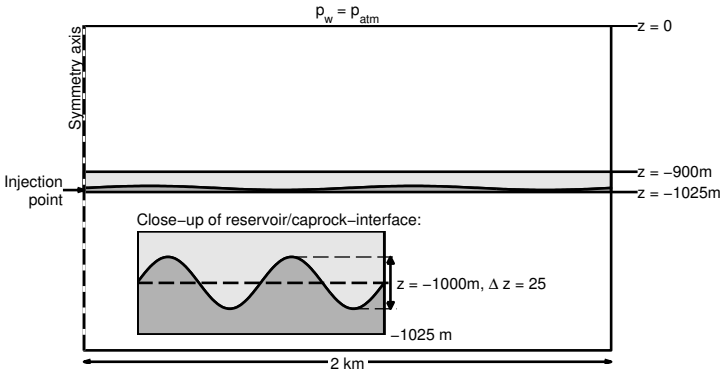

Figure K.3: Geometry of VE, single-phase flow model described in chapter 6.3. Note that the dimensions are not to scale. Reservoir has a topographic top boundary.

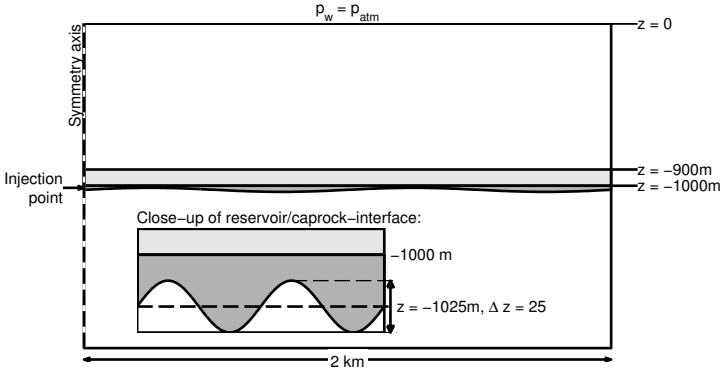

Figure K.4: Geometry of VE, single-phase flow model described in chapter 6.3. Note that the dimensions are not to scale. Reservoir has a topographic bottom boundary.

Table K.5: Hydraulic properties used in VE single-phase flow model.

Property	Overburden	Caprock	Reservoir	Underburden
Permeability, k [m^2]	10^{-15}	10^{-18}	10^{-12}	10^{-18}
Porosity, ϕ [-]	0.2	0.2	0.3	0.2

Table K.6: Model parameters used in VE single-phase flow model.

Property	Value
Density, water, ρ_w [kg/m^3]	1000
Dynamic viscosity, water, μ_w [mPa·s]	1
Injection rate, q_{inj}[kg/s]	0.1
Biot's coefficient, b [-]	0.8
Compressibility, water, c_w [1/GPa]	0.1
Compressibility, solid, c_s [1/GPa]	0.1

K.4 VE, two-phase flow

Description of models evaluated in chapter 6.3.2 (confined reservoir, two-phase flow only) and 6.6.2 (unconfined reservoir, two-phase flow and poroelasticity).

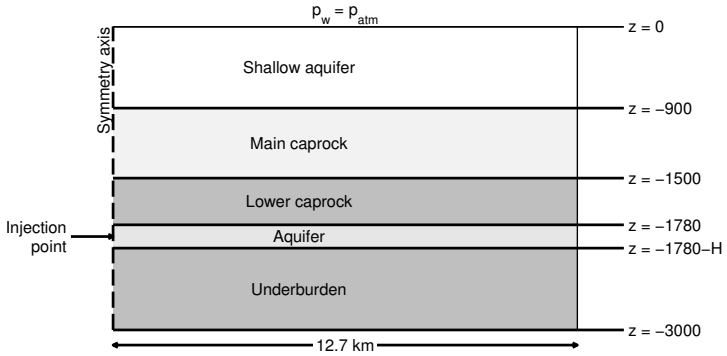

Figure K.5: Geometry of the validation model to compare a fully resolved model with a dimensionally reduced model. Note that the dimensions are not to scale. This geometry is only evaluated in chapter 6.6.2

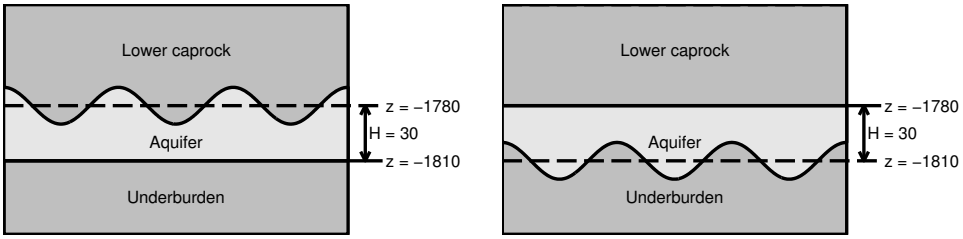

Figure K.6: Geometry of the aquifer when topography is considered, $H = 30 \pm 10$ m. Left: Topographic top boundary. Right: Topographic bottom boundary. Both geometries are evaluated in chapter 6.3.2 and 6.6.2.

Injection rate $q_n = 0.002811$ [kg/s] and $s_{rw} = s_{rn} = 0$ [-]. Initial non-wetting saturation $s_n^0 = 0$. Capillary pressure function is defined according to Nordbotten and Dahle [84] (see App. E.1.4) and relative permeability is defined according to Brooks and Corey [27] (see App. E.2.1).

Mechanical and hydraulic properties are given in table K.7. The fluid properties are evaluated from the equation of state from the online database [65] described in App. B using $T = 50°\text{C}$ and $p_w^0 = 20$ MPa and are given in table K.8.

Table K.7: Mechanical and hydraulic properties in two dimensional conceptual injection model. Note that the permeability is anisotropic, such that the vertical component is ten times lower than the value given in the table (except in the aquifer).

Property	Shallow aquifer	Main caprock	Lower caprock	Aquifer	Underburden
Permeability, [m^2]	10^{-17}	10^{-19}	10^{-17}	10^{-13}	10^{-17}
Porosity, [-]	0.1	0.01	0.01	0.17	0.01
Youngs modulus, [GPa]	1.5	20	20	6	20
Poissons ratio, [-]	0.2	0.15	0.15	0.2	0.15
Density (solid), [kg/m^3]	2200	2200	2200	2200	2200
Biot's coefficient, [-]	0.7	0.7	0.7	0.7	0.7
Entry pressure, p_d, [kPa]	-	-	-	500	-
Capillary pressure par., α, [Pa]	-	-	-	$0.9p_d$	-
Capillary pressure par., β, [Pa]	-	-	-	$0.1p_d$	-

Table K.8: Material data for wetting- and non-wetting phases in VE-validation model.

Phase	Density, [kg/m^3]	Viscosity, [mPa·s]	Compressibility, [1/GPa]
Water	996.5	0.55	0.42
CO_2	784.3	0.069	15.6

K.5 PLVD, static

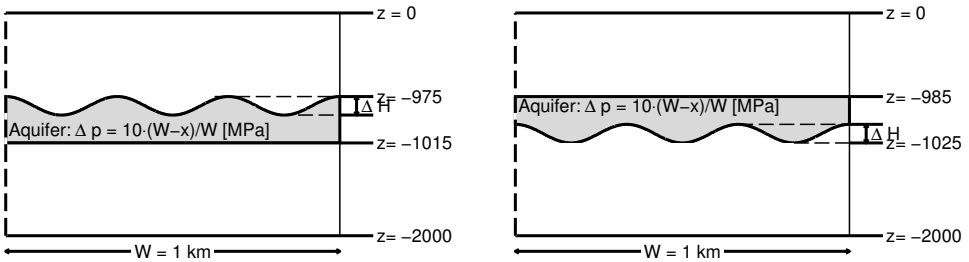

Figure K.7: Geometry of the aquifer with topography: $\Delta H = 20$ m, $H = 30 \pm 10$ m. (left) Topographic top boundary. (right) Topographic bottom boundary.

Table K.9: Mechanical properties.

Property	Overburden, underburden	Aquifer
Youngs modulus, [GPa]	20	6
Poissons ratio, [-]	0.25	0.2

Bibliography

[1] Addis, M. A. (1997). The Stress-Depletion Response Of Reservoirs. *Society of Petroleum Engineers, SPE 38720*, pages 55–65. 2.4

[2] Alam, M. M., Fabricius, I. L., and Christensen, H. F. (2012). Static and dynamic effective stress coefficient of chalk. *Geophysics*, 77(2):L1–L11. 3

[3] Altmann, J. B. (2010). *Poroelastic effects in reservoir modelling*. PhD thesis, Karlsruhe Institute of Technology. 2.4, 2.5

[4] Altmann, J. B., Müller, T. M., Müller, B. I., Tingay, M. R., and Heidbach, O. (2010). Poroelastic contribution to the reservoir stress path. *International Journal of Rock Mechanics and Mining Sciences*, 47(7):1104–1113. 7.5

[5] Andersen, O., Gasda, S. E., and Nilsen, H. M. (2014). Vertically Averaged Equations with Variable Density for CO_2 Flow in Porous Media. *Transport in Porous Media*, 107:95–127. 1.1, 6.2

[6] Anderson, E. M. (1951). *The Dynamics of Faulting and Dyke Formation With Application to Britain*. Oliver & Boyd, Edinburgh, 2 edition. 2.3

[7] Armitage, P. J., Faulkner, D. R., and Worden, R. H. (2013). Caprock corrosion. *Nature Geoscience*, 6:79–80. doi:10.1038/ngeo1716. 4.3

[8] Barucq, H., Madaune-Tort, M., and Saint-Macary, P. (2005). On nonlinear Biot's consolidation models. *Nonlinear Analysis*, 63:e985–e995. doi:10.1016/j.na.2004.12.010. 3.1

[9] Bear, J. (1988). *Dynamics of Fluids in Porous Media*. Courier Dover Publications, 2nd, illustrated, reprint edition. D

[10] Bear, J. and Corapcioglu, M. Y. (1981a). Mathematical Model for Regional Land Subsidence Due to Pumping: 1. Integrated Aquifer Subsidence Equations Based on Vertical Displacement Only. *Water Resources Research*, 17(4):937–946. 1.1

[11] Bear, J. and Corapcioglu, M. Y. (1981b). Mathematical Model for Regional Land Subsidence Due to Pumping: 2. Integrated Aquifer Subsidence Equations for Vertical and Horizontal Displacements. *Water Resources Research*, 17(4):947–958. 1.1

[12] Bemer, E., Boutéca, M., Vincké, O., Hoteit, N., and Ozanam, O. (2001). Poromechanics: From Linear to Nonlinear Poroelasticity and Poroviscoelasticity. *Oil & Gaz Science and Technology, Rev. IFP*, 56(6):531–544. 3.1

[13] Biot, M. A. (1935). Le problème de la consolidation de matières argileuses sous une charge. *Ann. Soc. Sci. Bruxelles, Ser. B*, 55:110–113. 3.1

[14] Biot, M. A. (1941). General Theory of Three-dimensional Consolidation. *Journal of Applied Phsyics*, 12(2):155–164.

[15] Biot, M. A. (1955). Theory of elasticity and consolidation for a porous anisotropic solid. *Journal of Applied Physics*, 26:182–185.

[16] Biot, M. A. (1972). Theory of finite deformations of porous solids. *Indiana University Mathematics Journal*, 21:597–620.

[17] Biot, M. A. (1973). Nonlinear and semilinear rheology of porous solids. *Journal of Geophysical Research*, 23:4924–4937. 3.1

[18] Bishop, A. W. (1959). The principle of effective stress. *Teknisk Ukeblad*, 39:859–863. 3.3

[19] Bishop, A. W. (1973). The influence of an undrained change in stress on the pore pressure in porous media of low compressibility. *Géotechnique*, 23(3):435–442. 4.2.1

[20] Bissell, R. C., Vasco, D. W., Atbi, M., Hamdani, M., Okwelegbe, M., and Goldwater, M. H. (2011). A full field simulation of the in Salah gas production and CO_2 storage project using a coupled geo-mechanical and thermal fluid flow simulator. *Energy Procedia*, 4:3290–3297. 10th International Conference on Greenhouse Gas Control Technologies. 5.3

[21] Bjørnarå, T. I., Bohloli, B., and Park, J. (2017). Field data analysis and hydromechanical modeling of CO_2 storage at In Salah, Algeria. Submitted. 8

[22] Bjørnarå, T. I. and Mathias, S. A. (2013). A pseudospectral approach to the McWhorter and Sunada equation for two-phase flow in porous media with capillary pressure. *Computational Geosciences*, 17(6):889–897. 1.2, 4.3.2, 4.3.2, 4.2, 7.2, 8

[23] Bjørnarå, T. I., Mathias, S. A., Nordbotten, J. M., and Park, J. (2014a). Fast Evaluation of Fluid-rock Coupling in CO_2 Storage. In *Fourth EAGE CO_2 Geological Storage Workshop 22-24. April 2014, Stavanger, Norway*. 8

[24] Bjørnarå, T. I., Mathias, S. A., Nordbotten, J. M., Park, J., and Bohloli, B. (2014b). Capturing the coupled hydro-mechanical processes occurring during CO_2 injection - example from In Salah. *Energy Procedia*, 63:3416–3424. 12th International Conference on Greenhouse Gas Control Technologies, GHGT-12. 8, 9

[25] Bjørnarå, T. I., Nordbotten, J. M., and Park, J. (2016). Vertically integrated models for coupled two-phase flow and geomechanics in porous media. *Water Resources Research*, 52(2):1398–1417. 7.6, 7.6, 8, 9, A, H.2

[26] Bohloli, B., Bjørnarå, T. I., Park, J., and Rucci, A. (2017). Can surface uplift be used as a tool for monitoring reservoir performance? A case study from In Salah, Algeria. Submitted. (document)

[27] Brooks, R. H. and Corey, A. T. (1964). Hydraulic properties of porous media. *Hydrology Paper 3, Colorado State University, Fort Collins, Colorado*. 4.3.2, 4.4.3, 7.1, 7.2, E.1.1, E.2, E.1.4, E.1.5, E.2.1, E.6, H.3, K.4

[28] Buckley, S. E. and Leverett, M. C. (1942). Mechanism of fluid displacement in sands. *Transactions of the AIME*, 146(1):107–116. 4.3.2, 8, 9

[29] Burdine, N. T. (1953). Relative permeability calculations from pore size distribution data. *Journal of Petroleum Technology*, 5(3):71–78. E.1.2

[30] Cavanagh, A. (2013). Benchmark Calibration and Prediction of the Sleipner CO_2 Plume from 2006 to 2012. *Energy Procedia*, 37:3529–3545. GHGT-11. B.3, B.11

[31] Chen, Z., Huan, G., and Ma, Y. (2006). *Computational methods for multiphase flows in porous media (Computational Science and Engineering)*. Society for Industrial and Applied Mathematics. 4.2.1, 4.3.1, D

[32] Chou, P. C. and Pagano, N. J. (1992). *Elasticity: Tensor, Dyadic, and Engineering Approaches*. Dover Civil and Mechanical Engineering Series. Dover Publications. F.1

[33] Civan, F. (2011). *Porous Media Transport Phenomena*. John Wiley & Sons, Inc. D

[34] Corapcioglu, M. Y. and Bear, J. (1983). A Mathematical Model for Regional Land Subsidence Due to Pumping: 3. Integrated Equations for a Phreatic Aquifer. *Water Resources Research*, 19(4):895–908. 1.1

[35] Court, B., Bandilla, K. W., Celia, M. A., Janzen, A., Dobossy, M., and Nordbotten, J. M. (2012). Applicability of vertical-equilibrium and sharp-interface assumptions in CO_2 sequestration modeling. *International Journal of Greenhouse Gas Control*, 10:134–147. 7.6

[36] Coussy, O. (2004). *Poromechanics*. John Wiley & Sons Ltd., West Sussex, England. 3.1, 3.4, C.2, C.2, 2, C.2

[37] Davies, R., Foulger, G., Bindley, A., and Styles, P. (2013). Induced seismicity and hydraulic fracturing for the recovery of hydrocarbons. *Marine and Petroleum Geology*, 45:171–185. 1.1

[38] Davis, R. O. and Selvadurai, A. P. S. (2002). *Plasticity and Geomechanics*. Cambridge University Press. F

[39] Dean, R. H., Gai, X., Stone, C. M., and Minkoff, S. E. (2006). A Comparison of Techniques for Coupling Porous Flow and Geomechanics. *Society of Petroleum Engineers*, 11(1):132–140. 3.6

[40] Detournay, E. and Cheng, A. H.-D. (1993). Fundamentals of Poroelasticity. Preprint. 3.1

[41] Doster, F., Nordbotten, J. M., and Celia, M. A. (2013). Impact of capillary hysteresis and trapping on vertically integrated models for CO_2 storage. *Advances in Water Resources*, 62, Part C:465–474. Computational Methods in Geologic CO_2 Sequestration. E.3

[42] Duan, Z. and Sun, R. (2003). An improved model calculating CO_2 solubility in pure water and aqueous NaCl solutions from 273 to 533 K and from 0 to 2000 bar. *Chemical Geology*, 193(3-4):257–271. 4.4.3, B.3, B.11, B.12, B.3

[43] Edenhofer, O., Pichs-Madruga, R., Sokona, Y., Farahani, E., Kadner, S., Seyboth, K., Adler, A., Baum, I., Brunner, S., Eickemeier, P., Kriemann, B., Savolainen, J., Schlömer, S., von Stechow, C., Zwickel, T., and (eds.), J. M. (2014). IPCC, 2014: Climate Change 2014: Mitigation of Climate Change. Contribution of Working Group III to the Fifth Assessment Report of the Intergovernmental Panel on Climate Change. Technical report, Cambridge University Press, Cambridge, United Kingdom and New York, NY, USA. 1.1

[44] Engelder, T. and Fischer, M. P. (1994). Influence of poroelastic behavior on the magnitude of minimum stress, S_h, in overpressured parts of sedimentary basins. *Geology*, 2:949–952. 2.4, 2.4

[45] Ferrill, D. A. and Morris, A. P. (2003). Dilational normal faults. *Journal of Structural Geology*, 25:183–196. 2.2

[46] Fjaer, E., Holt, R. M., Horsrud, P., Raaen, A. M., and Risnes, R. (2008). *Petroleum Related Rock Mechanics*. Elsevier, 2nd edition. 4.2.1, C.1, C.1, C.1

[47] Gasda, S. E., Nordbotten, J. M., and Celia, M. A. (2011). Vertically averaged approaches for CO_2 migration with solubility trapping. *Water Resources Research*, 47. W05528. 1.1, 6.1

[48] Geertsma, J. (1973). Land subsidence above compacting oil and gas reservoirs. *Journal of Petroleum Technology*, 25:734–744. 2.3, 3.3, 3.6, 1, C.1, C.1

[49] Gor, G. Y., Elliot, T. R., and Prévost, J. H. (2013). Effects of thermal stresses on caprock integrity during CO_2 storage. *International Journal of Greenhouse Gas Control*, 12:300–309. 5.1

[50] Hellevang, H. (2006). *Interactions between CO_2, saline water and minerals during geological storage of CO_2*. PhD thesis, University of Bergen, Norway. 1.1

[51] Helmig, R. (1997). *Multiphase Flow and Transport Processes in the Subsurface: A Contribution to the Modeling of Hydrosystems*. Environmental engineering. Springer Berlin. D, E.2.2, E.2.2, E.7, E.4

[52] Herrera, I. and Pinder, G. F. (2012). *Mathematical Modeling in Science and Engineering: An Axiomatic Approach*. John Wiley & Sons, Inc., Hoboken, NJ, USA. 3.6, D

[53] Hesse, M. A., Orr, F. M., and Tchelepi, H. A. (2008). Gravity Currents with Residual Trapping. *Journal of Fluid Mechanics*, 611:35–60. 1.1

[54] Hillis, R. R. (2003). Pore pressure/stress coupling and its implications for rock failure. *Geological Society, London, Special Publications*, 216:359–368. 2.4, 2.4

[55] Hirsch, C. (2007). *Numerical computation of internal and external flows*. Elsevier, Amsterdam, 2 edition. 7.2

[56] IEA (2010). Energy Technology Perspectives 2010 - Scenarios and Strategies to 2050. Technical report, International Energy Agency, Paris, France. 710 pp. ISBN: 9789264085978. 1.1

[57] IEAGHG (2009). Natural and Industrial Analogues for Geological Storage of Carbon Dioxide. Technical report, IEA GHG (International Energy Agency Greenhouse Gas R&D Programme). IEA Greenhouse Gas R&D Programme. 1.1

[58] Jaeger, J. C., Cook, N. G. W., and Zimmermann, R. (2007). *Fundamentals of Rock Mechanics*. Wiley-Blackwell, Malden, MA, 4th edition. 2.2, 2.3, 3.4, 3.4, 4.2.1, C.3, C.3, F, F

[59] Juanes, R., Hager, B. H., and Herzog, H. J. (2012). No geologic evidence that seismicity causes fault leakage that would render large-scale carbon capture and storage unsuccessful. *Proceedings of the National Academy of Sciences*, 109(52):E3623. 1.1

[60] Juanes, R., Spiteri, E. J., Orr, F. M., and Blunt, M. J. (2006). Impact of relative permeability hysteresis on geological CO_2 storage. *Water Resources Research*, 42(12):n/a–n/a. W12418. E.3

[61] Kaldi, J., Daniel, R., Tenthorey, E., Michael, K., Schacht, U., Nicol, A., Underschultz, J., and Backe, G. (2013). Containment of CO_2 in CCS: Role of Caprocks and Faults. *Energy Procedia*, 37:5403–5410. GHGT-11. 1.1

[62] Lake, L. W. (1989). *Enhanced Oil Recovery*. Prentice Hall, Englewood Cliffs, NJ. D

[63] Lee, I. and Gutierrez, M. (2006). Mandel-Cryer Effect for Non-Perfectly Rigid Motion. In *Proceedings of Golden Rocks 2006, The 41st U.S. Symposium on Rock Mechanics (US-RMS), June 17-21, 2006 , Golden, CO*. American Rock Mechanics Association. Document ID: 06-1028. 2

[64] Lewis, R. W. and Schrefler, B. A. (1998). *The Finite Element Method in the Static and Dynamic Deformation and Consolidation of Porous Media*. Wiley Series in Numerical Methods in Engineering. John Wiley, Chichester, West Sussex, England, 2nd edition. 3.3, 4.2.1, 4.2.1, 4.2.1, 4.2.1, 4.2.1, 5.2, 5.2, D, D

[65] Linstrom, P. and Mallard, W., editors (2015). *NIST Chemistry WebBook, NIST Standard Reference Database Number 69*. National Institute of Standards and Technology, Gaithersburg MD. 5.3, 7.4, B, B.3, K.2, K.4

[66] Longuemare, P., Mainguy, M., Lemonnier, P., Onaisi, A., Gérard, C., and Koutsabeloulis, N. (2002). Geomechanics in Reservoir Simulation: Overview of Coupling Methods and Field Case Study. *Oil & Gas Science and Technology - Rev. IFP*, 57(5):471–483. 3.4

[67] Lu, C., Lee, S.-Y., Han, W., McPherson, B. J., and Lichtner, P. C. (2009). Comments on "Abrupt Interface solution For Carbon Dioxide Injection into Porous Media" by M. Dentz and D. Tartakovsky. *Transport in Porous Media*, 79(1):29–37. 7.6

[68] Luo, Z. and Bryant, S. (2011). Influence of thermo-elastic stress on fracture initiation during CO_2 injection and storage. *Energy Procedia*, 4:3714–3721. 10th International Conference on Greenhouse Gas Control Technologies. 5.1

[69] Mandel, J. (1953). Consolidation Des Sols (Étude Mathématique). *Géotechnique*, 3(7):287–299. 3.6, 2, C.2, 2

[70] Mathias, S. A., Hardisty, P. E., Trudell, M. R., and Zimmerman, R. W. (2009). Screening and selection of sites for CO_2 sequestration based on pressure buildup. *International Journal of Greenhouse Gas Control*, 3(5):577–585. 2.1

[71] Mavko, G., Mukerji, T., and Dvorkin, J. (2009). *Rock Physics handbook*. Cambridge University Press, 2 edition. B, B.3, B.3, B.14, B.15

[72] McWhorter, D. B. and Sunada, D. K. (1990). Exact integral solutions for two-phase flow. *Water Resources Research*, 26(3):399–413. 1.2, 4.3.2, 8, 9

[73] McWhorter, D. B. and Sunada, D. K. (1992). Reply [to "Comment on 'Exact integral solutions for two-phase flow' by David B. McWhorter and Daniel K. Sunada"]. *Water Resources Research*, 28(5):1479. 1.4

[74] Metz, B., Davidson, O., de Coninck, H., Loos, M., and Meyer, L., editors (2005). *IPCC, 2005: IPCC Special Report on Carbon Dioxide Capture and Storage. Prepared by Working Group III of the Intergovernmental Panel on Climate Change*. Cambridge University Press, Cambridge, United Kingdom and New York, NY, USA. 4.3

[75] Morris, A., Ferrill, D. A., and Henderson, D. B. (1996). Slip-tendency analysis and fault reactivation. *Geology*, 24(3):275–278. 2.2

[76] Morris, J. P., Hao, Y., Foxall, W., and McNab, W. (2011). A study of injection-induced mechanical deformation at the In Salah CO_2 storage project. *International Journal of Greenhouse Gas Control*, 5(2):270–280. 2.6, 5.3, 5.1

[77] Mosavat, N., Abedini, A., and Torabi, F. (2014). Phase Behaviour of CO_2-Brine and CO_2-Oil Systems for CO_2 Storage and Enhanced Oil Recovery: Experimental Studies. *Energy Procedia*, 63:5631–5645. 12th International Conference on Greenhouse Gas Control Technologies, GHGT-12. 4.4.3

[78] Mualem, Y. (1976). A New Model for Predicting the Hydraulic Conductivity of Unsaturated Porous Media. *Water Resources Research*, 12(3):513–522. E.1.2, E.3

[79] Mykkeltvedt, T. S. and Nordbotten, J. M. (2012). Estimating convective mixing rates from commercial-scale CO_2 injection. *Environmental Earth Sciences*, 67(2):527–535. doi:10.1007/s12665-012-1674-3. 6.1

[80] Nordal, S. (2012). Soil Modeling. Lecture notes PhD course BA8304, NTNU, Trondheim, Norway. 3.2, F, F

[81] Nordbotten, J. M. and Celia, M. A. (2012). *Geological Storage of CO_2: Modeling Approaches For Large-Scale Simulation*. John Wiley, Hoboken, NJ. 6.1, 6.2, 6.3.2, H.1, H.5

[82] Nordbotten, J. M., Celia, M. A., Bachu, S., and Dahle, H. K. (2005). Semianalytical Solution for CO_2 Leakage through an Abandoned Well. *Environmental Science & Technology*, 39(2):602–611. 1.1

[83] Nordbotten, J. M. and Dahle, H. K. (2010). Impact of capillary forces on large-scale migration of CO_2. In XVIII International Conference on Water Resources, CMWR 2010, edited by J. Carrera, CIMNE, Barcelona. 6.3.2, H.1, H.3, H.3, H.5.1

[84] Nordbotten, J. M. and Dahle, H. K. (2011). Impact of the capillary fringe in vertically integrated models for CO_2 storage. *Water Resources Research*, 47. W02537. 1.1, E.1.4, E.5, E.1.5, H.1, K.4

[85] Orr, F. M. J. (2007). *Theory of Gas Injection Processes*. Tie-line publications. 4.3.2, 4.4.1, 4.4.1, 4.4.3, 4.3, J, J

[86] Parker, J. C., Lenhard, R. J., and Kuppusamy, T. (1987). A parametric model for constitutive properties governing multiphase flow in porous media. *Water Resources Research*, 23(4):618–624. E.1.3, E.4, E.2.3, E.8

[87] Peters, E. J. (2012). *Advanced Petrophysics: Volume 2: Dispersion, Interfacial Phenomena/Wettability, Capillarity/Capillary Pressure, Relative Permeability*, volume 2. Live Oak Book Company. J, J, J, J.1, J, J.1

[88] Piche, R. and Kanniainen, J. (2009). Matrix-based numerical modelling of financial differential equations. *Int. J. Mathematical Modelling and Numerical Optimisation*, 1(1/2):88–100. 4.3.2

[89] Pinder, G. F. and Gray, W. G. (2008). *Essentials of Multiphase Flow and Transport in Porous Media*. John Wiley & Sons, Inc., Hoboken, NJ, USA. doi: 10.1002/9780470380802. 4.2.1, 4.2.2, D

[90] Preisig, M. and Prévost, J. H. (2011). Coupled multi-phase thermo-poromechanical effects. Case study: CO_2 injection at In Salah, Algeria. *International Journal of Greenhouse Gas Control*, 5(4):1055–1064. 5.1

[91] Raffensperger, J. P. (1996). Chapter 3 Numerical simulation of sedimentary basin-scale hydrochemical processes. In Corapcioglu, M. Y., editor, *Advances in Porous Media*, volume 3, pages 185–305. Elsevier. D

[92] Ramsay, J. G. and Lisle, R. J. (2000). *The Techniques of Modern Structural Geology, Volume 3: Applications of Continuum Mechanics in Structural Geology*. Academic Press. 2.2

[93] Rice, J. R. and Cleary, M. P. (1976). Some Basic Stress Diffusion Solutions for Fluid-Saturated Elastic Porous Media With Compressible Constituents. *Reviews of Geophysics*, 14(2):227–241. 3.1

[94] Ringrose, P. S., Roberts, D. M., Gibson-Poole, C. M., Bond, C., Wightman, R., Taylor, M., Raikes, S., Iding, M., and Østmo, S. (2011). Characterisation of the Krechba CO_2 storage site: Critical elements controlling injection performance. *Energy Procedia*, 4:4672–4679. 10th International Conference on Greenhouse Gas Control Technologies. 5.3

[95] Rutqvist, J., Liu, H.-H., Vasco, D. W., Pan, L., Kappler, K., and Majer, E. (2011). Coupled non-isothermal, multiphase fluid flow, and geomechanical modeling of ground surface deformations and potential for induced micro-seismicity at the In Salah CO_2 storage operation. *Energy Procedia*, 4:3542–3549. 2.2

[96] Rutqvist, J. and Stephansson, O. (2003). The role of hydromechanical coupling in fractured rock engineering. *Hydrogeology Journal*, 11(1):7–40. 3.1, 3.1

[97] Rutqvist, J. and Tsang, C.-F. (2002). A study of caprock hydromechanical changes associated with CO_2-injection into a brine formation. *Environmental Geology*, 42:296–305. K.1, K.1

[98] Schmid, K. S. and Geiger, S. (2012). Universal scaling of spontaneous imbibition for water-wet systems. *Water Resources Research*, 48. 4.3.2

[99] Schön, J. H. (2011). *Physical Properties of Rocks: A Workbook*. Burlington: Elsevier Science, 1 edition. 5.3.1, K.2, K.4

[100] Schön, J. H. (2015). *Physical Properties of Rocks: Fundamentals and Principles of Petrophysics*. Elsevier B.V., 2 edition. 3.4

[101] Segall, P. (1989). Earthquakes triggered by fluid extraction. *Geology*, 17:942–946. 2.4a, 2.3

[102] Segall, P. and Fitzgerald, S. D. (1998). A note on induced stress changes in hydrocarbon and geothermal reservoirs. *Tectonophysics*, 289:117–128. 2.4

[103] Selvadurai, A. and Nguyen, T. (1995). Computational modelling of isothermal consolidation of fractured porous media. *Computers and Geotechnics*, 17(1):39–73. 4.2.1

[104] Sibson, R. H. (2000). Fluid involvement in normal faulting. *Journal of Geodynamics*, 29(3-5):469–499. 2.2, 2.2

[105] Simoni, L. and Schrefler, B. A. (1989). F.E. solution of a vertically averaged model for regional land subsidence. *International Journal for Numerical Methods in Engineering*, 27(1):215–230. 1.1

[106] Soong, Y., Jones, J. R., Harrison, D. K., Hedges, S. W., Goodman, A. L., and Baltrus, J. P. (2003). Mineral Trapping of CO_2 with Oriskany Brine. In *Second Annual Conference on Carbon Sequestration. May 5-8, 2003, Alexandria, Virginia, USA*. U. S. Department of Energy, National Energy Technology Laboratory. 4.3

[107] Stocker, T., Qin, D., Plattner, G.-K., Tignor, M., Allen, S., Boschung, J., Nauels, A., Xia, Y., Bex, V., and (eds.), P. M. (2013). IPCC, 2013: Summary for Policymakers. In: Climate Change 2013: The Physical Science Basis. Contribution of Working Group I to the Fifth Assessment Report of the Intergovernmental Panel on Climate Change. Technical report, Cambridge University Press, Cambridge, United Kingdom and New York, NY, USA. 1.1

[108] Teletzke, G. F. and Lu, P. (2013). Guidelines for Reservoir Modeling of Geologic CO_2 Storage. *Energy Procedia*, 37:39363944. GHGT-11. 1.1

[109] Terzaghi, K. (1923). Die Berechnung der Durchlässigkeitsziffer des Tones aus dem Verlauf der hydrodynamische Spannungserscheinungen. *Sitzber. Akad. Wiss. Wien, Abt. IIa*, 132:125–138. 3.3

[110] Terzaghi, K. (1925). *Erdbaumechanik auf bodenphysikalischer Grundlage*. Deuticke, Wien. 3.3

[111] Terzaghi, K., Peck, R. B., and Mesri, G. (1996). *Soil Mechanics in Engineering Practice*. John Wiley & Sons, New York, 3 edition. 3.6, 3

[112] Tingay, M. R. P., Hillis, R. R., Morley, C. K., Swarbrick, R. E., and Okpere, E. C. (2003). Pore pressure/stress coupling in Brunei Darussalam - implications for shale injection. *Geological Society, London, Special Publications*, 216:369–379. 10.1144/GSL.SP.2003.216.01.24. 2.4, 2.4

[113] Trémosa, J., Castillo, C., Vong, C. Q., Kervévan, C., Lassin, A., and Audigane, P. (2014). Long-term assessment of geochemical reactivity of CO_2 storage in highly saline aquifers: Application to Ketzin, In Salah and Snøhvit storage sites. *International Journal of Greenhouse Gas Control*, 20:2–26. B.3, B.11

[114] Van Der Knaap, W. (1959). Nonlinear behavior of elastic porous media. *Petoleum Transactions, AIME*, 216:179–187. 3.1

[115] van der Meer, B. (2005). Carbon Dioxide Storage in Natural Gas Reservoirs. *Oil & Gas Science and Technology*, 60(3):527–536. B

[116] van Genuchten, M. T. (1980). A closed-form Equation for Predicting the Hydraulic Conductivity of Unsaturated Soils. *Soil Science Society of America*, 44(5):891–898. E.1.2, E.3, H.3

[117] Verruijt, A. (2013). *Theory and Problems of Poroelasticity*. eBook, available at `http://geo.verruijt.net`. 4.2.1, 4.2.1, C, C.3

[118] Vidal-Gilbert, S., Tenthorey, E., Dewhurst, D., Ennis-King, J., Ruth, P. V., and Hillis, R. (2010). Geomechanical analysis of the Naylor Field, Otway Basin, Australia: Implications for CO_2 injection and storage. *International Journal of Greenhouse Gas Control*, 4(5):827–839. 2.2, 2.2

[119] Wang, H. F. (2000). *Theory of Linear Poroelasticity with Applications to Geomechanics and Hydrology*. Princeton University Press, Princeton, NJ. 3.1

[120] Wasch, L. J., Wollenweber, J., and Tambach, T. J. (2012). A novel concept for long-term CO_2 sealing by intentional salt clogging. In *Proceedings, TOUGH Symposium 2012*, Lawrence Berkeley National Laboratory, Berkeley, California, September 17-19, 2012. 7.3

[121] Weideman, J. A. C. and Reddy, S. C. (2000). A MATLAB Differentiation Matrix Suite. *ACM Transactions on Mathematical Software*, 24(4):465–519. The codes are available at `http://dip.sun.ac.za/~weideman/research/differ.html`. 4.3.2

[122] Wojtacki, K., Lewandowska, J., Gouze, P., and Lipkowski, A. (2015). Numerical computations of rock dissolution and geomechanical effects for CO_2 geological storage. *International Journal for Numerical and Analytical Methods in Geomechanics*, 39(5):482–506. 4.3

[123] Yan, W., Huang, S., and Stenby, E. H. (2011). Measurement and modeling of CO_2 solubility in NaCl brine and CO_2-saturated NaCl brine density. *International Journal of Greenhouse Gas Control*, 5(6):1460–1477. 4.4.3, 4.6

[124] Yortsos, Y. C. (1995). A theoretical analysis of vertical flow equilibrium. *Transport in Porous Media*, 18(2):107–129. 7.6

[125] Zimmerman, R. W. (1991). *Compressibility of Sandstones*. Elsevier, Amsterdam. 3.4

[126] Zoback, M. D. (2010). *Reservoir Geomechanics*. Cambridge University Press, 2nd edition. 2.2, 2.2, 2.2, 2.3, 2.4, 2.4

[127] Zoback, M. D. and Gorelick, S. M. (2012). Earthquake triggering and large-scale geologic storage of carbon dioxide. *Proc. Natl. Acad. Sci USA*, 109(26):10164–10168. 1.1

Grafisk design: Kommunikasjonsavdelingen, UiB / Trykk: Skipnes Kommunikasjon AS

uib.no

ISBN: 978-82-308-3828-0